University of Liège
Faculty of Sciences
Department of Astrophysics, Geophysics and Oceanography

Study of supernovae and massive stars and prospects with the 4m International Liquid Mirror Telescope

Brajesh Kumar

Supervisors:
Dr. Shashi Bhushan Pandey
Prof. Jean Surdej

A thesis submitted in fulfilment of the requirements for the degree of Doctor of Philosophy (Sciences)

in the

Extragalactic Astrophysics and Space Observations group

November 2014

Université de Liège

Faculté des Sciences

Département d'Astrophysique, Géophysique et Océanographie

Etude de supernovae et d'étoiles massives et perspectives d'avenir dans le cadre du projet international du télescope à miroir liquide de 4m

Brajesh Kumar

Promoteurs:

Dr. Shashi Bhushan Pandey

Prof. Jean Surdej

Dissertation présentée en vue de l'obtention du grade de Docteur en Sciences

au sein du groupe AEOS (Astrophysique Extragalactique et Observations Spatiales)

Novembre 2014

Members of the Jury – Prof. S. Habraken (President)
Prof. S. Covino (OAB)
Dr. E. Gosset (ULg)
Prof. P. Hickson (UBC)
Prof. Gregor Rauw (ULg)
Dr. S. B. Pandey (ARIES)
Prof. J. Surdej (ULg)

To,

Maaee, Babuji

and my family

Abstract

Massive stars are the progenitors of the most energetic explosions in the Universe such as core-collapse supernovae (CCSNe) and gamma ray bursts. During their life time they follow various evolutionary phases (e.g. supergiant, luminous blue variable and Wolf-Rayet). They strongly influence their environments through their energetic ionization radiation and powerful stellar winds. Furthermore, the formation of low- and intermediate-mass stars are also being regulated by them.

The Carina nebula region, which hosts a large population of massive stars and several young star clusters, provides an ideal target for studying the feedback of massive stars. In this thesis, we investigated a wide field ($32' \times 31'$) region located in the west of the Carina nebula and centered on the massive binary WR 22. For our study, we used new optical photometry (*UBVRI Hα*), along with some low resolution spectroscopy, archival near infra-red (2MASS), and X-ray (*Chandra, XMM-Newton*) data. We estimated several parameters such as reddening, reddening law, etc. and also identified young stellar objects located in the region under study (Kumar et al., 2014b).

Among the various types of CCSNe, Type IIb are recognized with their typical observational properties. Some of them show clear indication of double peaks in their light curves. The spectral features of these SNe show a transition between Type II and Type Ib/c events at early and later epochs, respectively. It has been noticed that the occurrence of these events is not common in volume limited surveys. In this thesis we have studied the properties of the light curve and spectral evolution of the Type IIb supernova 2011fu. The observational properties of this object show resemblance to those of SN 1993J with a possible signature of the adiabatic cooling phase (Kumar et al., 2013).

When light passes through the expanding ejecta of the SNe, it retains information about the orientation of the ejected layers. In general, CCSNe exhibit a significant level of polarization during various phases of their evolution at different wavelengths. We have investigated the broad band polarimetric properties of a Type II plateau SN 2012aw and compared it with other well-studied CCSNe of similar kinds (Kumar et al., 2014a).

In the framework of the present thesis, we have also contributed to the development of the 4m International Liquid Mirror Telescope (ILMT) project which is a joint collaborative effort among different universities and research institutes in

Belgium, India, Canada and Poland. We performed various experiments including the spin casting of the primary mirror, optical quality tests of the mercury surface, mylar film experiments, etc. The possible scientific capabilities and future contributions of this telescope are also discussed. We propose our plans to identify the transients (specially supernovae) with the ILMT and their further follow-up scheme.

The installation of the ILMT will start very soon at the Devasthal observatory, ARIES Nainital, India.

Résumé

Les étoiles massives sont à l'origine des explosions les plus énergétiques rencontrées dans l'Univers, comme les supernovae résultant de l'effondrement de l'étoile centrale (en anglais « core-collapse supernovae », dont l'acronyme est CCSNe) et les sursauts gamma. Au cours de leur existence, elles suivent différentes phases d'évolution comme la phase de supergéante, d'étoile variable lumineuse bleue et/ou d'étoile de type Wolf-Rayet. Les étoiles massives influencent fortement leur environnement grâce à leur prodigieux rayonnement ionisant et leur puissant vent stellaire. Elles peuvent, en outre, régir la formation d'étoiles à faible masse et d'étoiles de masse intermédiaire.

La région de la nébuleuse de la Carène, qui contient une importante population d'étoiles massives ainsi que plusieurs jeunes amas d'étoiles, constitue une cible idéale pour étudier les effets causés par la présence d'étoiles massives. Dans cette thèse, nous avons étudié un grand champ ($32' \times 31'$) situé à l'ouest de la nébuleuse de la Carène et centré sur l'étoile binaire massive WR 22. Au cours de notre étude, nous avons utilisé de nouvelles données photométriques dans le domaine visible (*UBVRI* et *Hα*), de la spectroscopie à basse résolution ainsi que des données d'archives qui couvrent des domaines de longueur d'onde allant du proche infra-rouge (2MASS) aux rayons X (*Chandra, XMM-Newton*). Nous avons estimé les valeurs de plusieurs paramètres physiques tels que le rougissement interstellaire, la loi de rougissement, etc. et également identifié des jeunes objets stellaires situés dans la région étudiée (Kumar et al., 2014b).

Parmi les différents types de CCSNe, les supernovae de type IIb sont reconnaissables grâce à des traits observationnels distincts. Certaines d'entre elles présentent clairement la présence d'un double pic dans leur courbe de lumière. Les caractéristiques spectrales de ces supernovae montrent une transition entre le type II ayant lieu dans les périodes les plus anciennes et les événements de type Ib/c se déroulant à des époques plus tardives. On a remarqué que la fréquence de ces événements n'est pas élevée dans un survey limité en volume. Dans le présent travail, nous avons étudié les propriétés de la courbe de lumière et l'évolution spectrale de la supernova 2011fu de Type IIb. Les caractéristiques observationnelles de cet objet montrent une forte ressemblance à celles de SN 1993J, avec une signature possible de la phase de refroidissement adiabatique (Kumar et al., 2013).

Lorsque la lumière passe au travers des éjectas en expansion de la supernova, elle conserve les informations relatives à l'orientation des couches éjectées. En général, les CCSNe présentent un niveau élevé de polarisation au cours des différentes phases de leur évolution et à différentes longueurs d'onde. Nous avons ainsi étudié les propriétés polarimétriques à larges bandes de la supernova SN 2012aw de type IIP, dont la courbe de lumière montre un plateau, et comparé celles-ci avec d'autres CCSNe du même type qui ont précédemment fait l'objet d'une étude détaillée (Kumar et al., 2014a).

Dans le cadre de cette thèse, nous avons également contribué à l'élaboration du projet du télescope à miroir liquide international (ILMT, en enanglais International Liquid Mirror Telescope) de 4m de diamètre qui est le fruit d'une collaboration conjointe entre différentes universités et instituts de recherche situés en Belgique, en Inde, au Canada et en Pologne. Nous avons réalisé diverses expériences, y compris le coulage d'une résine par centrifugation du miroir primaire, et nous avons aussi effectué des tests de qualité optique de la surface du mercure et des expériences avec un film Mylar. Les performances attendues de ce télescope sont discutées. Nous proposons notamment une stratégie observationnelle en vue d'identifier au moyen du ILMT des phénomènes astrophysiques transitoires tels que les explosions de supernovae et leur suivi observationnel avec d'autres grands télescopes et instruments.

L'installation du ILMT va bientôt commencer à l'observatoire de Devasthal (ARIES) situé dans l'état de l'Uttarakhand, en Inde.

Acknowledgments

A collaboration between ARIES (Aryabhatta Research Institute of Observational Sciences), India and University of Liège, Belgium provided me a great opportunity to fulfill the need of the present thesis. During my stay at both of these places I received enormous help and support from several people. Here I would like to acknowledge them.

First of all my heartfelt gratitudes and sincere thanks to my thesis supervisors, Prof. Jean Surdej and Dr. Shashi Bhushan Pandey. Since I started my career as a researcher, Dr. Shashi has always been encouraging and motivating me. I improved my scientific capabilities with the help of fruitful discussions with him throughout the tenure of my PhD. Since my association with the ILMT project, Prof. Jean has helped me not only through his scientific intellectualities but also as a guardian during my stay in Belgium. He provided me full freedom and support to work and establish new collaborations. I appreciate your financial supports at different stages of my work. I sincerely thank Prof. Ram Sagar for being with us over many years as the ARIES director and providing great contribution to develop ARIES as a premier institution in the area of astrophysics and atmospheric research. Your motivating words and scientific temperaments will always inspire me.

I acknowledge the members of my thesis committee, for having accepted to read and evaluate this PhD thesis.

I wish to pay my special thanks to my collaborators who have been involved in various affairs of my research work. Thank you Prof. P. Hickson and Prof. J. P. Swings for your precious advice for the development of the ILMT. I am grateful to Prof. G. C. Anupama and Dr. D. K. Sahu for providing data from HCT. Prof. G. Rauw, Dr. E. Gosset, Prof. V. V. Sokolov, Dr. A. S. Moskvitin, Dr. J. Vinko, Dr. J. Gorosabel and Dr. J. Manfroid are highly acknowledged for the fruitful scientific discussions.

I feel grateful to the Academic Committee of ARIES for their support, arranging lectures and discussion. I acknowledge the staff members of the 104 cm and 130 cm telescopes for their assistance during the observations. I also thank the ARIES library, computer, administrative, electrical and mechanical sections for their help in my research activities.

I acknowledge the support and suggestions from Dr. Wahab Uddin and Dr. A. K. Pandey. I thank Drs. Brijesh, Ramakant, Saurabh, Kuntal, Biman, Snehlata,

Jeewan, Hum Chand, Maheswar and Manish for their ever helpful attitude and discussions in various academic matters. I am also thankful to senior scientists and engineers at ARIES who helped me from time to time. Thanks to the supernova research group members at ARIES – Rupak, Subhash and Vijay for their support in observations and useful scientific discussions. I appreciate the observers at ARIES who provided their valuable observing time to support the transient follow-up programs.

It would not have been possible to complete my work without the help, support and encouragement of my colleagues and friends. I am lucky to have their company. Thank you Eswar for your continuous motivation, a lot of things I have learnt from you. I am indebted to Ram Kesh for his company and discussions on various topics. Arti, Manash, Himali, Jessy, Neelam, Sanjeev and Chavi are acknowledged for their timely help in any academic problems. It was enjoyable to discuss various scientific and non-scientific topics with Sumana, Akash, Narendra, Bindu, Ravi, Devesh, Hema, Tapaswini, Krishna, Archana, Sumit, Pradip, Rajiv, Piyush, Raman and Jai. I also thank research fellows Abhishek, Neha, Subhajeet, Parveen, Arti, Aditi, Aabha, Mridweeka, Mukesh and other researchers for their nice company in ARIES.

My stay at Liège could not have been easy and productive without the support and help of my friends, colleagues and well-wishers. I am indebted to François, Arnaud and Ludovic for their nice company and sharing various technical aspects of ILMT. Thank you Andrii and Olga for your helping nature, I still remember the very first evening in ULg when I forgot the way to return to my residing place but luckily found you. I spent fun filled time with Yassine, Tatyana, Chloi, Chandra, Balloo, Shubhayan and Renuka in Liège. Thanks to all of you.

It is impossible for me to forget the help and support of Sylvia and Denise. Whenever I faced any kind of problem either academic or residential, they solved it quickly and made my life easier. I gratefully acknowledge the association of Anna with us always. I felt homely by talking with her. Thank you Catalina for inducing me to learn French.

Most of all, I express my gratitude to my parents whose blessings, love and constant support made me to complete this work. Thank you *Maaee* and *Babuji*, I could have not completed my thesis work without your motivation and encouragement. I am very lucky to have my brothers Devesh, Yogendra and sister Urmila who have taken care of my parents as well as my children. Their belief and trust encouraged

me to do my work with freedom. I am thankful to my wife Suman who has been a constant source of support in my life. You have been my true companion and a constructive force. Dear Prakriti and Anant, I am sorry for not being with you on most of the occasions but I love you and carry the memories of the time we spend together. Thank you both for bringing so much joy in my life. I am grateful to all my near and dear ones who directly or indirectly helped me to complete the present work. And finally, I thank Almighty for his blessings to make this work reality for me!!

I sincerely acknowledge ARIES for the financial support, utilizing the observational facilities for the transient observations during my PhD thesis. I also thankfully acknowledge the University of Liège for the financial support, providing invaluable data and fruitful involvement in the ILMT project.

NOTATIONS AND ABBREVIATIONS

The notations and abbreviations which have been used in this thesis are collected here for a quick reference. All these notations and abbreviations have also been explained on their first appearance in the text.

Notations

Å	Angstrom (unit of wavelength)
α	Right ascension
$'$, arcmin	Arcminute
$''$, arcsec	Arcsecond
cm	Centimeter
$Dec.$, δ	Declination
$^\circ$, deg	Degree
Δm_{15}	Decline in magnitude for the first 15 days after maximum
e^-	Electron
A_λ	Total attenuation at wavelength λ
R_V	Ratio of total to selective extinction
$E(B-V)$	Colour excess in $B-V$ (reddening)
Fig.	Figure
GHz	Giga Hertz
Hz	Hertz (unit of frequency)
H_0	Hubble parameter
ISP_{HG}	Interstellar polarization due to host galactic dust
h, hr	Hour
hrs	Hours
ISP_{MW}	Milky Way interstellar polarization
$J2000$	Epoch of observation
km	Kilometer
λ	Wavelength
kpc	Kiloparsec (unit of distance)
$M_\odot$	Mass of the Sun
Mpc	Megaparsec
m	Meter
mm	Millimeter
μm	Micrometer

milliarcsec	Milliarcsecond
min	Minutes
$\Omega_{\rm m}$	Matter density of the Universe
Ω_{Λ}	Vacuum energy density
P_R	Polarization in R-band
PA	Polarization angle
P_{mean}	Mean polarization efficiency
pc	Parsec (unit of distance)
Ref.	References
RA	Right Ascension
$R_{\odot}$	Radius of the Sun
rms, σ	Root mean square
σ_{P_R}	Uncertainty in the polarization in R-band
σ_{θ_R}	Uncertainty in the polarization angle in R-band
s, sec	Second
Sect.	Section
θ_R	Polarization angle in R-band
$UBVRIJHKH\alpha$	Apparent magnitudes in U,B,V,R,I,J,H,K,$H\alpha$ bands
W	Watt
yr	Year
z	Redshift

Abbreviations

ADU	Analog to Digital Unit
AEOS	Astrophysique Extragalactique et Observations Spatiales
AGN	Active Galactic Nucleus
ARIES	Aryabhatta Research Institute of observational sciencES
ASAS-SN	All-Sky Automated Survey for Supernovae
CBET	Central Bureau for Electronic Telegrams
CCD	Charge Coupled Device
CCSNe	Core Collapse Supernovae

CF	Completeness Factor (CF)
CMD	Colour Magnitude Diagram
CNC	Carina Nebula Complex
CRTS	Catalina Real-Time Transient Survey
CSM	Circumstellar Medium
CSS	Catalina Sky Survey
CTTS	Classical T Tauri Star
DAOPHOT	Dominion Astrophysical Observatory Photometry (software)
DFOT	Devasthal Fast Optical Telescope
DOT	Devasthal Optical Telescope
DST	Department of Science and Technology, Govt. of India
FITS	Flexible Image Transport System
FWHM	Full Width at Half Maximum
ESO	European Southern Observatory
GELATO	GEneric cLAssification TOol
HCT	Himalayan Chandra Telescope
HST	Hubble Space Telescope
iPTF	intermediate Palomar Transient Factory
IAO	Indian Institute of Astrophysics
IAU	International Astronomical Union
IAUC	International Astronomical Union Circular
IIA	Indian Institute of Astrophysics
ILMT	International Liquid Mirror Telescope
IMF	Initial Mass Function *ISM* Interstellar Medium
IRAF	Image Reduction and Analysis Facility (software)
JD	Julian Date
KLF	K-band Luminosity Function
LC	Light Curve
LIDAR	LIght Detection and RAnging
LM	Liquid Mirror
LMT	Liquid Mirror Telescope
LOSS	Lick Observatory Supernova Search
LSST	Large Synoptic Survey Telescope
LZT	Large Zenithal Telescope
2MASS	Two Micron All Sky Survey

MIDAS	Munich Image and Data Analysis System
MS	Main Sequence
MST	Minimal Spanning Tree
NASA	National Aeronautics and Space Administration
NED	NASA Extragalactic Database
NGC	New General Catalog
NIR	Near-infrared
NOAO	National Optical Astronomy Observatories
NODO	NASA Orbital Debris Observatory
NOT	Nordic Optical Telescope
NTT	New Technology Telescope
Pan-STARRS	Panoramic Survey Telescope & Rapid Response System
PLC	Polarization Light Curve
PMS	Pre-main Sequence
PPS	Precision Precast Solutions
PSF	Point Spread Function
PTF	Palomar Transient Factory
QE	Quantum Efficiency
QSO	Quasi Stellar Object
ROTSE	Robotic Optical Transient Search Experiment
SCP	Supernova Cosmology Project
SDSS	Sloan Digital Sky Survey
SI	Spectral Instruments
SN, SNe	Supernova, Supernovae
SNLS	Supernova Legacy Survey
STRESS	Southern inTermediate Redshift ESO Supernova Search
SNID	Supernova Identification
ST	Sampurnanand Telescope
TCD	Two Colour Diagram
USNO	United States Naval Observatory
UT	Universal Time
UVOT	Ultra-Violet Optical Telescope
VLT	Very Large Telescope
WISE	Wide-Field Infrared Survey Explorer
WFI	Wide Field Imager

WR	Wolf-Rayet
WTTS	Weak line T Tauri Star
XMM	X-ray Multi-Mirror Mission
XRT	X-ray Telescope
YSO	Young Stellar Object
ZAMS	Zero Age Main Sequence
ZTF	Zwicky Transient Facility

Contents

List of Figures

List of Tables

Part I

Introduction

Chapter 1

Massive stars, supernovae and liquid mirror telescopes

1.1 Massive stars

There are billions of stars in our universe with different physical properties (e.g., mass, size, temperature, and age). Stars with an initial mass greater than 8 $M_{\odot}$ are broadly classified as massive stars. Rigel, Betelgeuse and Deneb having mass between 15 to 19 $M_{\odot}$ are a few examples of Galactic massive stars, prominently visible with the naked eye. Although in the present-day universe, massive stars are less in number than low and intermediate mass stars (see Kolmogorov, 1941; Salpeter, 1955), their paramount role in astrophysics is well known. They are usually born within the dense core of giant molecular clouds. During their short lifetime, the radiation output from these stars ionizes the interstellar medium and perhaps affects the subsequent formation of stars in their surrounding environments (Abbott, 1982; Leitherer et al., 1992).

Massive stars generally end their life as catastrophic explosions and enrich the interstellar medium in galaxies with the products of the various nucleosynthesis processes that have occurred during their lifetime (see Arnett, 1995, 1996; Fowler & Hoyle, 1964; Hoyle & Fowler, 1960; Woosley & Weaver, 1995). These explosions may be sources of compact objects (neutron stars, black holes) and many high energy objects such as pulsars, magnetars that occur when compact objects remain bound in a binary system (e.g., Remillard & McClintock, 2006). Therefore, indeed massive stars are very important astrophysical sources to understand the evolution of the universe.

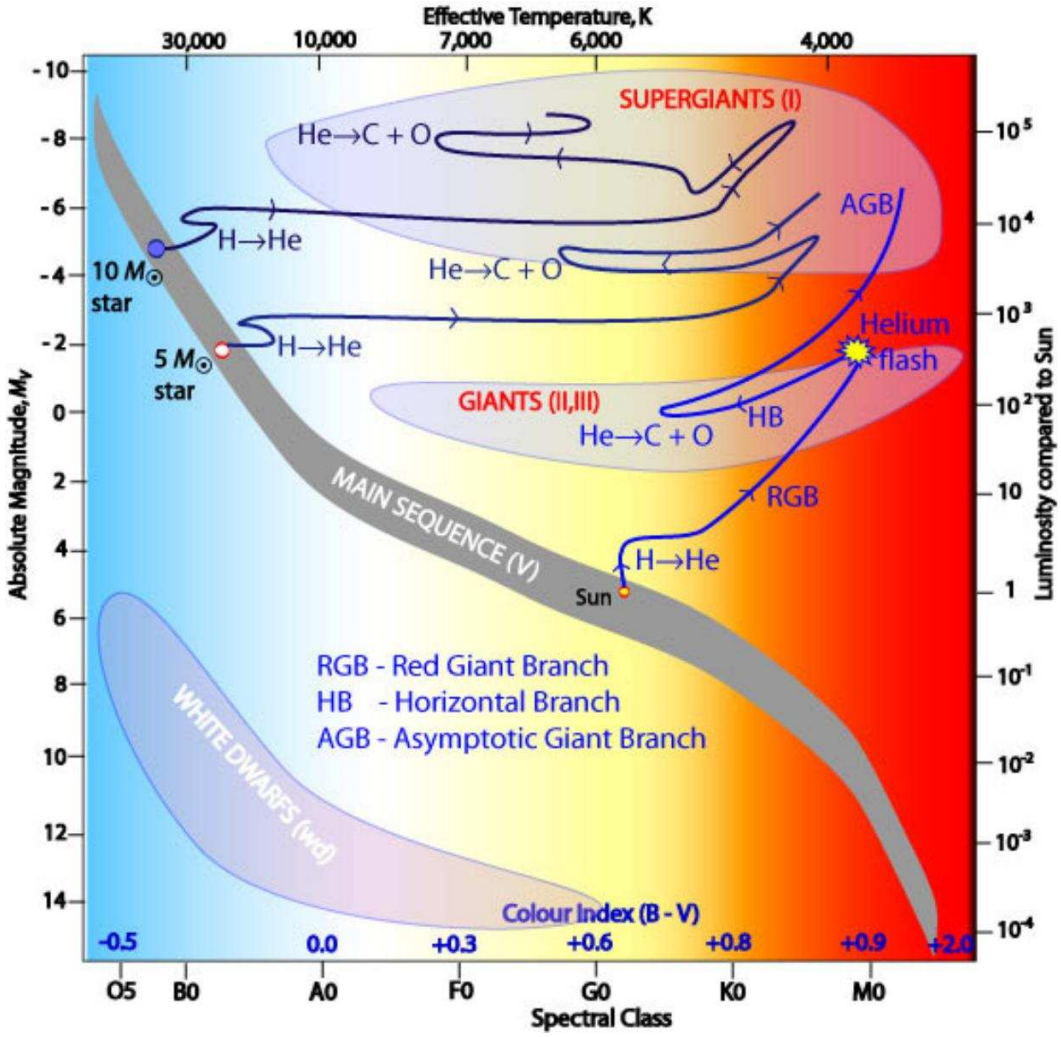

Figure 1.1: Hertzsprung-Russell diagram showing the main sequence tracks for 1, 5 and 10 solar mass stars. Additionally, regions for specific evolutionary phases are indicated. Image credit http://www.atnf.csiro.au.

1.1.1 Evolutionary phases of massive stars

Stars evolve during their life time. They end their formation phase, start their life with the onset of hydrogen burning in their core and become Zero Age Main Sequence (ZAMS) stars in the Hertzsprung-Russell (HR) diagram (see Fig. 1.1). From this stage, the initial mass of the star plays a major role in further evolution along with its composition, luminosity, initial rotational velocity and binarity. The period of core hydrogen burning, via the CNO cycle is known as the main sequence (MS) phase. During the MS phase, stars evolve from ZAMS towards high luminosity and larger radii. Low mass stars like our sun will become red giants and by losing

the outer shells of their atmosphere, they will finally cool to become white dwarfs.

Massive stars start at the ZAMS as an O or early B spectral type. On the main sequence, they will gradually increase in radius, reducing their effective temperature and to some extent increase their luminosity. In their path of evolution, massive stars may follow various phases like supergiant, luminous blue variable and Wolf-Rayet, and finally end their life as supernova explosions. In the following section we briefly describe different characteristics of these stars.

1.1.1.1 Supergiants (SGs)

Supergiant stars are evolved phases of massive stars. They tend to be situated towards the top of the HR diagram to the right of the main sequence (see Fig. 1.1). These stars can be broadly classified into three major groups.

- **Red supergiants (RSGs)**

  Red supergiant stars are massive stars with spectral type M (Chiosi & Maeder, 1986). They may have initial masses less than ∼30 $M_\odot$ (at solar metallicity) evolving beyond the main sequence and passing a fraction of their lives in the cool upper region of the HR diagram. Mostly they have effective temperature from 3000 K to 4000 K, and their luminosity is between 2×10^4 - 6×10^5 $L_\odot$. These stars may lose mass at a rate of 10^{-6} to 10^{-4} $M_\odot$ yr^{-1} (see Mauron & Josselin, 2011). Their radii are very huge, typically 500–1500 $R_\odot$. RSGs are proposed as metallicity indicators (Bergemann et al., 2012, 2013; Davies et al., 2010). They are also proposed as distance and age indicators (see Lançon et al., 2009). Examples: Betelgeuse, Mu Cephei, VY Canis Majoris, KW Sagitarii.

- **Blue supergiants (BSGs)**

  Blue supergiants are very hot and bright stars. They are classified as spectral class B or A (Chiosi & Maeder, 1986) and may have surface temperatures between 20,000K and 50,000K. These stars are highly illustrated in the night sky because of their extreme luminosity. They typically appear in open clusters, irregular galaxies, or the arms of spiral galaxies. At a solar metallicity, recent modelling by Ekström et al. (2012) indicates that a star with a sufficiently large initial mass ignites He in the center during the BSG stage, evolves to the RSG region, and returns to the BSG region during He burning (blue-red-blue evolution). The degree of mixing in radiative layers and the strength of

wind mass loss govern the lowest initial mass for the blue-red-blue evolution. Examples: Rigel, Sk-69 202, Sher 25.

- **Yellow supergiants (YSGs)**

  These are rare stars which appear in the middle of the HR diagram (F to G spectral type Chiosi & Maeder, 1986). Stars with initial masses between approximately 9 $M_{\odot}$ and 40 $M_{\odot}$ briefly pass through this region. Possibly these stars are post-RSGs, and usually have strong mass loss (Drout et al., 2012). In both binary and single-star models, the lifetime of the YSG phase is short-lived, only on the order of tens of thousands of years. Examples: Q Cas, V509 Cas (HD 217476).

1.1.1.2 Luminous blue variables (LBVs)

Luminous blue variable stars (also known as S Doradus stars) were first defined by Conti (1984). LBVs are very massive and intrinsically bright stars. They evolve from O-type main sequence stars to become Wolf-Rayet stars. LBVs are highly luminous (10^6 $L_{\odot}$), exhibit high mass-loss (up to 10^{-4} $M_{\odot}$ yr^{-1}) and sometimes giant eruptions occur (e.g. η Car). They are remarkably photometrically as well as spectroscopically variable on timescales of years (short S Dor phases) to decades (long S Dor phases, c.f. van Genderen, 2001). A significant increase in the degree of mass loss rate also appears in the form of a variability. Most of LBVs have strong winds and strong emission-line spectra (see Humphreys & Davidson, 1994, for various characteristics of LBVs).

On the basis of their luminosity and positions on the H-R diagram, LBVs can be categorized into three broad luminosity types (see Humphreys & Davidson, 1994; Vink, 2012): (i) The most luminous star, η Carinae, occupies a class of its own. (ii) A group containing stars which range from $-11 > M_{bol} > -9.9$. It includes most of the well-known LBVs: R127, S Dor, P Cyg and AG Car. (iii) The lowest luminosity LBVs are classified as R71 type (see Wolf et al., 1981).

1.1.1.3 WR stars

In 1867, Wolf-Rayet (WR) stars were first identified in the Cygnus constellation by Charles-Joseph-Étienne Wolf and Georges-Antoine-Pons Rayet. WR stars originate from O-type stars and have a typical mass range of 10-25 $M_{\odot}$. These stars spend a lifetime of a few 10^5 Myr i.e. 10% of the MS O phase (Crowther, 2007). Due to

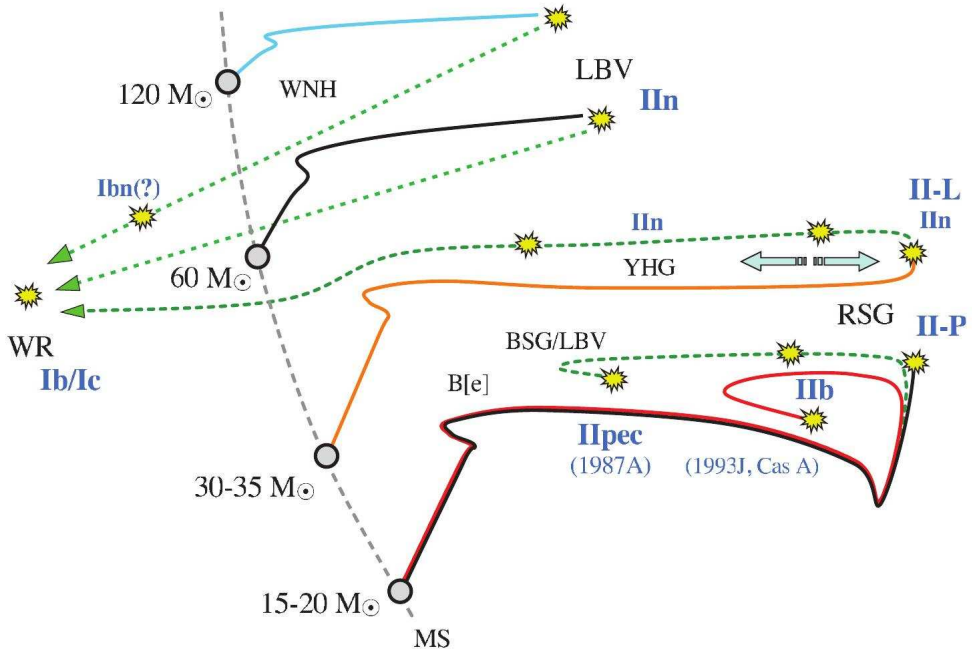

Figure 1.2: A sketch of the upper HR diagram with various evolutionary phases of massive stars. Possible tracks of the progenitors of SN 1987A, SN 1993J and Cas A are also indicated. Figure taken from Smith (2010).

powerful stellar winds ($\sim 10^{-5} M_\odot$ y^{-1}), strong broad emission lines are seen in the spectra of WR stars. The H envelope of the progenitor star is removed by a strong stellar wind or through a Roche lobe overflow if it is in a close binary system (see Crowther, 2007; Maeder & Meynet, 2012).

Based on the spectra (emission line strength and line ratios), WR stars are broadly classified in three major classes i.e. WN, WC and WO. For more details see Crowther (2007). **WN stars** show dominant He and N emission lines; although C, Si, and H emission can easily be seen in some of them. WN stars are further sub-divided as 'Early WN' (WNE) and 'late WN' (WNL). The spectra of **WC stars** are dominated by C and He emission lines while H and N emission lines are absent. 'early' (WCE) and 'late' (WCL) are the two subtypes of WC stars.

WO stars are very rare as compared to WN or WC and exhibit strong O VI $\lambda\lambda$3811-34 emission (Kingsburgh et al., 1995). Based on the relative strength of O V-VI and C VI emission lines, WO have WO1 to WO4 subtypes. In a few cases C VI λ5801-12 is found to be strong in otherwise normal WN stars, these are classified as WN/C stars (Conti & Massey, 1989) and are considered to be an intermediate

phase between the WN and WC stages. During the WC phase, the star spends most of its He burning therefore, WC stars share a large fraction of the total number of WR stars. On the contrary, the WO phase is short (∼10 000 years); consequently WO stars are very rare (see Groh et al., 2013b).

It is important to mention that the absolute number of WR stars and their subtype distribution are metallicity dependent. WR stars are located in the vicinity of massive star forming regions within the Galactic disk. Only a few hundred WR stars are known in the Milky Way while the Galactic disk may contain several thousands of them. van der Hucht (2001) has provided a catalog of 271 Galactic WR stars. However, a new compilation is also available with 637 of these stars[1].

It is believed that the single-star evolution scenario is the major cause behind the majority of the Galactic WR stars, yet there are some exceptions (e.g. V444 Cyg, Vanbeveren et al., 1998). Early WN and WC sub-types are preferably found in metal-poor galaxies, such as the SMC (Massey & Olsen, 2003). Late WC stars are more common at super-Solar metallicity (Hadfield et al., 2005). The binary frequency of WNL stars in the LMC has been found consistent with that of WNL stars in the Milky Way (Schnurr et al., 2008).

Evolutionary phases of WR stars

High rotational velocity can significantly affect a star's evolution due to mixing effects and increased mass loss (Maeder & Meynet, 2001). It must be mentioned here that the real evolution path between different stellar types depends on several parameters such as the metallicity, rotation, magnetic field, rotation, binarity, etc. (see e.g. Chiosi & Maeder, 1986; Maeder & Meynet, 2012).

Mass $\lesssim$ 20 $M_\odot$: The stars which have initial masses $\sim$ 20 $M_\odot$ will evolve to become RSGs, and then they end their life as supernovae:

O/B $\rightarrow$ RSG $\rightarrow$ SN (Type IIP).

20 $M_\odot$ $\gtrsim$ Mass $\lesssim$ 30 $M_\odot$: These massive stars also become supergiants (BSG/RSG) but due to strong stellar winds, their outer layers may be stripped off completely or partially. The helium rich inner layer becomes almost visible and the star will evolve as a WR star. Further evolution of the WR star will result in a supernova explosion of Type IIb/IIL:

O/B $\rightarrow$ (BSG) $\rightarrow$ RSG $\rightarrow$ WR $\rightarrow$ SN (SN IIb, SN IIL).

[1]Available at http://pacrowther.staff.shef.ac.uk/WRcat, v1.10, Feb. 2014

30 $M_\odot \gtrsim$ Mass $\lesssim$ 40 $M_\odot$: Due to mass loss, the outer hydrogen layer is completely removed. These stars have the following evolutionary phases:

O → BSG → RSG → WNE → WCE → SN (SN Ib).

Mass $\gtrsim$ 40 $M_\odot$: Above 40 $M_\odot$, the stars suffer severe mass loss to reach the LBV phase. LBV stars further evolve into WR stars and finally explode as Type Ib or Ic SN:

O → BSG → LBV → WR (WNL, WNE) → SN (SN Ib/c).

Mass $\gtrsim$ 90 $M_\odot$: Very massive stars probably suffer extreme mass loss to become WR stars. These are possible progenitors of hypernovae:

O → WR → SN (SN Ib/c, IIn).

A sketch of the above described evolutionary phases is shown in Fig. 1.2. However, it is important to mention that the sequence of intermediate phases (i.e. LBV and/or RSG) may or may not be always true. The SN explosion may not necessarily follow the sequential order as indicated. Some of the LBVs end their life as SN without going through any further transition phase. In case of the Type IIn SNe, SN 2006gj (Smith et al., 2008b; Smith & McCray, 2007), SN 2006tf (Smith et al., 2008a), the light curves have been found to be consistent with SN ejecta interacting with dense circumstellar material containing 10-20 $M_\odot$. Also, it was found that the progenitor of SN 2005gl (type IIn SN) was consistent with a very LBV star, and not a RSG (Gal-Yam & Leonard, 2009).

Massive stars contribute about 75% to the total number of all exploding supernovae (c.f. Arcavi et al., 2010; Eldridge et al., 2013; Mackey et al., 2003; Smartt et al., 2009; Smith et al., 2011). The remaining fraction belongs to thermonuclear explosions. Although it is still a matter of debate how the collapsing core of the massive star provides the explosion (Burrows, 2013; Janka, 2012), great success has been achieved during the last decades using hydro-dynamical simulations (e.g. Bruenn et al., 2009, 2013; Kotake et al., 2012; Kuroda et al., 2012; Marek & Janka, 2009).

There could be a number of factors which may govern the final fate of massive stars however, mass loss phenomenon plays a crucial role (Meynet et al., 1994). Stars show signature of winds during their evolutionary phases. Intermediate and low mass stars ($M_{ZAMS} \leq 8M_\odot$) exhibit wind evidence when they evolve through the post-AGB phases toward the white dwarf final stage (Pauldrach et al., 1988). These winds become more dominant in massive stars and are directly observable in their spectral energy distributions and spectral lines as soon as the stars are more

luminous than 10^4 $L_\odot$ in the HR diagram (for massive stars of spectral type O, B, and A; Kudritzki & Puls, 2000). The strength of wind depends upon various parameters such as luminosity (L), mass (M), and metallicity (Z) (see Vink, 2008).

In luminous stars, stellar winds are the main cause of mass loss as strong radiation pressure pushes the mass outside (see Castor et al., 1975; Pauldrach et al., 1986). Mass losses play an important role in the advanced evolutionary stages and consequently influence all the outputs of stellar evolution and nucleosynthesis. Mass loss rates of OB stars reach about 10^{-5} $M_\odot$ yr^{-1} with wind velocities up to 3000 km s^{-1}. Due to high mass loss these stars (red giants and supergiants) suffer from high extinction.

1.1.2 Massive stars forming regions and their environments

Massive stars are usually born in dense clusters. The formation of these stars originates with collapsing dense cores inside larger clumps of giant molecular clouds (Williams et al., 2000). It is believed that most stars in our Galaxy are to be born in massive star forming regions and therefore, in the neighborhood of massive stars (see Briceño et al., 2007, and references therein). Presence of high mass stars in star forming regions may profoundly influence their environments compared to those in the regions where only low/intermediate mass stars form (see, e.g., Preibisch et al., 2011c). First, their strong ionizing radiation, powerful stellar winds, and finally, supernova explosions can disperse the surrounding natal molecular clouds (e.g., Freyer et al., 2003), and thus terminate the star formation process. Secondly, the ionization fronts and expanding superbubbles can also compress nearby clouds and consequently trigger the formation of new generations of stars (e.g., Elmegreen, 1998; Gritschneder et al., 2010; Preibisch & Zinnecker, 2007) and new cluster formation (Beuther et al., 2008).

The dense gravitationally bound OB star clusters or loose unbound OB associations[1] are the final products of massive star formation (Briceño et al., 2007; Lada & Lada, 2003). The enormous amount of UV radiation from the OB stars ionizes the surrounding hydrogen, which is termed as HII region (also known as diffuse nebula or emission nebula). Some of the classical examples of OB star clusters are Orion Nebula Cluster (Hillenbrand, 1997; Hillenbrand & Hartmann, 1998); NGC 3603 (Drissen et al., 1995; Moffat et al., 1994); R136 (Massey & Hunter, 1998; Parker

[1]These are loose, easily identifiable concentrations of bright, high-mass stars (see Blaauw, 1964; Humphreys, 1978)

& Garmany, 1993). Scorpius OB2, Orion OB1 (Blaauw, 1964, 1991) are a few examples of OB associations. Studies of these regions have provided very important information. However, it should also be kept in mind that these nearby quiescent regions of low-mass star formation may not be representative, because most stars in our Galaxy form in a very different environment (see Preibisch, 2011).

Characterizing the nature of PMS stars in the vicinity of massive stars may play an important role to understand the characteristics and physical conditions of their evolution. Different stages of PMS are grouped into Classes 0-I-II-III that represent infalling protostars, evolved protostars, classical T-Tauri stars (CTTS) and Weak line T Tauri stars (WTTS), respectively (cf. Feigelson & Montmerle, 1999). Both CTTS and WTTS exhibit emission lines (Balmer emission lines of hydrogen) and absorption line of Li 6707 Å in their spectra but the near infra red (NIR) excess is limited in WTTS. Recent X-ray observations (eg. *Chandra* or *XMM-Newton*) of star clusters boosted general consensus to understand the physical processes of PMS stars.

The Carina nebula in Carina (NGC 3372) provides a unique target for studies of massive star feedback which hosts 65 known O-type stars, 3 WR stars and the well known luminous blue variable η Car (see also Smith & Brooks, 2008, for more details). This region represents the early stages of the birth of an OB association, and it is an environment where this young OB association is triggering the birth of a second generation of stars as they destroy their own natal giant molecular cloud (see Smith & Brooks, 2007). As most of the very massive stars in this complex are located in several clusters (e.g. Tr14, 15 and 16 etc.), a number of wide field surveys have been performed (for example, see Preibisch et al., 2011a,c,d; Roccatagliata et al., 2013; Smith, 2006a; Smith et al., 2010, and references therein).

We have studied the stellar content in a wide field located west of η Carinae and centered on the WN7ha + O binary system WR 22 (HD 92740). The data analysis and results are presented in Chapter 2.

1.2 Core collapse supernovae

In general, lives of massive stars end after millions of years with a catastrophic explosion. Some of these stellar explosions are termed supernovae (SN, plural: supernovae, SNe). Core collapse supernovae (CCSNe) are end stages of those massive stars which have a mass ≥ 8 $M_{\odot}$. An enormous amount of energy (order of 10^{46}

– 10^{49} erg) is liberated during these SNe explosions which outshine the entire host galaxy for a while. Brightness of these events may last over several months to years in different bands of the electromagnetic spectrum. Their ejecta sweep, compress and heat the interstellar medium which finally trigger new star formation processes. SNe explosions play an important role in galaxy formation and evolution.

Historical context

Over more than one thousand years, seven to eight supernovae have exploded in our galaxy and these events have historical records which are entirely based on observations made with the unaided eye. Probably the first bright CCSN was SN 1054. The identification records of this object are reported by Japanese, Koreans, Chinese and Europeans (see Green & Stephenson, 2003). The remnant of SN 1054 is presently recognized as the Crab nebula.

The next well defined and monitored SN was Cassiopeia A (Cas A). On the basis of the present size and rate of expansion of the remnant of this object, it is expected that the Cas A explosion has occurred sometimes in 1667. A latest study indicates that Cas A was a Type IIb supernova (see Sect. 1.2.1 for different types of SNe) and originated from the collapse of the helium core of a red supergiant that had lost most of its hydrogen envelope before explosion (Krause et al., 2008). In the era of modern telescopes, SN 1987A turned out to be the most remarkable SN, consequently this topic received a major boost after its discovery. It has exploded in the Large Magellanic Cloud and was easily observable with the naked eye.

Betelgeuse (α Orionis, HD 39801) is a possible SN candidate in the Orion nebula. Situated at a distance of 152–197 pc (Harper et al., 2008; Smith et al., 2009; van Leeuwen, 2007), it is one of the brightest RSGs (0.9–1.5 $\times$ 10^5 $L_\odot$, Smith et al., 2009). The mass of this star is between 15 and 20 $M_\odot$ (see Harper et al., 2008; Smith et al., 2009). However, its radius is about 1200 $R_\odot$ (Bester et al., 1996; Smith et al., 2009). It is losing its mass with a rate of 2–4 $M_\odot$ yr^{-1} (see Glassgold & Huggins, 1986; Harper & Brown, 2006; Harper et al., 2001; Smith et al., 2009). Astronomers are expecting that Betelgeuse will soon explode as a CCSN.

1.2.1 Observational features and classifications of CCSNe

The Observational features of SNe vary with time. However, in general they are classified on the basis of their light curve and spectrum near maximum light. The

light received from SNe provides valuable information about the underlying stellar activities and their evolution. Near the light maximum, diffusion through the exploded star's expanding debris reflects the size, mass, and the composition of the star along with its energy source. However, the chemical composition of the progenitor interior, synthesis of radioactive material in the SN explosion can be traced out from the decaying post maximum light of the SN (Kirshner, 1990).

Fig. 1.3 shows the cartoon of the general classification scheme of different type of supernovae. Broadly speaking, SNe are classified in two categories – Type I and Type II (Minkowski, 1941). The basic differentiating property is whether or not hydrogen is present in their spectra. In Type II, hydrogen lines are present contrary to Type I, where these lines are absent. Type I SNe are further sub-classified according to the features of spectra. While Type Ia[1] events show a strong 6150 Å Si II absorption line, Type Ib and Ic do not. The later two sub-types (i.e. Ib and Ic) can be further identified on the basis of strong He I lines. Type Ib SNe show He I λ 5876 but Type Ic SNe do not show He lines. Since the progenitors of Type Ib and Ic remove a large amount of their exterior hydrogen and/or helium envelopes before the explosion, they are also termed as stripped envelope core-collapse SNe (Filippenko, 1997).

The explosion sites at which SNe appear, provide important clues about their nature and progenitor star. SNe Ia occur in all types of galaxies, including ellipticals. Elliptical galaxies do not show recent star formation, therefore it is a common understanding that progenitors of Type Ia SNe are old, having low initial mass (c.f. Filippenko, 1991). CCSNe are only found in the arms of the spiral galaxies and H II regions (but see Sanders et al., 2013, and refernces therein). Type II SNe tend to be found in less bright regions than Type Ib and Ic host galaxies. Type Ic are found to be in the brightest regions of their host galaxies and more closely associated with H II regions in comparison to Type II and Ib SNe (Kelly et al., 2008).

- **Type Ib/Ic SNe**

  These SNe also do not show hydrogen in their spectra. The photospheric He I absorption line is dominant in Type Ib but in Type Ic this line is either very weak or absent. They show emission lines of O I λ 5577 at late times however,

[1]SNe of this category do not show hydrogen at any phase of their evolution. At early epochs they exhibit lines of O, S, Si, Mg, and other intermediate-mass elements. The strongest features are the lines of Si II λ 6355 and Ca II H&K $\lambda\lambda$ 3934, 3968. The late time spectrum is dominated by Fe II. These are known as thermonuclear SNe since they show homogeneous spectroscopic and photometric properties (Turatto, 2003).

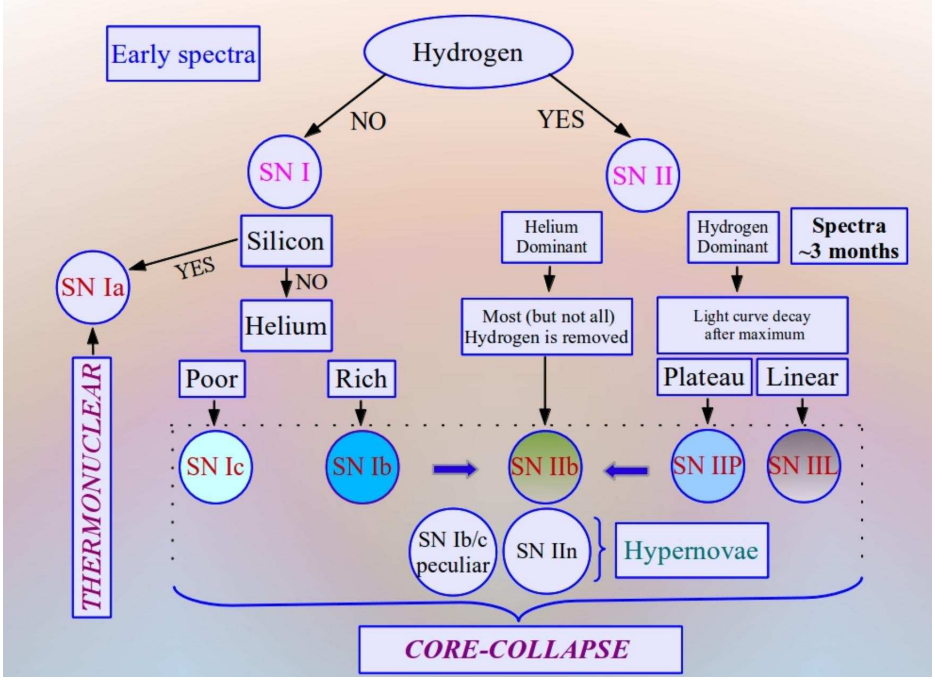

Figure 1.3: Classification scheme of the various types of supernovae based on the early optical spectra and light curve properties.

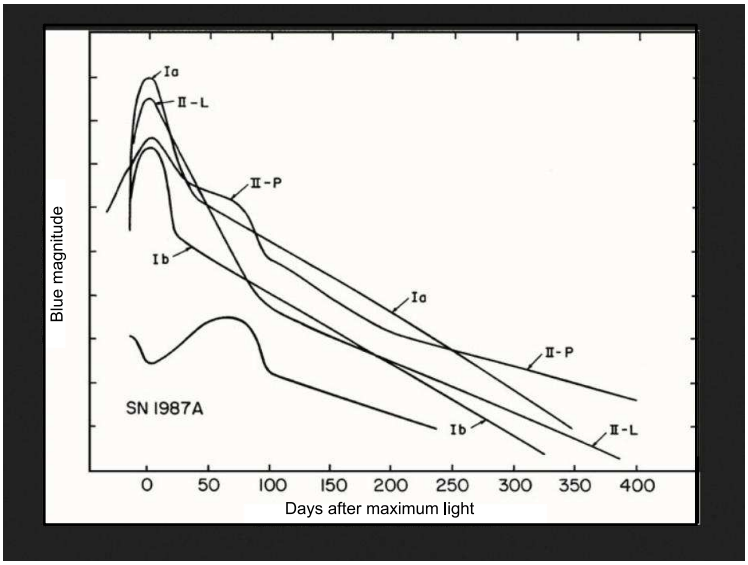

Figure 1.4: Schematic light curves for SNe of Type Ia, Ib, IIP, IIL and the peculiar SN 1987A, taken from Wheeler & Harkness (1990). The light curve for SNe Ib includes SNe Ic as well, and represents an average.

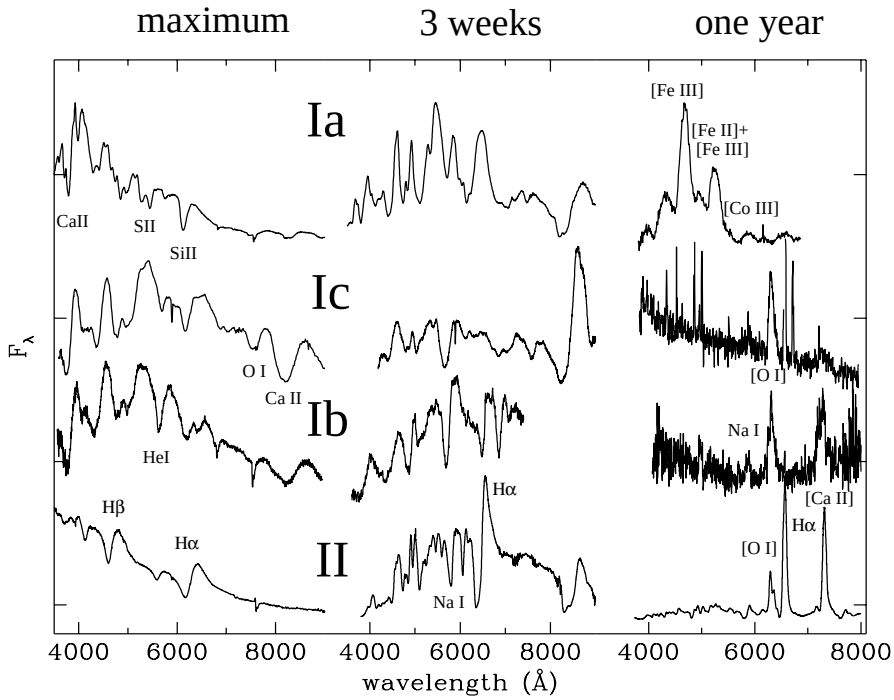

Figure 1.5: Spectral evolution of different types of SNe at various epochs – near maxima, 3 weeks and one year after maxima (from, Turatto, 2003)

Type Ic SNe exhibit strong features of O I λ 7774 absorption and Ca II H&K absorption. The shape of the light curves (in B and V bands) of both SNe are generally like those of Type Ia SNe but are less luminous by a factor of $\sim$4 than Type Ia (c.f. Filippenko, 1991).

There is a subclass of type Ib/Ic SNe which are known as "hypernovae" (Woosley & Weaver, 1982). It is believed that hypernovae represent more energetic events than normal CCSNe (kinetic energy $> 10^{52}$ erg). A few examples of hypernovae are SN 1998bw (Iwamoto et al., 1998), SN 2002ap (Mazzali et al., 2002), SN 2003dh (Mazzali et al., 2003), SN 1997ef (Mazzali et al., 2000). Some of the Type Ic hypernovae have been found to be associated with gamma ray bursts [1].

- **Type IIP('Plateau') SNe**

  These are the most common events in Type II. They contribute about 70% of the total population of Type II SNe (Lennarz et al., 2012). The lumi-

[1] These are the most luminous explosions in the universe with intense flashes of gamma rays (10 keV - 10GeV) and lasting from a fraction of a second to up to a few minutes. They may release an isotropic energy of the order of 10^{54} erg.

nosity of these SNe remains constant for about one hundred days forming a pronounced plateau like shape and then suddenly dropping off. This plateau phase is sustained by cooling down of the shock-heated expanding ejecta by recombination of H, strong Balmer lines and Ca II H&K with prominent P cygni profiles appearing in this phase. The post-plateau light curve is powered by the radioactive decay of ^{56}Co into ^{56}Fe, which in turn depends upon the amount of ^{56}Ni synthesized during the explosion.

- **Type IIL('Linear') SNe**

  The SNe of this category show a linear continuous decline in their light curves although a higher degree of heterogeneity has been observed (Patat et al., 1993, 1994). It is believed that progenitors of these SNe retain a smaller amount of hydrogen in the outer envelope in comparison to the progenitors of Type IIP SNe. In the early spectrum, IIL SNe may show a faint Hα profile which becomes strong at late phases. Some of the Type IIL SNe are dubbed as Type IId SNe (Benetti, 2000, e.g. SNe 1994aj, 1996L, 1996al, 2000P).

- **Type IIn('Narrow') SNe**

  These SNe are diverse in their luminosity and spectral properties and therefore, their progenitors are probably not unique (Smith, 2010). The spectra of these objects are dominated by strong emission lines, most prominently Hα, that have a complex but relatively narrow profile. Narrow emission lines of Type IIn SNe originate from the photoionized dense wind surrounding the progenitor stars (Chugai, 1991). In general, mass-loss rate of at least 10^{-3} to 10^{-2} $M_{\odot}$ per year are required for the narrow emission lines to be produced. Therefore, possible progenitors of this class SNe could be LBVs (Gal-Yam et al., 2007; Taddia et al., 2013) as well as extreme RSGs or YHGs (Smith et al., 2009). One such example of SN IIn and LBV connection has been found in case of the bright SN 2005gl where the progenitor of this SN has disappered in post-explosion images of the *Hubble Space Telescope* (Gal-Yam & Leonard, 2009).

- **Type IIb SNe**

  The spectra and light curves of IIb SNe show interesting features. Initially they show Type II properties (i.e. clear evidence for hydrogen), but later the hydrogen lines become weak or absent in their spectra (like Type Ib/c). An interesting property of the observed light curves of a few Type IIb SNe is the

initial peak and rapid decline, followed by a subsequent rise and a secondary maximum (for example SN 1993J (Barbon et al., 1995; Richmond et al., 1994); SN 2011dh (Arcavi et al., 2011) and SN 2011fu (Kumar et al., 2013)). The first maximum is associated with the shock heating of the hydrogen-rich envelope and the second maximum is caused by the radioactive decay of nickel (Benson et al., 1994). Type IIb SNe are further divided into two subgroups: Type cIIb with compact progenitors, (e.g. SNe 1996cb, 2001ig and 2008ax) and Type eIIb with extended progenitors, such as SNe 1993J and 2001gd (Chevalier & Soderberg, 2010). However, Maeda (2013) has expressed doubt about the existence of these two subgroups.

- **Superluminous SNe**

  In addition to the above described SNe, the past decade has seen the discovery of plentiful superluminous supernovae (SLSNe). They are characterized by peak magnitudes ($M_V \lesssim -21$ mag) that are 2–3 magnitudes higher than those of typical CCSNe and comparable, or brighter than Type Ia observed in the nearby universe (Quimby et al., 2013). Till now around 20 SLSNe have been discussed in the literature (see Gal-Yam, 2012). It should be noted that although in comparison to other Types of SNe, the SNLSe number is very small but due to their copious ultraviolet flux, these SLSN events may become useful cosmic beacons enabling studies of distant star-forming galaxies and their gaseous environments (Gal-Yam, 2012). Spectroscopically SLSNe belong to Type IIn or Ic.

  One of the possible mechanisms behind SLSNe is pair-instability. Extremely massive stars in the mass range of 100 – 260 $M_\odot$ may die in a thermonuclear runaway triggered by pair production instability and resulting as thermonuclear explosion known as pair instability supernova (PISN) (see Barkat et al., 1967; Bisnovatyi-Kogan & Kazhdan, 1967; Fowler & Hoyle, 1964; Fraley, 1967; Heger & Woosley, 2002; Kasen et al., 2011; Kippenhahn & Weigert, 1990; Rakavy & Shaviv, 1967). A number of SNe belonging to this class have been discovered during the last few years (see Gal-Yam, 2012; Gal-Yam et al., 2009; Quimby et al., 2011). PISN explosions completely disrupt very massive stars and a huge amount of newly formed heavy elements are expelled in the surrounding medium. Theoretical models predict that a PISN can produce up to 55 $M_\odot$ Ni (Heger & Woosley, 2002; Kozyreva et al., 2014; Umeda &

Nomoto, 2002). However, in the case of SN 2007bi the spectral and photometric analyses indicate that more than 3 $M_\odot$ of Ni were ejected during the explosion (Gal-Yam et al., 2009). This Ni mass production is significantly higher than the normal CCSN explosion which is limited to about 0.5 $M_\odot$ (Heger & Woosley, 2010; Umeda & Nomoto, 2008; Woosley & Weaver, 1995). SLSNe could also arise due to the pulsational pair instability process (Woosley et al., 2007) or magnetar-driven mechanisms (Dessart et al., 2012; Kasen & Bildsten, 2010; Woosley, 2010).

1.2.2 Explosion mechanisms of CCSNe

The core collapse SNe arise due to the gravitational collapse of massive stars ($M \geq 8$ $M_\odot$). Various stages occuring in CCSNe are shown schematically in Fig. 1.6. At the end stage of their evolutionary path massive stars reach the red supergiant phase or blue supergiant phase and finally explode as supernovae. Several research groups have performed detailed simulations for the pre-collapse evolutionary stages (see e.g. Woosley et al., 2002; Woosley & Weaver, 1995). A series of nuclear reactions occur before the explosion.

Starting from the fusion of hydrogen, the buildup of heavier elements in the core of a massive star continues until the isotope of iron ^{56}Fe is formed. The hydrogen nuclei first fuse to form helium for a few million years in the core of the star until the entire hydrogen is used up. Helium burning sets in when the core contracts, causing an increase in the density and temperature and the Helium fusion forms carbon. Simultaneously the hydrogen burning begins in the surrounding layers. After helium is exhausted, the core contracts further and becomes dense and hot enough to start the carbon burning to form oxygen and neon. Neon further undergoes photo-rearrangement reactions with oxygen and magnesium. Oxygen burns to silicon and silicon burning finally gives iron group elements through a series of reactions.

Since iron is the most stable nucleus, no further fusion reactions take place and thus, finally the star has an inert Fe core surrounded by an onion shell structure (left most in Fig. 1.6) in which silicon, oxygen, neon, carbon, helium, hydrogen are burning in different layers. Electron degeneracy pressure holds the inert Fe core against collapse under its own gravity. Ashes from the sorrounding burning layers keep increasing the mass of the core. Once the core goes beyond the Chandrasekhar limit of about $1.4M_\odot$ there is nothing to support it, and it collapses.

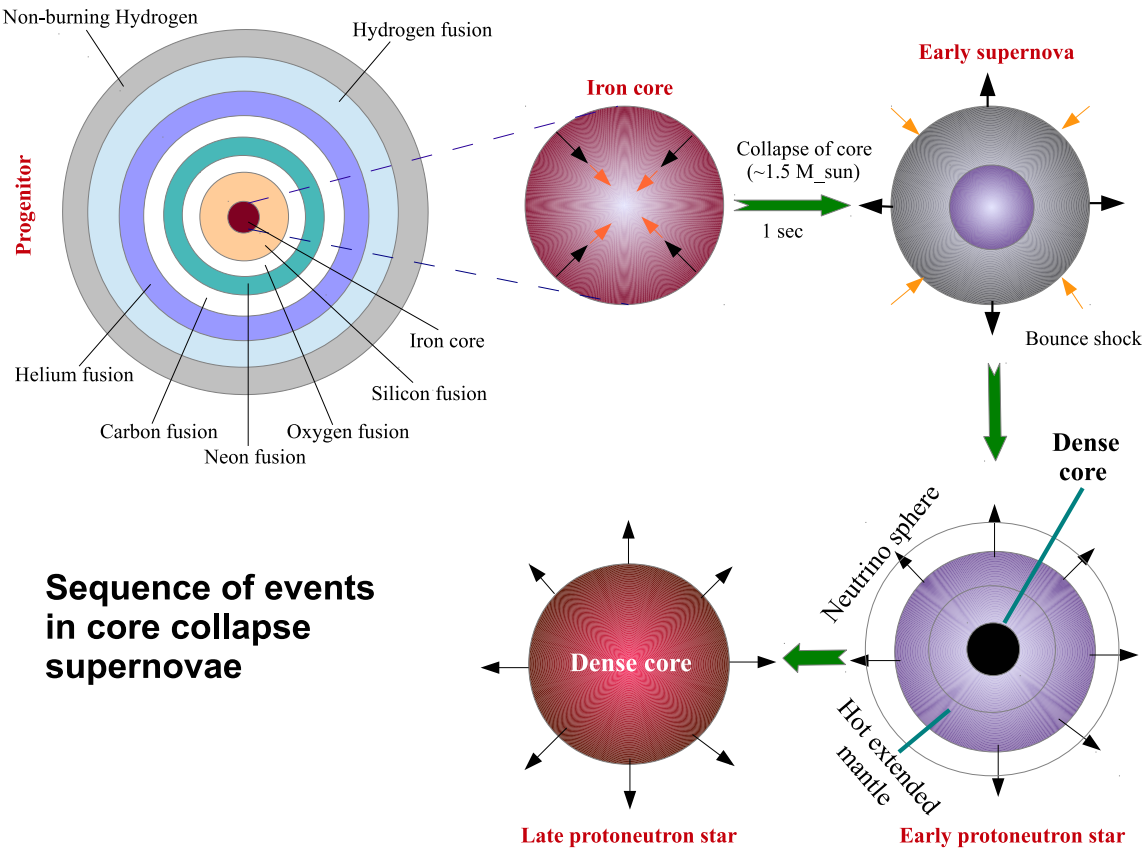

Figure 1.6: Sequence of events during the collapse of a typical stellar core to a nascent neutron star. It begins with a massive star with an 'onion-skin' structure, goes through white-dwarf core implosion, to core bounce and shock-wave formation, to the protoneutron-star stage before explosion, and finally to the cooling and isolated-neutron-star stage after explosion. Figure reproduced from Burrows (2000).

At the very high temperature now present in the core, the photons possess enough energy to destroy heavy nuclei and finally protons are liberated. Under the extreme conditions, the free electrons which had supported the star through degeneracy pressure are captured by these protons to form neutrons and neutrinos. The core is driven to a very dense state in a short time (approximately one second). What happens next is not completely understood, but the collapse results in an explosion in which most of the mass of the star is blown away. More details can be found in pioneering works done by Bethe & Wilson (1985); Burrows et al. (1995); Hoyle & Fowler (1960); Janka & Müller (1993); Müller (1994); Wilson (1983).

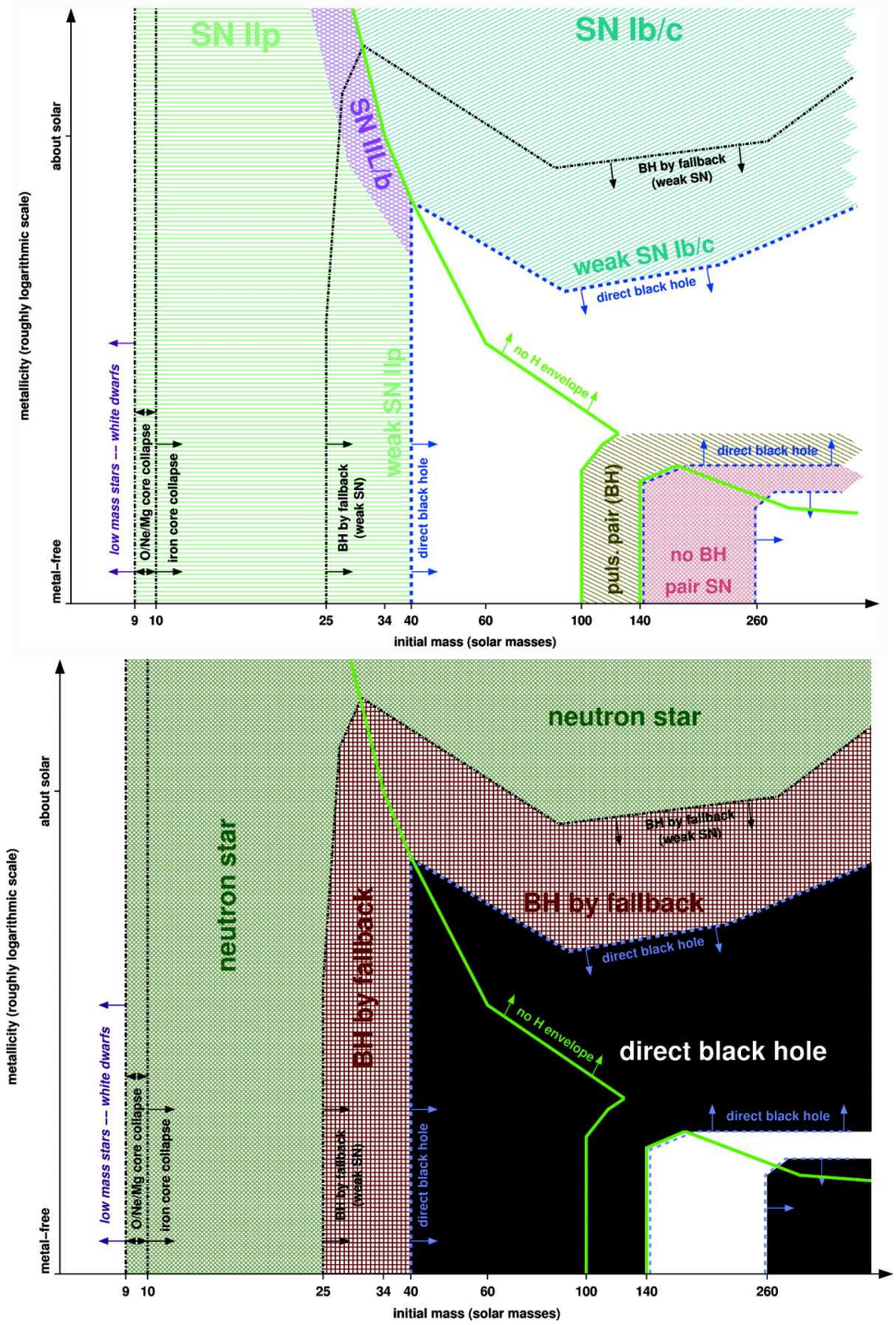

Figure 1.7: Different types of supernovae (upper panel) and their remnants (lower panel) generated from non rotating massive single stars having different initial mass and metallicity. The figures are taken from Heger et al. (2003a). The sharp lines are the boundaries, segregating the outcomes of different kinds of catastrophe generated from the progenitors of different masses and metallicities. A strip of pair-instability supernovae is also shown that leaves no remnant.

Fate of the progenitors of CCSNe

The fate of the progenitors of CCSNe (i.e. massive stars) mainly depends upon their mass, composition at birth and by the history of their mass loss. SN properties depend on the progenitor mass in a complex way. Large differences in the explosion characteristics are possible for small mass differences (Janka, 2012). In the literature, it is often argued that massive stars with initial masses higher than about $>$ 25–30 $M_{\odot}$ collapse to form a black hole rather than a neutron star (Burrows, 2013; Fryer, 1999; Heger et al., 2003b). However, it is not fully understood which stars die as bright supernovae leaving neutron stars as remnants and which stars collapse into black holes with or without supernovae. For example recently Ugliano et al. (2012) have investigated the question of the mass-dependence of the neutron star/black-hole formation and show that stars less massive than 20 $M_{\odot}$ can result in black holes and stars of 20–40 $M_{\odot}$ can end their evolution with the formation of a neutron star.

Fig. 1.7 represents the nature of the explosion (upper panel) and its remnant (lower panel) on the basis of the initial mass of the progenitor and metallicity of the environment. Here, the progenitor is assumed to be non-rotating. For each area (top panel), the type of the SN is indicated. The shading on the bottom panel indicates the area where formation of a black hole is expected; elsewhere, the remnant is a neutron star. In between the dark shaded region (bottom panel, white colour), a strip of pair-instability supernovae is also indicated which leave no remnant. See Heger et al. (2003b) for more details.

1.2.3 Polarization properties of CCSNe

It is interesting that SNe are traditionally assumed to be spherically symmetric. However, there are observational evidences such as aspherical structure of many young Galactic SN remnants (see Fesen, 2001; Manchester, 1987), the asymmetric distribution of material inferred from direct speckle imaging of young SNe (e.g., SN 1987A, Papaliolios et al., 1989) which indicate that there is an asymmetry in the explosion mechanism and/or distribution of the SN ejecta (see also Filippenko & Leonard, 2004).

The first SN polarization observations have been reported by Serkowski (1970). But a direct observational test for the presence of asphericity in SNe was proposed by Shapiro & Sutherland (1982). With growing attention in the SNe study, subsequent polarimetric observations of additional SNe led to the conclusion that

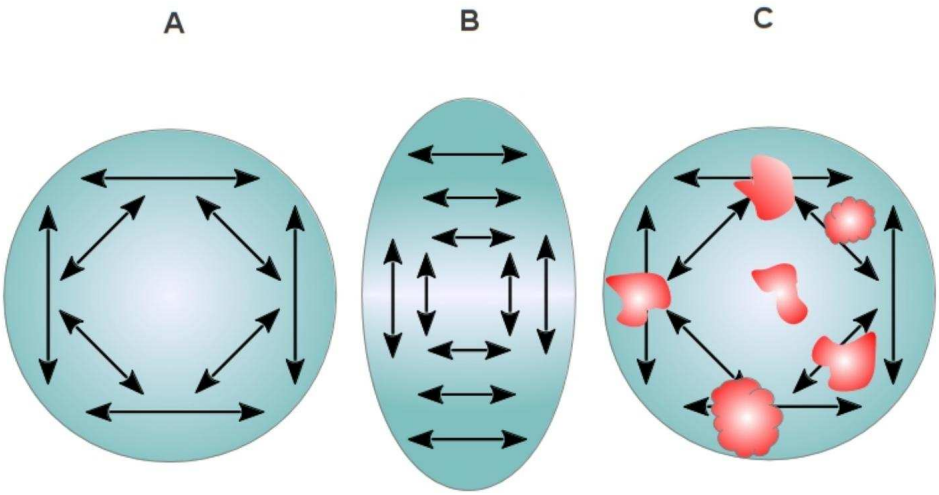

Figure 1.8: Sketch of polarization production in supernovae. Panel A: Zero net polarization is produced in case of a spherical supernova atmosphere. For a non-spherical atmosphere, there will be some level of polarization (panel: B). The uneven blocked light due to clumps of material may also produce a net supernova polarization (panel: C). Image is reproduced from Leonard (2007).

all core-collapse supernovae exhibit polarization (for a recent review, see Wang & Wheeler, 2008).

Polarization is believed to be produced due to electron scattering within the SN ejecta. Millions of light years after the SN explosion occured, the light which passes through the expanding ejecta, it retains the information about the orientation of the layers. In case of a perfectly spherical SN, all directions will be present in the light so, there will be no net direction to the electrical component (zero net polarization, see Fig. 1.8A). However, if the source is aspherical, some parts of the SN matter may provide more light. Finally it will produce a net polarization (see Fig. 1.8B). There may be several other processes inside the SN atmosphere that can imprint a polarization (see Fig. 1.8C). For example clumpy ejecta, asymmetrically distributed radioactive material within the SN envelope (Chugai, 2006; Hoeflich, 1995), etc.

In comparison to Type Ia SNe, CCSNe exhibit a significant level of polarization. Observationally it has been also found that the degree of polarization seems to increase with the decreasing mass of the progenitor envelope at the time of explosion. Type II SNe are typically polarized at a level of ∼1–1.5%. However, Type Ib/c SNe demonstrate a significantly higher amount of polarization than Type II SNe (for

more details, see Gorosabel et al., 2006; Kawabata et al., 2003, 2002; Leonard & Filippenko, 2001; Maund et al., 2013, 2007; Patat et al., 2012; Tanaka et al., 2012; Wang et al., 2003a, and references therein).

We have studied the polarimetric properties of the Type II plateau supernova SN 2012aw. The analysis and results are presented in Chapter 4.

1.2.4 Supernova rate: observational and theoretical overview

With a growing interest in supernovae science, several scientific groups such as the Catalina Real-Time Transient Surveys (Drake et al., 2009), the Lick Observatory Supernova Search (Leaman et al., 2009), the Palomar Transient Factory (Rau et al., 2009), and the La Silla Quest (Hadjiyska et al., 2011) are engaged in supernovae discovery. While the majority of SNe discoveries are done by professional astronomers, groups of amateur astronomers also contribute significantly to it. There are also many robotic telescopes which are involved in prompt optical observations of GRBs and discovery of new SNe (e.g. the Robotic Optical Transient Search Experiment, ROTSE (Akerlof et al., 2000), the Rapid Eye Mount, REM (Covino et al., 2004; Cutispoto et al., 2004; Zerbi et al., 2004), the Globle Master Robotic Net). In addition, there are two upcoming big facilities like the Panoramic Survey Telescope And Rapid Response System, Pan-STARRS (Hodapp et al., 2004) and the Large Synoptic Survey Telescope, LSST (Ivezic et al., 2008). Both of these have a wide field imaging facility which will be useful for transient imaging.

Along with the above cited ground based observatories, there are several space based telescopes which are mainly used in high energy bands. Some of them are the Swift (Barthelmy et al., 2005), the GALaxy Evolution eXplorer, GALEX (Martin et al., 2005), the Rossi X-ray Timing explorer, RXT (Jahoda et al., 1996), the Monitor of All-sky X-ray Image, MAXI (Matsuoka et al., 2009) and the Fermi Large Area Telescope, LAT (Atwood et al., 2009). The most recently launched GAIA spacecraft will possibly detect thousands of supernovae before they reach their maximum brightness.

As can be seen from Fig. 1.9, the SNe discovery enhanced after the SN 1987A event. Presently several hundreds of SNe are discovered every year, though the number of bright SNe (brighter than 15 mag) is still very small. There have been a few volume-limited studies of nearby CCSNe in different SNe search programs[1] (e.g. the Lick observatory Supernova Search, LOSS; the Katzman Automatic Imaging

[1]see also (Arcavi et al., 2010; Cappellaro et al., 1997; Li et al., 2011; Smartt et al., 2009)

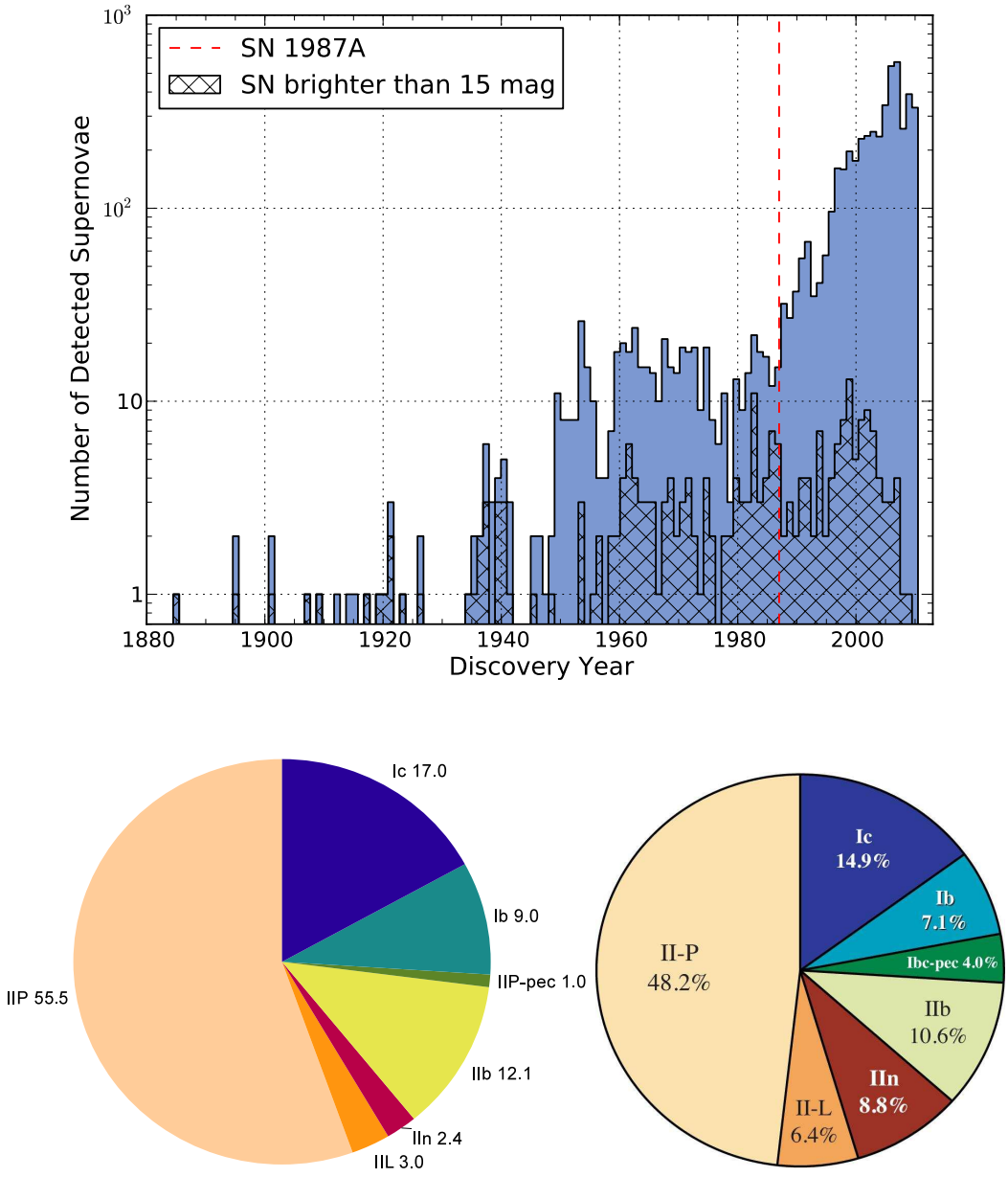

Figure 1.9: Upper panel: Number of detected SNe per year. The discovery year of SN 1987A is marked with a dashed line. The fraction of bright SNe, which have a magnitude at maximum $V < 15$, is indicated by the hatched area. The figure is from Lennarz et al. (2012). Lower left and right panels: percentage of CCSNe of a particular type in the respective studies of Eldridge et al. (2013) and Smith et al. (2011).

Table 1.1: Core-collapse SN fractions from theoretical models (rotating and non-rotating) and observed samples (see text).

SN Type	Non-rotating model (%)	Rotating model (%)	Observed sample (%) (Eldridge et al., 2013)	Observed sample (%) (Smith et al., 2011)
IIP	70.7	64.9	55.5 ± 6.6	$48.2\ ^{+5.7}_{-5.6}$
IIL + IIb	16.2	13.1	15.1 ± 3.4	$17.0\ ^{+4.6}_{-4.0}$
IIn	–	–	2.4 ± 1.4	$8.8\ ^{+3.3}_{-2.9}$
IIpec	–	–	1.0 ± 0.9	–
Ib	8.1	7.8	9.0 ± 2.7	$8.4\ ^{+3.1}_{-2.6}$
Ic	5.0	14.2	17.0 ± 3.7	$17.6\ ^{+4.2}_{-3.8}$

Telescope, KAIT; the Palomar Transient Factory, PTF). Two most recent studies of the observed fraction of CCSNe have been analysed by Smith et al. (2011) and Eldridge et al. (2013). Their results are presented in the lower left and right panels of Fig. 1.9 and summarized in Table 1.1. It is obvious from this figure that the majority of CCSNe belong to the Type II category.

Recently, Groh et al. (2013b) have presented their rotating and non-rotating models of stellar evolution for different SNe progenitors. It is interesting to note that within the errors, the results of Groh et al. (2013b) modelling yields similar SNe rates as those found by Smith et al. (2011) and Eldridge et al. (2013). While the modelled Type IIP SNe rate is relatively high for both rotating and non-rotating models in comparison to the observed ones, the Type Ic SNe rate is found to be slightly low (see Table 1.1).

1.3 Liquid mirror telescopes (LMTs)

Presently it is feasible to construct large high-quality liquid mirrors at a relatively low cost, thanks to advancements in the liquid-mirror technology. This technology is now so proven that large liquid mirror telescopes for astronomical purposes can be easily built and existing advanced techniques can be used (e.g. adaptive optics and interferometry, etc.) to achieve such goals. In the past, several LMTs were proposed but presently only a few of them are in a working condition (see `http://www.astro.ubc.ca/lmt/projects.html`).

Although it is difficult to mention the precise time of the start of the various LMT projects yet some contributors and their role are described below (for more detail see Gibson, 1991; Olsson-Steel, 1986).

1.3.1 LMT history and recent progress

The idea of using a rotating liquid to create a perfect paraboloid was originally proposed by **Sir Isaac Newton** however, **E. Capocci** at Naples Observatory in Italy, first presented an article before the Royal Academy of Belgium in 1850 (Mailly, 1872) about an astronomical telescope made of a parabolic mirror out of a rotating vessel containing liquid mercury. **Henry Skey** in 1872 built the first 0.35m working LMT in Dunedin, New Zealand. He applied two different techniques (regulated electromagnetic device and small hydroelectric turbine) and got clear images using each. Skey work was mainly to show that LMT could work. Professor Robert Wood from the Johns Hopkins University was the person who made LMTs of different sizes. His major contribution was to quantify the optical degrading effects caused by ripples in the reflecting surface of the mercury mirror and minimize it. He concluded that the most practical way to eliminate the surface ripples was to cover the mercury surface with a thin layer of transparent glycerine (glycerol) or castor oil. Despite of early successes in LMT making, Wood stopped the LMT because of its restriction to zenith pointing only and limited astronomical observations.

The present era of LMT research began with Ermanno Borra's important paper (Borra, 1982). He reassessed the details of the theory and the practical limitations of LMTs as true astronomical tools in the light of the technological advances since Wood's time. He proposed the use of near-frictionless air bearings upon which a mercury container could be rotated by a synchronous motor driven by an oscillator-stabilized AC power supply, consequently eliminating the various sources of image-degrading ripples in the mercury's surface (see Gibson, 1991). The preliminary research of Borra's group was based upon the 1.2m ($f/4.58$) LMT, situated at Laval University near Quebec City in Canada. The initial experiments with this telescope can be found in Borra et al. (1985) and Beauchemin (1985). The optical shop tests (e.g. Hartmann, Ronchi, knife-edge, direct imaging etc.) demonstrated that diffraction limited images can be achieved using LMTs. Further optical tests were performed on the 1m ($f/1.6$) and 1.65m ($f/0.89$) LMTs but due to few possible aberrations some of the tests were limited to a 0.4m diameter. In these experiments the thickness of the mercury layer was between 4 to 7 mm (see Borra et al., 1985).

In a second stage of their work, the Laval group produced two mirrors of 1m ($f/4.7$) and 1.2m ($f/4.58$). These telescopes were operated over two consecutive summers in 1986 and 1987. More information can be found in Borra, Beauchemin,

Arsenault & Lalande (1985) and Borra, Content & Boily (1988). A 35mm photographic camera was used to acquire data. The FWHM of a star trail was ∼2" which was excellent considering the sea level location (elevation ∼175m). Furthemore the 1.2m ($f/4.58$) telescope was operated to collect more than 200 hours of data. The major difference of imaging in this later telescope was that the mercury surface was covered with a mylar film to protect the layer from wind induced waves. With continuous progress, presently, the 6.0 m Large Zenithal Telescope (see Sect. 1.3.4) in Vancouver (Canada) is the largest working liquid mirror (Hickson et al., 2007).

1.3.2 Basic principle

The basic principle of the liquid mirror has been described by Borra (1982). If a liquid in a container is rotated around the vertical axis, the equipotential surface of the liquid undergoes two different forces; the gravity that follows a constant vertical downward direction and the centrifugal pseudo-force that is horizontal and increases linearly with the radius. Hence, the surface of the liquid sets in a paraboloid shape under the combined action of both forces (Fig. 1.10; see also Finet, 2013; Magette, 2010).

Suppose a dish with an angular velocity ω and filled with a liquid, is rotating around the vertical z direction as shown in Fig. 1.10. The tangent of the angle between the vertical axis and the net force, θ will be

$$\tan\theta = \frac{dz}{dr} = \frac{\omega^2 r}{g}, \tag{1.1}$$

where $\omega^2 r$ is the centrifugal acceleration and g is the acceleration of gravity.

Now by keeping the origin of the z axis at the fluid surface and integrating Eq. 1.1, we can get the shape of the liquid surface as follows:

$$z = \frac{\omega^2 r^2}{2g}. \tag{1.2}$$

Eq. 1.2 represents the equation of a parabola with a focal length of $F = g/2\omega^2$.

This relation is used to set the angular velocity ω that corresponds to the desired focal length of the telescope at a particular place under constant local gravity.

As shown in Fig. 1.10, the parallel light rays coming from a distant stellar object are reflected from the surface of the parabolic surface and finally get at the focal point which is located at a zenithal distance F from the center of the mirror. An

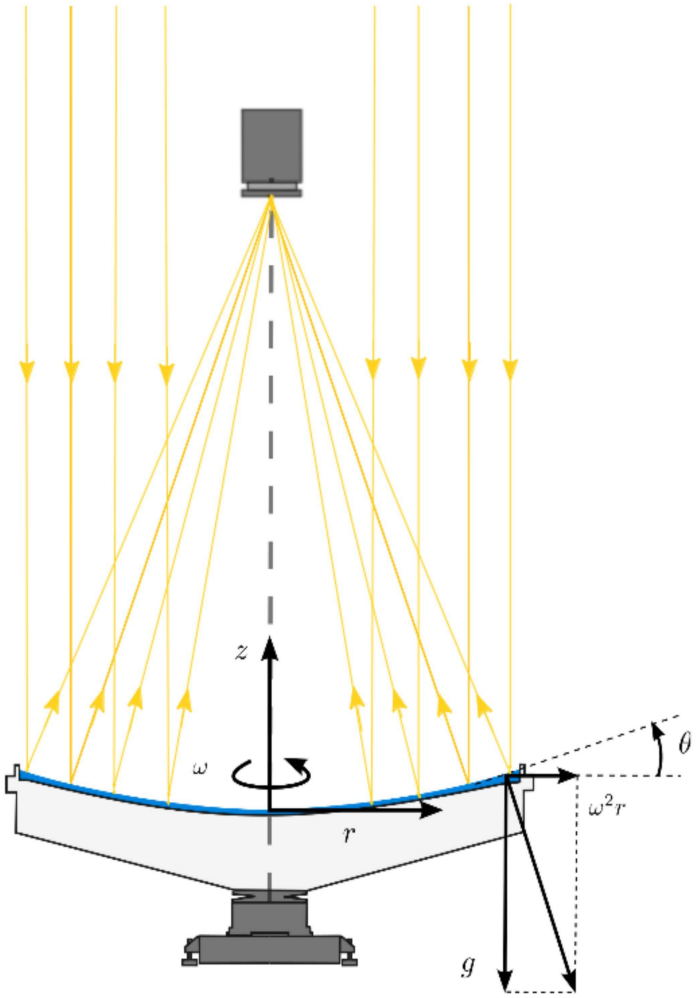

Figure 1.10: Illustration of the basic principle of a liquid mirror telescope. The parabolic shape of the rotating fluid results from the combined effect of the centrifugal acceleration (horizontal arrow) and the gravitational one (vertical arrow). A CCD camera inserted at the focal plane will image the stellar objects passing over the zenith. Figure reproduced from Finet (2013).

imaging equipment (e.g. CCD camera, sensor) can be inserted at this focal point to capture the images.

Initial setup of a LMT

It basically consists of three major components as follows:

- **A dish container**

  - Initially, a large amount of mercury is poured to build up the mirror. With a density of 13.534 g/cm^3, mercury turns out to be a very heavy metal. Therefore, a very stiff and light designed container is important. For the mirrors with average aperture size, a simple dish spincast with epoxy or other polymer-resin has sufficient stiffness.

- **An air bearing system**

  - The optical quality of the liquid surface depends mainly on three parameters: the Hg-air interface, vibrations and the vertical alignment of the rotation axis. The third parameter implies that wobbling should be controlled accurately. A search for the available technology (late 80's) showed that only air-bearings provided a sufficient angular stiffness, low friction and a precision compatible with LMT requirements.

- **A drive system**

  - This component of the mirror has undergone a major evolution in its design since the first LMTs. The drive system has to be regular (precision better than 10^{-6}) and must not transmit vibrations to the mirror that would disturb the surface.The first designs used a synchronous motor linked to a precise oscillator. Previously, the mirror was driven by a belt over a pulley attached to its base. This design was sufficient for a laboratory LMT but it was not adapted for night observing conditions. The system suffered from moisture and temperature variations.

1.3.3 Usefulness of LMTs

The technology advancements have led to construct several sophisticated large glass mirror telescopes and presently, up to ∼10 m diameter telescopes are already contributing to astronomical research. In the upcoming future, various ground based giant-telescope projects are proposed (e.g. the Thirty Meter Telescope (TMT) and the European Extremely Large Telescope (E-ELT)) projects[1]. However, LMTs have some unique advantages over the glass mirror telescopes as described below.

[1]TMT is a 30m diameter telescope project while E-ELT is even larger than TMT consisting of a 39m diameter for the primary mirror; for more details on TMT and E-ELT see the respective sites e.g. http://www.tmt.org/ and http://www.eso.org/public/teles-instr/e-elt/.

- **Inexpensive and simple design**

  The most important advantage of LMTs is its low cost. In comparison to glass mirror telescopes, LMTs will cost an order of magnitude less for an equivalent aperture (Borra, 1982). A 4m diameter glass telescope may cost more than $100 millions, while similar diameter LMs will be very cheap, around $5 millions. More complicated designs of glass mirror will further increase the total cost of these telescopes. Because of its very simple design, a small team of people can run large LMTs working full-time on a specific project. Unlike the traditional telescopes where a rotating dome is essential while the telescope tracks stellar objects in different directions of the sky, the LMT dome structure is very simplified. Only a roll off roof is sufficient in a LMT enclosure building.

- **Easy maintenance**

  LMTs are low maintenance instruments. The complex tracking system of the telescope and of a complex mirror support is not required in LMTs. Therefore, maintenance is very easy. In case of glass mirror telescopes, when dust is settled over the aluminized coating surface of the glass mirror, the telescope is stopped and the mirror is removed from the tube. After that, several days of precise work of mirror aluminizing starts. Once aluminizing is completed, the next step begins with the alignment of the mirror. The whole process of aluminizing and re-installing the mirrors kills several days up to one week before new observations may start. In contrast to glass mirrors, the cleaning of LMs is extremely simple. After a continuous run of 1-2 months, if the image quality of a LMT degrades, the LM can be stopped to clean the mercury. The complete process of cleaning and restarting the liquid mirror takes less than one day.

- **Optimal imaging position**

  Since the seeing and atmospheric transparency are best at zenith, LMTs are mostly benefited with zenithal pointing. Therefore, images obtained with these telescopes are of optimal quality. The image acquisition procedure in LMTs (TDI mode, see Sect.5.2.4 for more details) are in such a way that stellar images are formed by averaging the signal over the whole range of CCD rows. Consequently, the image reduction is done by dividing each column by a one-dimensional flat field.

- **Continuous data acquisition**

  During the observations with traditional telescopes, a significant fraction of the observing time is lost in slewing, making flat acquisition, waiting for the readout time, etc. On the contrary, LMTs continuously observe each night the same strip of sky without losing any time.

- **Appropriate for survey programs**

  LMTs have the restriction to point towards the zenith only but these telescopes are still very suitable for many survey programs (e.g. large-scale structure, galaxy evolution, galaxy survey, long term photometric monitoring programs etc.). As these kinds of survey programs are very much time consuming, it is therefore not possible to get sufficient time on traditional telescopes to properly carrying them out.

1.3.4 Major LMT observing facilities and their scientific contributions

LMTs were initially developed for astronomical research. However, they have been found to be useful in other fields of science, such as LIDAR science, atmospheric science, optical testing and search for space debris. In the following section we present some of the LMT facilities which were working till recently.

2.7 m UBC/Laval LMT

This LMT was jointly built by the Universities of British Columbia and Laval (Canada). It had a 2048 $\times$ 2048 CCD detector to capture images over its field of view. The primary scientific program of this project was to obtain spectral energy distributions of all objects in the survey area. The quasar survey program using this telescope has been presented in Gibson & Hickson (1991). Hickson et al. (1994) have reported the successful construction and operation of the UBC/Laval LMT. The primary mirror and an image obtained are shown in Fig. 1.11.

3.0 m NODO LMT

The NASA Orbital Debris Observatory (NODO) project was located near Cloudcroft in New Mexico. It was a three meter class LMT. This telescope was started

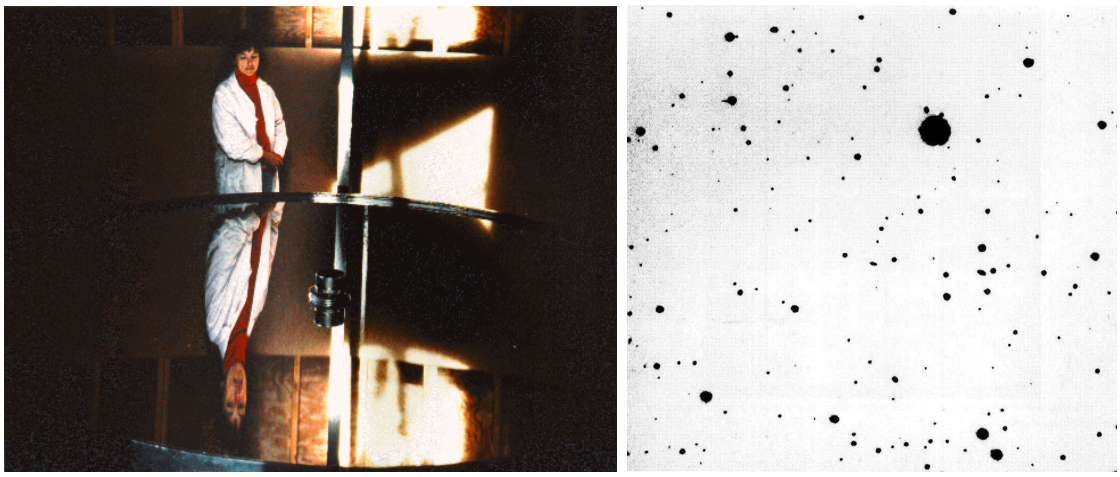

Figure 1.11: Left panel: Image of UBC/Laval 2.7m LMT, taken from http://www.astro.ubc.ca/lmt/lm/. Right panel: Narrow band TDI image (∼19'×19') of a field at 15^h 29^m +49° 14' (1950) obtained with a single scan by this telescope. North is up and east is to the left. The bright star is SAO 045572. The effective integration time is 129 sec. This image has been taken from Hickson et al. (1994).

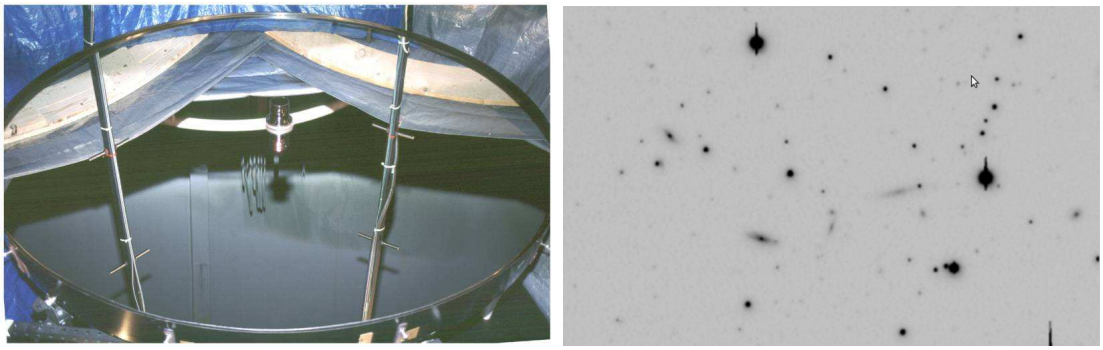

Figure 1.12: Left panel: Image of the primary mirror NODO telescope. Image is from http://www.astro.ubc.ca/lmt/Nodo. Right image: an image taken with the NODO. The field is 5' × 7'. R.A. = 12^h 08^m, Dec. = 33° 00' (J2000.0). Image credit Cabanac et al. (1998).

in October 1996. Its operation lasted up to September 2002, but many of its components have been incorporated into the 6.0m Large Zenithal Telescope (see Sect. 1.3.4). The goal of the NODO LMT was to study the population distribution of orbiting space debris (Potter & Mulrooney, 1997). In addition it was used to survey galaxies and QSOs at redshift < 0.5 (Hickson & Mulrooney, 1998). Using intermediate bandwidth filters (wavelength range 455nm to 948nm), a catalog of thousands of galaxies and quasars was presented in Cabanac (1997) and Hickson & Mulrooney (1998). It also provided photometry and spectral energy distribution for all objects

Figure 1.13: Left panel: LZT primary mirror filled with mercury. Right panel: Colour composite image (100 sec exposure in g, r and i filters) obtained with the LZT. Images taken from http://www.astro.ubc.ca/ lmt/lzt/index.html.

in the strip.

2.0 m CSL LMT

A 2.0m diameter LMT was built at the Liège Space Center (CSL), Belgium. The objective was to get images of the sky with a LM for optical shop tests. The turntable was rotated by means of a motor, connected with a belt. During the operation of the CSL LMT, the functioning of the CCD camera, its cooling and vacuum system were verified. Several optical tests were also performed which are presented in Ninane & Jamar (1996) and Magette (2010). No observations were ever carried out with this telescope because the shape of the mirror got deteriorated with time and the belt was constantly posing problems.

2.65 m Purple crow LIDAR (PCL)

This facility is under the University of Western Ontario (see http://pcl.physics.uwo.ca). It is a laser radar (LIDAR) which operates from the Echo Base Observatory located at Western's Environmental Science Field Station. The primary mirror is a 2.65 m diameter rotating liquid mercury. The LIDAR measurements at this place are useful for the atmospheric research which mainly includes air density, pressure, temperature and water vapor measurements. It could be further useful in research of global warming and weather forecasting.

6.0 m Large Zenithal Telescope (LZT)

The LZT is a 6.0 m class telescope built at the university of British Columbia (UBC) by Prof. Paul Hickson and his team. The aim of this project was to develop and test the technology needed for the LM telescopes that are comparable in size and performance to the largest optical telescopes in existence (Hickson et al., 2007). LZT is located at UBC Liquid-Mirror Observatory (latitude: 49°17.257', longitude: 122°34.374'). This observatory is situated on a hill top in the UBC Malcolm Knapp Research forest at an altitude of 400 m.

The specially designed air bearing used in LZT has a lift capacity of 10 tons and the whole dish including mercury rests upon it. Filtered and dehumidiated compressed air is transferred inside the air bearing for providing different pressures to the upper and lower thrust plates of the bearing. Once the mirror is formed, a 12μm thick mylar film is used to cover the mirror to protect the mirror surface from wind effects (see Sect. 6.4 for details about mylar film tests to be used for the ILMT).

Regular scientific operations with LZT were started in October 2005. A comprehensive description of the LZT project is presented in Hickson et al. (2007) (see also Hickson et al., 1998). An analysis of the image quality is described in Hickson & Racine (2007).

The principal scientific goals of the project include supernovae detection and to measure the spectral energy distributions and redshifts of over millions of galaxies and quasars. These observations will be helpful to study cosmology, the large-scale structure of the universe, and the evolution of galaxies. Since 2008, a new project has been started named LZT LIDAR[1] (see Pfrommer et al., 2008). This project has two main scientific goals. One is to explore in detail the structure and dynamics of the upper atmosphere of the Earth, and the processes that produce and destroy metallic atoms there. The second is to determine the impact of variability in this region on adaptive optics systems planned for the next generation large ground-based optical and infrared telescopes such as the TMT (Thirty Meter Telescope, `http://www.tmt.org/`) and E-ELT (European Extremely Large Telescope, `http://www.eso.org/sci/facilities/eelt/`).

In addition to the above stated LMTs, several other projects were also proposed in the past such as ALPACA - Advanced Liquid mirror Probe for Astrophysics, Cosmology and Asteroids, LAMA - Large Aperture Mirror Array, LLMT - Lunar

[1]LIght Detection And Ranging

Liquid Mirror Telescope (for more details visit http://www.astro.ubc.ca/lmt/projects.html). Utilizing the emergence of the LM technology, a 4.0m LM project (known as the International Liquid Mirror Telescope, ILMT) is in an advanced stage. The first light of this telescope is expected in the year 2015. Part III of this thesis is associated with it where we describe the design, construction, operational experiments made with the ILMT and also present the current status of the telescope site.

Part II

Massive stars and supernovae

Chapter 2

Study of the Carina nebula massive star forming region

2.1 Introduction

Massive stars ($M > 8-10\ M_{\odot}$) in star-forming regions significantly influence their surroundings. In the course of their life, the feedback provided by their energetic ionization radiation and powerful stellar winds regulate the formation of low- and intermediate-mass stars (Garay & Lizano, 1999; Zinnecker & Yorke, 2007). After a short life time ($\lesssim 10^7$ years), they explode as supernovae or hypernovae (supernovae with substantially higher energy than standard supernovae) enriching the interstellar medium with the products of the various nucleosynthesis processes that have occurred during their lifetime (see Arnett, 1995, 1996; Nomoto et al., 2003; Woosley & Weaver, 1995, and references therein). The shock waves produced in these events may trigger new star formation (e.g. Elmegreen, 1998). Characterizing the young stellar objects (YSOs) in massive star-forming regions is therefore of utmost importance to understand the link with the neighboring massive star population.

The Carina nebula (NGC 3372) region, which hosts several young star clusters made of very massive stars along with YSOs, provides an ideal laboratory for studying the ongoing star formation (see Smith & Brooks, 2008). The CO survey of this region demonstrates that the Carina nebula is on the edge of a giant molecular cloud extending over ∼130 pc and has a mass in excess of $5 \times 10^5\ M_{\odot}$ (see Grabelsky et al., 1988). It contains ∼200 OB stars (Povich et al., 2011; Smith, 2006a), more than ∼60 massive O stars (see Feinstein, 1995; Smith, 2006a), and three WN(H)[1]

[1]These are late type WN stars with hydrogen; for a review of WR stars, see Abbott & Conti

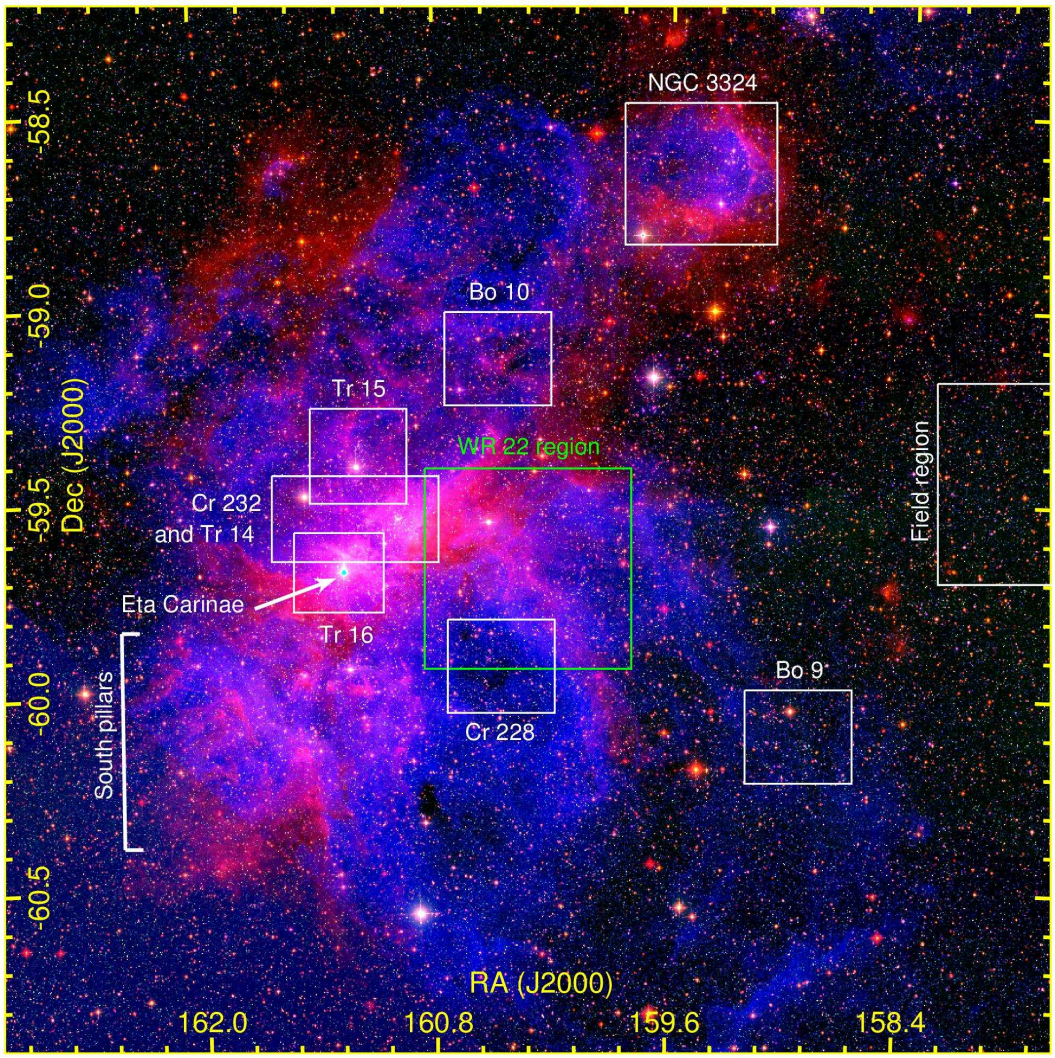

Figure 2.1: Colour composite image of the large ($2.7^\circ \times 2.7^\circ$) area containing the Carina Nebula and centered at $\alpha(\mathrm{J2000}) = 10^\mathrm{h}\ 41^\mathrm{m}\ 17''\!.5$ and $\delta(J2000) = -59^\circ\ 40'\ 36''\!.9$. This RGB image was made using the WISE 4.6 μm (red), 2MASS K_s band (green), and DSS R band (blue) images. Approximate locations of different star clusters (Tr 14, 15, 16; Bo 9, 10; Cr 228, 232, and NGC 3324) are denoted by white boxes. η Carinae is marked by an arrow and in the lower left part of the image, south pillars (Smith et al., 2000) are seen. The region covered in the present study is shown by the green box. Part of the selected field region can be seen in the extreme western part of the image. North is up and east is to the left. Image from Kumar et al. (2014b).

stars (i.e. WR 22, 24, and 25; Smith 2006a; Smith & Brooks 2008).

Initially, on the basis of infrared (IR) and molecular studies of the central Carina

(1987) and Crowther (2007).

region, several authors (see Cox, 1995; de Graauw et al., 1981; Ghosh et al., 1988; Harvey et al., 1979) have reported that the Carina nebula is an evolved HII region and that there is a paucity of active star formation. However, following the detection of several embedded IR sources, Smith et al. (2000) showed that star formation is still going on in this region. Later, Brooks et al. (2001) also identified two compact HII regions possibly linked with very young O-type stars. Rathborne et al. (2002) traced the photodissociation regions (PDRs) that are expected to be present in the massive star-forming regions. They conclude that the star formation within the Carina region has certainly not been completely halted despite prevailing unfavorable conditions imposed by the very hot massive stars (see for more details Claeskens et al., 2011). Detection of proplyds-like objects in these regions (see Dufour et al., 1998; Smith et al., 2003) proves the ongoing active low- and intermediate-mass star formation. Very recently, an isolated neutron star candidate discovered in the neighborhood of η Carinae suggests there have been at least two episodes of massive star formation (Hamaguchi et al., 2007; Pires et al., 2009).

Figure 2.1 shows a three-colour composite image, using the WISE 4.6 μm, 2MASS K_s band and DSS R band images, of the large region of the Carina nebula. The prominent V-shaped lane is associated with the nebular complex and consists of dust and molecular gas (Dickel, 1974). Trumpler (Tr) 16 is located near the central portion of this lane and thought to be $\sim$3 Myr old. This cluster also hosts one of the most massive stars in our galaxy, η Carinae (indicated by an arrow in the image), which has an estimated initial mass $\gtrsim 150$ M$_\odot$ (Hillier et al., 2001). Tr 14 is younger with an age of < 2 Myr (Carraro et al., 2004; Smith & Brooks, 2008). In between Tr 14 and Tr 16, there is another cluster named Collinder (Cr) 232. The cluster Cr 228 near Tr 16 is very young and probably located in front of the Carina nebula complex (Carraro & Patat, 2001). Finally NGC 3324 (upper part in the image) is believed to be located inside the Carina spiral arm and embedded in a filamentary elliptical shaped nebulosity (see Carraro et al., 2001).

Since the Carina nebula is a typical star-forming region, feedback from the young and massive stars has cleared out the nebulosity in the central region and a large number of elongated structures, so-called Pillars (Smith et al. 2000, seen in the lower left part of the image) have formed in the outer regions. We can see many of them in the southern part of the image. We also observe large bubbles in the northern region, probably caused by the gusts of hot gas leaking from the powerful stars at the center of the nebula (Smith et al., 2000). The central clusters Tr 14 and Tr 16

tend to be devoid of star formation (Smith & Brooks, 2008), but there are active sites of ongoing star formation in the outer regions of the nebula. In the present study, our aim was to understand the star formation in one of the peripheral regions of the Carina nebula, influenced by the presence of hot massive stars.

Because of its relatively low obscuration and proximity and its rich stellar content, this nebula is one of the most extensively explored nearby objects (Smith & Brooks, 2008). Several wide-field surveys of the Carina Nebula complex (CNC) have recently been carried out at different wavelengths. The combination of a large *Chandra* X-ray survey (see Townsley et al., 2011) with a deep near-infrared (NIR) survey (Preibisch et al., 2011c,d), Spitzer mid-infrared (MIR) observations (Povich et al., 2011; Smith et al., 2010), and Herschel far-infrared (FIR) observations (Gaczkowski et al., 2013; Roccatagliata et al., 2013) provides comprehensive information about the young stellar populations. In the remainder, we discuss our new optical photometry, along with some low resolution spectroscopy, archival NIR (2MASS), and X-ray (*Chandra*, *XMM-Newton*) data of a field located west of η Carinae (hereafter CrW) and centered on the WN7ha + O binary system WR 22 (HD 92740; Conti et al., 1979; Crowther et al., 1995; Gosset et al., 2009, 1991; Hamann et al., 1991; Niemela, 1979; Rauw et al., 1996; van der Hucht et al., 1981) positioned just outside the V-shaped dark lane.

2.2 Observations and data analysis

2.2.1 Optical photometry

A set of $UBVRI$ and $H\alpha$ observations of CrW (α(J2000) = $10^{\rm h}$ $41^{\rm m}$ $17''.5$ and $\delta(J2000) = -59°$ $40'$ $36''.9$) were obtained with the Wide Field Imager (WFI) instrument at the ESO/MPG 2.2 m telescope at La Silla in March 2004 (service mode, 72.D-0093 PI: E. Gosset). The WFI instrument has a field of view of about $34' \times 33'$, covered by a mosaic of eight CCD chips with a pixel size of 0.238 arcsec. The observations typically consisted of three dithered frames with a short exposure time (about 50s in U, 10s in $BVRI$, and 100s in $H\alpha$) and three dithered frames with about 18 times longer exposures to allow measurements of both bright and faint objects. Additional frames of a field located closer to the main Carina region were also acquired in order to connect our photometric system to those of previous works.

The data were bias-subtracted, flat-fielded and corrected for cosmic-rays using the standard tasks available in *IRAF.*[1] The photometry in the natural system was obtained with the *DAOPHOT*[2] (Stetson, 1987, 1992) software. We also performed aperture photometry of Stetson's and Landolt's standard fields and of the additional frames. All of them, along with ESO recommendations, were used to determine the colour transformation coefficients. The zero points were fixed via comparison with data published by Massey & Johnson (1993), Vazquez et al. (1996), DeGioia-Eastwood et al. (2001) and mainly with the unpublished catalog of Tapia et al. (2003).

The following equations were adopted, together with appropriate zero points:

$$V_{std} = V_{wfi} - 0.107 * (B - V)_{wfi},$$

$$(B - V)_{std} = 1.440 * (B - V)_{wfi},$$

$$(U - V)_{std} = 1.08 * (U - V)_{wfi} + 0.02 * (B - V)_{wfi},$$

$$(V - R)_{std} = 0.98 * (V - R)_{wfi} - 0.09 * (B - V)_{wfi},$$

$$(V - I)_{std} = 0.94 * (V - I)_{wfi} - 0.08 * (B - V)_{wfi}.$$

The colour transformation coefficients and the zero points obtained above were then used further to calibrate the aperture photometry of 50 well-isolated bright sources in the CrW region. The astrometry was established by matching the instrumental coordinates with the 2MASS point source catalog. The rms of the astrometric calibration is $0.15''$ in RA and $0.19''$ in Dec. To avoid source confusion due to crowding, PSF (point spread function) photometry was collected for all the sources in the CrW region. PSF photometric magnitudes were generated by the *ALLSTAR* task inside the *DAOPHOT* package. The calibrated aperture magnitudes of the same 50 stars were then used to calibrate the magnitudes of all the stars in the CrW region obtained from the PSF photometry.

These final PSF calibrated magnitudes were used in further analysis. The typical *DAOPHOT* errors are found to increase with the magnitude and become large (≥ 0.1 mag) for stars fainter than $V \geq 22$ mag. The measurements beyond this magnitude

[1] *IRAF* (Image Reduction and Analysis Facility) is distributed by the National Optical Astronomy Observatories, which is operated by the Association of Universities for Research in Astronomy, Inc. under co-operative agreement with the National Science Foundation.

[2] *DAOPHOT* stands for Dominion Astrophysical Observatory Photometry.

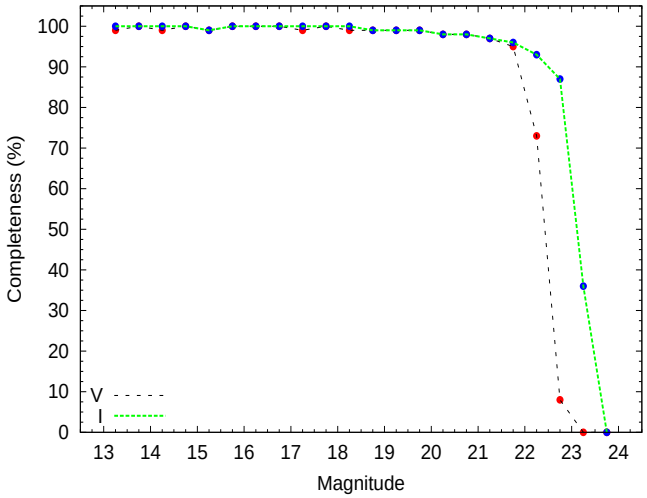

Figure 2.2: Completeness levels for the V and I bands as a function of magnitude derived from an artificial star experiment (*ADDSTAR*, see Sect. 2.2.2).

were not considered in our analysis. In addition, for the present study, we used only the $32' \times 31'$ inner area of the mosaic.

2.2.2 Completeness of the data

There could be various reasons (e.g., crowding of the stars) that the completeness of the data sample may be affected. Establishing the completeness is very important to study the luminosity function (LF)/mass function (MF). The *IRAF* routine *ADDSTAR* of *DAOPHOT* II was used to determine the completeness factor (CF). Briefly, in this method, artificial stars of known magnitudes and positions from the original frames are randomly added, and then artificially generated frames are reduced again by the same procedure as used in the original reduction. The ratio of the number of stars recovered to those added in each half a magnitude bin gives the CF as a function of magnitude. In Fig. 2.2, we show the CF as a function of the V magnitude. As expected, the CF decreases as the magnitude increases. Our photometry is more than 90% complete up to $V = 21.5$ and $I = 22$. For the distance of 2.9 kpc (cf. Sect. 2.3.3), this will limit our study to pre-main-sequence (PMS) stars more massive than 0.5 $M_{\odot}$.

2.2.3 Spectroscopy

For a set of 15 X-ray sources[1] identified using *XMM-Newton* observations in the CrW field (see Claeskens et al., 2011), we obtained their optical spectra between 4 and 6 March 2003 using the EMMI instrument mounted on the ESO 3.5 m New Technology Telescope (NTT) at La Silla (PI: E. Gosset). This instrument was used in the Red Imaging and Low Dispersion Spectroscopy (RILD) mode with grism #5 (wavelength range 4000 - 8700 Å). One spectrum was obtained with the VLT + FORS1 (see Claeskens et al., 2011). The data were reduced in the standard way using the `long` context of the ESO-*MIDAS* (European Southern Observatory Munich Image Data Analysis System) package[2]. Since the observing conditions were favorable during our run, target spectra were calibrated using the flux spectrum of the standard star LTT 2415 (Hamuy et al., 1992).

2.2.4 Archival data: 2MASS

We used the 2MASS Point Source Catalog (PSC) (Cutri et al., 2003) for NIR (JHK_s) photometry of point sources in the CrW region. This catalog is said to be 99% complete up to the limiting magnitudes of 15.8, 15.1 and 14.3 in the J (1.24μm), H (1.66μm), and K_s (2.16μm) bands, respectively[3]. We selected only those sources that have a NIR photometric accuracy < 0.2 mag and detection in at least the K_s and H bands. Since the seeing (∼FWHM of the stars intensity profile) for the WFI observations was around 1 arcsec, the optical counterparts of the 2MASS sources were searched using a matching radius of 1 arcsec.

2.3 Basic parameters

2.3.1 Reddening

The $(U-B)/(B-V)$ two-colour diagram (TCD) was used to estimate the extinction toward the CrW region. In Fig. 2.3, we show the TCD with the zero-age-main-sequence (ZAMS) from Schmidt-Kaler (1982) shifted along the reddening vector with a slope of $E(U-B)/E(B-V) = 0.72$ to match the observations. This shift

[1] Throughout this paper, we used the numbering convention of X-ray sources as introduced in Claeskens et al. (2011).

[2] ESO-*MIDAS* has been developed by the European Southern Observatory.

[3] http://tdc-www.harvard.edu/catalogs/tmpsc.html

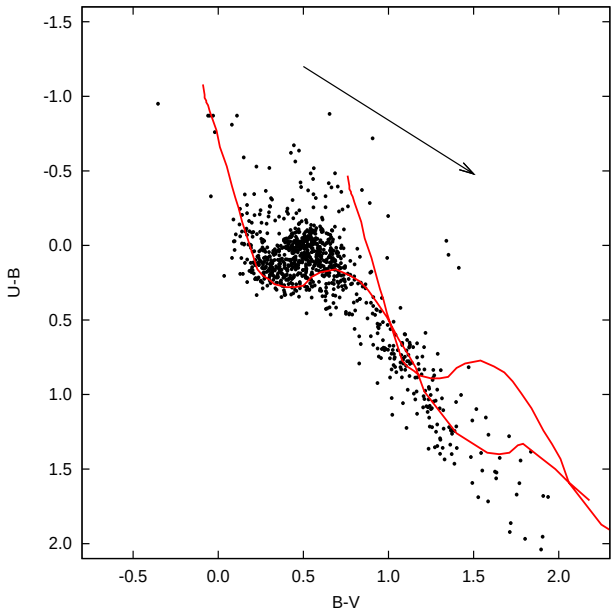

Figure 2.3: $(U-B)/(B-V)$ two colour diagram for all the stars lying in the CrW region with $V < 16$ mag. The two continuous curves represent the ZAMS by Schmidt-Kaler (1982) shifted for the minimum ($E(B-V) = 0.25$, left) and maximum ($E(B-V) = 1.1$, right) reddening values. The reddening vector with a slope of 0.72 and size of $A_v = 3$ mag is also shown.

will give the extinction directly toward the observed CrW region. The distribution of stars shows a wide spread in the diagram along the reddening line indicating the clumpy nature of the molecular cloud associated with this star-forming region. If we look at the MIR image of CrW (for detail see Sect. 2.5 and Fig. 2.16), we see the dark dust lane along with several enhancements of nebular materials at many places that are likely to be responsible for this spread in reddening. Figure 2.3 yields a minimum reddening value $E(B-V)$ of 0.25 with a wide spread leading to values up to 1.1 mag. Recent works (see Table 2.1) also indicate a spread in the value of $E(B-V)$ ($\sim$0.3 $-$ 0.8 mag) toward the η Carinae region. Smith & Brooks (2008) suggest that a detailed optical study of the Carina nebula can easily be done since our sight line toward this nebula suffers little extinction and reddening compared to most of the massive star-forming regions. This seems true for the line of sight up to the first stars belonging to the complex, but it could perhaps not remain applicable to objects farther away and embedded inside the molecular cloud.

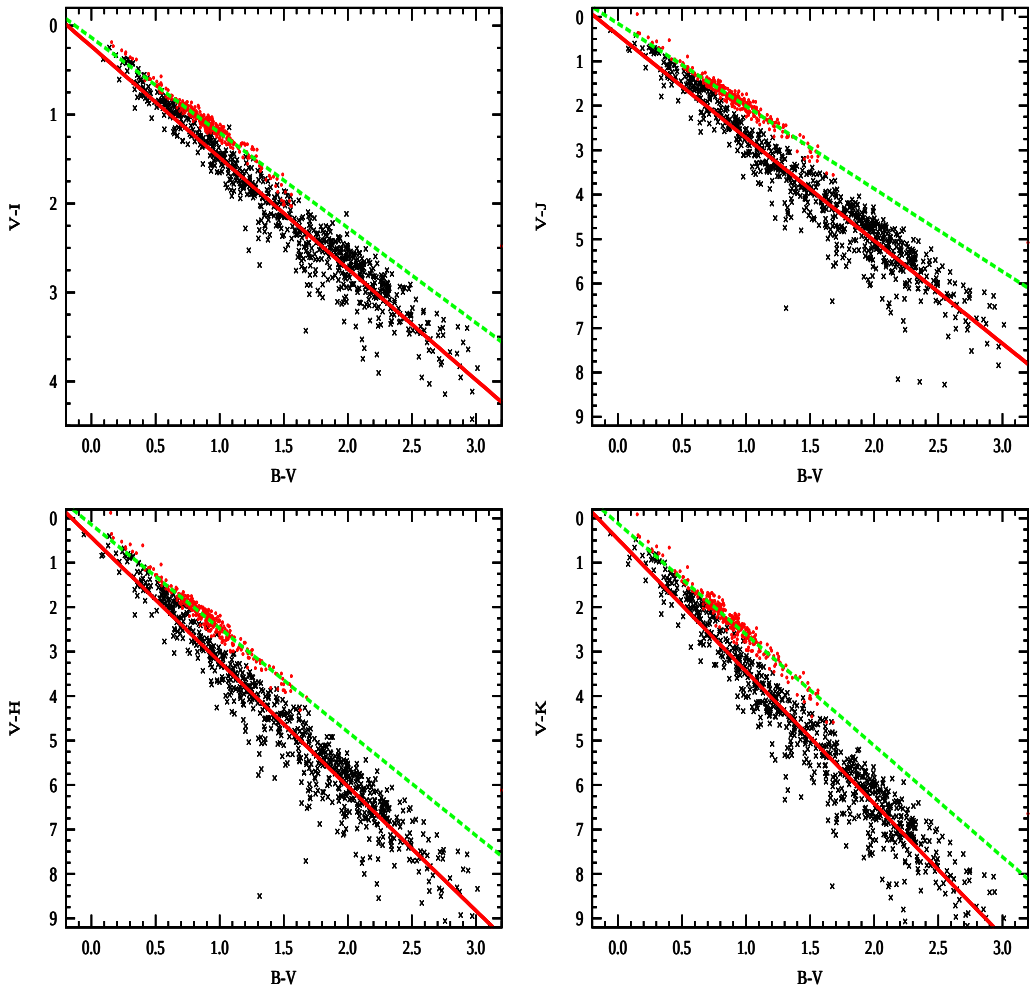

Figure 2.4: $(V-I), (V-J), (V-H)$, and $(V-K)$ versus $(B-V)$ TCDs for the stars in the CrW region ($r < 10'$ from WR 22). The cross and dot symbols represent the stars with abnormal and normal reddening, respectively. Straight and dotted lines show least-squares fits to the data.

2.3.2 Reddening law

To study the nature of the gas and dust in young star-forming regions, it is very important to know the properties of the interstellar extinction and the ratio of total-to-selective extinction, i.e., $R_V = A_V/E(B-V)$. The normal reddening law for the solar neighborhood has been estimated to be $R_V = 3.1 \pm 0.2$ (cf. Guetter & Vrba, 1989; Lim et al., 2011; Whittet, 2003) but in the case of the η Carinae region, several studies claim that R_V is anomalously high (see Feinstein et al., 1973; Forte, 1978; Herbst, 1976; Smith, 2002, 1987; Tapia et al., 1988; Thé et al., 1980; Vazquez et al., 1996). Recently, using 141 early type members in this region, Hur et al. (2012)

Table 2.1: Extinction, distance, and reddening values for the Carina region collected from the literature.

Region/cluster	$E(B-V)$	R_V	$M_0 - M_V$	d(kpc)	References	Method/techniques
WR 22 (CrW)	0.36	3.1	12.15	2.7	Gosset et al. (2009)	–
Trumpler 14	–	–	11.1	–	Becker & Fenkart (1971)	–
	0.5	–	11.5	2.0	Thé & Vleeming (1971)	–
	–	–	12.7 ± 0.2	3.5	Walborn (1973)	Spectroscopic parallax
	–	3.2	12.7 ± 0.1	–	Humphreys (1978)	–
	–	–	–	2.8	Thé et al. (1980)	–
	–	–	12.3 ± 0.1	–	Walborn (1982)	–
	0.55 ± 0.08	–	12.2 ± 0.2	–	Feinstein (1983)	–
	–	3.2	12.7 ± 0.1	3.5	Morrell et al. (1988)	Spectroscopic parallax
	–	–	12.3 ± 0.1	2.8	Morrell et al. (1988)	Spectroscopic parallax
	0.82 ± 0.12	–	11.9 ± 0.2	2.4 ± 0.3	Tapia et al. (1988)	Main-sequence fitting
	–	3.2	12.8 ± 0.2	–	Massey & Johnson (1993)	Spectroscopic parallax
	0.57 ± 0.13	4.7 ± 0.7	12.5 ± 0.2	3.1 ± 0.3	Vazquez et al. (1996)	Main-sequence fitting
	0.58	3.2	12.8 ± 0.1	–	DeGioia-Eastwood et al. (2001)	Spectroscopic parallax
	–	–	12.2 ± 0.7	–	Tapia et al. (2003)	Spectroscopic parallax
	0.57 ± 0.12	4.2 ± 0.2	12.0 ± 0.2	2.5 ± 0.3	Carraro et al. (2004)	Main-sequence fitting
	0.36 ± 0.04	4.4 ± 0.2	12.3 ± 0.2	2.9 ± 0.3	Hur et al. (2012)	Proper motion
Trumpler 15	–	–	11.1	–	Becker & Fenkart (1971)	–
	0.4	–	11.5	1.6	Thé & Vleeming (1971)	–
	–	–	12.9	3.7	Walborn (1973)	Spectroscopic parallax
	–	–	12.9	–	Humphreys (1978)	–
	–	–	–	2.5	Thé et al. (1980)	–
	–	3.2	11.8 ± 0.1	2.3	Morrell et al. (1988)	Spectroscopic parallax
	–	–	12.1 ± 0.3	2.6	Morrell et al. (1988)	Spectroscopic parallax
	0.49± 0.09	–	12.1 ± 0.2	2.6 ± 0.3	Tapia et al. (1988)	Main-sequence fitting
	0.49± 0.09	–	12.1 ± 0.2	2.9	Tapia et al. (2003)	Spectroscopic parallax
	–	–	12.3 ± 0.2	–	Carraro et al. (2004)	Main-sequence fitting
Trumpler 16	0.44	–	11.9	2.5	Thé & Vleeming (1971)	–
	0.4	–	12.1	2.7	Feinstein et al. (1973)	–
	–	3.0	12.1 ± 0.2	2.6	Walborn (1973)	Spectroscopic parallax
	–	–	12.2 ± 0.1	–	Humphreys (1978)	–
	–	–	12.0	2.8	Thé et al. (1980)	–
	–	3.1	11.8 ± 0.1	2.3	Levato & Malaroda (1982)	Spectroscopic parallax
	–	–	12.3 ± 0.1	–	Walborn (1982)	–
	0.68 ± 0.15	–	12.0 ± 0.2	2.5 ± 0.2	Tapia et al. (1988)	Main-sequence fitting
	–	–	12.5 ± 0.1	–	Massey & Johnson (1993)	Spectroscopic parallax
	0.58	3.2	12.8 ± 0.1	–	DeGioia-Eastwood et al. (2001)	Spectroscopic parallax
	–	–	12.0 ± 0.6	2.5	Tapia et al. (2003)	Spectroscopic parallax
	0.61 ± 0.15	3.5 ± 0.3	13.0 ± 0.3	3.9 ± 0.5	Carraro et al. (2004)	Main-sequence fitting
	0.36 ± 0.04	4.4 ± 0.2	12.3 ± 0.2	2.9 ± 0.3	Hur et al. (2012)	Proper motion
Collinder 228	–	–	12.0 ± 0.2	2.5	Feinstein et al. (1973)	–
	–	–	12.2	–	Walborn (1973)	Spectroscopic parallax
	–	–	12.0 ± 0.3	–	Humphreys (1978)	–
	–	3.2	–	2.5	Thé et al. (1980)	–
	–	–	12.06	2.6	Levato & Malaroda (1981)	Spectroscopy
	0.64 ± 0.26	–	11.6 ± 0.4	2.1 ± 0.4	Tapia et al. (1988)	Main-sequence fitting
	–	–	–	1.9 ± 0.2	Carraro & Patat (2001)	–
Collinder 232	0.68 ± 0.21	–	12.0 ± 0.2	2.5 ± 0.2	Tapia et al. (1988)	Main-sequence fitting
	0.48 ± 0.12	3.7± 0.03	11.8 ± 0.2	2.3 ± 0.3	Carraro et al. (2004)	Main-sequence fitting
Bochum 9	0.63 ± 0.08	–	–	4.7	Patat & Carraro (2001)	–
Bochum 10	–	–	12.8	–	Feinstein (1981)	–
	–	–	12.2	–	Fitzgerald & Mehta (1987)	–
	0.48 ± 0.05	–	12.2	2.7	Patat & Carraro (2001)	–
NGC 3324	–	–	12.5 ± 0.2	–	Clariá (1977)	–
	–	–	12.4 ± 0.03	3.0 ± 0.1	Carraro & Patat (2001)	–
Trumpler 14, 15, 16 and Cr 228	–	3.2 ± 0.3	12.2	2.7 ± 0.2	Turner et al. (1980)	–

derived an abnormal total-to-selective extinction ratio $R_V = 4.4 \pm 0.04$.

We used the TCDs as described by Pandey et al. (2003) to study the nature of the extinction law in the CrW region. The TCDs of the form of $(V - \lambda)$ versus $(B - V)$, where λ indicates one of the wavelengths of the broad-band filters (R, I, J, H, K, L), provide an effective method for distinguishing the influence of the normal extinction produced by the diffuse interstellar medium from that of the abnormal extinction arising within regions having a peculiar distribution of dust sizes (cf. Chini & Wargau, 1990; Pandey et al., 2000).

We clearly see in Fig. 2.4 that there are two types of distribution having different

slopes. We selected all the stars belonging to these two populations and plotted their $(V-I), (V-J), (V-H)$ and $(V-K)$ vs. $(B-V)$ TCDs in Fig. 2.4. The respective slopes relating these colours were found, for the red-dot stars, to be $1.07\pm0.02, 1.86\pm 0.02, 2.33\pm0.03$, and 2.50 ± 0.03, which are approximately equivalent to the normal galactic values, i.e., 1.10, 1.96, 2.42, and 2.60, respectively. The objects with black crosses display steeper slopes, i.e., $1.28\pm0.01, 2.34\pm0.03, 2.84\pm0.03$ and 3.03 ± 0.03 for $(V-I), (V-J), (V-H)$ and $(V-K)$ vs. $(B-V)$, respectively. If we plot the spatial distribution of the red dots and black crosses, we clearly see that all the red dots are uniformly distributed, whereas all the black crosses are distributed away from the obscured region of the molecular cloud. It means that the black crosses are most probably background stars, and their light is seen through the molecular cloud (see Preibisch et al., 2011a; Roccatagliata et al., 2013, and references therein). Therefore, the ratios $[E(V-\lambda)]/[E(B-V)]$ $(\lambda \geq \lambda_I)$ for the stars in the background yield a high value for R_V ($\sim$3.7 $\pm$ 0.1), indicating an abnormal grain size in the observed region. Many investigators (see column 3 of Table 2.1) have also found evidence of larger dust grains in the Carina region. Marraco et al. (1993) have found that the value of λ_{max} (the wavelength at which maximum polarization occurred, which is also an indicator of the mean dust grain size distribution) is higher than the canonical value for the general diffuse ISM.

Several studies have already pointed toward an anomalous reddening law with a high R_V value in the vicinity of star-forming regions (see, e.g., Pandey et al., 2003). However, for the Galactic diffuse interstellar medium, a normal value of $R_V = 3.1$ is well accepted. The higher-than-normal value of R_V has usually been attributed to the presence of larger dust grains. There is evidence that, within the dark clouds, accretion of ice mantles on grains and coagulation due to colliding grains change the size distribution towards larger particles. On the other hand, in star-forming regions, radiation from massive stars may evaporate ice mantles resulting in small particles. Here, it is interesting to mention that Okada et al. (2003) suggest that efficient dust destruction is undergoing in the ionized region on the basis of the [Si II] 35 to [N II] 122 μm ratio. Chini & Kruegel (1983) and Chini & Wargau (1990) have shown that both larger and smaller grains may increase the ratio of total-to-selective extinction.

2.3.3 Distance

The Carina nebula is a very large (angular size $> 2^\circ \times 1.5^\circ$) active star-forming region containing a number of young star clusters featuring very massive O-type stars. Recently many authors have considered that the distance to η Carinae and to the whole Carina region is 2.3 kpc (see, e.g., Povich et al., 2011; Smith, 2006b). There is a large discrepancy in the measured distances to the clusters situated within this nebula, as can be seen from Table 2.1. This large scatter in the distance occurs because, as noted by Smith & Brooks (2008), the direction of the Galactic plane in the Carina nebula nearly looks down the tangent point of the Sagittarius-Carina spiral arm. The two clusters Tr 14 and Tr 16, located towards the center of the Carina nebula, have been extensively studied by several authors, but the debate about their distance is still open. Vazquez et al. (1996) estimated a distance modulus of $V_0 - M_V = 12.5 \pm 0.2$ mag for Tr 14. By applying an abnormal reddening law, Tapia et al. (2003) derived $V_0 - M_V = 12.1$ mag. In their study, they adopted $A_V = 1.39E(V-J)$ and found that both clusters are situated at the same distance. But in another study, Carraro et al. (2004) concluded that both clusters are situated at different distances with $V_0 - M_V = 12.3 \pm 0.2$ mag for Tr 14 and 13.0 ± 0.3 mag for Tr 16. Recently, Hur et al. (2012) concluded that Tr 14 and Tr 16 are at the same distance within the observational errors ($V_0 - M_V = 12.3 \pm 0.2$ mag, i.e., d $= 2.9 \pm 0.3$ kpc). Their derived distance is based upon the proper motion, which is comparatively more accurate than other methods. Since we are concentrating on the western side of the Carina nebula containing some part of Tr 14, for the present study, we have adopted a distance of 2.9 kpc for CrW as given by Hur et al. (2012).

2.4 Results

2.4.1 Spectroscopically identified sources

The MK spectral types of 15 X-ray emitting sources in the CrW region have been established using newly acquired spectra (see Sect. 2.2.3) and their comparison with the digital spectral classification atlas compiled by R.O. Gray and available on the web[1]. The results are summarized in Table 2.2, from which we may infer that the majority of identified sources are late-type stars (see Fig. 2.5 for different spectral types), and none of these stars features an $H\alpha$ emission.

[1]http://www.ned.ipac.caltech.edu/level/Gray/frames.html

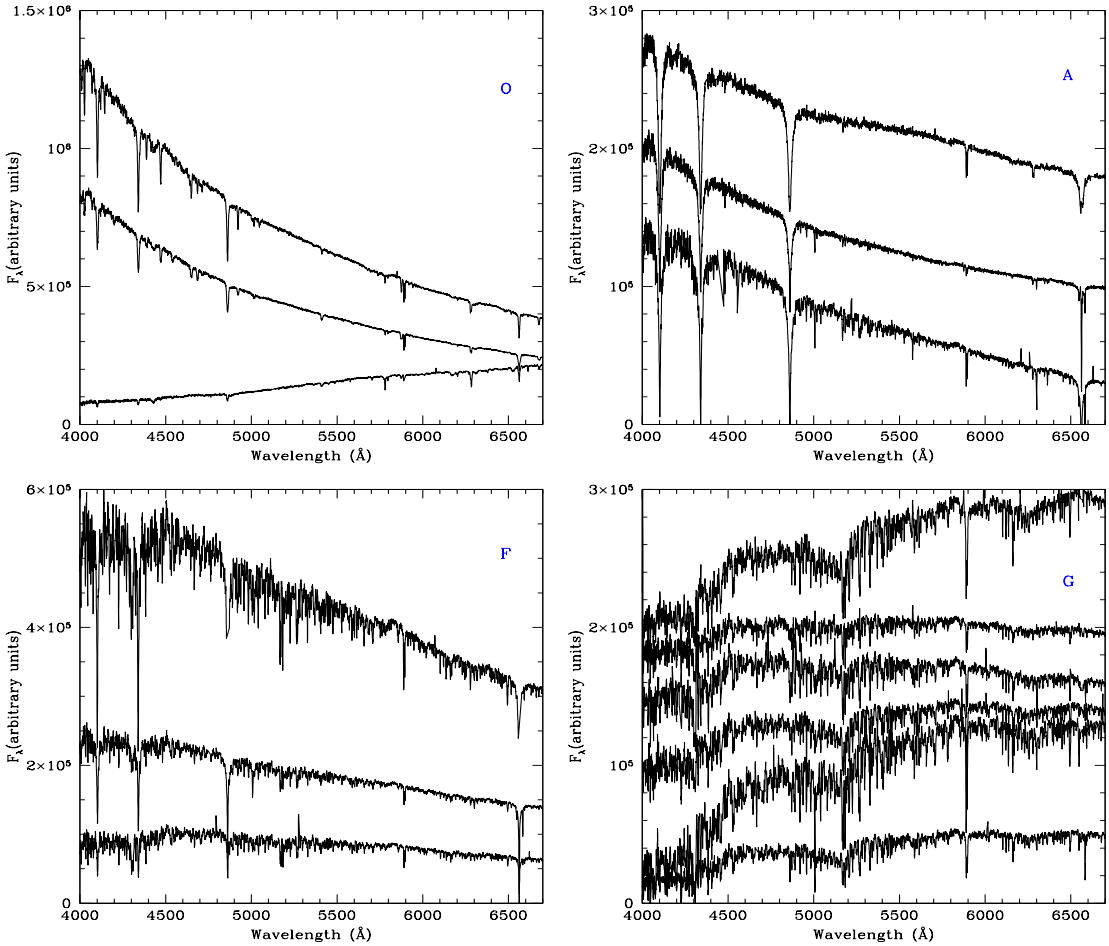

Figure 2.5: Flux-calibrated spectra of the O-A-F-G type stars in our spectroscopic sample of the CrW region. The spectra have been randomly shifted vertically for clarity. The spectral types become progressively later from left to right and from top to bottom.

Three X-ray sources (i.e. #6, #9, and #20; in Table 2.2) belong to spectral type O, of which #6 and #9 are correlated with HD 92607 and HD 92644, respectively. Houk & Cowley (1975) classify them as O type stars (HD 92607 – O9 II/III and HD 92644 – O9.5/B0III). Our present analysis rather favors spectral types O8.5 III for #6 and O9.7 V for #9. These results broadly confirm previous classifications of these sources (see also Claeskens et al., 2011). The X-ray properties of both stars are discussed in detail by Claeskens et al. (2011, see their discussion and notes on individual objects). They find that the observed X-ray count rate for #9 is 3.8 times lower than #6, but both are quite soft. Star #20 is identified as a reddened O7 star with observed $V = 13.03$ and $(B - V) = 1.83$ mag (cf. Table 2.2).

The remaining 12 sources have counterparts that are classified as late-type stars: three are of spectral type A, three are F stars, and six are classified as G-type stars. Stars #11, #19, and #37 are identified as A5 V, A1 III, and A1 V, respectively. Similarly #3, #10, and #23 belong to F5 V, F8 V, and F3 V spectral types, respectively. Claeskens et al. (2011) in their study found that source #18 is among the brightest X-ray sources in this field; however, they could not identify any optical counterpart for this object from the GSC2.2 catalog. Based on IR colours, they computed the V band magnitude of this object to be in between $20.2 - 21.5$. Later on by visual inspection of Digital Sky Survey images, they found a star having brightness $V = 18 - 19$ at the exact source location. We also found a star with magnitude 18.214 ± 0.012 (cf. Table 2.2, column 4) at a similar position. Binarity could explain why this star is brighter in the optical than expected from its near-IR magnitudes (Claeskens et al., 2011). It could reside in front of the Carina, but it could also be intrinsically brighter than a main-sequence (MS) star. Sources #7, #12, #15, #32, #40, and #42 are characterized as G6 III, G9 V, G8 III, G3 V-III, G8 V, and G9 III spectral type, respectively. Based on the observed X-ray counts, Claeskens et al. (2011) claim that #42 is a variable star. It is also worthwhile to mention that two sources (#7 and #15) are identified as PMS sources (see Table 2.2) in the present study (cf. Sect. 2.4.2.3).

2.4.2 YSOs identification

The PMS stars (YSOs) are mainly grouped into the classes 0-I-II-III, which represent in-falling protostars, evolved protostars, classical T-Tauri stars (CTTSs), and weak line T Tauri stars (WTTSs), respectively (cf. Feigelson & Montmerle, 1999). Class 0 & I YSOs are so deeply buried inside the molecular clouds that they are not visible at optical wavelengths. The CTTSs feature disks from which the material is accreted, and emission in $H\alpha$ can be seen as due to this accreting material. These disks can also be probed through their IR excess (compared to normal stellar photospheres). WTTSs, on the contrary, have little or no disk material left, hence have no strong $H\alpha$ emission and IR excess. It is evident from the recent studies that the X-ray luminosity from WTTSs is significantly higher than for the CTTSs with circumstellar disks or protostars with accreting envelopes (Prisinzano et al., 2008; Stassun et al., 2004; Telleschi et al., 2007). In this section we report the tentative identification of YSOs on the basis of their $H\alpha$ emission, IR excess, and X-ray emission.

2.4.2.1 On the basis of $H\alpha$ emission

The stars showing emission in $H\alpha$ might be considered as PMS stars or candidates, and the strength of the $H\alpha$ line (measured by its equivalent width 'EW($H\alpha$)') is a direct indicator of their evolutionary stage. The conventional distinction between CTTSs and WTTSs is an EW($H\alpha$) $> 10\mathring{A}$ for the former (see Herbig & Bell, 1988). However, Bertout (1989) has suggested that a limiting value of $5\mathring{A}$ might be more appropriate. More recently, investigators have tied the definition to the shape (width) of the $H\alpha$ line profile (see Jayawardhana et al., 2003; White & Basri, 2003). In the study of NGC 6383, Rauw et al. (2010) find that an $H\alpha$ equivalent width of $10\mathring{A}$ corresponds to an $(R-H\alpha)$ index of 0.24 ± 0.04 above the MS relation of Sung et al. (1997). They have further used this as a selection criterion for identifying $H\alpha$ emitters. In our study, we have considered a source as probable $H\alpha$ emitter only if the $(R - H\alpha)$ index is 0.24 above the MS relation by Sung et al. (1997).

The $H\alpha$ filter at WFI has a special passband, therefore it cannot be directly linked to any existing standard photometric system (see also Rauw et al., 2010). By selecting ten stars observed with EMMI (see Sect. 2.2.3), whose spectra do not exhibit $H\alpha$ emission, we calibrated the zero point by comparing the observed $R-H\alpha$ and dereddened $(V-I)$ with the $(R-H\alpha)_0$ versus the $(V-I)_0$ relation of emission free MS stars as determined by Sung et al. (1997) for NGC 2264. The $(V-I)$ colour is dereddened by the $E(V-I)$ value of $E(B-V)_{min} \times 1.5$. In Fig. 2.6, we plotted the $(R-H\alpha)_0$ vs. $(V-I)_0$ distribution of all the stars along with the MS given by Sung et al. (1997).

Since there is a large scatter in the distribution (cf. Fig. 2.6; left panel), there may be false identifications of $H\alpha$ emitters. To minimize this, we introduced another selection criterion to identify the $H\alpha$ emitters in addition to the previous one. We used the V vs. $(R-H\alpha)_0$ colour magnitude diagram (CMD) (cf. Fig. 2.6; right panel) and defined an envelope that contains most of the stars following the MS. The stars that have a value of $(R-H\alpha)_0 - \sigma_{(R-H\alpha)}$ greater than that of the envelope of the MS can be assumed to be probable $H\alpha$ emitters. In our study, we therefore consider that a star is a good $H\alpha$ emission candidate if it satisfies both conditions. We have identified 41 YSOs in our study as potential $H\alpha$ emitters, and these can be seen in Fig. 2.16.

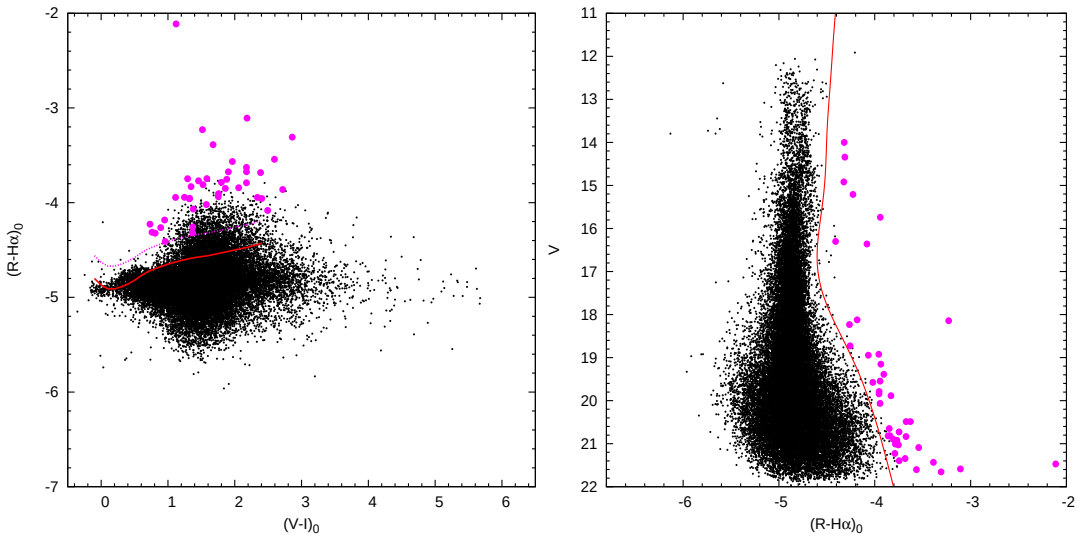

Figure 2.6: Left panel: The $(R-H\alpha)_0$ index is shown as a function of the $(V-I)_0$ colour. The solid line indicates the relation for MS stars as taken from Sung et al. (1997). The dashed line (magenta) yields the thresholds for $H\alpha$ emitter candidates. Right panel: V versus $(R-H\alpha)_0$ CMD. The magenta circles represent $H\alpha$ emitter candidates. An envelope as discussed in Sect. 2.4.2.1 is indicated by a solid line.

2.4.2.2 On the basis of IR excess

Recently Gaczkowski et al. (2013) have obtained Herschel PACS and FIR maps that cover the full area of the CNC and reveal the population of deeply embedded YSOs, most of which are not yet visible at the MIR or NIR wavelengths. They studied the properties of the 642 objects that are independently detected as point-like sources in at least two of the five Herschel bands. For those objects that can be identified with apparently single Spitzer counterparts, they used radiative transfer models to derive information about the basic stellar and circumstellar parameters. They found that about 75% of the Herschel-detected YSOs are Class 0 protostars and that their masses (estimated from the radiative transfer modeling) range from ∼1 $M_\odot$ to ∼10 $M_\odot$. Out of these 642 sources, 105 fall in our studied region.

Using NIR/MIR data of 2MASS and Spitzer, Povich et al. (2011) present a catalog of 1439 YSOs spanning a 1.42 deg^2 field surveyed by the *Chandra* Carina Complex Project (CCCP) (for more details about CCCP see Townsley et al., 2011). This field includes the major ionizing clusters and the most active sites of ongoing star formation within the Great Nebula in Carina. YSO candidates were identified via IR excess emission from dusty circumstellar disks and envelopes, using data from the Spitzer Space Telescope (the Vela–Carina survey) and the 2MASS database.

They model the 1-24 μm IR spectral energy distributions of the YSOs to constrain their physical properties. Their Pan-Carina YSO Catalog (PCYC) is dominated by intermediate-mass (2 $M_\odot$ < M $\leq$ 10 $M_\odot$) objects with disks, including Herbig Ae/Be stars and their less evolved progenitors. Out of these 1439 sources, 136 fall in our studied region.

Recently, Preibisch et al. (2011b) used HAWK-I at the ESO VLT to produce a deep and wide NIR survey that is deep enough to detect the full low-mass stellar population (i.e. down to $\sim$0.1$M_\odot$ and for extinctions up to A_V $\sim$15 mag) in all the important parts of the CNC, including the clusters Tr 14, 15, and 16, as well as the South Pillars region. They analyzed CMDs to derive information about the ages and masses of the low-mass stars. Unfortunately, their surveyed region does not cover our studied region. Therefore for the present study we used NIR data from the 2MASS survey to identify sources with IR excess. We used the following scheme to make the distinction between the sources with IR excess and those that are simply reddened by dust along the line of sight (Gutermuth et al., 2005). First we measure the line of sight extinction to each source as parameterized by the E_{H-K} colour excess due to the dust present along the lines of sight. For objects where we have J photometry in addition to H and K_s with the condition that they are positioned above the extension of the CTTSs locus and have a colour $[J-H] \geq 0.6$, we used the equations given by Gutermuth et al. (2009) to derive the adopted intrinsic colours. The difference between the intrinsic colour and the observed one will give the extinction value. Once we had the extinction value for the stars, we generated an extinction map for the whole CrW region. The extinction values in a sky plane were calculated with a resolution of 5 arcsec by taking the mean of extinction value of stars in a box having a size of 17 arcsec. The resulting extinction map, smoothed to a resolution of 0.6 arcmin, is shown in Fig. 2.7. This IR extinction map represents the column density distribution of the molecular cloud associated with the CrW region. We can clearly see the high density region toward the northeast of CrW and then the density following the dust lane as visible in the 4.6 μm image (cf. Sect. 2.5, see Fig. 2.16). Thanks to less extinction, longer wavelength observations can penetrate deeper inside the nebulosity than do shorter wavelength ones. For this reason, there are many stars in the CrW region that do not have J band photometry. Once we constructed the extinction map, we used this to also deredden the stars having no J band detection. Here it is worthwhile to note that we used CTTSs loci to estimate reddening by back-tracing all the stars located

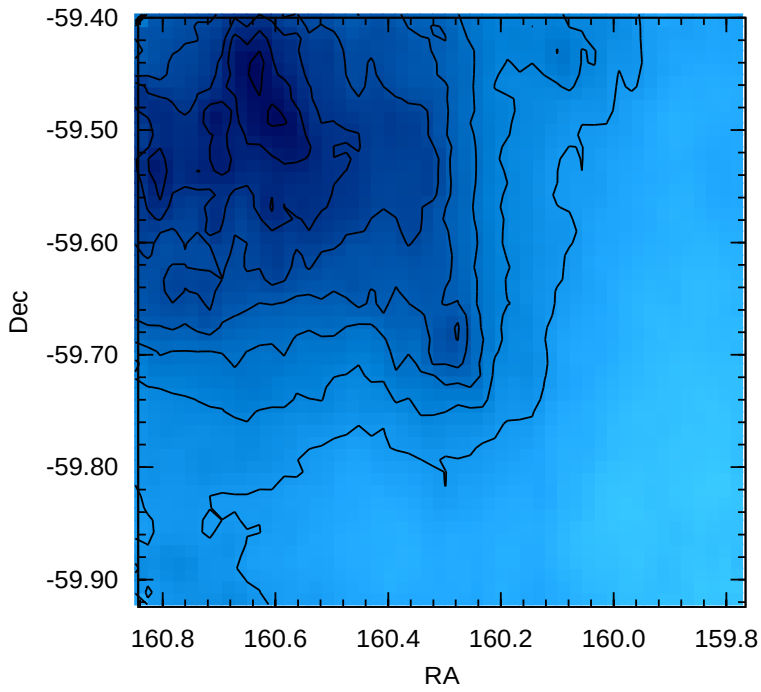

Figure 2.7: Column density distribution of the molecular cloud in our field of view, as derived from the near-infrared reddening of stars. The lowest contour corresponds to $A_v = 3.4$, the step size of the contours is 0.2. The RA and Dec are in degrees.

above the CTTSs loci or its extension to the CTTSs loci or its extension. It is quite probable that the genuine CTTSs are mixed with deeply embedded MS stars that could fall above the CTTSs locus in the 2MASS colour-colour diagram. Therefore, when we deredden this mixed sample of stars, the reddening value for CTTSs will get overestimated because of their surrounding cocoon of dust/gas, whereas for the MS stars, it will get underestimated because the intrinsic colour of MS stars lies below CTTSs loci.

In Fig. 2.8, we have plotted the dereddened NIR CMDs, K_0 versus $(H-K)_0$, for the CrW region and the nearby reference field region covering the same area as CrW. Since both the field and CrW region CMDs are dereddened by the same technique, the underestimation/overestimation of the A_v value will not affect our analysis much. However, owing to the clumpy nature of the molecular cloud associated with the CrW region, the dereddened CMD for CrW will show more scatter than the field CMD. A comparison with the reference field CMD reveals that there might be many stars showing excess emission that is apparent from their distribution at $(H-K)_0 \lesssim 0.6$ mag. Therefore, we defined an envelope representing a cut-off line (Figs. 2.8b,c) on the basis of the CMD of the CrW region and of the field one. We then designed an

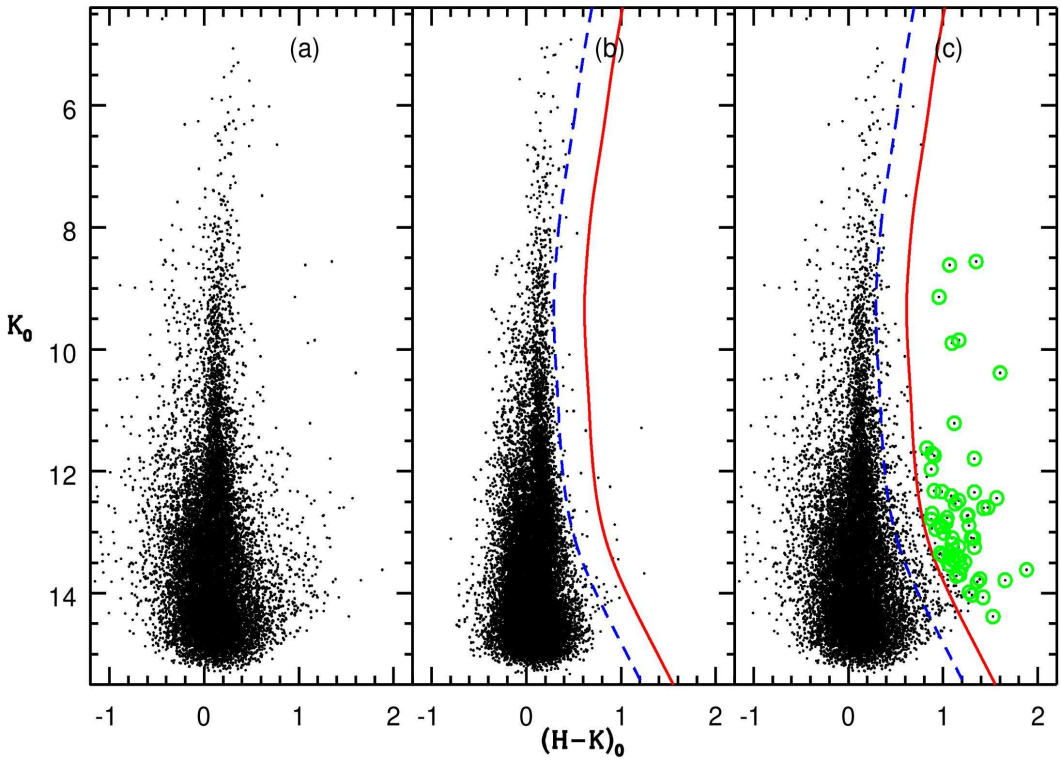

Figure 2.8: $K_0/(H-K)_0$ CMD for (a) stars in the CrW region, (b) stars in the field region and (c) same stars as in panel (a) along with identified probable NIR-excess stars. The blue dashed line represents the envelope of field CMD, whereas the red solid line demarcates the distribution of IR excess sources from MS stars.

additional envelope (solid line in red) shifted to the red from the previous one by an amount corresponding to $A_v = 5$ (to compensate for the scattering due to the clumpy nature of the molecular clouds). Doing that, we aim at isolating probable NIR excess stars from reddened MS stars. Since we know that the photometric error is larger at the fainter end of the CMD, the shape of the cut-off line at the fainter end is adjusted accordingly. All the stars having a colour '$(H-K)_0 - \sigma_{(H-K)_0}$' greater than the red cut-off line might have an excess emission in the K band and thus can reasonably be considered to be probable YSOs (see also Mallick et al., 2012). While this sample is dominated by YSOs, it may also contain the following types of contaminations: variable stars, dusty asymptotic giant branch (AGB) stars, unresolved planetary nebulae, and background galaxies (Povich et al., 2011; Robitaille et al., 2008). We used the CMD of the reference field covering the same area as the CrW region to calculate the fraction of contaminating objects in our sample. The reference field was around 1.5° westward from the center of the CrW region (cf. Fig. 2.1).

The number of probable NIR excess stars in the reference field is about 8 whereas

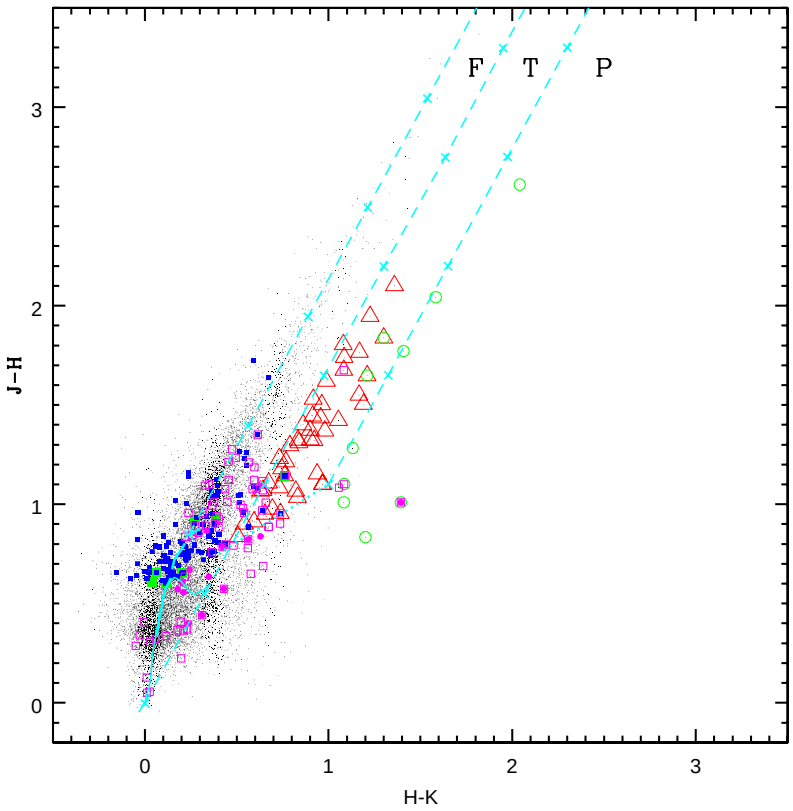

Figure 2.9: $(J-H)/(H-K)$ colour-colour diagram of sources detected in the $JHKs$ bands in the CrW region. The sequences of dwarfs (solid curve) and giants (thick dashed curve) are from Bessell & Brett (1988). The dotted line represents the locus of T Tauri stars (Meyer et al., 1997). Parallel dashed straight lines represent the reddening vectors (Cohen et al., 1981). The crosses on the dashed lines are separated by $A_V = 5$ mag. YSO candidates are also shown. Open magenta squares = Spitzer; filled magenta circles = $H\alpha$; filled squares = X-ray emitting WTTSs (green = *XMM-Newton*, blue = *Chandra*); open red triangles = CTTSs and open green circles = probable NIR-excess sources (see text for the classification scheme).

the number of probable NIR excess stars in the CrW region is 60. This means that we have a contamination of about 13% in our sample. The majority of these probable NIR excess stars follow the high density region in the CrW region (see Fig. 2.16) and may be deeply embedded in that nebulosity. Povich et al. (2011) have identified many YSOs that are mainly in the irradiated surface of the cloud (see Fig. 2.16) but recently, based on Herschel FIR data, Gaczkowski et al. (2013) have identified YSOs that are also located within the dark lane of the CrW region.

YSOs such as CTTSs, WTTSs, and Herbig Ae/Be stars tend to occupy different regions on the NIR TCDs. In Fig. 2.9, we have plotted the NIR TCD using

the 2MASS data for all the sources lying in the observed region. All the 2MASS magnitudes and colours were converted into the California Institute of Technology (CIT) system[1]. All the curves and lines are also in the CIT system. The shown reddening vectors are drawn from the tip (spectral type M4) of the giant branch ("upper reddening line"), from the base (spectral type A0) of the MS branch ("middle reddening line") and from the tip of the intrinsic CTTSs line ("lower reddening line"). The extinction ratios $A_J/A_V = 0.265, A_H/A_V = 0.155$ and $A_K/A_V = 0.090$ have been taken from Cohen et al. (1981). We classified the sources according to three regions in this diagram (cf. Ojha et al., 2004). The 'F' sources are located between the upper and middle reddening lines and are considered to be either field stars (MS stars, giants) or Class III and Class II sources with small NIR-excess. 'T' sources are located between the middle and lower reddening lines. These sources are considered to be mostly CTTSs (or Class II objects) with large NIR-excess. There may be an overlap of Herbig Ae/Be stars in the 'T' region (Hillenbrand et al., 1992). 'P' sources are those located in the region redward of the lower reddening line and are most likely Class 0/I objects (protostellar-like objects; Ojha et al. (2004)). It is worthwhile also mentioning that Robitaille et al. (2006) show that there is a significant overlap between protostars and CTTSs. The NIR TCD of the observed region (Fig. 2.9) indicates that a significant number of sources that have previously been identified as probable NIR-excess stars lie in the 'T' region. Forty-one sources have been designated as CTTSs in our study under the condition that they fall in the 'T' region of the NIR TCD (Fig. 2.9) and are redward of the dashed blue cut-off line in the dereddened CMD (Fig. 2.8). We also have plotted probable NIR excess sources that are detected in 'J' band (10 out of 60). Most of these sources are located in the 'P' region in Fig. 2.9, which means that they are most likely Class 0/I objects.

2.4.2.3 On the basis of X-ray emission

The NIR-excess-selected YSO candidate samples are generally considered incomplete because the NIR-excess emission in young stars disappears on timescales of just a few Myr (see Briceño et al., 2007). At an age of ∼3 Myr, only ∼50% of the young stars still show NIR excesses, and by ∼5 Myr this fraction is reduced to ∼15% (Preibisch et al., 2011c). Since the expected ages of most young stars in the CNC are several Myr, any IR-excess-selected YSO sample will be highly incomplete. To

[1] http://www.astro.caltech.edu/~jmc/2mass/v3/transformations/

tackle this problem, we used the X-ray emitting point sources in the region to identify YSO candidates. The X-ray detection methods are sensitive to young stars that have already dispersed their circumstellar disks, thus avoiding the bias introduced when selecting samples only based on IR excess (Preibisch et al., 2011c).

XMM-Newton observations

The *XMM-Newton* satellite has observed the CrW region in the course of the study of the massive binary WR 22. The corresponding results have been presented in separate papers (see Claeskens et al., 2011; Gosset et al., 2009). In this section we cross-correlated the sources detected in our photometric data of the CrW region with the positions of 43 X-ray sources from Claeskens et al. (2011). The positions of the X-ray sources as given by Claeskens et al. (2011, columns 8 and 9 of their table 2) refer to the astrometric frame as determined from the *XMM-Newton* on-board Attitude and Orbit Control System. The cross-correlation with the GSC and the present optical catalog suggests making a small correction. We therefore suggest decreasing the right ascension of Claeskens et al. (2011) by $0''.25$ and increasing the declination by $0''.96$. No rotation was detected. We adopt these new positions for the 43 X-ray sources.

We defined an optimal cross-correlation radius to find a compromise between correlations missed due to astrometric errors and spurious associations in the CrW field. To derive the optimal correlation radius, we applied the technique of Jeffries et al. (1997). In this method, the distribution of the cumulative number of cataloged sources as a function of the cross-correlation radius r_c is given by

$$\Phi(d \leq r_c) = A \left[1 - \exp\left(\frac{-r_c^2}{2\,\sigma^2}\right)\right] + (N - A)\,\left[1 - \exp(-\pi\,B\,r_c^2)\right]. \qquad (2.1)$$

In this equation N, A, σ, and B represent the total number of cross-correlated X-ray sources ($N = 43$), the number of true correlations, the uncertainty in the X-ray source position, and the surface density of the catalog of photometric sources, respectively. In the course of fitting the integrated number of correlations with the CrW photometric catalog as a function of the separation (where 43 X-ray sources have an optical source located closer than 8 arcsec), we derived the fitting parameters as $A = 33.78$, $\sigma = 0.9\,\mathrm{arcsec}$, and $B = 2.3 \times 10^{-2}\,\mathrm{arcsec}^{-2}$ (see Fig. 2.10). The optimal correlation radius was chosen to be $r_c = 2.7''$, which implies that there is

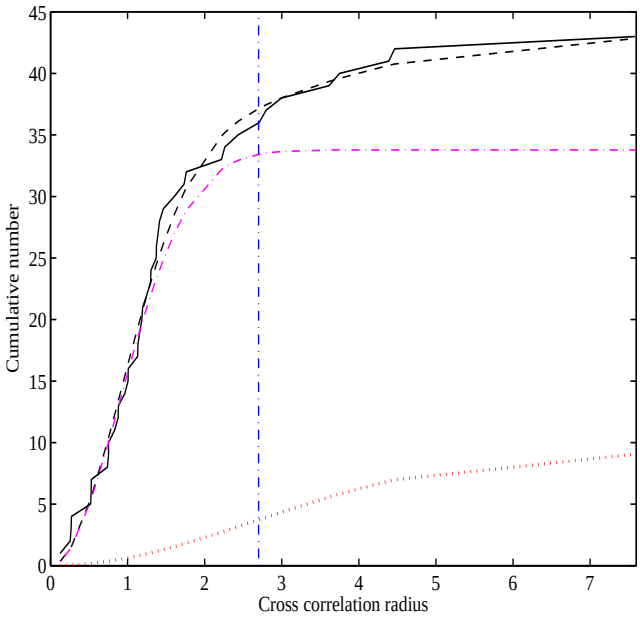

Figure 2.10: Cumulative numbers of correlations between the X-ray detected sources and the WFI catalog. The thick curve represents the observed numbers, the dashed curve shows the best fit, and the dot-dashed line (magenta) and dotted (red) curves correspond to the expected numbers of real and spurious sources, respectively. The vertical line indicates the optimal correlation radius r_c.

no more than one spurious association among the 34 correlations; i.e., the optical counterparts of 79% of the *XMM-Newton* sources in the CrW field should thus be reliably identified.

Claeskens et al. (2011) also cross-correlated these X-ray sources ($N = 43$), but they searched the optical counterparts using the Guide Star Catalog version 2.2 (GSC2.2). Their fitting parameters are $A = 35.4$, $B = 2 \times 10^{-3}\,\mathrm{arcsec}^{-2}$, and $\sigma = 1.8\,\mathrm{arcsec}$. The number of true correlations (A) of both studies are very much consistent. The surface density (B) of the catalog of optical sources in the present study is an order of magnitude higher than in Claeskens et al. (2011), while our σ value is half that of these authors. The results of the cross-identification are listed in Table 2.2. When several optical counterparts are present, only the closest one is given. The first column is the ID of the X-ray sources from Claeskens et al. (2011). Columns 2 and 3 are their respective RA and Dec in degree (from our photometric catalog). In the next columns the V magnitude, $(V - I)$, $(V - R)$, $(B - V)$ and $(U - B)$ colours are reported. Sources with a spectral classification are mentioned

Table 2.2: Cross-identification of 43 X-ray sources from Claeskens et al. (2011) with CrW optical photometry. Stars brighter than $V = 11.3$ are from the literature. The YSOs identified in Section 2.4.2 are also mentioned in the last column.

ID(X-ray)	α(J2000)	δ(J2000)	V	$(V-I)$	$(V-R)$	$(B-V)$	$(U-B)$	Spectral type	YSO number†
#1	159.894496	-59.737510	20.386	2.860	1.438	2.250	N/A	–	183
#2	159.947016	-59.608981	12.991	0.809	0.436	0.653	-0.042	–	–
#3	159.948029	-59.746218	10.470	N/A	N/A	0.440	N/A	F5 V	–
#4	159.983333	-59.618056	11.279	N/A	N/A	0.668	N/A	–	–
#5	160.042973	-59.619011	17.720	2.299	1.195	1.721	1.051	–	57
#6	160.051779	-59.802809	8.140	N/A	N/A	-0.020	-0.780	O8.5 III	–
#7	160.069977	-59.534346	14.720	1.386	0.787	1.006	0.673	G6 III	13
#8	–	–	–	–	–	–	–	–	–
#9	160.132138	-59.778854	8.880	N/A	N/A	-0.030	-0.900	O9.7 V	–
#10	160.161981	-59.462519	12.839	0.807	0.419	0.590	0.028	F8 V	–
#11	160.174252	-59.621872	12.609	0.429	0.258	0.320	0.108	A5 V	–
#12	160.174412	-59.539547	14.974	0.954	0.540	0.736	0.149	G9 V	–
#13	160.184003	-59.826372	17.565	3.222	1.551	2.103	1.018	–	–
#14	160.193248	-59.700809	19.680	2.144	1.115	1.544	N/A	–	–
#15	160.214424	-59.622191	15.365	1.332	0.716	1.109	0.609	G8 III	18
#16	–	–	–	–	–	–	–	–	–
#17	160.229239	-59.639602	17.422	1.552	0.835	1.217	0.607	–	48
#18	160.230446	-59.710999	18.214	1.586	0.928	1.086	0.373	F8 V	–
#19	160.235367	-59.862561	11.363	0.340	N/A	N/A	N/A	A1 III	–
#20	160.247070	-59.457005	13.031	1.825	0.860	1.340	-0.031	O7	–
#21	–	–	–	–	–	–	–	–	–
#22[a]	160.322983	-59.676915	6.420	N/A	N/A	0.080	-0.730	–	–
#23	160.335850	-59.589894	11.692	0.718	N/A	0.841	-0.285	F3 V	–
#24	160.338038	-59.659587	17.131	1.316	0.758	0.978	0.259	–	–
#25	–	–	–	–	–	–	–	–	–
#26	160.362639	-59.656561	16.698	1.334	0.774	0.896	0.494	–	–
#27	160.364564	-59.686933	16.339	1.174	0.658	0.903	0.215	–	–
#28	160.387108	-59.604288	19.416	2.737	1.136	1.667	N/A	–	–
#29	160.426017	-59.635431	16.982	1.335	0.712	1.054	0.482	–	–
#30	160.437963	-59.807270	19.050	2.058	0.922	1.818	N/A	–	–
#31	160.464076	-59.720771	12.626	0.782	0.442	0.550	-0.019	–	–
#32	160.478811	-59.689836	13.146	1.224	0.793	0.935	0.923	G3 V-III	–
#33	–	–	–	–	–	–	–	–	–
#34	–	–	–	–	–	–	–	–	–
#35	–	–	–	–	–	–	–	–	–
#36	–	–	–	–	–	–	–	–	–
#37	160.523400	-59.604232	14.022	0.554	0.316	0.357	0.158	A1 V	–
#38	160.556738	-59.599388	18.204	2.910	1.446	2.081	0.479	–	87
#39	160.564481	-59.565945	19.215	2.738	1.145	1.679	N/A	–	–
#40	160.603836	-59.669004	14.842	1.105	0.636	0.576	0.164	G8 V	–
#41	160.636112	-59.611374	16.242	1.834	0.975	1.461	1.079	–	30
#42	160.652591	-59.731771	15.372	1.454	0.764	1.096	0.746	G9 III	–
#43	160.679111	-59.591296	15.898	1.365	0.738	1.165	0.425	–	–

[a] WR 22 itself; [†]The YSO entry numbers are from Table 2.3, see also Appendix 8.

in the next-to-last column.

Chandra X-ray observations

Recently, a wide area (1.42 deg^2) of the Carina complex has been mapped by the *Chandra* X-ray Observatory (CCCP, Townsley et al., 2011). These images were obtained with the Advanced CCD Imaging Spectrometer (ACIS; Garmire et al.,

2003). This CCCP study mainly includes the data from the ACIS-I array, although ACIS-S array CCDs S2 and S3 were also operational during the observations. But most of the sources on S2 and S3 are crowded and dominated by the background in the CCCP data (Townsley et al., 2011). In this survey, 14369 X-ray sources were detected over the whole CCCP survey region. Out of these, the CrW region contains 1465 sources. Since the on-axis *Chandra* PSF is 0.5″ and because it degrades at large off-axis angles (see, e.g., Broos et al., 2010; Getman et al., 2005), we have taken an optimal matching radius of 1 arcsec to determine the optical/NIR counterparts of these X-ray sources. This size of the matching radius is well established in other studies as well (see, e.g., Feigelson et al., 2002; Wang et al., 2007). We identified 469 sources that have 2MASS NIR counterparts and fall in the CrW region.

Classification of X-ray emitters based on NIR TCD

We have identified WTTSs based on their X-ray emission, as well as on their respective position in NIR TCD (Fig. 2.9) through *Chandra* and *XMM-Newton* observations. The sources having X-ray emission and lying in the 'F' region above the extension of the intrinsic CTTSs locus, as well as sources having $(J-H) \geq 0.6$ mag and lying to the left of the first (leftmost) reddening vector (shown in Fig. 2.9) are assigned as WTTSs/Class III sources (see, e.g., Jose et al., 2008; Pandey et al., 2008; Sharma et al., 2012). Here it is worthwhile to mention that some of the X-ray sources classified as WTTSs/Class III sources, lying near the middle reddening vector, could be CTTSs/ Class II sources. Out of 34 (*XMM-Newton*) and 469 (*Chandra*) sources, 7 and 119, respectively, were identified as WTTSs, with 4 in common. These are identified in Table 2.3 (by numbers 4-5 in the last column and filled squares in Fig. 2.9).

2.4.3 Age and mass of YSOs

2.4.3.1 Using NIR CMD

The CMDs are useful tools for studying the nature of the stellar population within star-forming regions. In Fig. 2.11, we plotted the $J/(J-H)$ CMD for all the YSO candidates identified in the previous sections having NIR counterparts and located in the CrW region. For cross-matching the $H\alpha$, X-ray, Spitzer, and Herschel identified YSO candidates with the 2MASS data, we took a search radius of 1 arcsec. For the FIR Herschel identified YSOs, we did not find any NIR counterpart. We used

the relation $A_J/A_V = 0.265$, $A_H/A_V = 0.155$ (Cohen et al., 1981), isochrones for age- 2 Myr and PMS isochrones for ages 0.1, 1, 2, 5, and 10 Myr by Marigo et al. (2008) and Siess et al. (2000), respectively, to plot the CMD assuming a distance of 2.9 kpc and an extinction $E(B-V)_{min} = 0.25$. In the present analysis, we used $R_V = 3.7$ as discussed in Sect. 2.3.2. Different classes of probable YSOs are also shown in the figure. Most of the probable T Tauri, $H\alpha$ emission stars and IR excess stars have an apparent age under 1 Myr. The Spitzer identified YSOs are located mainly in two groups, one shows ages less than 1 Myr, whereas other groups have ages between 1−10 Myr. Smith et al. (2010) also find that the majority of YSOs in Carina have ages of ∼1 Myr.

The mass of the probable YSO candidates can be estimated by comparing their location on the CMD with the evolutionary models of PMS stars. The slanted dashed curve, taken from Siess et al. (2000), denotes the locus of 1 Myr old PMS stars having masses in the range of 0.1 to 3.5 $M_\odot$. To estimate the stellar masses, the J luminosity is recommended rather than that of H or K, because the J band is less affected by the emission from circumstellar material (Bertout et al., 1988). The majority of the YSOs have masses in the range 3.5 to 0.5 $M_\odot$, indicating that these may be T Tauri stars. A few stars with a mass higher than 3.5 $M_\odot$ may be candidates for Herbig Ae/Be stars. Gaczkowski et al. (2013) state that this region exhibits a low number of very massive stars. However, since the more massive stars form more quickly and tend to be more obscured, and since they may not exhibit the same signatures of youth for as long a time as lower mass stars, a more extensive analysis is required to confirm their presence or absence in this region.

The NIR counterparts of YSOs in a nebular star-forming region are easier to find than their optical counterparts. Therefore in the NIR CMD we have statistically more YSOs but to derive the exact age/mass of individual YSOs is somewhat difficult since at the lower end of the NIR CMD, the isochrones of different ages and masses nearly coincide with each other. Age and mass of individual YSOs can be derived more accurately using the optical CMDs.

2.4.3.2 Using optical CMD

In Fig. 2.12, the $V/(V-I)$ CMD has been plotted for the optical counterparts of YSOs identified in Sect. 2.4.2. We have taken the same 1 arcsec matching radius for identifying the optical counterparts of the presumed YSOs. Here also we have not found any optical counterpart of the Herschel identified YSOs. The dashed lines

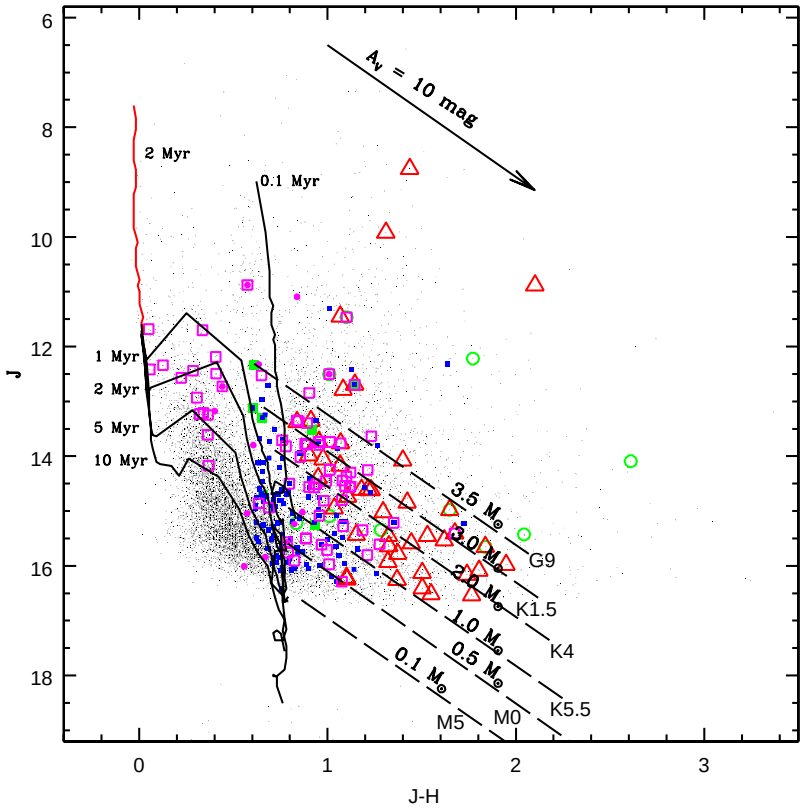

Figure 2.11: $J/(J-H)$ CMD for the stars in the CrW region. The isochrone of 2 Myr (Z = 0.02) by Marigo et al. (2008) and PMS isochrones of age 0.1, 1, 2, 5 and 10 Myr taken from Siess et al. (2000) corrected for a distance of 2.9 kpc and a reddening $E(B-V)_{min} = 0.25$ are also shown. The symbols are the same as in Fig. 2.9 (see Sect. 2.4.3.1 for the classification scheme). The indicated masses and spectral types have been taken from the 1 Myr PMS isochrone of Siess et al. (2000).

Table 2.3: Sample of the optically identified YSO candidates along with their derived ages and masses. Error bars in magnitude and colour represent formal internal (comparative) errors and do not include the colour transformation and zero-point uncertainties.

ID	α(J2000) (°)	δ(J2000) (°)	$V \pm \sigma$ (mag)	$(V-I) \pm \sigma$ (mag)	Age $\pm\sigma$ (Myrs)	Mass $\pm\sigma$ ($M_\odot$)	Technique [1,2,3,4,5,6]
(1)	(2)	(3)	(4)	(5)	(6)	(7)	(8)
1	160.544858	-59.643538	12.316±0.009	0.373±0.018	0.9±0.2	3.7±0.2	1
2	160.586232	-59.898926	12.726±0.011	0.211±0.018	2.6±2.1	4.8±0.3	1
3	160.556561	-59.735036	13.079±0.011	0.422±0.014	1.4±0.2	2.8±0.3	1
4	159.827622	-59.759030	13.508±0.006	0.677±0.010	2.5±0.4	2.0±0.3	1
5	160.509158	-59.674841	13.527±0.009	1.000±0.014	1.4±0.2	3.4±0.3	1
–	–	–	–	–	–	–	–

[1] Spitzer identified sources, [2] $H\alpha$ sources, [3] CTTS, [4] *Chandra* sources, [5] *XMM-Newton* sources, [6] Probable NIR excess

(This table is fully available in Appendix 8)

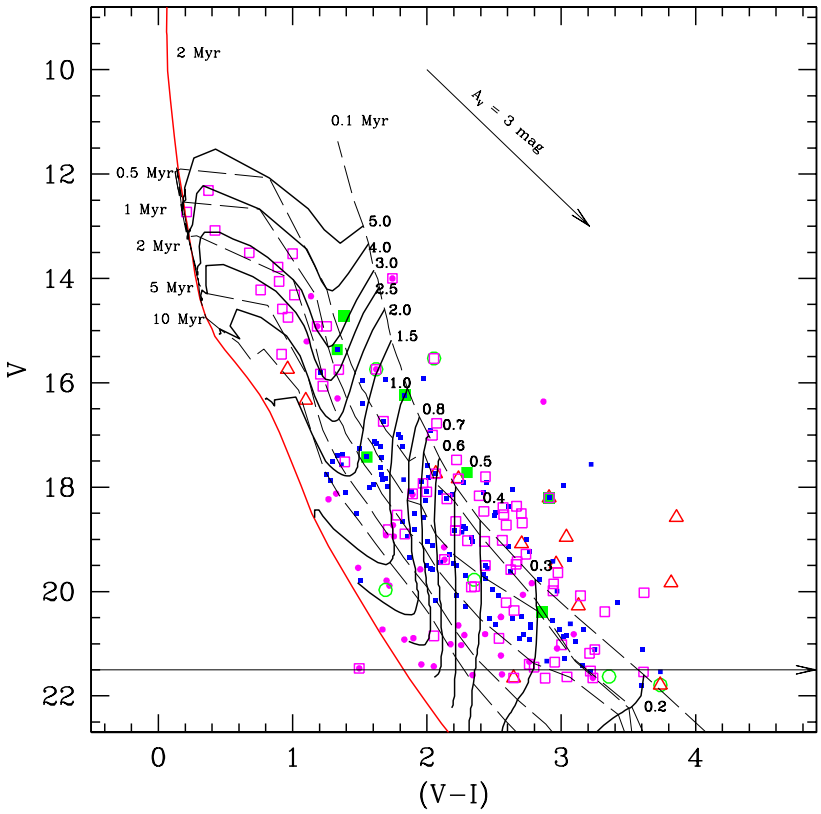

Figure 2.12: $V/(V-I)$ CMD for all the detected YSOs (symbols as in Fig. 2.9, see Sect. 2.4.2.2 for details). The isochrone for 2 Myr by Marigo et al. (2008) (continuous line) and PMS isochrones for 1, 2, 5, and 10 Myr by Siess et al. (2000) (dashed lines) are also shown. All the isochrones are corrected for a distance of 2.9 kpc and reddening $E(B-V) = 0.25$. The horizontal line with an arrow corresponds to the completeness limit of the observations.

(for different ages 0.1, 0.5, 1, 2, 5 and 10 Myr) show PMS isochrones by Siess et al. (2000) and the post-main-sequence isochrone (continuous line) for 2 Myr by Marigo et al. (2008). These isochrones are corrected for the CrW distance (2.9 kpc) and minimum reddening ($E(B-V) = 0.25$ mag, see previous section). It is clear from Fig. 2.12 that a majority of the sources have ages < 1 Myr with a possible age spread up to 10 Myr.

The age and mass of the YSOs have been derived using the $V/(V-I)$ CMD. The Siess et al. (2000) isochrones have very coarse resolution (30 points over their whole mass range of 0.1 to 7 $M_\odot$); therefore, for a better estimation of mass, these isochrones were interpolated (2000 points). We used photometric errors along with the error in the distance modulus and reddening to draw an error box around each

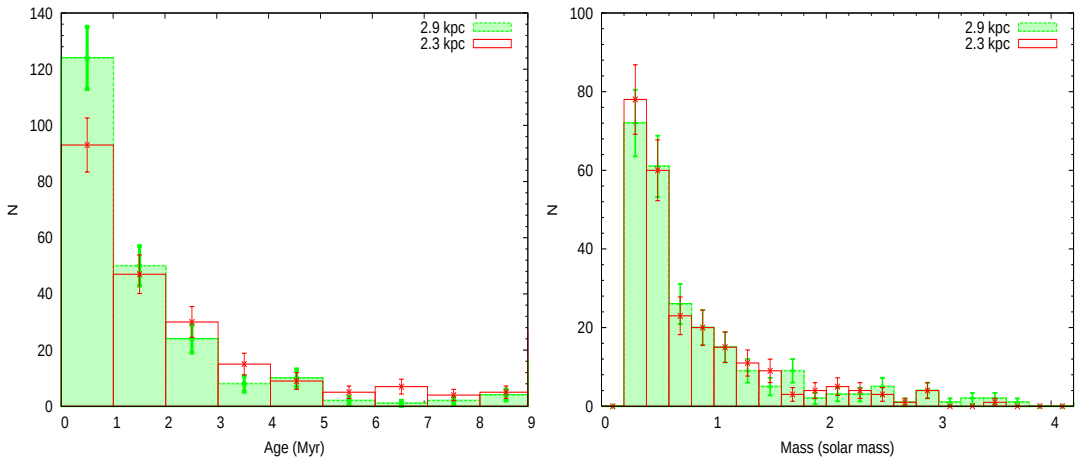

Figure 2.13: Histograms showing the distribution of YSO candidates ages (left panel) and masses (right panel) in the observed CrW region. The green and red histograms are for the estimated ages and masses of YSOs assuming a distance of 2.9 kpc and 2.3 kpc, respectively. The error bars along the ordinates represent $\pm\sqrt{N}$ Poisson errors.

data point. In this box, we generated 500 random points using Monte Carlo simulations. For each generated point, we calculated the age and mass as derived from the nearest passing isochrone. For this study we used a bin size of 0.1 Myr for the Siess et al. (2000) isochrones. At the end we took the mean and standard deviation as the final derived values.

It is important to note that estimating the ages and masses of the PMS stars by comparing their locations in the CMDs with theoretical isochrones is prone to both random and systematic errors (see Chauhan et al., 2009, 2011; Hillenbrand, 2005; Hillenbrand et al., 2008). The effect of random errors due to photometric errors and reddening estimation in determining the ages and masses has been evaluated by propagating the random errors to their observed measurements by assuming a normal error distribution and using Monte Carlo simulations (cf. Chauhan et al., 2009). The systematic errors could be due to the use of different PMS evolutionary models and an error in the distance estimation. Barentsen et al. (2011) mention that the ages may be incorrect by a factor of two owing to systematic errors in the model. The presence of variable extinction in the region will not affect the age estimation significantly because the reddening vector in the $V/(V-I)$ CMD is nearly parallel to the PMS isochrone.

The presence of binaries may also introduce errors into the age determination. Binarity will brighten the star, consequently the CMD will yield a lower age estimate.

In the case of an equal-mass binary, we expect an error of ∼50% to ∼60% in the PMS age estimation. However, it is difficult to estimate the influence of binaries/variables on the mean age estimation because the fraction of binaries/variables is not known. In the study of TTSs in the HII region IC 1396, Barentsen et al. (2011) point out that the number of binaries in their sample of TTSs could be very low since close binaries lose their disk significantly faster than single stars (cf. Bouwman et al., 2006).

We have calculated ages and masses for 241 optically identified individual YSO candidates classified using different schemes (see Table 2.3). Here we would like to point out that out of six optically identified probable NIR excess stars, five have ages $\lesssim$1 Myr. They may be YSOs that are deeply embedded and are formed by the collapse of the core of a molecular cloud. Estimated ages and masses of the YSOs range from ∼0.1 to 10 Myr and ∼0.3 to 4.8 $M_{\odot}$, respectively. This age range indicates a wide spread in the formation of stars in the region. The histograms of age and mass distribution of YSOs are shown in Fig. 2.13.

As stated in Sect. 2.3.3, several authors have used different distances (2.3 kpc) than ours (2.9 kpc) for the Carina nebula. Therefore, we also examined the above results (ages and masses of YSOs) for the distance of 2.3 kpc. The ages and masses of YSOs are once again derived using the same procedure as described above and the corresponding histograms are overplotted in Fig. 2.13. As can be seen in this figure, both derived values are more or less similar within their corresponding errors, although there are slight differences in the numbers of YSOs that are less than 1 Myr. By looking at this figure, we can safely conclude that the majority of the YSOs are younger than 1 Myr and have a mass lower than 2 $M_{\odot}$. These age and mass are comparable with the lifetime and mass of TTSs.

2.4.4 Initial mass function

The distribution of stellar masses that formed in one star-formation event in a given volume of space is called the initial mass function (IMF), and together with the star formation rate, the IMF dictates the evolution and fate of galaxies and star clusters. The effects of environment may be more revealing at the low-mass end of the IMF, since one might imagine that the lower end of the mass spectrum is most strongly affected by external effects. The goals of this study are to identify the PMS populations in order to study the IMF down to the substellar regime.

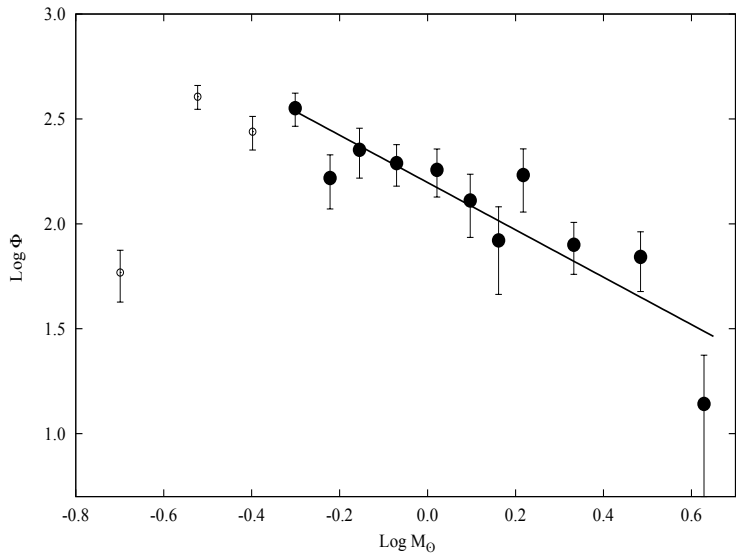

Figure 2.14: Plot of the mass function in the CrW region. Log Φ represents $\log N(\log\, m)$. The error bars represent $\pm\sqrt{N}$ errors. The solid line shows a least-squares fit over the entire mass range $0.5 < \mathrm{M/M_\odot} < 4.8$. Open and filled circles represent the points below and above the completeness limit of our data, respectively.

The mass function (MF) is often expressed by a power law, $N(\log m) \propto m^{\Gamma}$ and the slope of the MF is given as

$$\Gamma = d\log N(\log m)/d\log m \tag{2.2}$$

where $N(\log m)$ represents the number of stars per unit logarithmic mass interval.

The IMF in the Galaxy has been estimated empirically. The first such determination by Salpeter (1955) gave $\Gamma = -1.35$ for the stars in the mass range $0.4 \leq \mathrm{M/M_\odot} \leq 10$. However, more recent works (e.g., Kroupa, 2002; Miller & Scalo, 1979; Rana, 1991; Scalo, 1986) suggest that the mass distribution deviates from a pure power law. It has been shown (see, e.g., Chabrier, 2003; Corbelli et al., 2005; Kroupa, 2002; Scalo, 1998, 1986) that, for masses above $\sim$1M$_\odot$, the IMF can generally be approximated by a declining power law with a slope similar to what is found by Salpeter (1955). However, it is now clear that this power law does not extend to masses much below $\sim$1M$_\odot$. The distribution becomes flatter below 1 M$_\odot$ and turns off at the lowest stellar masses. It has also often been claimed that some (very) massive star-forming regions have a truncated IMF, i.e., contain much smaller numbers of low-mass stars than expected from the field IMF. However, most of the more recent and sensitive studies of massive star-forming regions (see, e.g., Espinoza

et al., 2009; Liu et al., 2009) find the numbers of low-mass stars in agreement with the expectation from the "normal" field star IMF. Preibisch et al. (2011c) confirm these results for the Carina Nebula and support the assumption of a universal IMF (at least in our Galaxy). In consequence, this result also supports the notion that OB associations and very massive star clusters are the dominant formation sites of the galactic field star population, as already suggested by Miller & Scalo (1978).

We have optically identified 241 YSO candidates (cf. Sect. 2.4.2) in the region of CrW and then calculated their masses (cf. Sect. 2.4.3) with the help of optical CMD using the theoretical PMS of Siess et al. (2000). Here we would like to mention that for our photometry, the completeness limit is 0.5 $M_\odot$ for a distance of 2.9 kpc. The MF of the CrW region is plotted in Fig. 2.14. The slope of the MF 'Γ' in the mass range $0.5 < M/M_\odot < 4.8$ comes out to be -1.13 ± 0.20, which is a bit shallower than the value given by Salpeter (1955), and there seems to be no break in the slope at M ∼1 $M_\odot$, as has been noticed in previous works (Jose et al., 2008; Pandey et al., 2008; Sharma et al., 2007). On the other hand, Preibisch et al. (2011c) show that, down to a mass limit around $0.5 - 1$ $M_\odot$, the shape of the IMF in Carina is consistent with that in Orion (and thus the field IMF). Their results directly show that there is clearly no deficit of low-mass stars in the CNC down to ∼1$M_\odot$.

2.4.5 *K*-band luminosity function

The *K*-band luminosity function (KLF) represents the number of stars as a function of the *K*-band magnitude. It is frequently used in studies of young clusters and star-forming regions as a diagnostic tool of the mass function and the star formation history of their stellar populations. The interpretation of KLF has been presented by several authors (see, e.g., Lada & Lada, 2003; Muench et al., 2000; Zinnecker et al., 1993, and references therein).

To obtain the KLF, it is essential to take the incompleteness of the data and the foreground and background source contaminations into account. The completeness of the data is estimated using the *ADDSTAR* routine of *DAOPHOT* as described in Section 2.2.2. To consider the foreground/background field star contaminations, we used both the Besançon Galactic model of stellar population synthesis (Robin et al., 2003) and the nearby reference field stars. Star counts are predicted using the Besançon model in the direction of the control field. We checked the validity of the simulated model by comparing the model KLF with that of the control field and found that both KLFs match rather well. An advantage to using the model is

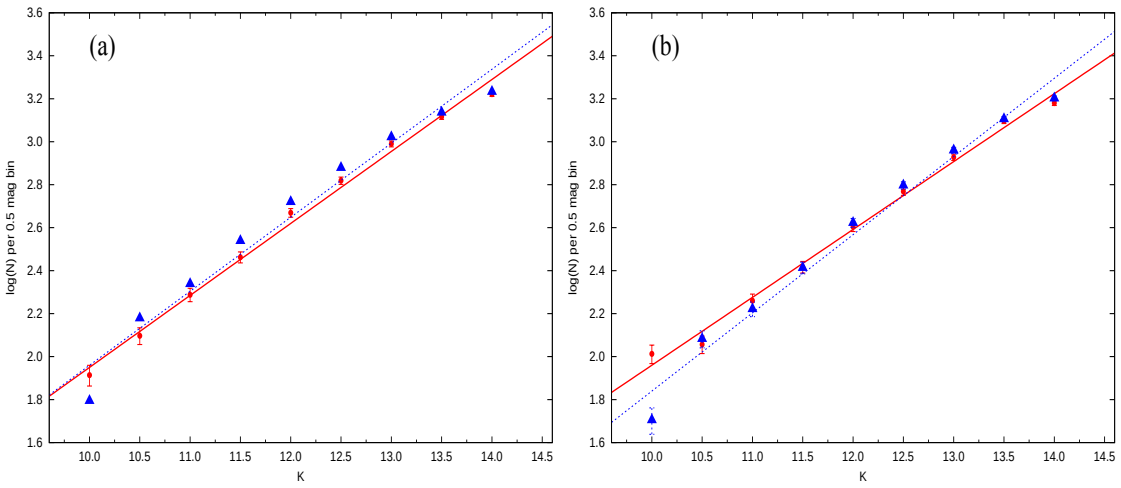

Figure 2.15: Panel (a) Comparison between the observed KLF in the reference field (red filled circles) and the simulated KLF from star counts modeling (blue filled triangles). If the star counts represent the number N of stars in a bin, the associated error bars are $\pm\sqrt{N}$. The KLF slope (α, see Sect. 2.4.5) of the reference field (solid line) is 0.34 ± 0.01. The simulated model (dashed line) also gives the same value of slope (0.34 ± 0.02). Panel (b) The KLF for the CrW region (filled red circles) and the simulated star counts (blue filled triangles). In the magnitude range 10.5 − 14.25, the best-fit KLF slope (α) for the CrW region (solid line) is 0.31 ± 0.01, whereas for the model (dashed line), after taking extinction into account, it comes out to be 0.36 ± 0.02.

that we can separate the foreground (d < 2.9 kpc) and background (d > 2.9 kpc) field stars. As mentioned in Section 2.3.1, the foreground extinction using optical data was found to be A_V ∼0.93 mag. The model simulations with $A_V = 0.93$ mag and d < 2.9 kpc gives the foreground contamination.

The background population (d > 2.9 kpc) was simulated with $A_V = 3.4$ mag in the model. We thus determined the fraction of the contaminating stars (foreground + background) over the total model counts. This fraction was used to scale the nearby reference field. The KLF is expressed by the power law $\frac{dN(K)}{dK} \propto 10^{\alpha K}$, where $\frac{dN(K)}{dK}$ is the number of stars per 0.5 magnitude bin, and α is the slope of the power law.

Figures 2.15a and b show the KLF for the reference field and CrW region, respectively. The α for the reference field and simulated model is 0.34 ± 0.01 and 0.34 ± 0.02, respectively. Similarly α for the CrW region is 0.31 ± 0.01, whereas for the model, after taking the extinction into account, it comes out to be 0.36 ± 0.02.

2.5 Discussion: star formation scenario in the CrW region

Povich et al. (2011) using Spitzer MIR data identified 1439 YSOs (Pan Carina YSO Catalog) in the field surveyed by the CCCP. The spatial distribution of these YSOs throughout the Carina Nebula shows a highly complex structure with clustering at several positions. The majority of YSOs identified by them are located inside the HII cavities near, but less frequently within, the boundaries of dense molecular clouds and the ends of the pillars. They also found that the high concentration of the intermediate mass YSOs is in Tr 14 itself. They have concluded that the recent star formation history in the Carina Nebula has been driven or at least regulated by feedback from the massive stars.

Recently, Gaczkowski et al. (2013) identified 642 YSOs in the Carina Complex with the help of FIR Herschel data. These YSOs are also found to be highly heterogeneously distributed in the region, and they do not follow the distribution of cloud mass. Gaczkowski et al. (2013) show that the Herschel selected YSO candidates are located near the irradiated surfaces of clouds (see Fig. 2.16) and pillars, whereas the Spitzer selected 'YSO' candidates (Povich et al., 2011) often surround these pillars. This characteristic spatial distribution of the young stellar populations in different evolutionary stages has been related by Gaczkowski et al. (2013) to the idea that the advancing ionization fronts compress the clouds and lead to cloud collapse and star formation in these clouds, just ahead of the ionization fronts. They further state that some fraction of the cloud mass is transformed into stars (and these are the YSOs detected by Herschel), while another fraction of the cloud material is dispersed by the process of photo-evaporation. As time proceeds, the pillars shrink, and a population of slightly older YSOs is left behind and revealed after the passage of the ionization front. Their results provide additional evidence that the formation of these YSOs was indeed triggered by the advancing ionization fronts of the massive stars as suggested by the theoretical models (see Gritschneder et al., 2010).

Roccatagliata et al. (2013) with the help of the wide-field Herschel SPIRE and PACS maps, determined the temperatures, surface densities, and the local strength of the far-UV irradiation for all the cloud structures over the entire spatial extent of the CNC. They find that the density and temperature structure of the clouds in most parts of the CNC are dominated by the strong feedback from the numerous massive stars, rather than by random turbulence. They also conclude that the CNC

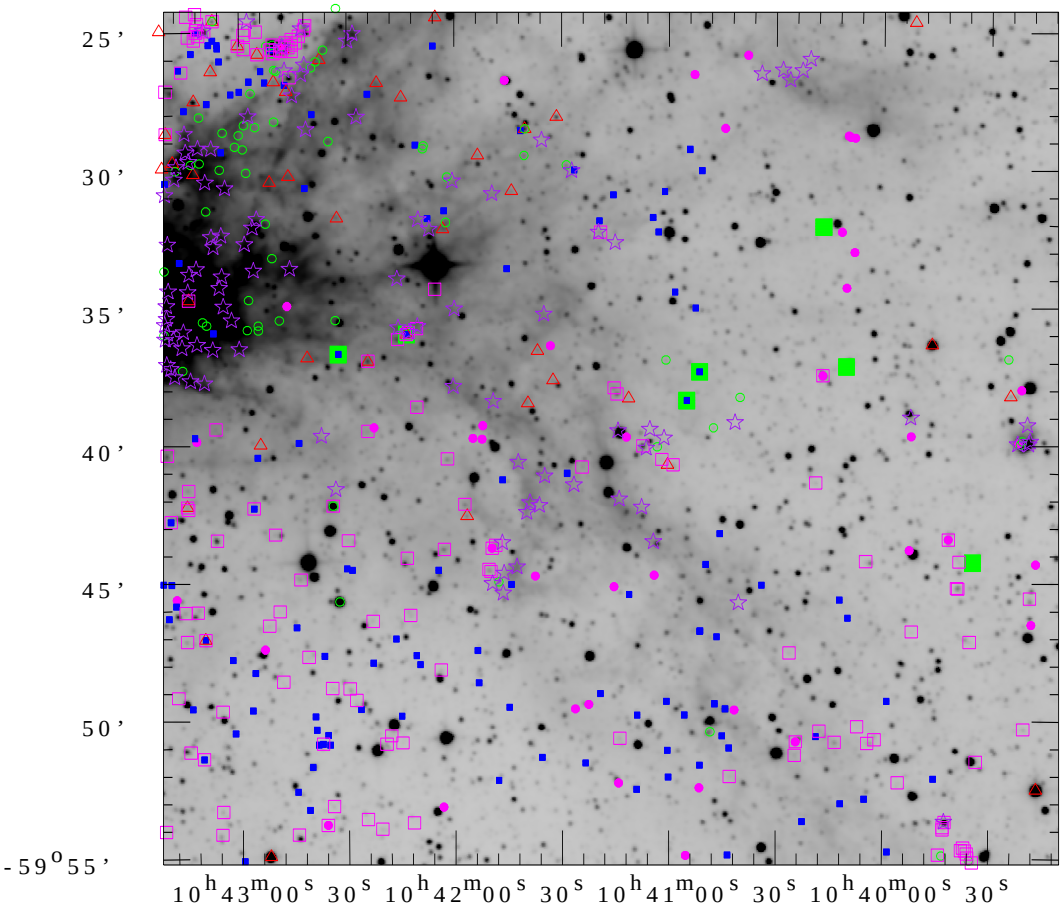

Figure 2.16: Spatial distributions of different classes of YSOs. Various symbols are overlaid on the WISE 4.6 μm image. The filled square symbols represent X-ray identified sources (*XMM-Newton* bigger green, *Chandra* sources small blue). Open magenta squares, open red triangles, filled magenta circles, and open green circles are Spitzer-identified YSOs, CTTSs, $H\alpha$ emission stars, and probable NIR-excess YSOs, respectively. Purple star symbols are Herschel YSO sources. The abscissae and the ordinates represent RA and Dec, respectively for the J2000 epoch.

is forming stars in a particularly efficient way, which is a consequence of triggered star formation by radiative cloud compression due to numerous high mass stars.

In the center of Carina, there are the young clusters, Trumpler 14, 15, and 16, that host about 80% of the high mass stars of the entire complex (Roccatagliata et al., 2013). This is also the hottest region of the nebula with temperatures ranging between 30 and 50 K, whereas the molecular cloud at the western side of Tr 14 has a temperature of about 30 K and a decrease in density from the inner to the edge part (Roccatagliata et al., 2013). Our studied region CrW contains this cloud, which can be seen in our infrared extinction map (see Fig. 2.7). In Fig. 2.16, different classes of

YSOs identified in our study are overlaid on the WISE 4.6 μm (MIR) image. We can easily see the extension of the dust lane in the figure from northeast to southwest of the CrW region. The northeast region contains the outer most part of the cluster Tr 14 along with the high density region of the molecular cloud (see Fig. 2.7). Smith & Brooks (2008) show the spatial relationship of Tr 14, the ionized gas, the PDR emission, the molecular gas, and the dust lane. The brightest molecular emission is concentrated towards the dark western dust lane offset from the center of Tr 14 by 4 arcmin. The radio continuum for emission source "Car I" can also be seen here at the interface of the dust lane and the bright HII region. Between this source and the molecular cloud, a widespread PDR emission can also be seen in the form of an arc like PAH emission feature at 3.3 μm (Rathborne et al., 2002). At a projected distance of $\sim$2 pc, the UV output of Tr 14 dominates the other Carina Nebula clusters such as Tr 16 in determining the local flux at the PDR in the northern cloud (Brooks et al., 2003; Smith, 2006a; Smith & Brooks, 2008). This spatial sequence of Tr 14, radio source, PAH emission, and then strong molecular emission delineates a classical edge-on PDR (Brooks et al., 2003). The edge of this region contains many Spitzer-identified YSOs. The alignment of the YSOs in this region may be due to the star formation triggered by high mass stars of Tr 14.

The Herschel-identified YSOs (Gaczkowski et al., 2013) are located mainly in the high density region of the molecular clumps and in small groupings at several places along the dust lane. Gaczkowski et al. (2013) have derived an age of $\sim$0.1 Myr for their sample of YSOs. The probable NIR excess stars identified in this study also follow this region. For some of them, we derived ages $\lesssim$1 Myr. These sets of identified YSOs are basically very young in nature and are embedded in the cores of the molecular cloud. We could not say anything about the northwest region of CrW, which is not well covered by previous surveys.

Smith et al. (2010) observed in their western mosaic (which contains most of our observed region including the dark lane, see their Fig. 3), the YSOs density of around 500 sources/deg^2 with little signs of clustering. In this study we have identified 467 YSOs falling in the CrW region. The overall density of this region then turns out to be $\sim$1700 sources/deg^2 which is higher than three times the YSOs density given by Smith et al. (2010). Here it is worthwhile to mention that the PCYC used in previous studies has a sensitivity problem at the ionization front between Tr 14 and the Car I molecular cloud core to the west (Ascenso et al., 2007;

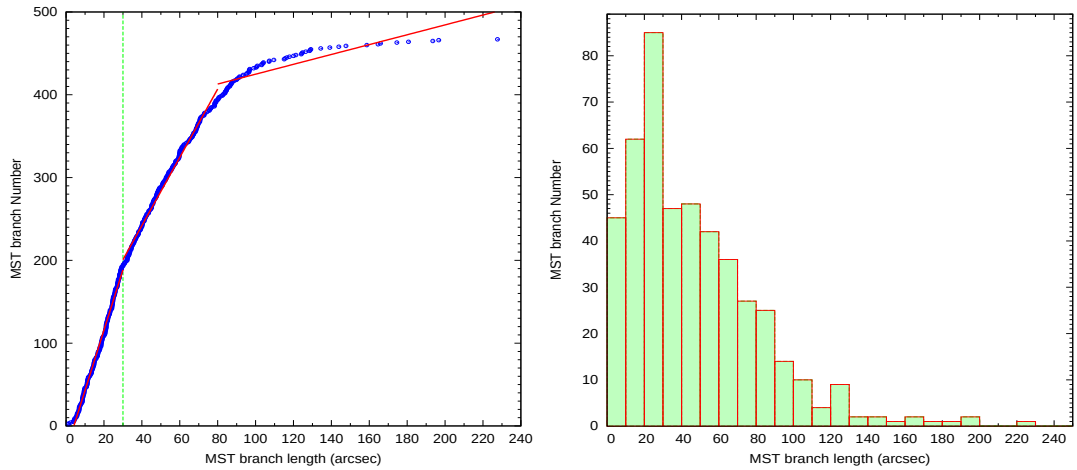

(a) (b)

Figure 2.17: Cumulative distribution of the MST branch lengths. In panel (a), the solid lines represent the linear fits to the points smaller and larger than the chosen critical branch length. The critical radius is shown by a vertical line. Panel (b) is the histogram of the MST branch lengths for the YSOs in the CrW region (see text).

Table 2.4: The YSO cores identified in the CrW region and their characteristics.

Core number	Radius (pc)	Number of YSOs in core (N)	Number density (N/pc^2)	Median branch length (pc)
A	0.45	6	9.43	0.32
B	0.37	6	13.95	0.26
C	0.51	8	9.79	0.36
D	0.56	7	7.11	0.33
E	0.18	4	39.30	0.12
F	0.26	5	23.54	0.20
G	0.39	4	8.37	0.36
H	0.49	6	7.95	0.31
I	0.64	6	4.66	0.30
J	0.44	7	11.51	0.28
Average	0.43	5.9	13.56	0.28

Yonekura et al., 2005) where the diffuse MIR nebular emission is bright (Povich et al., 2011).

The complex observational patterns (e.g., filaments, bubbles, and irregular clumps, etc.) in a molecular cloud such as Carina nebula are resulting from the interplay of fragmentation processes. The star formation usually takes place inside the dense cores of the molecular clouds, and the YSOs often follow clumpy structures of their

parent molecular clouds (see, e.g., Allen et al., 2002; Gomez et al., 1993; Gutermuth et al., 2005, 2008; Lada et al., 1996; Motte et al., 1998; Teixeira et al., 2006; Winston et al., 2007). Recently, fragmentations in gas with turbulence (e.g., Ballesteros-Paredes et al., 2007) and magnetic fields (e.g., Ward-Thompson et al., 2007) have been discussed, leading to detailed predictions for the distributions of fragment spacings. The spatial distribution of YSOs in a region can be analyzed in terms of a typical spacing between them in order to compare this spacing to the Jeans fragmentation scale for a self-gravitating medium with thermal pressure (Gomez et al., 1993). Some recent observations of star-forming regions have been analyzed in terms of the distribution of nearest neighbor (NN) distances (see Gutermuth et al., 2005; Teixeira et al., 2006) and find a strong peak in their histogram of NN spacings for the protostars in young embedded clusters. This peak indicated a significant degree of Jeans fragmentation, since this most frequent spacing agreed with an estimate of the Jeans length for the dense gas within which the YSOs are embedded. These results also suggest that the tendency for a narrow range of spacings among YSOs in a cluster can last into the Class II phase of YSO evolution.

Recently, Gutermuth et al. (2009) have done a complete characterization of the spectrum of source spacings using the minimal spanning tree (MST) of source positions. The MST is defined as the network of lines, or branches, that connect a set of points together such that the total length of the branches is minimized and there are no closed loops (see, e.g., Cartwright & Whitworth, 2004; Gutermuth et al., 2009, and references therein). Gutermuth et al. (2009) demonstrate that the MST method yields a more complete characterization than the NN method. Therefore, for the present study, we used the same MST algorithm to analyze the spatial distribution of YSOs in the CrW region.

In Fig. 2.17b, we plotted the histogram of MST branch lengths for the YSOs in the CrW region. From this plot, it is clear that they have a peak at small spacings and that they also have a relatively long tail of large spacings. Peaked distance distributions typically suggest a significant subregion (or subregions) of relatively uniform, elevated surface density. By adopting an MST length threshold, we can isolate those sources that are closer together than this threshold, yielding populations of sources that make up a local surface density enhancement. To get this threshold distance, in Fig. 2.17a, we plotted the cumulative distribution function (CDF) for the branch length of YSOs. The curve shows three different slopes: first a steep-sloped segment at short spacings then a transition segment that approximates

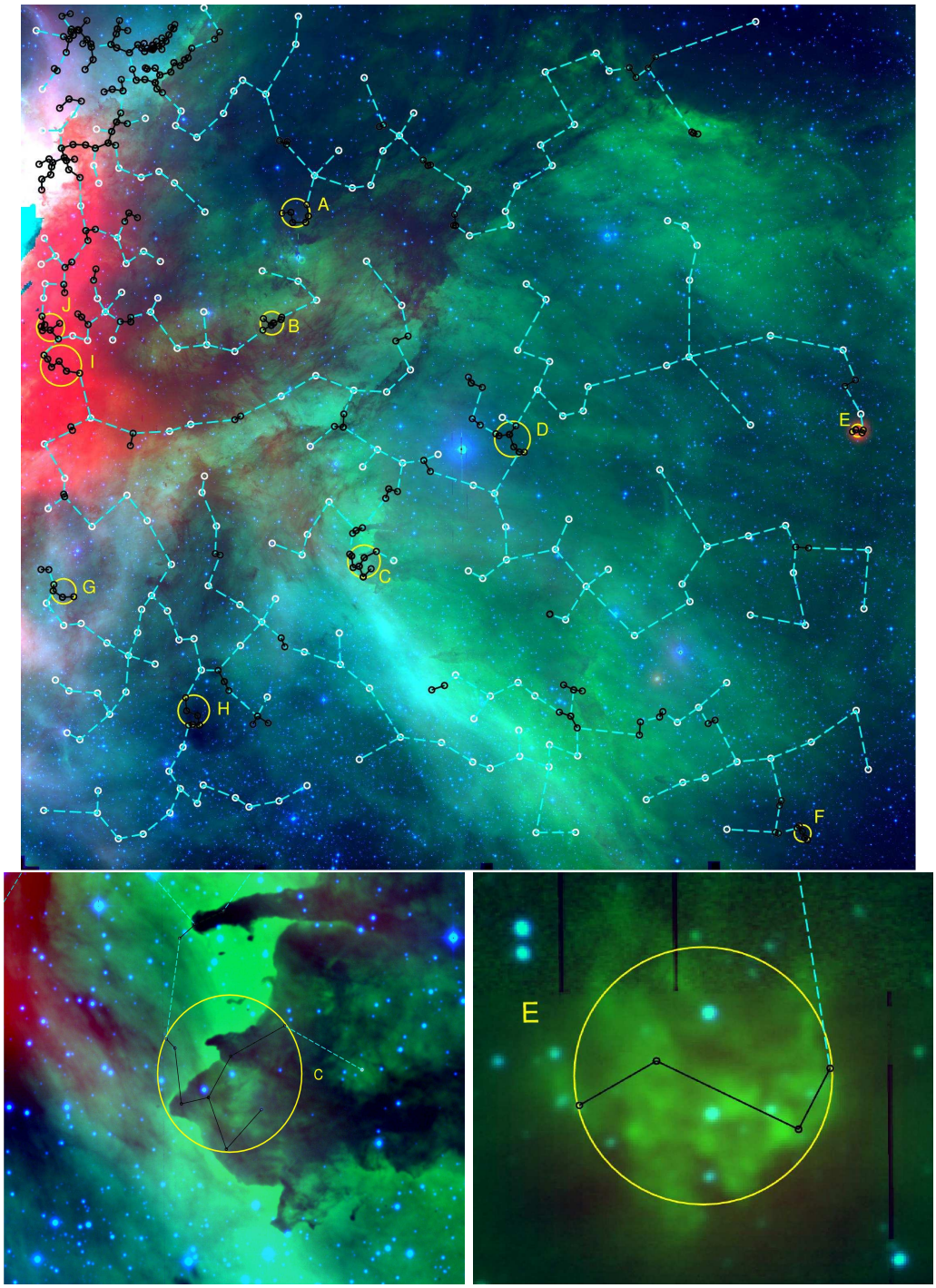

Figure 2.18: Top: Minimal spanning tree of the YSOs overplotted on a colour composite image of the CrW region (WISE 22 μm (red), $H\alpha$ band (green), and V band (blue) images). WR 22 is situated in the center. The white circles connected with dotted lines, and black circles connected with solid lines are the branches that are larger and smaller than the basic critical length, respectively. The identified ten cluster cores are encircled with yellow colour and labeled with A to J. Bottom: Two zoomed images of YSO cores, C and E, are shown in the lower left and right panels, respectively (see text for detail).

the curved character of the intermediate-length spacings, and finally a shallow-sloped segment at long spacings. For the present study, we have chosen the peak in the histogram (∼30 arcsec i.e. ∼0.42 pc), which corresponds to the first steep-sloped segment, as a threshold or critical length.

In Fig 2.18, the results from the MST analysis are overplotted on the RGB image of the CrW region. This image was created using red, green, and blue colours for the WISE 22 μm, $H\alpha$, and V band images, respectively. Circles and MST connections in black deal with the objects that are more closely spaced than the critical length (0.42 pc).

A close inspection of Fig. 2.18 reveals that the CrW region exhibits heterogeneous structures, and there are several close concentrations of YSOs distributed along the molecular clumps. Prominent YSO clustering can be seen in the northeastern part of this figure and are possibly part of the star cluster Tr 14. There are also ten cores (having MST branch lengths less than the critical distance) distributed along the molecular cloud (indicated in Fig. 2.18). A close view of the cores C and E can be seen in the lower left and right panels of Fig 2.18. The details about these cores have been given in Table 2.4. The majority of the members of all these cores are the YSOs identified in the Herschel survey having very young ages. Our result agrees with the conclusions of Gutermuth et al. (2009) and Günther et al. (2012), indicating that the young protostars are found in a region having marginally higher surface densities than the more evolved PMS stars. The average of median branch length and core radius is found to be 0.28 pc and 0.43 pc, respectively (see Table 2.4).

To check the role of WR 22 in the formation of stars in this region, we tried to look at the spatial distribution of YSOs (Fig. 2.19) with optical counterparts (whose age has been derived using the $V/(V-I)$ CMD, cf. Sect. 2.4.3.2) in the CrW region. The general observation is that within the detection limit of optical observations, the YSOs show mixed populations of different ages throughout the CrW region. The extreme northeastern region contains a group of YSOs that are under the direct influence of the high-mass stars of Tr 14, and it also shows a mixed population. For most of the YSOs in the dust lane, we have not found their optical counterparts. This age distribution around CrW does not show any trend even in the presence of a very massive star such as WR 22. It seems that WR 22 has not influenced these YSOs much. Smith et al. (2010) presented Spitzer observations of a part of the CrW region studied here. These authors reached similar conclusions, suggesting that this

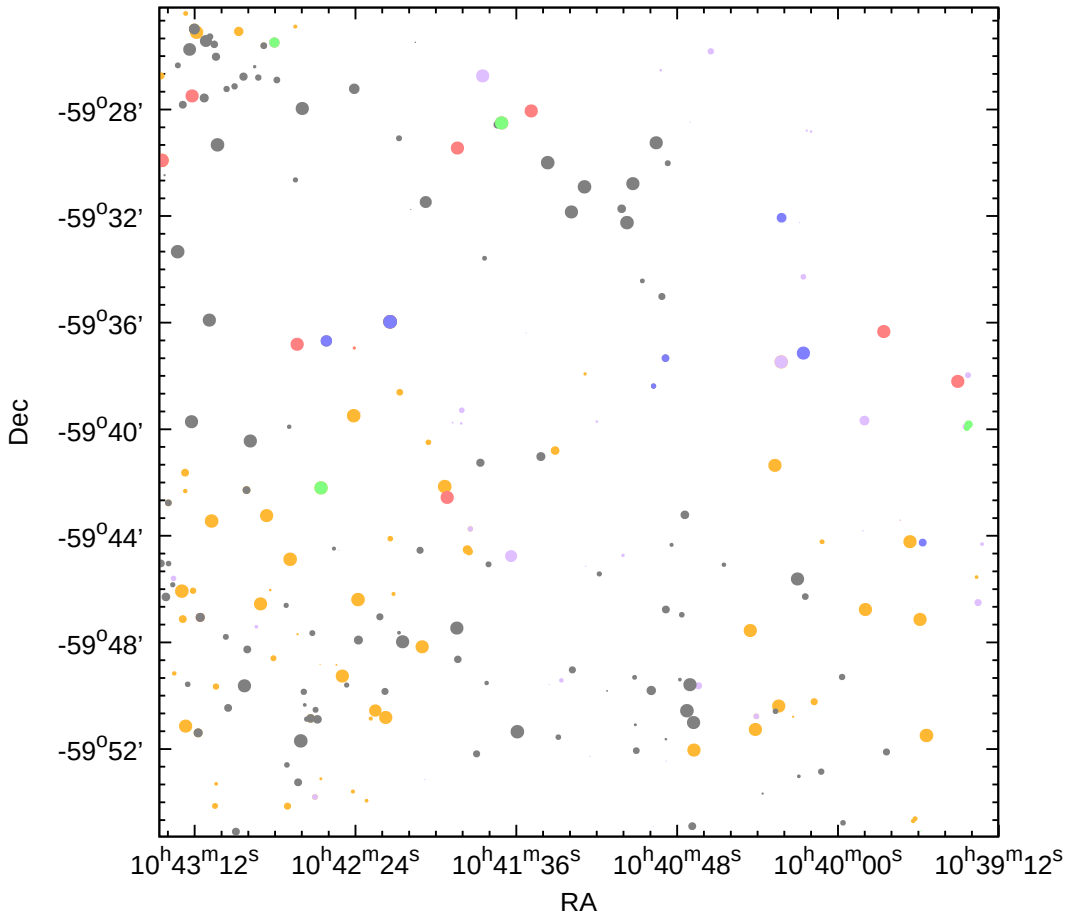

Figure 2.19: Spatial distribution of the optically identified YSO candidates in the CrW region. The size of the symbols represents the age of the YSO candidate, i.e. bigger the size younger the YSO is. Various colours represent YSO candidates identified using different schemes (Spitzer - orange, $H\alpha$ - purple, CTTS - red, *Chandra* sources - black, *XMM-Newton* - blue, and IR excess - green).

very massive star may be projected in the foreground or background compared to the surrounding molecular gas, or it could have only recently arrived at its present location.

2.6 Summary and conclusions

Although the center of the Carina nebula has been studied extensively, the outer region has been neglected due to the absence of wide field optical surveys. In this study, we investigated a wide field ($32' \times 31'$) located in the west of the Carina nebula and centered on the massive binary WR 22. To our knowledge, this is the first

detailed study of this region. We used deep optical ($UBVRI$) and $H\alpha$ photometric data obtained with the WFI instrument at the ESO/MPG 2.2 m telescope (La Silla). Our V band photometry is complete up to ∼21.5 mag. Low-resolution spectroscopy along with *Chandra*, *XMM-Newton*, and 2MASS archival data sets, were also used in this analysis. We generated various combinations of optical and NIR TCD, CMDs and calculated several parameters such as reddening, reddening law, etc. We also identified the YSOs located in the region and studied their spatial distribution using the MST method. Ages and masses of the 241 YSOs having optical counterparts, were derived based on $V/(V-I)$ CMD. These YSOs have been further used to constrain the IMF of the region. The main scientific results from our study are as follows:

- The region shows a large amount of differential reddening with minimum and maximum $E(B-V)$ values of 0.25 and 1.1 mag., respectively. This region shows an unusual reddening law with a total-to-selective extinction ratio $R_V = 3.7 \pm 0.1$.

- The MK spectral types for a subsample of 15 X-ray emitting sources in the CrW region are established that indicates that the majority of them are late spectral type stars. There are three sources belonging to each O, A, and F spectral types; however, six sources are of spectral type G.

- We cross-correlated the 43 *XMM-Newton* X-ray sources from Claeskens et al. (2011) with our optical photometry and found that 34 of them are well matched. Out of these 34 sources, 7 have been identified as YSOs. We also cross-identified the *Chandra* X-ray sources (1465 in our region) with our source list and found 469 objects with optical/NIR counterparts. In total, 119 X-ray sources are identified as YSOs, four of them in common with *XMM-Newton*.

- We collected a sample of 467 YSOs identified in the CrW region based on their IR-excess, $H\alpha$ and X-ray emission. In some cases, the same YSOs were identified in more than one scheme. Out of these, there are 41 $H\alpha$ emitters, 105 Herschel identified YSOs, 136 Spitzer identified YSOs, and 225 2MASS identified YSOs in our list. The YSO density for the CrW region turns out to be ∼1700 sources/degree^2, which is higher when compared to the reported values (500 sources/degree^2, Smith et al. 2010).

- We calculated the age and mass of 241 individual optically identified YSOs. Estimated ages and masses of the YSOs range from ∼0.1 to 10 Myr and ∼0.3 to 4.8 $M_{\odot}$, respectively. This age range indicates a wide spread in the formation of stars in the region. The majority of these YSOs are younger than 1 Myr, and their mass is below 2 $M_{\odot}$.

- We derived the IMF and calculated the slope 'Γ' in the CrW region. In the mass range $0.5 < M/M_{\odot} < 4.8$, it comes out as -1.13 ± 0.20 which is a bit shallower than the value of -1.35 given by Salpeter (1955), and there seems to be no break in the slope at M ∼1$M_{\odot}$. The slope of the K-band luminosity function is found to be $\alpha = 0.31 \pm 0.01$.

- The spatial distribution of all 467 YSOs has been studied in detail. The edge of the irradiated surface between Tr 14 and the molecular cloud contains many Spitzer identified YSOs whose formation was probably triggered by the high-mass stars of Tr 14. The high-density region of molecular clumps contains many probable NIR excess stars, as well as Herschel-identified YSOs that are very young in age ($\lesssim$1 Myr).

- We used the well-established MST method to identify local density enhancements in the YSO distributions. The northeastern part of the studied region presents a more prominent YSO clustering. However, there are at least ten cores of four or more very young YSO members distributed all over the CrW region and having different core radii. The average core radii and median branch length values for these cores are found to be 0.43 pc and 0.28 pc, respectively. The YSOs having optical counterparts in CrW are uniformly distributed having mixed populations of different ages. The age distribution around CrW does not show any trend in the presence of the very massive star WR 22. It seems that WR 22 is a foreground/background star which has not influenced the formation of YSOs in the CrW region.

Chapter 3

CCSNe, progenitors: the Type IIb supernova 2011fu

3.1 Introduction

It is commonly recognized that core-collapse supernovae (CCSNe) represent the final stages of the life of massive stars ($M > 8{-}10$ $M_{\odot}$; Anderson & James, 2009; Heger et al., 2003a; Smartt, 2009). Generally, the fate of a massive star is governed by its mass, metallicity, rotation and magnetic field (Fryer, 1999; Heger et al., 2003a; Woosley & Janka, 2005). Massive stars show a wide variety in these fundamental parameters, causing diverse observational properties among various types of CCSNe. The presence of dominant hydrogen lines in the spectra of Type II SNe strongly suggests that their progenitors belong to massive stars, which are still surrounded by significantly thick hydrogen envelopes before the explosion (for a review on different types of SNe, see Filippenko, 1997). In contrast, Type Ib events are H-deficient but He is still present in their spectra, unlike Type Ic SNe, where both H and He features are absent. After the discovery of SN 1987K, another class, referred as Type IIb (see Filippenko, 1988; Woosley et al., 1987), was included in the CCSN zoo. The observational properties of these SNe closely resemble those of Type II SNe during the early phases, while they are more similar to Type Ib/c events at later epochs.

However, in a few cases, the spectral classification of Type IIb SNe is more controversial: for example, SN 2000H (Benetti et al., 2000; Branch et al., 2002; Elmhamdi et al., 2006); SN 2003bg (Filippenko & Chornock, 2003; Soderberg et al., 2006); SN 2007Y (although this event is classified as Type Ib/c by e.g. Monard (2007); Stritzinger et al. (2009) however, Maurer et al. (2010) suggested that it is a

Type IIb) and SN 2009mg (Prieto, 2009; Roming et al., 2009a; Stritzinger, 2010)). SNe of Type IIb are further divided into two subgroups: Type cIIb with compact progenitors like SNe 1996cb, 2001ig and 2008ax, and Type eIIb with extended progenitors, e.g SNe 1993J and 2001gd (Chevalier & Soderberg, 2010).

Type IIb and Type Ib/c SNe are collectively known as "stripped envelope" CCSNe (Clocchiatti et al., 1997) because the outer envelopes of hydrogen and/or helium of their progenitors are partially or completely removed before the explosion. The possible physical mechanisms behind this process may be stellar winds (Puls et al., 2008) or interaction with a companion star in a binary system where mass transfer occurs due to Roche lobe overflow (Podsiadlowski et al., 1992). There have been several studies about the discovery of the progenitors of Type IIb SNe but, there is still a debate about how they manage to keep only a thin layer of hydrogen (Aldering et al., 1994; Arcavi et al., 2011; Crockett et al., 2008; Maund et al., 2011, 2004; Ryder et al., 2006; Soderberg et al., 2012; Sonbas et al., 2008; Van Dyk et al., 2011).

To date, approximately 77[1] Type IIb SNe are known, but only a few of them have been properly monitored and well-studied. Among these, SNe 1987K (Filippenko, 1988); 1993J (Lewis et al., 1994; Richmond et al., 1994; Schmidt et al., 1993); 1996cb (Qiu et al., 1999), 2003bg (Hamuy et al., 2009; Mazzali et al., 2009); 2008ax (Chornock et al., 2011; Pastorello et al., 2008; Roming et al., 2009b; Taubenberger et al., 2011); 2009mg (Oates et al., 2012); 2011ei (Milisavljevic et al., 2013) and more recently 2011dh (Arcavi et al., 2011; Bersten et al., 2012; Bietenholz et al., 2012; Horesh et al., 2013; Krauss et al., 2012; Martí-Vidal et al., 2011; Maund et al., 2011; Soderberg et al., 2012; Van Dyk et al., 2011; Vinkó et al., 2012) have been remarkably well-studied.

An interesting property of the observed light curves (LCs) of a few Type IIb SNe is the initial peak and rapid decline followed by a subsequent rise and a secondary maximum. The first peak is thought to be a result of break-out of the SN shock from the extended progenitor envelope (Falk & Arnett, 1977). The properties of the shock break-out peak depend on the envelope mass and the density structure of the outer layers. The shock break-out phase can last from seconds to days. Therefore, early discovery and rapid-cadence early-time observations might help us to better understand the properties of the outer envelope of massive stars (Gal-Yam et al., 2011).

[1]http:heasarc.gsfc.nasa.gov/W3Browse/star-catalog/asiagosn.html

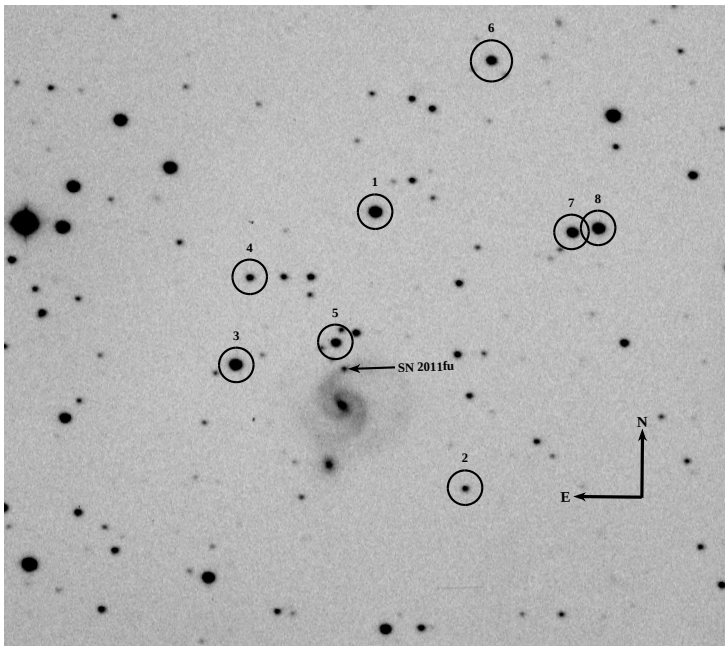

Figure 3.1: V-band image of the SN 2011fu field around the galaxy UGC 01626, observed on 2011 November 16 with the 1-m ST, India. The SN is marked with a black arrow. The reference standard stars used for calibration are marked with numbers 1-8. On this image, north is up and east is to the left.

In this paper, we present the results from photometric and spectroscopic monitoring of SN 2011fu starting shortly after the discovery and extending up to nebular phases. The photometric and spectroscopic properties of this event have revealed that SN 2011fu is a Type IIb supernova. The type determination for this SN was verified with SNID (Blondin & Tonry, 2007), highlighting the fact that the object has an excellent resemblance to SN 1993J.

3.2 Observations and Data Analysis

SN 2011fu was discovered in a spiral arm of the galaxy UGC 01626 (type SAB(rs)c) by F. Ciabattari and E. Mazzoni (Ciabattari et al., 2011) on 2011 September 21.04 (UT) with a 0.5-m Newtonian telescope in the course of the Italian Supernovae Search Project. The brightness of the SN at the time of discovery was reported to be at mag $\sim$ 16 (unfiltered). It was located 2″, west and 26″, north of the center of the host galaxy, with coordinates $\alpha = 02^h08^m21^s41$, $\delta = +41°29'12''3$ (equinox 2000.0) (Ciabattari et al., 2011). The host galaxy has a heliocentric velocity and

Table 3.1: Identification number (ID), coordinates (α, δ) and calibrated magnitudes of standard stars in the field of SN 2011fu.

Star ID	α_{J2000} (h m s)	δ_{J2000} (° ′ ″)	U (mag)	B (mag)	V (mag)	R (mag)	I (mag)
1	02 08 19.66	+41 30 53.4	15.59±0.02	15.47±0.02	14.80±0.01	14.38±0.02	14.03±0.02
2	02 08 14.25	+41 27 51.8	18.39±0.09	18.17±0.02	17.59±0.02	17.16±0.02	16.83±0.03
3	02 08 27.70	+41 29 11.4	16.29±0.02	15.70±0.02	14.86±0.02	14.34±0.02	13.93±0.03
4	02 08 26.92	+41 30 07.5	17.53±0.04	17.58±0.02	17.07±0.02	16.70±0.02	16.40±0.03
5	02 08 21.94	+41 29 26.9	16.78±0.03	16.77±0.02	16.21±0.01	15.84±0.02	15.54±0.02
6	02 08 12.72	+41 32 34.8	16.36±0.02	16.45±0.02	15.85±0.01	15.44±0.02	15.07±0.02
7	02 08 08.04	+41 30 41.3	16.32±0.02	16.07±0.02	15.38±0.01	14.97±0.02	14.61±0.02
8	02 08 06.54	+41 30 43.7	17.23±0.03	16.03±0.02	14.93±0.02	14.32±0.02	13.78±0.02

redshift of 5543 ± 11 km s^{-1} and $z = 0.01849 \pm 0.00004$[1], respectively. The first spectrum of SN2011fu was obtained on 2011 September 23.84 UT with the Ekar-Copernico 1.82-m telescope (range 360-810 nm; resolution 2.2 nm) by Tomasella et al. (2011), showing a blue continuum with superimposed weak H and He I 587.6-nm features, which led to the classification as a young Type II SN.

3.2.1 Optical Photometry

The prompt photometric follow-up of SN 2011fu started shortly after the discovery and continued using three ground-based telescopes in India. The majority of the observations were made using the 2-m *Himalayan Chandra Telescope* (HCT) of the Indian Astronomical Observatory, Hanle and the 1-m *Sampurnanand Telescope* (ST) at the Aryabhatta Research Institute of observational sciencES (ARIES), Nainital, India. All observations were performed in the Bessell *UBVRI* bands.

The HCT photometric observations started on 2011 September 28 using the Himalaya Faint Object Spectrograph Camera (HFOSC). The central 2k × 2k region of a 2k × 4k SITe CCD chip was used for imaging which provided an image scale of 0.296 arcsec pixel^{-1} across a 10 × 10 arcmin^2 field-of-view.

Further photometric observations were carried out using a 2k × 2k CCD camera at the f/13 Cassegrain focus of the 1-m ST telescope situated at ARIES, Nainital. The CCD chip has square pixels of $24 \times 24\,\mu$m, a scale of 0.38 arcsec per pixel and the entire chip covers a field of 13 × 13 arcmin^2 on the sky. The gain and readout noise of the CCD camera are 10 electrons per ADU and 5.3 electrons, respectively. A finding chart showing the field of the SN 2011fu along with the local standard stars is presented in Fig. 3.1.

[1]HyperLEDA - http://leda.univ-lyon1.fr

In addition, we also observed this SN in the V and R bands on 2011 December 01 and 2012 March 02 using the 1.3m Devasthal Fast Optical Telescope (DFOT) (Sagar et al., 2012, 2011), recently installed at Devasthal, Naintial. DFOT uses a 2048 × 2048 ANDOR CCD camera having $13.5\mu m \times 13.5\mu$m pixels mounted at the f/4 Cassegrain focus of the telescope. With a 0.54 arcsec per pixel plate scale, the entire chip covers a 18 × 18 arcmin^2 field-of-view on the sky. The CCD can be read out with 31, 62, 500 and 1000 kHz speed, with a system RMS noise of 2.5, 4.1, 6.5, 7 electrons and a gain of 0.7, 1.4, 2, 2 electrons/ADU respectively. We selected the 500 kHz readout frequency during our observations.

To improve the signal-to-noise ratio (S/N), all the photometric observations were carried out with a 2×2 binning. Along with the science frames several bias and twilight flat frames were also collected. Alignment and determination of the mean FWHM on all science frames were performed after the usual bias subtraction, flat fielding and cosmic-ray removal. The standard tasks available in IRAF and DAOPHOT (Stetson, 1987, 1992) were used for pre-processing and photometry.

The pre-processing steps for images taken with all three telescopes were performed in a similar fashion. The stellar FWHM on the V-band frames typically varied from 2″, to 4″, with a median value of around 2″5. We also co-added individual frames, wherever necessary, before computing the final photometry.

For photometric calibration, we observed the standard field PG0231 (Landolt, 2009) in $UBVRI$ bands with the 1-m ST on 2011 December 17 under good photometric conditions (transparent sky, seeing FWHM in $V \sim 2''$). The profile fitting technique was applied for the photometry of SN 2011fu and Landolt field and then instrumental magnitudes were converted into standard system following least-square linear regression procedures outlined in Stetson (1992). The average atmospheric extinction values (0.57, 0.28, 0.17, 0.11 and 0.07 mag per unit airmass for U, B, V, R and I bands, respectively) for the site were adopted from Kumar et al. (2000). The chosen Landolt stars for calibration were in the brightness range of $12.77 \leq V \leq 16.11$ mag and colour range of $-0.33 \leq B - V \leq 1.45$ mag. Using these stars, transformation to the standard system was derived by applying the following zero-points and colour coefficients:

$$u - U = (7.27 \pm 0.01) + (-0.08 \pm 0.02)(U - B)$$

$$b - B = (4.90 \pm 0.004) + (-0.04 \pm 0.01)(B - V)$$

$$v - V = (4.34 \pm 0.01) + (-0.04 \pm 0.01)(B - V)$$

$$r - R = (4.19 \pm 0.01) + (-0.04 \pm 0.01)(V - R)$$

$$i - I = (4.60 \pm 0.02) + (0.04 \pm 0.02)(V - I)$$

Here U, B, V, R, I are the catalog magnitudes and u, b, v, r, i are the corresponding instrumental magnitudes. Table 3.1 lists the coordinates and magnitudes of the eight local secondary standard stars in the SN field.

To estimate the possible contribution from the host galaxy to the measured supernova fluxes, we used the *ISIS*[1] image subtraction package. We acquired deep images (having total exposure times of more than 20 minutes) in the $BVRI$ bands with the HCT telescope on 25 August 2012 under good sky conditions. As the supernova was not detected in any of these frames, we used them as template frames for image subtraction. We found minor differences, not exceeding 0.1 mag, between the SN magnitudes with and without applying the image subtraction for the data at later epochs i.e. 70 days after the first observation. The final results of our SN photometry (without applying image subtraction corrections) along with robustly determined PSF errors, are presented in Table 3.2.

3.2.2 Spectroscopic observations

Spectroscopic observations of SN 2011fu were obtained at 8 epochs, between 2011 September 28 (JD 2455833.27) and December 22 (JD 2455918.11). A journal of these observations is given in Table 3.3. The SN spectra were taken with the HFOSC instrument mounted at the 2-m Himalayan Chandra Telescope. All spectra were obtained using grisms Gr#7 (wavelength range 3500 - 7800 Å) and Gr#8 (wavelength range 5200 - 9200 Å). FeAr and FeNe arc lamp spectra were applied for wavelength calibration. Spectrophotometric standards were also observed with a broader slit to correct for the instrumental response and flux calibration.

The reduction of the spectroscopic data were carried out in a standard manner using various tasks available within IRAF. First, all images were bias-subtracted and flat fielded. Then, one dimensional spectra were extracted from the two-dimensional cleaned images using the optimal extraction algorithm (Horne, 1986). The wavelength calibration was computed using the arc spectra mentioned above. The accuracy of the wavelength calibration was checked using the night sky emission lines and small shifts were applied to the observed spectra whenever required. The instrumental response curves were determined using the spectrophotometric standards

[1]http://www2.iap.fr/users/alard/package.html

Table 3.2: Photometric observational log of SN 2011fu

JD	Phase[a] (Days)	U (mag)	B (mag)	V (mag)	R (mag)	I (mag)	Telescope
2455833.23	+10.73	17.36± 0.03	17.68 ± 0.02	17.35± 0.01	16.99 ± 0.02	16.74 ± 0.02	HCT
2455834.49	+11.99	17.66± 0.03	17.87 ± 0.02	17.48± 0.01	17.11 ± 0.02	16.86 ± 0.02	HCT
2455836.15	+13.65	–	17.92 ± 0.03	17.46± 0.01	17.08 ± 0.02	16.88 ± 0.02	HCT
2455837.26	+14.76	17.73± 0.03	17.89 ± 0.02	17.42± 0.01	17.02 ± 0.02	16.83 ± 0.02	HCT
2455841.23	+18.73	17.65± 0.03	17.65 ± 0.02	17.15± 0.01	16.77 ± 0.02	16.59 ± 0.02	ST
2455842.30	+19.80	17.69± 0.05	17.63 ± 0.03	17.07± 0.01	16.70 ± 0.02	16.56 ± 0.03	ST
2455843.27	+20.77	17.62± 0.09	17.51 ± 0.05	17.05± 0.02	16.67 ± 0.02	16.57 ± 0.04	ST
2455844.21	+21.71	17.48± 0.06	17.49 ± 0.03	17.01± 0.02	16.62 ± 0.02	16.48 ± 0.03	ST
2455845.44	+22.94	17.43± 0.03	17.48 ± 0.03	16.95± 0.02	16.59 ± 0.02	16.45 ± 0.03	ST
2455845.43	+22.93	–	17.43 ± 0.02	16.93± 0.01	16.54 ± 0.02	16.43 ± 0.02	HCT
2455846.44	+23.94	17.51± 0.03	17.47 ± 0.03	16.92± 0.02	16.57 ± 0.02	16.43 ± 0.03	ST
2455846.43	+23.93	–	17.45 ± 0.02	16.92± 0.01	16.54 ± 0.02	16.45 ± 0.02	HCT
2455849.41	+26.91	17.68± 0.03	17.58 ± 0.03	16.95± 0.01	16.53 ± 0.02	16.38 ± 0.02	HCT
2455850.40	+27.89	17.76± 0.04	17.65 ± 0.03	16.96± 0.01	16.57 ± 0.02	16.43 ± 0.03	HCT
2455851.31	+28.81	18.21± 0.13	17.82 ± 0.04	17.06± 0.03	16.56 ± 0.02	16.44 ± 0.03	ST
2455857.30	+34.80	18.99± 0.06	18.52 ± 0.03	17.44± 0.01	16.80 ± 0.02	16.58 ± 0.03	ST
2455858.32	+35.82	19.00± 0.09	18.60 ± 0.03	17.47± 0.01	16.84 ± 0.02	16.61 ± 0.03	ST
2455859.18	+36.68	–	18.74 ± 0.03	17.51± 0.01	16.92 ± 0.02	16.69 ± 0.02	HCT
2455860.30	+37.80	19.10± 0.08	18.73 ± 0.03	17.60± 0.01	16.93 ± 0.02	16.68 ± 0.02	ST
2455862.30	+39.80	19.24± 0.15	18.86 ± 0.03	17.69± 0.02	16.97 ± 0.02	16.71 ± 0.03	ST
2455864.40	+41.90	19.55± 0.08	19.05 ± 0.03	17.77± 0.01	17.09 ± 0.02	16.84 ± 0.02	HCT
2455865.35	+42.85	–	19.12 ± 0.02	17.81± 0.01	17.11 ± 0.02	16.85 ± 0.02	HCT
2455866.23	+43.73	–	18.97 ± 0.05	17.88± 0.02	17.14 ± 0.02	16.83 ± 0.03	ST
2455866.26	+43.76	–	19.10 ± 0.02	17.86± 0.02	17.17 ± 0.02	16.88 ± 0.02	HCT
2455875.22	+52.72	–	–	18.06± 0.06	17.33 ± 0.04	16.95 ± 0.05	ST
2455879.28	+56.78	–	19.30 ± 0.10	18.17± 0.03	17.55 ± 0.03	17.18 ± 0.03	ST
2455881.26	+58.76	–	–	18.19± 0.02	17.50 ± 0.02	17.18 ± 0.03	HCT
2455882.33	+59.83	–	19.38 ± 0.07	18.19± 0.03	17.56 ± 0.02	17.20 ± 0.03	ST
2455884.27	+61.78	19.94± 0.05	19.49 ± 0.03	18.28± 0.01	17.62 ± 0.01	17.30 ± 0.02	HCT
2455894.23	+71.73	19.67± 0.20	19.37 ± 0.05	18.41± 0.03	17.76 ± 0.02	17.42 ± 0.03	ST
2455896.28	+73.78	19.75± 0.07	19.49 ± 0.03	18.43± 0.01	17.87 ± 0.02	17.57 ± 0.03	HCT
2455897.08	+74.58	–	–	18.39± 0.03	17.79 ± 0.03	–	DFOT
2455898.30	+75.80	–	19.28 ± 0.05	18.41± 0.02	17.79 ± 0.02	17.45 ± 0.03	ST
2455900.17	+77.66	–	19.47 ± 0.08	18.50± 0.03	17.83 ± 0.03	17.53 ± 0.03	ST
2455901.24	+78.74	–	19.36 ± 0.06	18.48± 0.04	17.88 ± 0.03	17.39 ± 0.03	ST
2455904.28	+81.78	–	19.31 ± 0.17	–	17.97 ± 0.05	17.72 ± 0.04	HCT
2455909.18	+86.68	–	19.52 ± 0.07	18.60± 0.03	17.96 ± 0.03	17.63 ± 0.03	ST
2455912.28	+89.78	–	19.45 ± 0.05	18.64± 0.03	18.06 ± 0.03	17.67 ± 0.04	ST
2455913.24	+90.73	19.56± 0.12	19.47 ± 0.05	18.59± 0.03	18.09 ± 0.03	17.70 ± 0.03	ST
2455918.18	+95.68	–	19.55 ± 0.03	–	18.21 ± 0.03	17.82 ± 0.03	HCT
2455919.11	+96.61	–	19.58 ± 0.04	18.75± 0.01	18.22 ± 0.02	17.87 ± 0.02	HCT
2455922.17	+99.67	–	19.48 ± 0.06	18.74± 0.03	18.24 ± 0.03	17.81 ± 0.04	ST
2455924.10	+101.60	–	19.65 ± 0.03	18.86± 0.01	18.34 ± 0.02	18.02 ± 0.02	HCT
2455929.17	+106.67	–	19.73 ± 0.09	18.92± 0.04	18.36 ± 0.05	18.00 ± 0.04	ST
2455930.27	+107.76	–	–	19.04± 0.11	18.47 ± 0.07	17.99 ± 0.12	ST
2455930.27	+108.73	–	–	18.89± 0.15	18.29 ± 0.10	17.93 ± 0.10	ST
2455932.15	+109.65	–	19.80 0.16	19.00± 0.05	–	18.11 ± 0.03	HCT
2455936.25	+113.75	–	–	–	–	18.27 ± 0.06	HCT
2455937.16	+114.66	–	19.69 ± 0.09	19.09± 0.04	18.58 ± 0.03	18.13 ± 0.04	HCT
2455938.08	+115.58	–	19.70 ± 0.04	19.11± 0.02	18.65 ± 0.03	18.35 ± 0.03	HCT
2455939.23	+116.73	–	–	19.00± 0.07	–	18.11 ± 0.05	ST
2455947.06	+124.56	–	–	19.21± 0.02	18.74 ± 0.02	18.46 ± 0.04	HCT
2455947.16	+124.66	–	–	–	18.55 ± 0.04	18.16 ± 0.07	ST
2455953.08	+130.58	–	19.64 ± 0.08	–	18.68 ± 0.03	18.38 ± 0.06	ST
2455954.16	+131.66	–	–	19.33± 0.02	18.87 ± 0.02	18.49 ± 0.03	HCT
2455963.14	+140.64	–	–	19.23± 0.07	–	18.54 ± 0.10	ST
2455967.11	+144.61	–	–	19.18± 0.07	18.87 ± 0.05	18.48 ± 0.08	ST
2455969.09	+146.59	–	–	–	18.91 ± 0.05	–	ST
2455976.07	+153.56	–	–	19.40± 0.03	18.88 ± 0.03	18.58 ± 0.07	ST
2455979.12	+156.62	–	–	–	18.92 ± 0.05	18.51 ± 0.09	ST
2455989.08	+166.58	–	–	19.59± 0.09	19.24 ± 0.10	18.87 ± 0.08	DFOT, ST
2455998.08	+175.58	–	–	–	19.07 ± 0.05	18.89 ± 0.10	ST
2456159.34	+336.84	–	>22.5	>22	>21.5	>21	HCT

[a] with reference to the explosion epoch JD 2455822.5 (days since explosion)

HCT : 2-m Himalayan Chandra Telescope, IAO, Hanle; DFOT : 1.3-m Devasthal Fast Optical Telescope, ARIES, India; ST : 1-m Sampurnanand Telescope, ARIES, India

observed on the same night as the SN, and the SN spectra were calibrated to a relative flux scale. When the spectrophotometric standards could not be observed, the response curve based on observations in a night close in time to the SN observation was adopted. The flux calibrated spectra in the two regions were combined to a weighted mean to obtain the final spectrum on a relative flux scale.

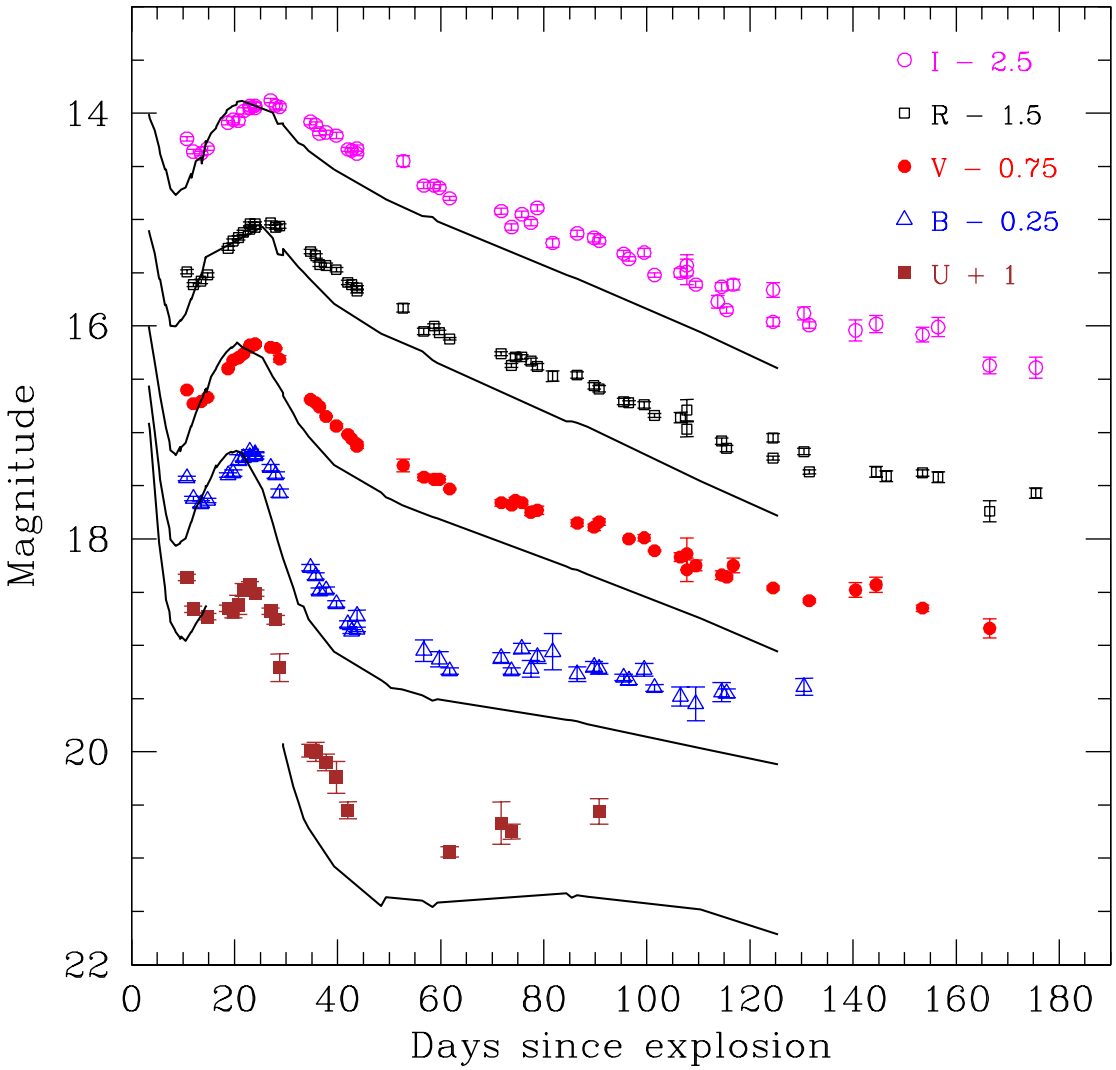

Figure 3.2: Observed *UBVRI* light curves of SN 2011fu. For clarity, the light curves in different bands have been shifted vertically by the values indicated in the legend. Black solid lines represent the light curves of SN 1993J (Lewis et al., 1994) overplotted with appropriate shifts. The explosion date of SN 2011fu was taken to be 2011 September 18 ± 2, as described in Sect. 3.3.1.

Finally, the spectra were brought to an absolute flux scale using zero points determined from the calibrated, broad-band *UBVRI* magnitudes. The SN spectra were also corrected for the redshift of the host galaxy (z = 0.018), and de-reddened assuming a total reddening of $E(B-V) = 0.22$ mag (see Sect. 3.3.3). The telluric lines have not been removed from the spectra.

Table 3.3: Log of spectroscopic observations of SN 2011fu.

Date	J.D.	Phase[a] (Days)	Range (Å)	Resolution (Å)
2011-09-28	2455833.28	+10.78	3500-7800; 5200-9250	7
2011-09-29	2455834.41	+11.92	3500-7800; 5200-9250	7
2011-10-01	2455836.23	+13.73	3500-7800; 5200-9250	7
2011-10-14	2455849.43	+26.93	3500-7800; 5200-9250	7
2011-10-29	2455864.41	+41.91	3500-7800; 5200-9250	7
2011-10-31	2455866.36	+43.86	3500-7800; 5200-9250	7
2011-11-23	2455889.15	+66.65	3500-7800; 5200-9250	7
2011-12-22	2455918.11	+95.61	3500-7800	7

[a] with reference to the explosion epoch JD 2455822.5 (days since explosion).

Table 3.4: Epochs of the LC valley (t_v) and the secondary peak (t_p) in days after explosion, and their respective apparent magnitudes for SN 2011fu and SN 1993J.

SN	Band	LC valley t_v (days)	Apparent magnitude at t_v	LC peak t_p (days)	Apparent magnitude at t_p
2011fu	U	15.51±4.34	17.67±0.42	22.93±3.64	17.43±3.34
	B	13.75±1.47	17.93±0.80	23.29±2.89	17.51±0.83
	V	12.87±1.69	17.45±1.32	24.96±2.01	16.95±0.42
	R	12.95±1.81	17.01±1.20	26.40±2.90	16.50±0.11
	I	13.50±1.89	16.86±0.67	26.64±2.80	16.41±0.32
1993J	U	10.33±1.52	11.94±0.76	–	–
	B	8.82 ±3.36	12.27±1.74	19.92±0.70	11.40±0.17
	V	8.96 ±1.41	11.89±1.14	21.67±0.66	10.87±0.12
	R	8.81 ±1.06	11.47±0.61	22.53±3.24	10.52±0.37
	I	9.17 ±1.58	11.25±0.93	23.06±1.91	10.39±0.21

3.3 Multi-band light curves of SN 2011fu

In this section, we present the multi-band light curves of SN 2011fu and their comparison with the SN 1993J light curves and their temporal properties. A brief discussion about the explosion epoch of SN 2011fu is presented in the following sub-section.

3.3.1 Explosion epoch of SN 2011fu

The detection of very early time light curve features of SN 2011fu, similar to those seen for SN 1993J, indicates a very young age at the time of discovery. The very sharp rise followed by a relatively fast decline are explained as the detection of the cooling phase and depends mainly on the ^{56}Ni mixing and the progenitor radius, as shown by hydrodynamical models of H-stripped CCSNe (Bersten et al., 2012; Blinnikov et al., 1998; Shigeyama et al., 1994; Woosley et al., 1994). For example, in the case of SN 2011dh, for a progenitor radius of < 300 $R_{\odot}$, the cooling phase ends at ~ 5 days after the explosion (see Fig. 10 of Bersten et al., 2012).

In the literature, the first detection of SN 2011fu has been reported to be 2011 September 20.708 (Z. Jin and X. Gao, Mt. Nanshan, China). However, according to Ciabattari et al. (2011), this object was not visible on 2011 August 10 at its SN location, putting a stringent limit to the explosion date. We collected following pieces of evidence to put a constraint on the explosion date of SN 2011fu.

1. For CCSNe of Type Ib and IIb, the explosion dates have been estimated to be $\sim$ 20 days prior to the V-band maxima (Drout et al., 2011; Richardson et al., 2006) (see also Milisavljevic et al., 2013).

2. Type IIb SNe also exhibit a bluer $B-V$ colour $\sim$ 40 days after the explosion (Pastorello et al., 2008), giving an indication about the explosion epoch.

3. The SNID (Blondin & Tonry, 2007) fitting on initial four spectra of SN 2011fu indicates that explosion of this event would have occurred around 2011 September 20. However, the SNID fit for the later three epochs of the spectra (after V band maximum) gives rise to 2011 September 17 as the explosion date.

4. In some of the well studied type IIb SNe, the explosion epoch is better constrained (e.g SN 1993J, SN 2008ax and SN 2011dh) and their early light curve features indicate that the adiabatic cooling phase may be observable for several days after the explosion and this duration depends upon the volume of the photospheric shell (Roming et al., 2009b), as determined for SN 1993J (Barbon et al., 1995; Lewis et al., 1994; Wheeler et al., 1993), SN 2008ax (Roming et al., 2009b) and SN 2011dh (Arcavi et al., 2011).

Based on the above evidences, we have adopted 2011 September 18 ± 2 as the explosion epoch for SN 2011fu and it will be used for the further discussions in this article.

3.3.2 Light curve analysis

In Fig. 3.2, we plot the calibrated *UBVRI* light curves of SN 2011fu. The LCs span $\sim$ 175 days after the explosion. It is clear from Fig. 3.2 that the photometric observations of this supernova started shortly after the explosion, showing the early declining phase in all bands, which is possibly related to the cooling tail after the shock break-out from an extended progenitor envelope (Chevalier, 1992; Chevalier & Fransson, 2008; Nakar & Sari, 2010; Waxman et al., 2007). The LCs of SN 2011fu

are strikingly similar to those of SN 1993J, both in the initial and the following phases, exhibiting valley-like structures followed by rising peaks in all bands. At late epochs the LCs are monotonically decreasing in all bands, as expected for expanding, cooling ejecta heated by only the radioactive decay of ^{56}Ni and ^{56}Co.

Beside SNe 1993J and 2011dh, SN 2011fu is the third known case among IIb SNe to date where all the initial decline phase, the rise of the broader secondary peak and the final decline have been observed (although Roming et al. (2010) reported similar observations for SN 2008ax). In the following, we refer the first minimum of the LC (when the initial decline stops and the rise to the secondary maximum starts) as the "valley".

To determine the epochs of the valleys (t_v, in days), the subsequent peaks (t_p, in days) and their corresponding brightness values, we fitted a third-order polynomial using a χ^2 minimization technique to the LCs of both SN 2011fu and SN 1993J. The errors in the fitting procedure were estimated by the error propagation method. We have taken 1993 March 27.5 as the explosion date for SN 1993J (Wheeler et al., 1993). The derived values of t_v, t_p and corresponding brightness values for both SNe are listed in Table 3.4.

The values of t_v and t_p for both these SNe are similar within the errors in all the bands. However, for both SNe, the light curves peak earlier in the blue bands than in the red bands (see Table 3.4) which is a common feature seen in CCSNe. By applying the linear regression method, the decline and rising rates (in mag day^{-1}) were also estimated for the three phases, i.e. the pre-valley (α_1), valley-to-peak (α_2) and after-peak phases (α_3). The results of the fitting are shown in Table 3.5. These values suggest that for SN 2011fu the pre-valley decay rates (α_1) are steeper (i.e. the decay is faster) at shorter wavelengths. This is also true for SN 1993J, where the decay rates (α_1) were even steeper. Thus, the initial LC decay of SN 1993J was steeper than that of SN 2011fu during this early phase (see also Barbon et al., 1995). Between valley to peak phase (α_2), the LC of SN 2011fu evolved with a similar rate in all the bands, but slower than that seen for SN 1993J. During the post-peak phase, the LCs gradually became flatter at longer wavelengths (see the α_3 values in Table 3.5). This trend has also been observed for SN 1993J and other Type IIb SNe. The B-band LC of SN 2011fu between 50 and 100 days after explosion might even show a plateau, similar to SNe 1993J (see Fig. 3 of Lewis et al., 1994) and 1996cb (see Fig. 2 and the discussions of Qiu et al., 1999). The plateau-like behaviour of the U-band LC of SN 2011fu is more prominent than the U-band LC of SN 1993J.

Table 3.5: Magnitude decay rate (in mag day^{-1}) before valley (α_1), rising rate between valley to peak (α_2) and decay rate after the peak (α_3) for SN 2011fu and SN 1993J.

SN	Band	Decay rate before valley (α_1)	Rising rate between valley to peak (α_2)	Decay rate after peak (α_3)
2011fu	U	0.24 ± 0.05	−0.04 ± 0.01	0.13 ±0.01
	B	0.15 ± 0.02	−0.05 ± 0.01	0.10 ±0.01
	V	0.11 ± 0.03	−0.06 ± 0.01	0.05 ±0.01
	R	0.09 ± 0.02	−0.05 ± 0.01	0.04 ±0.01
	I	0.09 ± 0.02	−0.03 ± 0.01	0.02 ±0.01
1993J	U	0.38 ± 0.03	–	–
	B	0.24 ± 0.02	−0.08 ± 0.01	0.11 ±0.01
	V	0.24 ± 0.01	−0.10 ± 0.01	0.06 ±0.01
	R	0.20 ± 0.01	–	–
	I	0.16 ± 0.01	−0.09 ± 0.01	0.05 ±0.01

We also determined the Δm_{15} parameter for the V-band LCs of both SNe, Δm_{15} is defined as the decline in magnitude after 15 days post-maximum. We got Δm_{15}(V) = 0.75 mag for SN 2011fu which is slightly lower than that for SN 1993J (Δm_{15}(V) = 0.9 mag). Both of these values are consistent with the mean Δm_{15}(V) $\sim$ 0.8 ±0.1 mag for Type Ib/c SNe (Drout et al., 2011).

3.3.3 Colour evolution and reddening towards SN 2011fu

In Fig. 3.3, we compare the evolution of the optical colour indices of SN 2011fu with those of other Type IIb SNe. While constructing the colour curves, we interpolated the measured data points (listed in Table 3.2) wherever necessary. Before plotting the colours, reddening corrections were applied to all the bands. $E(B-V) = 0.068$ mag was adopted as the reddening due to Milky Way interstellar matter (ISM) in the direction of SN 2011fu (Schlegel et al., 1998). The empirical correlation given by Munari & Zwitter (1997) was used to estimate the SN host galaxy extinction based on the measured Na I D lines. For this purpose we calculated the weighted equivalent width (EW) of the un-resolved Na I D absorption feature in the three spectra (taken on 2011 Oct 01, 14 and 31, see the log in Table 3), resulted in EW (Na I D) $\sim$ 0.35 ±0.29 Å. This corresponds to $E(B-V) \sim 0.15$ ±0.11 mag according to the relation given by Munari & Zwitter (1997). Finally, we adopted the sum of the two components, resulting in a total $E(B-V) = 0.22 \pm 0.11$ mag for the reddening in the direction of SN 2011fu.

The bottom panel of Fig. 3.3 shows the $B-V$ colour evolution of SN 2011fu along with that of SNe 1993J (Lewis et al., 1994), 1996cb (Qiu et al., 1999), 2008ax

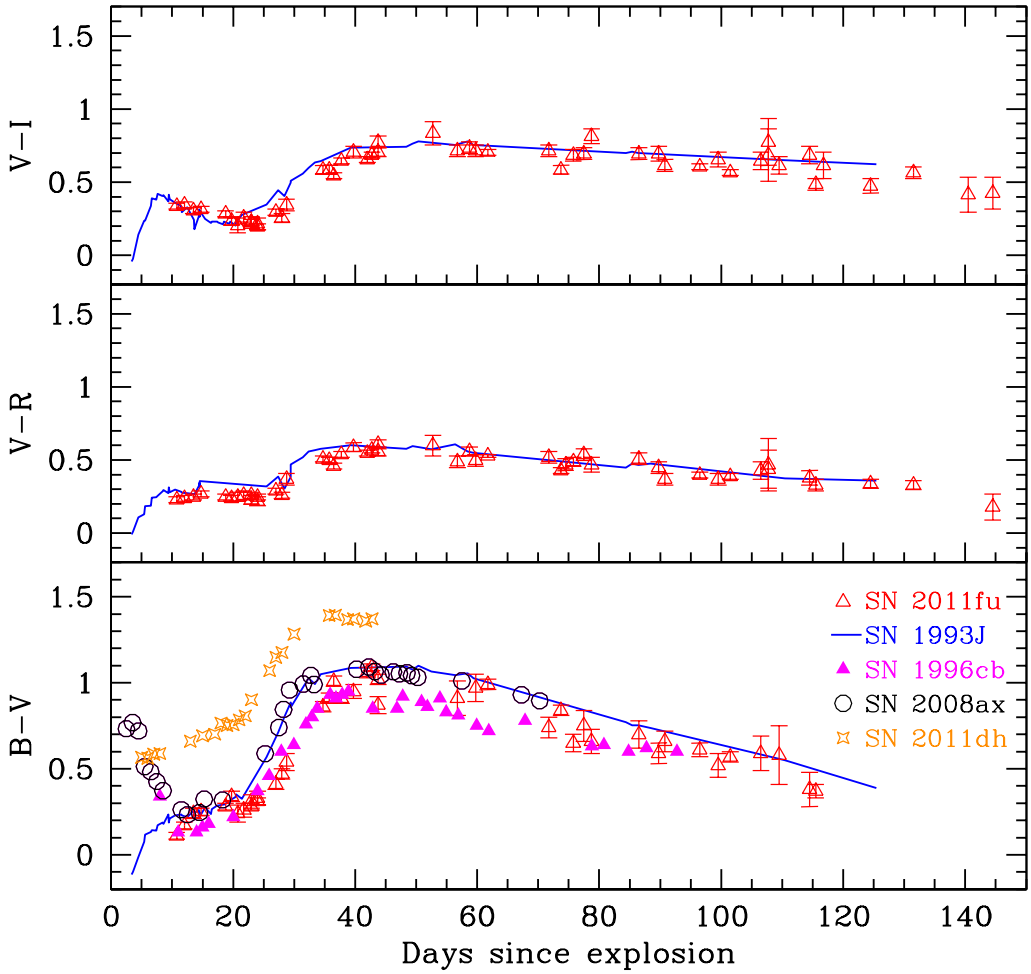

Figure 3.3: Colour curves of SN 2011fu and other Type IIb SNe. Bottom panel: $B-V$ colour evolution of SNe 2011fu, 2011dh, 2008ax, 1996cb (symbols) and 1993J (blue line). Middle panel: $V-R$ colour of SN 2011fu and SN 1993J. Top panel: the same as below but for the $V-I$ colour.

(Pastorello et al., 2008) and 2011dh (Vinkó et al., 2012). It is seen in Fig. 3.3 that the colour curves of SN 2011fu are similar to those of the majority of well-observed Type IIb SNe, except SN 2011dh which looks redder than the others.

Similar to SN 1993J, the initial $B-V$ colour of SN 2011fu increased (reddened) during the first 10 days (note that during the same phase SNe 2008ax and 1996cb showed the opposite trend). Between days +10 and +40, the $B-V$ colour continued to redden, then after day +40 it started to decrease and became bluer until the end of our observations. This kind of colour evolution seems to be a common trend for

Type Ib/c and IIb SNe. It may suggest that the SN ejecta became optically thin after 40 days. The $V-R$ (middle pannel) and $V-I$ (upper pannel) colour indices evolve with a similar trend as the $B-V$ colour.

3.3.4 Comparison of the absolute magnitudes

The distribution of the absolute magnitudes of CCSNe provides us information about their progenitors and explosion mechanisms. Richardson et al. (2002) made a comparative study of the distribution of the peak absolute magnitudes in the B-band (M_B) for various SNe. They found that for normal and bright SNe Ib/c, the mean peak M_B values are -17.61 ± 0.74 and -20.26 ± 0.33 mag, respectively. The M_B values were found to be -17.56 ± 0.38 mag and -19.27 ± 0.51 mag for normal and bright Type II-L SNe, while for Type II-P and IIn SNe the M_B values were found to be -17.0 ± 1.12 mag and -19.15 ± 0.92 mag, respectively.

In a recent study by Li et al. (2011), the absolute magnitudes of SNe Ibc (Type Ib, Ic and Ib/c) and II were derived using the LOSS samples and the average absolute magnitudes (close to R-band as claimed by authors, see discussions of Li et al. (2011)) were found to be -16.09 ± 0.23 mag and -16.05 ± 0.15 mag for SNe Ibc and II respectively. In a similar study, Drout et al. (2011) also reported that the R-band absolute magnitudes of SNe Ib and Ic peaked arround -17.9 ± 0.9 mag and -18.3 ± 0.6 mag respectively.

Fig. 3.4, shows the comparison of the V-band absolute LC of SN 2011fu along with seven other well-observed Type IIb SNe i.e. 1993J (Lewis et al., 1994), 1996cb (Qiu et al., 1999), 2003bg (Hamuy et al., 2009), 2008ax (Pastorello et al., 2008), 2009mg (Oates et al., 2012), 2011dh (Vinkó et al., 2012) and 2011ei (Milisavljevic et al., 2013). For SN 2011fu, the distance $D = 77.9 \pm 5.5$ Mpc has been taken from the NED[1] along with a total $E(B-V) = 0.22 \pm 0.11$ mag as discussed in Sect. 3.3.3. However, all other LCs presented in the figure have been corrected for interstellar extinctions and distance values collected from the literature. Fig. 3.4, illustrates that the peak M_V for various Type IIb SNe has a range between ~ -16 mag and ~ -18.5 mag. In this distribution, SN 2011fu is the brightest from early to late epochs with a peak absolute magnitude of $M_V \sim$ -18.5 $\pm$0.24 mag.

[1] http://ned.ipac.caltech.edu/

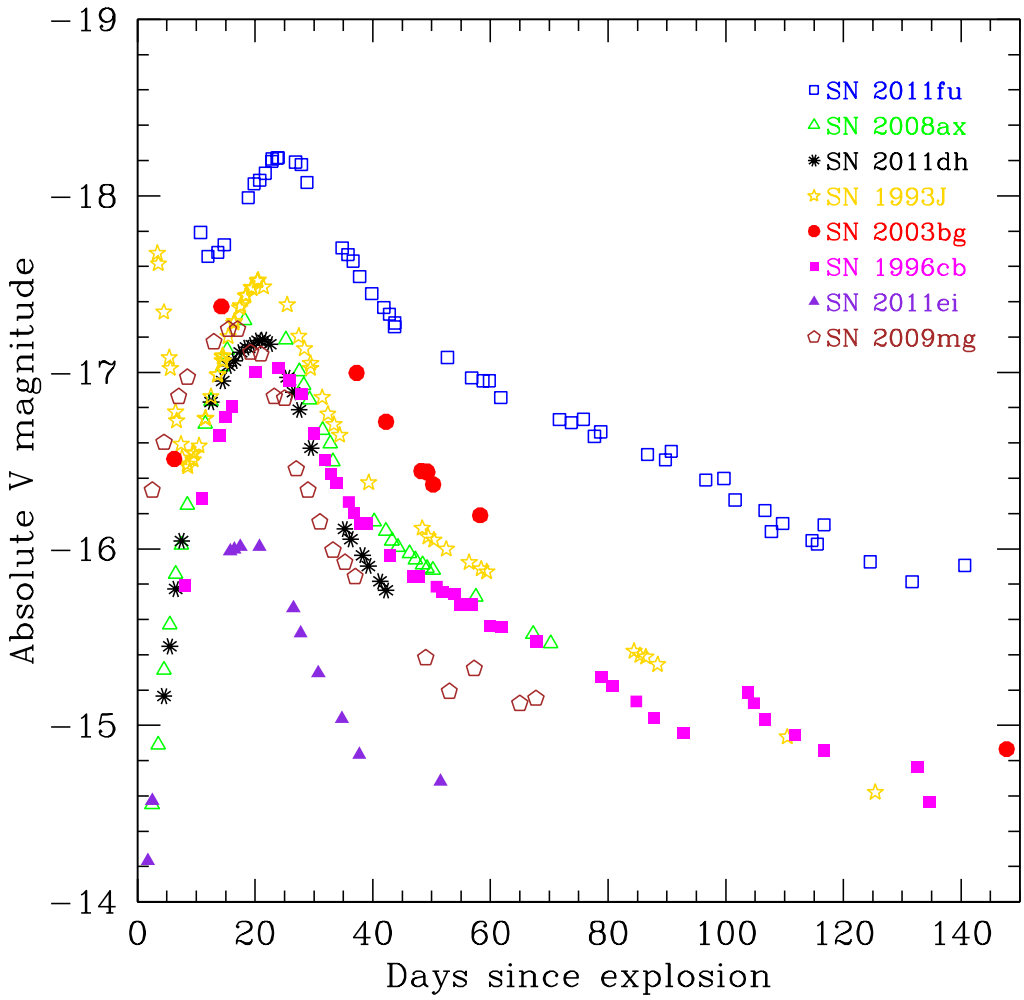

Figure 3.4: The M_V light curve of SN 2011fu is compared to those of other similar IIb events: SN 2011ei, 2011dh, 2009mg, 2008ax, 2003bg, 1996cb and 1993J.

3.4 Bolometric light curve

3.4.1 Construction of the bolometric light curve

The quasi-bolometric lightcurve ($UBVRI$) was computed by integrating the extinction-corrected flux[1] in all 5-bands. The data were interpolated wherever it was necessary and total $UBVRI$ flux was integrated using a simple trapezoidal rule.

[1]Fluxes were corrected for interstellar reddening using the IDL program *ccm_unred.pro* available at ASTROLIB (http://idlastro.gsfc.nasa.gov/ftp/) by adopting $E(B-V) = 0.22$ mag for the total (Milky Way plus in-host) reddening and by assuming the classical reddening law for the diffused interstellar medium ($R_v = 3.1$).

In Fig. 3.5, we compare the quasi-bolometric LC of SN 2011fu along with other three Type IIb events i.e. SNe 1993J (Lewis et al., 1994), 2008ax (Pastorello et al., 2008) and SN 2011dh (Ergon et al., 2014). It is obvious that the shape of the quasi-bolometric LC of SN 2011fu is similar to that of SN 1993J. However, SN 2011fu is more luminous in comparison with the other SNe during the observed phases.

The un-observed part of the bolometric LC in the Infra-red was approximated by assuming blackbody flux distributions fitted to the observed R- and I-band fluxes for each epoch. At first, we used the Rayleigh-Jeans approximation for the fluxes redward of the I-band, and integrated the flux distribution between the I-band central wavelength and infinity. This resulted in an analytic estimate for the IR (infra-red) contribution as $L_{IR} \approx \lambda_I \cdot F_I/3$, where λ_I and F_I are the I-band central wavelength and monochromatic flux, respectively. Second, we fitted a blackbody to the R- and I-band fluxes at each epoch, and numerically integrated the fitted blackbody flux distributions from the I-band to radio wavelengths ($\sim$ 1 mm). These two estimates gave consistent results within a few percent, which convinced us that they are more-or-less realistic estimates of the IR-contribution. Because the R-band fluxes may also be affected by the presence of $H\alpha$, we adopted the result of the first, analytic estimate as the final result. Comparison of the integrated $UBVRI$- and IR-fluxes showed that the IR-contribution was $\sim$ 20 percent at the earliest observed phases, but it increased up to $\sim$ 50 percent by day +40 and stayed roughly constant after that.

3.4.2 Bolometric light curve modelling

The bolometric light curve (see Sect. 3.4.1) was fitted by the semi-analytic light curve model of Arnett & Fu (1989) (see also Chatzopoulos et al., 2009). This model assumes homologously expanding spherical ejecta having a constant opacity, and solves the photon diffusion equation by taking into account the laws of thermodynamics. This approach was first introduced by Arnett (1980) and Arnett (1982), and further extended by Arnett & Fu (1989) by taking into account the rapid change of the opacity due to recombination. The extended diffusion-recombination model was succesfully applied to describe the observed light curve of SN 1987A assuming realistic physical parameters (Arnett & Fu, 1989).

The bolometric LC of SN 2011fu is qualitatively similar to that of SN 1987A, because of the presence of the rapid initial decline and the secondary bump, after which the LC settles down onto the radioactive tail due to the ^{56}Co-decay. This

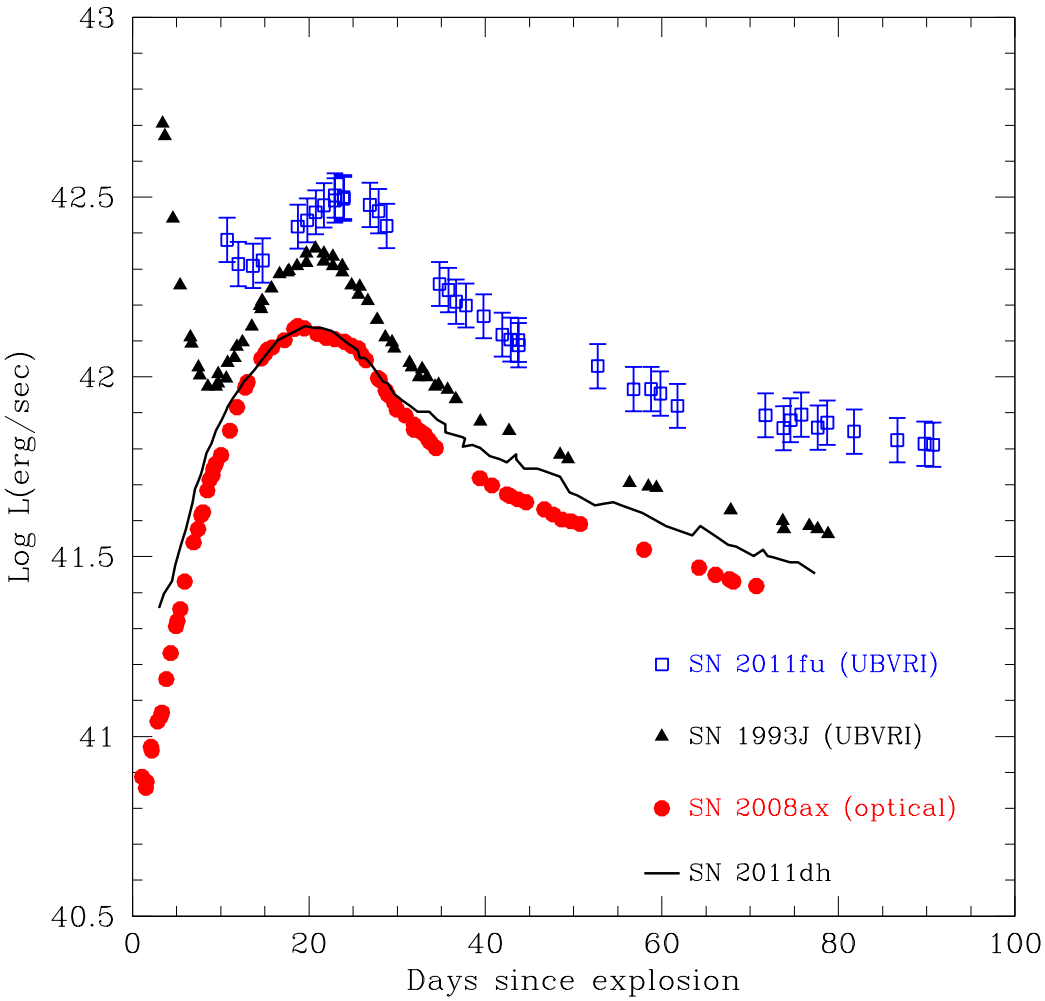

Figure 3.5: The bolometric light curve of SN 2011fu compared to the similar Type IIb events SN 1993J (Lewis et al., 1994), SN 2008ax (Pastorello et al., 2008) and SN 2011dh (Ergon et al. 2012).

early LC decline in not unusual for Type IIb SNe (however, see Fig. 3.2 at early epochs where we compare the LCs of SN 2011fu with those of SN 1993J), and it is usually modelled by a two-component ejecta configuration: a dense compact core and a more extended, lower density envelope on top of the core (Bersten et al., 2012). The fast, initial decline is thought to be due to the radiation of the cooling outer envelope (which was initially heated by the shock wave passing through it after the explosion), while the secondary bump is caused by the photons diffusing slowly out from the inner, denser ejecta which is mainly heated from inside by the radioactive decay of ^{56}Ni $\rightarrow$ ^{56}Co $\rightarrow$ ^{56}Fe. After the secondary maximum, the decline

Table 3.6: Log of parameters derived from bolometric light curve modelling (Kumar et al., 2013).

Parameters	He-core	H-envelope	remarks
R_{prog} (cm)	2×10^{11}	1×10^{13}	progenitor radius
M_{ej} ($M_{\odot}$)	1.1	0.1	ejecta mass
κ_T (cm^{2}g^{-1})	0.24	0.4	Thompson scattering opacity
M_{Ni} ($M_{\odot}$)	0.21	–	initial nickel mass
E_{kin} (10^{51} erg)	2.4	0.25	ejecta kinetic energy
$E_{th}(0)$ (10^{51} erg)	1.0	0.3	ejecta initial thermal energy

of the LC is faster than the rate of the radioactive decay, which may be due to a recombination front moving inward into the ejecta, similar to the condition at the end of the plateau phase in Type II-P SNe.

In order to simulate this kind of LC behavior, we slightly modified the original diffusion-recombination model of Arnett & Fu (1989). Instead of having a H-rich, one-component ejecta, we added an extended, low-density, pure H envelope on top of a denser, He-rich core. Following Arnett & Fu (1989), we also assumed that the opacity is due to only Thompson-scattering, and it is constant in both the envelope and the core. Because the envelope was thought to contain only H, $\kappa = 0.4$ cm^2 g^{-1} was selected as the Thompson-scattering opacity for this layer, while $\kappa = 0.24$ cm^2 g^{-1} was applied for the inner region to reflect its higher He/H ratio.

The system of differential equations given by Arnett & Fu (1989) were then solved by simple numerical integration (assuming a short, $\Delta t = 1$ s timestep which was found small enough to get a reasonable and stable solution). Because the photon diffusion timescale is much lower in the envelope than in the core, the contribution of the two regions to the overall LC is well separated: during the first few days the radiation from the outer, adiabatically cooling envelope dominates the LC, while after that only the photons diffusing out from the centrally heated inner core contribute. Thus, the sum of these two processes determines the final shape of the LC.

Because of the relatively large number of free parameters, we have not attempted a formal χ^2 minimization while fitting the model to the observations. Instead, we searched for a qualitative agreement between the computed and observed bolometric LCs. The parameters of our final, best-fit-by-eye model are collected in Table 3.6, while the LCs are plotted in Fig. 3.6.

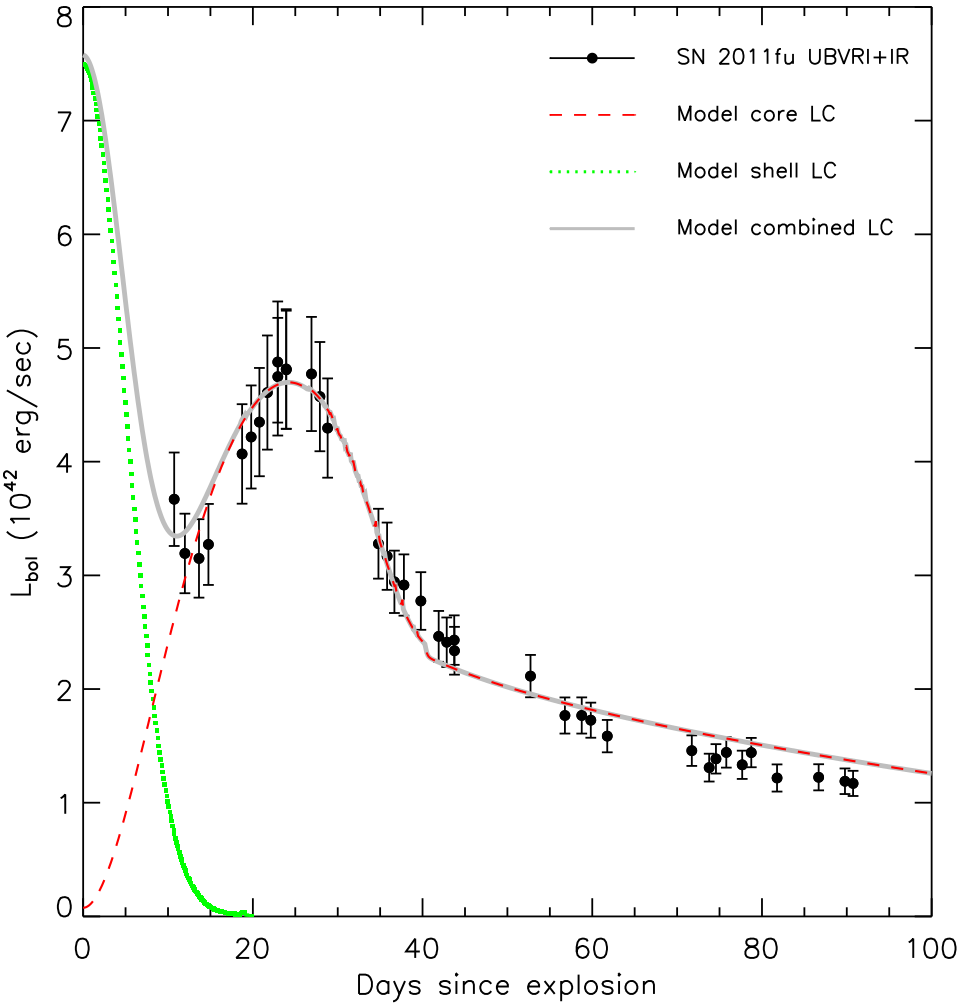

Figure 3.6: Comparison of the observed bolometric LC (dots) with the best-fit two-component diffusion-recombination model. The dashed (red) and dotted (green) curves show the contribution from the He-rich core and the low-mass H-envelope, respectively, while the thick (grey) curve gives the combined LC.

It is seen that the best-fit model consists of a dense, 1 $M_{\odot}$ He-rich core and a more extended, low-mass (0.1 $M_{\odot}$) H-envelope. This is very similar to the progenitor configuration found by Bersten et al. (2012) when modelling the LC of another Type IIb event, SN 2011dh, although they assumed a more massive ($\sim$ 3 $M_{\odot}$) He-core. Nevertheless, it was concluded by Bersten et al. (2012) and confirmed by the present study that the secondary bump is entirely due to radiation coming from the dense inner core of the ejecta, and the outer extended envelope is only responsible for the initial fast decline of the LC. The estimated ejecta mass for SN 2011fu, $\sim$ 1.1 $M_{\odot}$

is consistent with the observed rise time ($\sim$ 24 days) to the secondary maximum of the LC (see Eq.10 of Chatzopoulos et al., 2012). The parameters in Table 3.6 are also qualitatively similar to the ones derived by Young et al. (1995) for modelling the LC of SN 1993J.

There are a number of caveats in the simple diffusion-recombination model used above, which naturally limit the accuracy of the derived physical parameters. The most obvious limitation is the assumption of constant opacity in the ejecta. The pre-selected density and temperature profiles in the ejecta (assumed as exponential functions) are also strong simplifications, but they enable the approximate, semi-analytic treatment of the complex problem of radiative diffusion, as shown by Arnett & Fu (1989). Thus, the parameters in Table 3.6 can be considered only as order-of-magnitude estimates, which could be significantly improved by more sophisticated modelling codes (e.g. Bersten et al., 2012).

3.5 Spectral analysis

Properties of the SN 2011fu ejecta were investigated with the multi-parametric resonance scattering code `SYNOW` (Fisher et al., 1997) (see also Baron et al., 2005; Branch et al., 2002; Elmhamdi et al., 2006). The evolution of temperature and velocities of layers were traced through several months of spectral observations. The `SYNOW` code is based on several assumptions: spherical symmetry; homologous expansion of layers ($v \sim r$); sharp photosphere producing a blackbody spectrum and associated with a shock wave at early stages.

3.5.1 Comparison between observed and synthetic spectra

In the photospheric phase the spectral lines with P Cygni profiles are formed by resonance scattering in a shell above the optically thick photosphere which produces the continuum (see Branch et al., 2001). On the other hand, during the nebular phase the ejecta is transparent (optically thin) in the optical wavelength range. In this case the spectrum is dominated by strong emission features including forbidden lines. Each of these two phases of SN evolution can be explained with individual approximations and the modelling of the observed spectra should be generated with different synthetic codes. There is no sharp boundary between these two phases. No strong transition to the nebular phase with conspicuous emission features can be seen in the observed spectra of SN 2011fu (Fig. 3.7). The shape of the lines remains

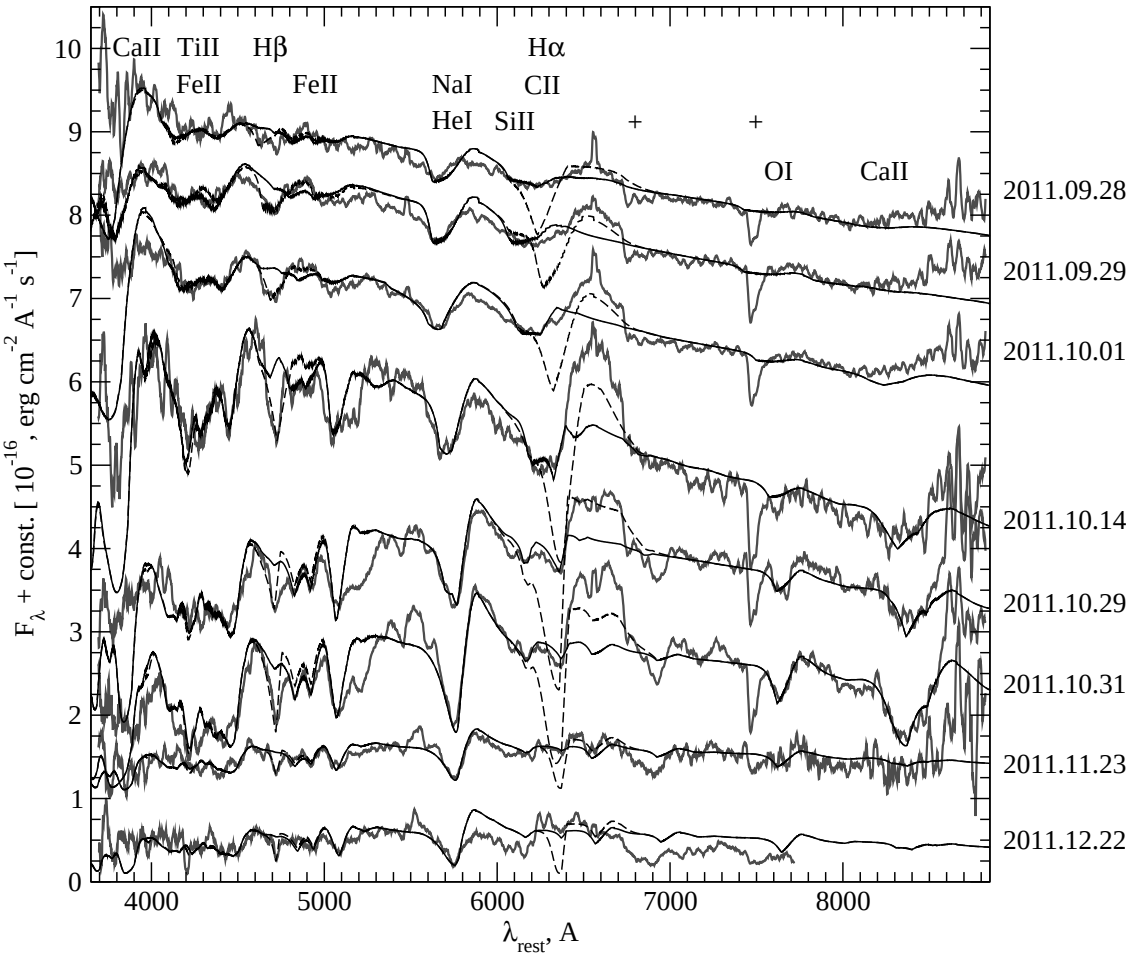

Figure 3.7: Evolution of the SN 2011fu spectra (grey thick curves, smoothed by a 20Å-wide window function) overplotted with SYNOW models. The main models are shown by the solid black line. The models with $H\beta$ fitting are shown with dashed black lines. The most conspicuous ions are marked. Atmospheric lines are marked with "+".

the P Cyg profile, which suggests that they are formed by resonance scattering, as assumed in SYNOW. Thus, we modelled all spectra of SN 2011fu with this code. Before modelling, all spectra have been corrected for redshift (see Sect. 3.2).

The strong emission component of the $H\alpha$ line (probably with the C II and Si II contamination) can not be fully fitted in terms of the SYNOW code. We focused primarily on the absorption parts of the P Cyg line profiles which provide information about the expansion velocities of different line-forming layers. The SYNOW code allows the usage of different optical depth (i.e. density) profiles. Two of them are the exponential profile with the parameter of e-folding velocity "v_e" ($\tau \propto exp(-v/v_e)$) which can be adjusted for each ion, and the power-law profile with the index "n"

($\tau \propto v^{-n}$) which is applied to all ions in the model. We checked both cases and found that the exponential law is more suitable for our spectra. The original paper of the SYNOW developers and further studies showed a possibility of spectral features which can be detached or undetached from the photosphere. These two configurations produce different shapes for the line profiles, which were described in the paper by Sonbas et al. (2008).

The first three observed spectra are separated by only one and two days. That is why they can be modelled by similar sets of parameters (see Table 3.7). Even the spectrum obtained on Oct 14 has a similar continuum slope ($T_{bb} \approx 6500 - 6700K$). To verify the pseudo-photospheric temperature derived by the SYNOW modelling, we also evaluated the colour temperature (T_{col}) of the SN using the models of Dessart & Hillier (2005b) and Bersten & Hamuy (2009). We used the $B - V$ colours for those epochs where spectra were available, and then estimated the temperature from the corresponding $B - V$ colour. Both of these temperature estimates seem to be consistent except for the spectra taken on Oct 14 and Dec 22, 2011.

3.5.2 Velocity of the pseudo-photosphere

The velocity of the pseudo-photosphere (an optically thick layer, the surface of last scattering for continuum photons) can be located from the velocities of heavy elements such as Fe II and Ti II, which may produce optically thin spectral features. However, during the very early phases these features are very weak and blended. Therefore, fitting the first three spectra by these ions gives a wide range of possible photospheric velocities, extending from 13 000 to 19 000 km s^{-1}. The most prominent, narrow absorption feature in these spectra is the feature near 5650Å produced by He I (which may be blended with Na I D). This feature is useful to better constrain the velocity at the pseudo-photosphere, and decrease the uncertainty of this parameter at the earliest phases. All velocities derived this way are shown in the V_{phot} column of Table 3.7.

3.5.3 Hydrogen and the 6200Å absorption feature

The wide absorption feature near 6200Å can be fitted with the help of a high-velocity H-layer (up to V ∼20 000 km s^{-1}) which may be detached from the pseudo-photosphere. On the other hand, fitting the emission peak of Hα with SYNOW needs lower velocities, but those models cannot reproduce the absorption profile (see

Table 3.7: Velocities of the pseudo-photosphere, $H\alpha$ and $H\beta$ at different epochs for SN 2011fu, derived with SYNOW. We assumed that the photospheric velocity (V_{phot}) is equal to the velocity of Fe II. All velocities are given in km s^{-1}. T_{bb} is the blackbody temperature of the pseudo-photosphere in Kelvin degrees. The colour temperature (T_{col}) derived from the effective temperature − colour relations (see Bersten & Hamuy, 2009; Dessart & Hillier, 2005b) is given in the last column.

UT Date (yyyy/mm/dd)	V_{phot} ($FeII$)	$V(H\alpha)$	$V(H\beta)$	T_{bb}	T_{col}
2011/09/28	14000	16000	16000	6700	6952
2011/09/29	14000	16000	14000	6500	6476
2011/10/01	11000	15000	11000	6500	6052
2011/10/14	8000	11000	8500	6700	5791
2011/10/29	6200	9500	9500	5000	4698
2011/10/31	6000	9000	9000	5000	4795
2011/11/23	6000	9000	9000	5000	5094
2011/12/22	5000	9000	9000	5000	5718

Fig. 3.7). In the $V(H\alpha)$ column of Table 3.7 we list the results from the latter, more conservative solution.

The broad absorption at 6200Å can be also explained with the presence of the C II ion having a high-velocity almost identical to that of Hα. Moreover, C II also produces a small feature near 4400Å. This feature can constrain the reference optical depth (τ) for ionized carbon. But the contamination from heavy elements in the blue region makes the fitting of the C II 4400Å feature uncertain. Thus, the presence of carbon cannot be confirmed from these spectra.

It is also possible to explain the 6200Å feature by singly ionized silicon. In this case the velocity of Si II must be very low. On the other hand, it is expected that the velocity of Si II should be equal or only slightly higher than the photospheric velocity. It turned out that only the blue wing of this wide feature can be fitted by Si II. Although the small absorption near 5880 Å might be explained by the presence of Si II, the observed shape of the 6200Å feature does not confirm this hypothesis.

In order to look for other possibilities, we also checked different blends of H, Si II, C II and some other ions with different velocities (assuming undetached as well as detached line formation) in our models. At the early phases the range of derived velocities turned out to be wide due to the lack of observable spectral features formed close to the photosphere, as discussed above. At the late phases, the wide absorption near 6200Å splitted into at least three separate features (6100Å, 6200Å, 6350Å). These features might be explained as a line formation effect for Hα in layers with different velocities or the appearance of blending due to the ions

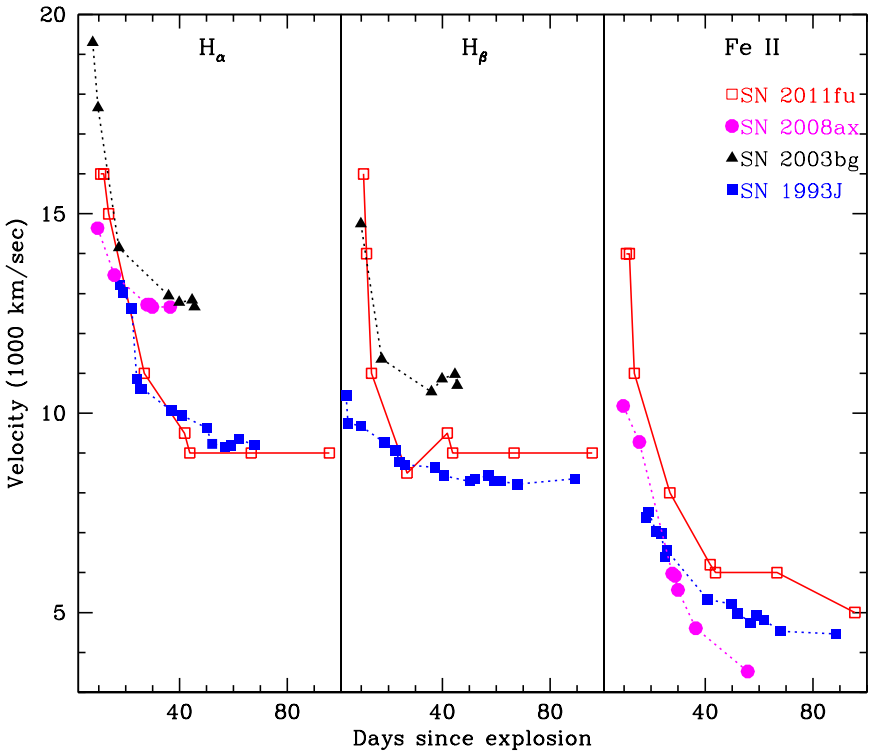

Figure 3.8: Evolution of $H\alpha$, $H\beta$ and Fe II line velocities by fitting the SYNOW model (see Table 3.7). The photospheric velocities for SN 2011fu, 2003bg (Hamuy et al., 2009), 1993J (Barbon et al., 1995; Lewis et al., 1994) and 2008ax (Pastorello et al., 2008) are shown. The symbols of SN 2011fu are connected with lines, those of other SNe with dotted lines.

mentioned above. Unfortunately, no firm conclusion can be drawn based on the simple parametric models that SYNOW can produce.

The deep absorption near 4700Å can be naturally explained identifying it as the $H\beta$ line. We fitted this line and the $H\alpha$ line independently because they cannot be modeled by the same set of parameters: τ, v_{phot} and v_e (see also Quimby et al., 2007). From Table 3.7 it is visible that for the spectra obtained before Oct 29 the fitting of $H\alpha$ needs higher velocities than the fitting of $H\beta$. Although both the $H\alpha$ and $H\beta$ velocities declined in time, the formation of the absorption component of $H\alpha$ stayed at higher velocities than for $H\beta$. This may suggest that $H\alpha$ remained optically thick for a longer time than $H\beta$ in the expanding, diluting H-rich envelope.

3.5.4 Other ions

To fit the main features in the spectra, we included the following elements and ions in SYNOW: H, Fe II, Ti II, Na I, Si II, O I and Ca II. Some models were also computed containing the following elements and ions as alternatives: C II, He I, Fe I, Ti I, Sc II, Mg I and the consistency of these ions were cross-examined with Hatano et al. (1999). The heavier atoms/ions should have velocities close to v_{phot} but the lighter ones may be detached due to e.g. stratification of elements in the ejecta.

In the following, we show some possibilities to explain these features in the observed spectra. Weak features near 4810Å and 6370Å can be explained by the presence of low-velocity He I. He can also be found as a blend with Na I in the deep absorption near 5650Å mentioned above, and as a blend with Ti II and Fe II near 4300Å. However, the velocity of He I may be higher than the photospheric velocity. Even in this case, the presence of He can explain all these features.

A small absorption in the blue wing of $H\alpha$ at 6630Å could be modeled by He I or low-velocity C II. The feature near 5050Å could be fitted with Mg I as well. The Ca II H+K feature cannot be fitted well around 3730Å, because this regime is at the blue end of our observed spectra and all of them are very noisy at these wavelengths. But the absorption feature near 8400Å is compatible with the Ca II IR-triplet.

3.5.5 Results of spectral modelling

Almost all spectral features are well described with elements and ions which are usually applied to the case of Type IIb SNe. However, the strong emission of $H\alpha$ dominating during some intermediate epochs cannot be fully fitted with the models applied.

The fitting of redder and especially bluer parts has some uncertainties due to strong blending of metal lines such as Ca II, Ti II, Fe II and others. Even without a precise modelling, all spectral sequences can be divided into two groups: the first four spectra (up to Oct 14) which are fitted with models with the blackbody temperature $T_{bb} \approx 6500$ - 6700 K and the following four spectra with $T_{bb} \approx 5000$ K.

Generally, the modelling of the SN 2011fu spectra shows a decline of the photospheric velocities up to $\sim$ 40 days after the explosion (see Fig. 3.8). Then, all velocities remain approximately at the same, stable level. This behaviour was also described in previous works on CCSNe (Branch et al., 2002; Moskvitin et al., 2010;

Quimby et al., 2007). In Fig. 3.8 we plot the velocities of Hα, Hβ and Fe II for SN 2011fu, SN 2008ax, SN 2003bg and SN 1993J, illustrating this effect.

3.6 Metallicity-Brightness comparison of host galaxies

In several earlier studies of CCSNe hosts, it has already been mentioned that various SNe subtypes occur in different environments (see Anderson et al., 2010; Arcavi et al., 2010; Kelly & Kirshner, 2012; Modjaz et al., 2011; Prieto et al., 2008; Sanders et al., 2012). Metallicity is a key factor in all these studies. Recent studies by Arcavi et al. (2010) and Prieto et al. (2008) found that SN Ib/c host galaxies are metal-rich as compared to SN II hosts. Modjaz et al. (2011) found that SNe Ic are more metal-rich (up to 0.20 dex) than SNe Ib. In a similar study on SNe Ib/c locations, Leloudas et al. (2011) found a smaller gap between the two metallicities (the environment of SNe Ic is richer by $\sim$ 0.08 dex than Ib). In a recent study with a different approach (using local emission-line for metallicity estimates), where 74 H II regions in CCSNe hosts were analyzed, Anderson et al. (2010) did not find any difference between the metallicities of these two environments.

Type IIb host galaxies have been claimed to be more metal-poor than those of SNe Ib or Ic (see Arcavi et al., 2010; Kelly & Kirshner, 2012), although in another recent study which is based on the SN sample from untargeted searches (although with a rather small sample of 8 SNe IIb) Sanders et al. (2012) found that the median metallicity of both SNe Ib and IIb host galaxies is very similar.

In an attempt to understand the metallicity scenario for the SN 2011fu host galaxy, we collected the latest sample of metallicity data for hosts of CCSNe, and their absolute magnitudes in the B-band from the literature (Leloudas et al., 2011; Modjaz et al., 2011; Stoll et al., 2013) and available online [1]. In Fig. 3.9, the data for these host galaxies (36 for Ib, 15 for IIb and 167 for remaining II SNe) were then overplotted to the sample containing all star forming galaxies from SDSS DR4 (This sample was taken from Prieto et al., 2008). The relations between metallicity and $M_{\rm B}$ for galaxies from several papers are also over-plotted (Contini et al., 2002; Kobulnicky & Zaritsky, 1999; Melbourne & Salzer, 2002; Richer & McCall, 1995; Skillman et al., 1989; Tremonti et al., 2004).

[1] www.astro.princeton.edu/$\sim$jprieto/snhosts/

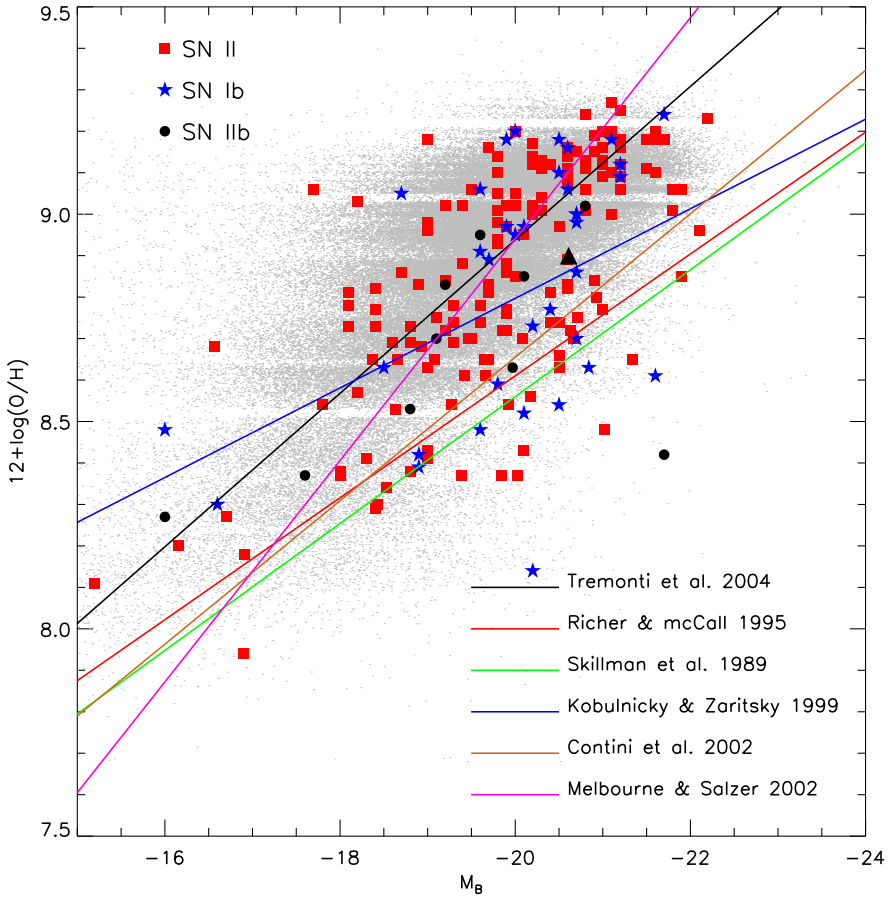

Figure 3.9: Metallicity-luminosity relation for various types of SNe host galaxies. The tiny dots belong to all galaxies used by Prieto et al. (2008) (This catalog is based on SDSS DR4 Adelman-McCarthy et al., 2006, database). Red squares refere to Type II, stars to Type Ib/c and black dots to Type IIb SNe, respectively. The analytic relations collected from several papers (see text) are also over-plotted. The SN 2011fu host metallicity is denoted by a black triangle.

We estimated the metallicity of the host of SN 2011fu using the relation given by Garnett (2002) (see their equation 6). We considered $M_B = -20.62$ mag for UGC 01626 from HyperLeda. The calculated $\log(O/H) + 12$ for UGC 01626 is $8.90^{+0.10}_{-0.06}$. This value is slightly higher than $\log(O/H) + 12 = 8.55$ (Arcavi et al., 2010) and $\log(O/H) + 12 = 8.44$ (Sanders et al., 2012) for the SN type II sample. Our analysis using the most updated sample of absolute magnitudes and metallicities of CCSNe host galaxies also supports the results described in Sanders et al. (2012). However, it is noticeable that methods used to determine metallicities are based on statistical samples, affected by incompleteness of the sample and should be used with caution.

3.7 Conclusions

We present a comprehensive *UBVRI* photometric and low-resolution spectroscopic monitoring of the Type IIb SN 2011fu. To date, only a handful of SNe belonging to this class have been observed and studied in detail.

To the best of our knowledge, our photometric and spectroscopic observations described here are the earliest ones reported for this event. The early photometric observations strongly suggest the presence of the early-time decline of the light curve (which is thought to be related to the shock break-out phase) as seen in case of SN 1993J. The early-time LC decay rate (α_1) of this SN is slower than that derived for SN 1993J in all the bands. The rising rates between the LC valley to peak (α_2) observed in SN 2011fu is also somewhat slower than in SN 1993J. However, the post peak LC decay rate (α_3) are similar in the two events.

The colour evolution of SN 2011fu was studied using our *UBVRI* band observations. Our data showed that during the very early phases the $B-V$ colour was very similar to that of SN 1993J. A similar trend has been found in the $V-R$ and $V-I$ colours as well. The evolution of these three colours after +40 days were also similar to those seen in other CCSNe. The V-band absolute magnitudes of a sample of 8 Type IIb SNe were compared after applying proper extinction corrections and taking into account distances collected from the literature. In this sample, SN 2011fu seems to be the most luminous event. However, the peak V-band absolute magnitude of SN 2011fu is not an outlier when it is compared to the peak brightness of CCSNe of other types.

The quasi-bolometric LC of SN 2011fu was assembled using our *UBVRI* data and accounting for the IR contribution as specified in Section 3.4. Comparison of these data with other known Type IIb SNe also shows that SN 2011fu is the brightest Type IIb SN in the sample. The bolometric LC was modeled by applying a semi-analytical model of Arnett & Fu (1989). This model suggests a 1.1 $M_{\odot}$ He-rich core and an extended, low-mass ($\sim 0.1\ M_{\odot}$) H-envelope as the progenitor of SN 2011fu, similar to that of SN 2011dh. However, the progenitor radius of SN 2011fu ($\sim 1 \times 10^{13}$ cm) turned out to be smaller than that of SN 1993J ($\sim 4 \times 10^{13}$ cm) (Woosley et al., 1994). The ejected nickel mass for SN 2011fu was $\sim 0.21\ M_{\odot}$, higher than that of SN 1993J ($0.07 - 0.11\ M_{\odot}$).

The spectra of SN 2011fu taken at eight epochs were analyzed using the multi-parameter resonance scattering code `SYNOW`. The derived parameters describe the

evolution of the velocities related to various atoms/ions and the variation of the blackbody temperature of the pseudo-photosphere. The photospheric velocities at the early epochs were higher than those of other Type IIb SNe. The pseudo photospheric temperatures were found to be between 6700 K and 5000 K, decreasing from initial to later phases. The temperatures from `SYNOW` were also checked by comparing them with colour temperatures calculated from $B-V$ vs T_{eff} relations (Bersten & Hamuy, 2009; Dessart & Hillier, 2005b). These different temperature estimates were found to be consistent. The appearance of the main observed spectral features was also successfully modeled with `SYNOW` by assuming H, He I and various metals (mostly Fe II, Ti II and Ca II), which are typical of CCSNe spectra. The estimated value of the metallicity of the host galaxy of SN 2011fu is $8.90^{+0.10}_{-0.06}$ similar to those for other Type IIb SNe.

Chapter 4

Broad Band Polarimetric study of the Type IIP SN 2012aw

4.1 Introduction

Core-collapse supernovae (CCSNe) exhibit significant level of polarization during various phases of their evolution at optical/infrared wavelengths. In general, the degree of polarization of different types of SNe seems to increase with decreasing mass of the stellar envelope at the time of explosion (see Leonard & Filippenko, 2005; Leonard et al., 2001; Wang et al., 2001; Wheeler, 2000). Type II SNe are polarized at a level of $\sim$1 – 1.5 %. However, Type Ib/c SNe (also known as stripped-envelope SNe, as the outer envelopes of hydrogen and/or helium of their progenitors are partially or completely removed before the explosion) demonstrate a significantly higher polarization in comparison to Type II SNe (for more details, see Gorosabel et al., 2006; Kawabata et al., 2003, 2002; Leonard & Filippenko, 2001; Maund et al., 2013, 2007; Patat et al., 2012; Tanaka et al., 2012; Wang et al., 2003a, and references therein). The higher polarization values observed in case of Type Ib/c SNe most probably arise due to an extreme departure from the spherical symmetry (Chugai, 1992; Höflich et al., 2001; Khokhlov & Höflich, 2001).

Theoretical modelling predicts that in general CCSNe show a degree of asymmetry of the order of 10 – 30 per cent if modelled in terms of oblate/prolate spheroids (e.g. Hoflich, 1991). Numerical simulations (see Dessart & Hillier, 2011; Kasen et al., 2006) indicate that in case of Type II SNe, the level of polarization is also influenced by the SN structure (e.g., density and ionization), apart from their initial mass and rotation. The possible progenitors of Type IIP SNe are low-mass red/blue

supergiants and their polarization studies are extremely useful to understand the SN structure in detail. In spite of being the most common subtypes among the known CCSNe, polarization studies of Type IIP SNe have only been done for a handful of cases (e.g. Barrett, 1988; Chornock et al., 2010; Chugai, 2006; Leonard et al., 2012a; Leonard & Filippenko, 2001; Leonard et al., 2001, 2006). In general, intrinsic polarization in these SNe is observed below 1 per cent but a few exceptions exist in the literature (for example Chornock et al. (2010) reported ∼1.5% for SN 2006ov).

Systematic polarimetric studies have been started, only after the observations of Type IIP SN 1987A (see Cropper et al., 1988; Jeffery, 1991; Mendez et al., 1988). Shapiro & Sutherland (1982) first pointed out that polarimetry provides direct powerful probe to understand the SN geometry (see also Hoflich, 1991; McCall, 1984). Polarization is believed to be produced due to electron scattering within the SN ejecta. When light passes through the expanding ejecta of CCSNe, it retains information about the orientation of the layers. In the spherically symmetric scenario, the equally present directional components of the electric vectors will be canceled out to produce a zero net polarization. If the source is aspherical, incomplete cancellation occurs which finally imprints a net polarization (see Fig. 1 of Filippenko & Leonard 2004 and Leonard & Filippenko 2005). In addition to asphericity of the electron scattering atmosphere, there are several other processes which can produce polarization in CCSNe such as scattering by dust (e.g. Wang & Wheeler, 1996), clumpy ejecta or asymmetrically distributed radioactive material within the SN envelope (e.g. Chugai, 2006; Hoeflich, 1995), and aspherical ionization produced by hard X−rays from the interaction between the SN shock front and a non-spherical progenitor wind (Wheeler & Filippenko, 1996).

To diagnose the underlying polarization in SNe explosions, two basic techniques i.e. broad-band polarimetry and spectropolarimetry have been used. Both of these techniques have advantages and disadvantages relative to each other. One of the main advantages of spectropolarimetry of SNe with respect to broad-band polarimetry is its ability to infer geometric and dynamical information for the different chemical constituents of the explosion. Broad-band polarimetric observations construct a rather rough picture of the stellar death but require a lesser number of total photons than spectropolarimetry. Hence broad-band polarimetric observations can be extended to objects at higher red-shifts or/and allow to enhance the polarimetric coverage and sampling of the light curve (LC), especially at epochs far from the maximum when the SN is dimmer.

Table 4.1: Polarimetric observation log and estimated polarimetric parameters of SN 2012aw.

UT Date (2012)	JD 2450000	Phase[a] (Days)	Observed		Intrinsic (ISP_{MW} subtracted)		Intrinsic (ISP_{MW}+ISP_{HG} subtracted)	
			$P_R \pm \sigma_{P_R}$ (%)	$\theta_R \pm \sigma_{\theta_R}$ (°)	$P_R \pm \sigma_{P_R}$ (%)	$\theta_R \pm \sigma_{\theta_R}$ (°)	$P_R \pm \sigma_{P_R}$ (%)	$\theta_R \pm \sigma_{\theta_R}$ (°)
Mar 26	6013.35	10.75	0.58 ± 0.46	131.4 ± 22.9	0.61 ± 0.46	138.9 ± 21.6	0.39 ± 0.46	134.2 ± 33.4
Mar 28	6015.23	12.63	0.56 ± 0.03	132.0 ± 1.5	0.60 ± 0.03	139.6 ± 1.4	0.38 ± 0.03	135.1 ± 2.2
Mar 29	6016.28	13.68	0.49 ± 0.08	132.2 ± 4.6	0.53 ± 0.08	140.8 ± 4.3	0.31 ± 0.08	136.1 ± 7.3
Apr 16	6034.18	31.58	0.24 ± 0.17	132.0 ± 21.0	0.30 ± 0.17	147.8 ± 16.7	0.07 ± 0.17	150.5 ± 72.8
Apr 17	6035.25	32.65	0.26 ± 0.01	142.6 ± 1.0	0.36 ± 0.01	154.0 ± 0.8	0.15 ± 0.01	164.8 ± 1.8
May 15	6063.05	60.45	0.87 ± 0.08	123.8 ± 2.6	0.85 ± 0.08	129.0 ± 2.6	0.68 ± 0.08	123.3 ± 3.3
May 19	6067.04	64.44	0.54 ± 0.01	124.3 ± 0.5	0.54 ± 0.01	132.7 ± 0.5	0.35 ± 0.01	123.6 ± 0.8
May 21	6069.08	66.48	0.43 ± 0.06	112.3 ± 4.0	0.37 ± 0.06	122.7 ± 4.6	0.28 ± 0.06	103.4 ± 6.2
Jun 14	6093.23	90.63	0.47 ± 0.14	128.2 ± 8.5	0.49 ± 0.14	137.5 ± 8.2	0.29 ± 0.14	129.9 ± 14.1

[a] with reference to the explosion epoch JD 2456002.6 (days since explosion).

The scope of the present research uses imaging polarimetric observations in R-band using a metre class telescope when the SN 2012aw was bright enough ($R < 13.20$).

4.1.1 SN 2012aw

SN 2012aw was discovered in a face-on ($i \sim 54.6°$, from HyperLEDA[1]), barred and ringed spiral galaxy M95 (NGC 3351) by P. Fagotti on CCD images taken on 2012 March 16.85 UT with a 0.5-m reflector (cf. CBET 3054, Fagotti et al., 2012). The SN was located 60″ west and 115″ north of the center of the host galaxy with coordinates $\alpha = 10^h43^m53^s73$, $\delta = +11°40'17''9$ (equinox 2000.0). This SN discovery was also confirmed independently by A. Dimai on 2012 March 16.84 UT, and J. Skvarc on March 17.90 UT (more information available in Fagotti et al. 2012, CBET 3054; see also special notice no. 269 available at AAVSO[2]). The spectra obtained on March 17.77 UT by Munari, Vagnozzi & Castellani (2012) with the Asiago Observatory 1.22-m reflector showed a very blue continuum, essentially featureless, with no absorption bands and no detectable emission lines. In subsequent spectra taken on March 19.85 UT (Itoh, Ui & Yamanaka, 2012) and 19.92 UT (Siviero et al., 2012), the line characteristics finally led to classify it as a young Type II-P supernova. The explosion date of this event is precisely determined by Fraser et al. (2012) and Bose et al. (2013). We adopt 2012 March 16.1 ± 0.8 day (JD 2456002.6 ± 0.8, taken from the later study) as the time of explosion throughout this chapter. At a distance of about 10 Mpc (cf. Bose et al., 2013; Freedman et al., 2001; Russell, 2002), this event provided us a good opportunity to study its detail polarimetric properties.

[1] http://leda.univ-lyon1.fr - Paturel et al. (2003)
[2] http://www.aavso.org/aavso-special-notice-269

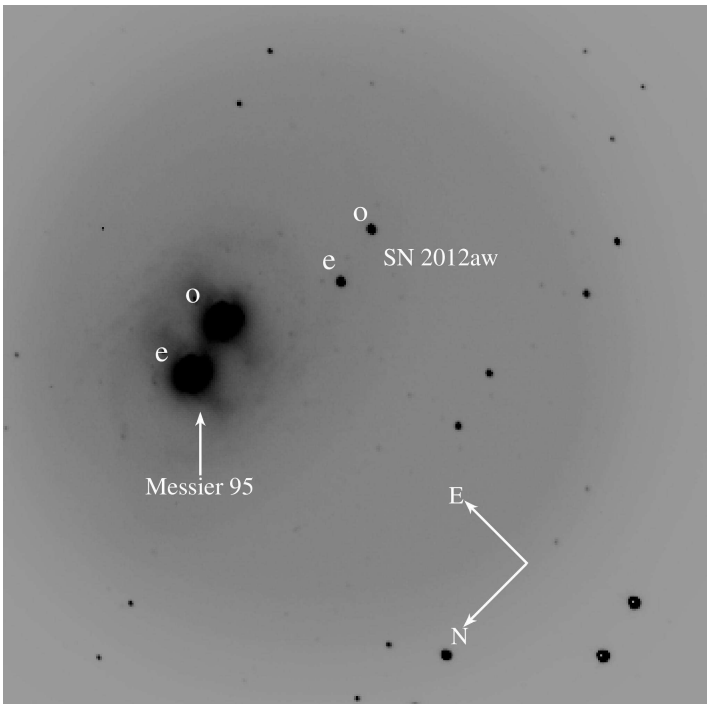

Figure 4.1: *R*-band image of the SN 2012aw field around the host galaxy M95, observed on 2012 April 17 using AIMPOL with the 1.04 m ST, India. Each object has two images. The ordinary and extra-ordinary images of SN 2012aw and its host galaxy are labeled as o and e, respectively. The galaxy is marked with a white arrow and the SN is located 60″ west, 115″ south of the center of the M95 galaxy. The North and East directions are also indicated.

The progenitor of this SN has been detected both in ground and space based pre-explosion images and its distinct characteristics are analyzed. In pre-SN explosion images obtained with *HST*[1] + WFPC2[2], VLT[3] + ISAAC[4] and NTT[5]+SOFI[6], Fraser et al. (2012) found that the progenitor is a red super-giant (mass 14−26 $M_{\odot}$). An independent study by Van Dyk et al. (2012) confirm these findings (mass 15−20 $M_{\odot}$). However, Kochanek, Khan & Dai (2012) have a different view and have concluded that the progenitor mass in earlier studies is significantly overestimated and that the progenitor's mass is < 15 $M_{\odot}$. Immediately after the discovery, several groups have started the follow-up observations of this event at different wavelengths (see, e.g. Bayless et al., 2013; Immler & Brown, 2012; Munari et al., 2013; Stockdale et al.,

[1]Hubble Space Telescope
[2]Wide-Field and Planetary Camera 2
[3]Very Large Telescope
[4]Infrared Spectrometer And Array Camera
[5]New Technology Telescope
[6]Infrared spectrograph and imaging camera

Table 4.2: Observational detail of 14 isolated field stars selected to subtract the interstellar polarization. Observations of all field stars were performed on 20 January 2013 in R band with the 1.04 m ST. All these stars were selected with known distances and within 10° radius around SN 2012aw. The distance mentioned in the last column has been taken from the van Leeuwen (2007) catalog.

Star id	RA (J2000) (°)	Dec (J2000) (°)	$P_R \pm \sigma_{P_R}$ %	$\theta_R \pm \sigma_{\theta_R}$ (°)	Distance (in pc)
HD 99028†	170.98071	+10.52960	0.08 ± 0.00	167.9 ± 1.7	23.7 ± 0.5
HD 88830†	153.73935	+09.21180	0.10 ± 0.01	116.8 ± 1.8	36.3 ± 3.8
HD 87739†	151.78235	+08.76970	0.05 ± 0.01	99.9 ± 6.6	85.0 ± 8.3
HD 97907†	168.96624	+13.30750	0.17 ± 0.05	59.6 ± 9.5	99.6 ± 12.1
HD 88282†	152.72730	+07.69460	0.12 ± 0.01	79.1 ± 1.8	118.5 ± 10.0
HD 87635†	151.57707	+07.94470	0.17 ± 0.00	89.0 ± 0.5	135.7 ± 19.9
HD 87915†	152.08824	+07.57300	0.11 ± 0.01	86.4 ± 1.6	193.1 ± 34.7
HD 87996†	152.20123	+06.71740	0.20 ± 0.04	62.5 ± 5.6	243.3 ± 91.2
HD 88514†	153.15102	+07.67730	0.18 ± 0.03	90.5 ± 4.5	254.5 ± 82.9
G 452	160.45186	+12.10886	0.10 ± 0.01	22.6 ± 2.4	261.1 ± 70.9
BD+12 2250	161.08996	+11.33560	0.12 ± 0.08	100.1 ± 18.0	286.5 ± 91.1
BD+13 2299	161.41026	+12.46724	0.20 ± 0.00	72.4 ± 0.8	314.5 ± 87.0
HD 93329	161.65268	+11.18412	0.12 ± 0.03	144.8 ± 5.8	358.4 ± 118.2
HD 92457	160.15550	+12.07868	0.05 ± 0.07	27.8 ± 41.3	460.8 ± 191.1

† Stars with available V-band polarimetry from the Heiles (2000) catalog.
BD+12 2250, BD+13 229, G 452, HD 93329 and HD 92457 are the stars within 2° radius field around the SN.

2012; Yadav et al., 2014). Early epoch (4 to 270 days) low-resolution optical spectroscopic and dense photometric follow-up (in $UBVRI/griz$ bands) observations of SN 2012aw have been analyzed by Bose et al. (2013). In a recent study, Jerkstrand et al. (2014), have presented nebular phase (between 250 − 451 days) optical and near-infrared spectra of this event and have analyzed it with spectral model calculations. Furthermore, the preliminary analysis of optical spectropolarimetric data of SN 2012aw, revealed that the outer ejecta are substantially asymmetric (Leonard et al., 2012b).

We present hereafter, Cousins R-band polarimetric follow-up observations of SN 2012aw. The observations and data reduction procedures are presented in Section 4.2. Estimation of the intrinsic polarization is described in Section 4.3. Finally, results and conclusions are presented in Sections 4.4 and 4.5, respectively.

4.2 Observations and data reduction

Polarimetric observations of SN 2012aw field were carried out during nine nights, i.e., 26, 28, 29 March; 16, 17 April; 15, 19, 21 May and 12 June 2012 using the ARIES Imaging Polarimeter (AIMPOL, Rautela et al., 2004) mounted at the Cassegrain focus of the 104-cm Sampurnanand telescope (ST) at Manora Peak, Nainital. This telescope is operated by the Aryabhatta Research Institute of Observational sciences (ARIES), India. A complete log of these observations is presented in Table 4.1. The position of the SN, which is fairly isolated from the host galaxy and lies on a smooth and faint galaxy background is shown in Fig. 4.1. The observations were carried out in the R ($\lambda_{R_{eff}} = 0.67\mu$m) photometric band using a liquid nitrogen cooled Tektronix 1024 $\times$ 1024 pixel^2 CCD camera. Each pixel of the CCD corresponds to 1.73 arcsec and the field-of-view (FOV) is $\sim$8 arcmin in diameter on the sky. The full width at half-maximum of the stellar images vary from 2 to 3 pixels. The readout noise and the gain of the CCD are 7.0 e^- and 11.98 e^-/ADU respectively.

Fig. 4.2 illustrates the optical design of AIMPOL. The f/13 beam from the telescope falls on the field lens (50mm, f/6 Karl Lambrecht part no. 322305) which in combination with the camera lens (85mm, f /1.8) makes the image of the object on the CCD chip. A rotatable HWP modulator and a Wollaston beam splitter prism (analyzer) are mounted in between the camera lens and the field lines. The Wollaston prism provides ordinary and extra-ordinary beams separated by 28 pixels along the north-south direction on the sky plane. This set-up gives one of the Stoke's parameter Q or U. The other Stoke's parameters can be obtained by rotating the plane of polarization of the incoming light. This is accomplished by introducing a HWP. When the half-wave plate is rotated through an angle α, the plane of polarization rotates through an angle 2α. At this new position of the HWP another measurement of the orthogonally polarized beams can be made to determine the second Stoke parameter.

In order to get measurements with a good signal-to-noise ratio for the present set of observations ratio, the images that were acquired at each position of the half-wave plate were combined. Since AIMPOL is not equipped with a narrow-window mask, care was taken to exclude the stars that were contaminated because of the overlap of their ordinary and extraordinary images with those of another star in the FOV.

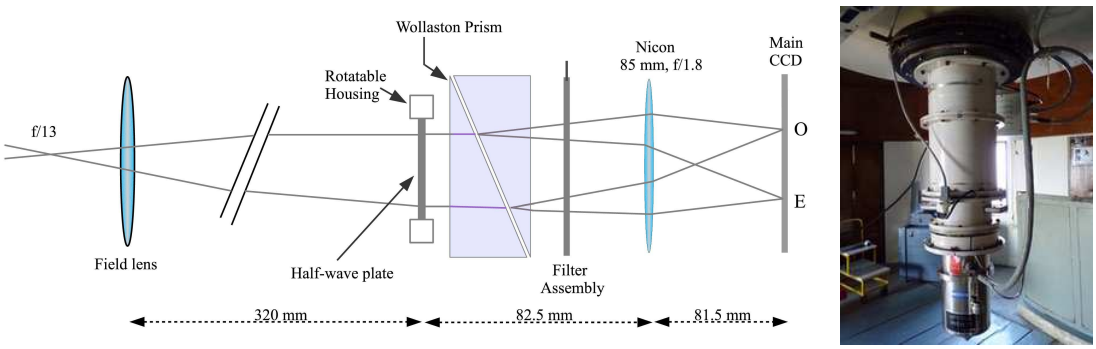

Figure 4.2: Left panel: Optical layout of the AIMPOL (image reproduced from Rautela et al. (2004)). Right panel: AIMPOL mounted on the 1.04-m ST telescope.

Fluxes of the ordinary (I_o) and extra-ordinary (I_e) beams of the SN and of the field stars with a good signal-to-noise ratio were extracted by standard aperture photometry after preprocessing using the IRAF package. The ratio $R(\alpha)$ is given by:

$$R(\alpha) = \frac{\frac{I_e(\alpha)}{I_o(\alpha)} - 1}{\frac{I_e(\alpha)}{I_o(\alpha)} + 1} = P\cos(2\theta - 4\alpha), \tag{4.1}$$

where, P is the fraction of the total linearly polarized light and, θ is the polarization angle of the plane of polarization. Here α is the position of the fast axis of the half-wave plate at 0°, 22.5°, 45° and 67.5° corresponding to the four normalized Stokes parameters respectively, q [R(0°)], u [R(22.5°)], q_1 [R(45°)] and u_1 [R(67.5°)]. The detailed procedures used to estimate the polarization and polarization angles for the programme stars are described by Ramaprakash et al. (1998); Rautela et al. (2004) and Medhi et al. (2010). Since the polarization accuracy is, in principle, limited by photon statistics, we estimated the errors in normalized Stokes parameters $\sigma_{R(\alpha)}$ (σ_q, σ_u, σ_{q_1} and σ_{u_1} in %) using the expression (Ramaprakash et al., 1998):

$$\sigma_{R(\alpha)} = \sqrt{(N_e + N_o + 2N_b)}/(N_e + N_o) \tag{4.2}$$

where, N_e and N_o are the counts in the extra-ordinary and ordinary rays respectively, and $N_b[= \frac{N_{be}+N_{bo}}{2}]$ is the average background counts around the extra-ordinary and ordinary rays of a source. The individual errors associated with the four values of $R(\alpha)$, estimated using equation (4.2), are used as weights in the calculation of P and θ for the programme stars.

To correct the measurements for the instrumental polarization and the zero-point

Table 4.3: Estimated polarimetric parameters for ISP_{MW} (see Section 4.3.1 for detail).

Number of stars	Distance (pc)	$<Q_R \pm \sigma_{Q_R}>$ (%)	$<U_R \pm \sigma_{U_R}>$ (%)	$<P_R \pm \sigma_{P_R}>$ (%)	$<\theta_R \pm \sigma_{\theta_R}>$ (°)
14[#]	all distances	− 0.101 ± 0.002	0.012 ± 0.002	0.102 ± 0.002	86.49 ± 0.54
10	> 100	− 0.154 ± 0.002	0.032 ± 0.002	0.157 ± 0.002	84.10 ± 0.43

[#] All stars within a 10° radius around the SN.

polarization angle, we observed a number of unpolarized and polarized standards, respectively, taken from Schmidt et al. (1992). Measurements for the standard stars are compared with those taken from Schmidt et al. (1992). The observed values of the degree of polarization ($P(\%)$) and position angle ($\theta(^\circ)$) are in good agreement (within the observational errors) with those published in Schmidt et al. (1992). The instrumental polarization of AIMPOL on the 1.04-m ST has been characterized and monitored since 2004 for different projects and found to be ∼0.1% in different bands (e.g., Eswaraiah et al., 2013, 2011, 2012; Pandey et al., 2009; Rautela et al., 2004, and references therein).

4.3 Estimation of the intrinsic polarization

The observed polarization measurements of a distant SN could be composed of various components such as interstellar polarization due to Milky Way dust (ISP_{MW}), interstellar polarization due to host galactic dust (ISP_{HG}) and due to instrumental polarization. As described in the previous section, we have already subtracted the instrumental polarization. Therefore, now it is essential to estimate the contributions due to ISP_{MW} and ISP_{HG}, and to remove them from the total observed polarization measurements of the SN. However, there is no totally reliable method to observationally derive the ISP_{MW} and/or ISP_{HG} of SN and utmost careful analysis is required to avoid any possible fictitious result. In the following sections, we discuss in detail about the ISP_{MW} and ISP_{HG} estimation in the present set of observations.

4.3.1 Interstellar polarization due to the Milky Way (ISP_{MW})

To estimate the interstellar polarization in the direction of SN 2012aw, we have performed R-band polarimetric observations of 14 isolated and non-variable field stars (which do not show either emission features or variability flag in the SIMBAD database) distributed in a region of 10° radius around SN. All 14 stars have distance

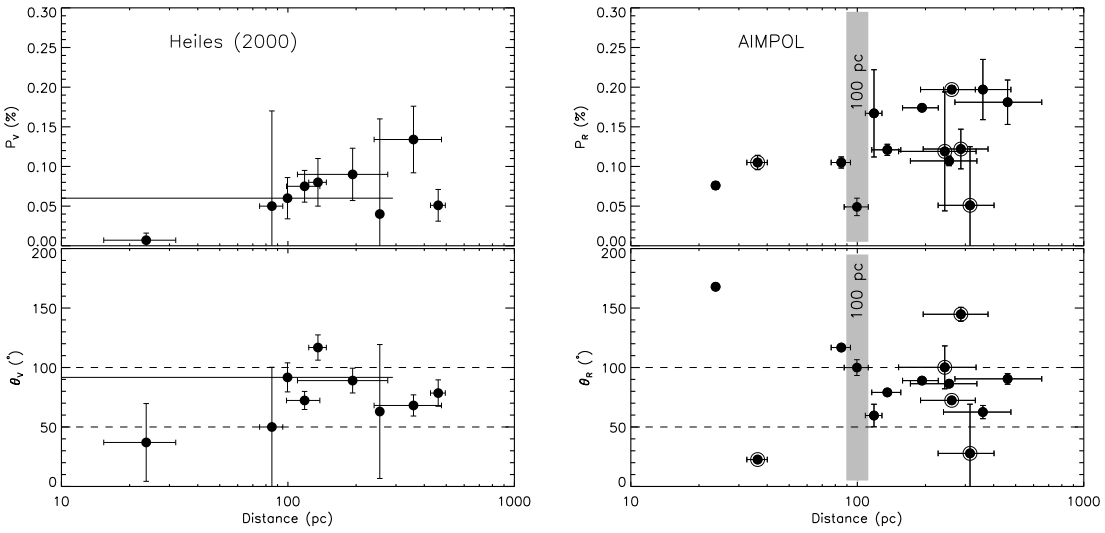

Figure 4.3: Distribution of the polarization and polarization angle of stars around SN 2012aw. Left panel: 9 isolated field stars with known polarization and parallax measurements from Heiles (2000) and van Leeuwen (2007), respectively. Right panel: same as left panel but for 14 isolated stars with R band polarimetric data using AIMPOL and with distance from van Leeuwen (2007) catalog. Filled circles denote 9 common stars in both left and right panels. The encircled filled circles are 5 stars distributed within a 2° radius around the location of SN 2012aw. The gray region represents the possible presence of a dust layer at a 100 pc distance.

information from Hipparcos parallax (van Leeuwen, 2007) and out of these, 9 stars have both polarization (Heiles, 2000) and distance measurements. In Fig. 4.3 (left panels), we show the distribution of the degree of polarization and polarization angles for these 9 stars. The weighted mean values of P_V and θ_V of 8 out of these 9 stars (after excluding one star whose P_V is 0.007%) are found to be 0.071% ± 0.010% and 83° ± 4°, respectively. Because our polarimetric observations are performed in the R-band, we have used polarization measurements of 14 field stars observed on 20 January 2013 in order to correct for the $\mathrm{ISP_{MW}}$ component and to study the intrinsic behavior of the SN. The distribution of P_R and θ_R values of these stars is shown in right panels of Fig. 4.3. All the 14 observed stars are shown with filled circles. As revealed by both left and upper right panels of Fig. 4.3, the amount of degree of polarization shows an increasing trend with distance. It is worthwhile to note that, in the upper right panel, the degree of polarization (P_R) seems to show a sudden jump from ∼0.1% at a distance of ∼100 pc to ∼0.2% at a distance of ∼250 pc, thereby indicating the presence of a dust layer (shown with a gray region in

Fig. 4.3) at ∼100 pc. Whereas, the polarization angles of the stars from the Heiles catalog (left bottom panel) and those observed from the present set-up in R-band (except few stars) are distributed between $50° - 100°$ as shown with the dashed lines (in Fig. 4.3). The Gaussian mean value of θ_R using the 14 stars is found to be ∼82°. This indicates the presence of a uniform dust layer towards the direction of SN 2012aw, which nearly contributes ∼0.1% to ∼0.2% of polarization and having a mean magnetic field orientation ∼82°. Therefore, we believe that most probably, the $\mathrm{ISP_{MW}}$ component is dominated by the contribution from this dust layer.

To determine the $\mathrm{ISP_{MW}}$ component, firstly the P_R and θ_R values of all the field stars as well as the SN were transformed into the Stokes parameters using the following relations[1]:

$$Q_R = P_R \cos 2\theta_R, \tag{4.3}$$

$$U_R = P_R \sin 2\theta_R. \tag{4.4}$$

Then, the weighted mean Stokes parameters were estimated considering (a) all the 14 field stars distributed over all distances, and (b) only 10 field stars distributed beyond a distance of 100 pc. These weighted Stokes parameters ($<U_R>$, $<Q_R>$) were converted back to P_R and θ_R using the following relations:

$$P_R = \sqrt{{Q_R}^2 + {U_R}^2}, \tag{4.5}$$

$$\theta_R = 0.5 \times \arctan\left(\frac{U_R}{Q_R}\right). \tag{4.6}$$

The $<U_R>$, $<Q_R>$, $<P_R>$ and $<\theta_R>$ values (as estimated following two ways) are listed in Table 4.3. It is clear from this table that the $<P_R>$ of the 14 stars is relatively smaller than that determined using the 10 stars. This could be due to the fact that the weighted mean values for stars at all distances may skew the result towards the brighter and more nearby stars which is likely incorrect. Whereas the $<\theta_R>$ values in the two cases nearly matches each other and mimic the mean magnetic field orientation (∼82°) of the dust layer as noticed above. To avoid the values biased towards the lower end due to nearby and brighter stars, we have

[1]Our polarimeter and software have been designed in such a way that we get P and θ through fitting the equation 4.1 on four Stokes parameters obtained at four positions of the half-wave plate as mentioned in Section 4.2

considered the polarization measurements of the 10 stars distributed beyond a 100 pc distance to estimate the $\mathrm{ISP_{MW}}$ component. In addition, using these 10 stars which are distributed beyond 100 pc essentially may take care of the contribution from the dust layer at a distance of 100 pc. Therefore, we consider the $<Q_R>$ = − 0.154 ± 0.002%, $<U_R>$ = 0.032 ± 0.002% values as the $\mathrm{ISP_{MW}}$ component (i.e. $<Q_{ISP_{MW}}> = <Q_R>$ and $<U_{ISP_{MW}}> = <U_R>$). These weighted mean values have been subtracted vectorially from the Stokes parameters of the SN using the relations:

$$Q_{int} = Q_{SN} - <Q_{ISP_{MW}}>, \tag{4.7}$$

$$U_{int} = U_{SN} - <U_{ISP_{MW}}>, \tag{4.8}$$

where Q_{SN}, U_{SN} and Q_{int} , U_{int} denote respectively the observed and intrinsic ($\mathrm{ISP_{MW}}$ corrected) Stokes parameters of the SN. The resulting intrinsic Stokes parameters (Q_{int}, U_{int}) were converted into P_{int} and θ_{int} using the relations 4.5 and 4.6. These intrinsic values for the SN are respectively listed in columns 6 and 7 in Table 4.1 and plotted in Fig. 4.5(a) and (b), with filled circles connected with a thick line.

The reddening, $E(B-V)$ due to Milky Way dust in the direction of SN 2012aw, as derived from the 100-μm all-sky dust extinction map of Schlegel, Finkbeiner & Davis (1998), was found to be 0.0278 ± 0.0002 mag. According to the mean polarization efficiency relation $P_{mean} = 5 \times E(B-V)$ (Serkowski et al., 1975), the polarization value is estimated to be P_{mean} ∼0.14% which closely matches with the weighted mean polarization value, 0.157 ± 0.002% obtained using the 10 fields stars distributed beyond a 100 pc distance (cf. Table 4.3). It is clear that polarization values obtained both from the present observations of the field stars and the mean polarization efficiency relation are similar which implies that the dust grains in the local interstellar medium (ISM) probably exhibit a mean polarization efficiency.

4.3.2 Interstellar polarization due to the host galactic dust ($\mathrm{ISP_{HG}}$)

The reddening, $E(B-V)$, due to dust in the SN 2012aw host galaxy was found to be 0.046 ± 0.008 mag (see Bose et al., 2013). This value was derived using the empirical correlation, between reddening and the Na I D lines, given by Poznanski et al.

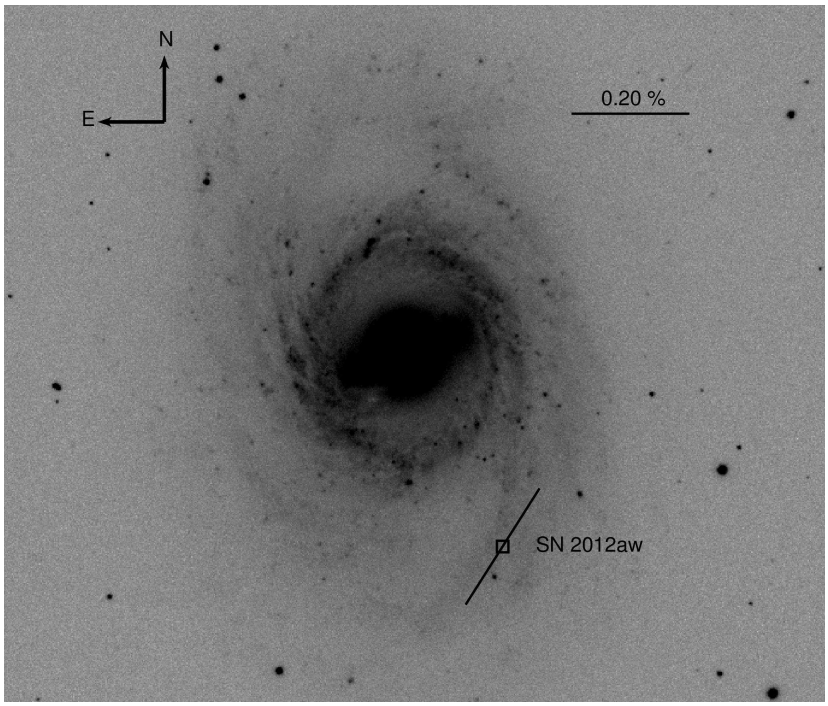

Figure 4.4: SDSS g-band image (7'.7 × 7'.2) of the SN field containing the galaxy M95. A vector with a degree of polarization 0.23% and position angle of 147° is drawn at the location of SN 2012aw (see text in Section 4.3.2 for details). A vector with a 0.20% polarization and polarization angle of 90° is shown for reference (top right). The approximate orientation of the magnetic field at the location of the SN has been determined on the basis of the structure of the spiral arm (see Section 4.3.2 for more details). The location of the SN is represented by a square symbol. North is up and east is to the left as shown in the figure.

(2012). As described in Section 4.3.1, the weighted mean value of the polarization of the 10 field stars situated beyond a 100 pc distance (0.157% ± 0.002%) and the extinction (0.0278±0.0002 mag) due to the Galactic dust along the line-of-sight to the SN suggest that Galactic dust exhibits a mean polarization efficiency. To subtract the ISP_{HG} component we should estimate the degree of polarization and the magnetic field orientation of the host galaxy at the location of the SN.

The properties of dust grains in nearby galaxies have been investigated in detail for a handful of cases and diverse nature of dust grains have only been established in the following studies. For the case of SN 1986G, Hough et al. (1987) probed the ISP_{HG} component due to the dust lanes in the host galaxy NGC 5128 (Centaurus A) and validated that the size of the dust grains is smaller than that of typical Galactic dust grains. In another study (SN 2001el), the grain size was found to be smaller for NGC 1448 (Wang et al., 2003a). However, in some cases polarization efficiency of

dust has been estimated to be much higher than the typical Galactic dust (see e.g. Clayton et al., 2004; Leonard et al., 2002). In the present study, we assume that the dust grain properties of M95 are similar to that of the Galactic dust, and follow the mean polarization efficiency relation (i.e. $P_{mean} = 5 \times E(B-V)$; Serkowski et al. 1975). Therefore, the estimated polarization value would be ∼0.23%.

Another required parameter is the orientation of the magnetic field near the location of the SN. It is well known that large-scale Galactic magnetic field runs almost parallel (i.e. perpendicular to the line connecting a point with the galaxy center) to the spiral arms (Han, 2009; Heiles, 1996; Scarrott et al., 1990, 1991). Interestingly, as shown in Fig. 4.1, SN 2012aw is located nearer to one of the spiral arms of the host galaxy. On the basis of the structure of the spiral arm and the location of the SN, we have estimated the tangent to the spiral arm at the location of the SN (see Fig. 4.4), which makes approximately 147° from the equatorial north increasing towards the east. We assume, on the basis of the structure of the spiral arms and the magnetic field orientation that the magnetic field orientation in the host galaxy at the location of the SN is to be ∼147°. Here, we would like to emphasize that the present procedure of considering a magnetic field for the host of SN 2012aw is well established in previous spectropolarimetric studies of the Type IIP SN 1999em (Leonard et al., 2001) and Type IIb SN 2001ig (Maund et al., 2007).

As shown in Fig. 4.4, a black vector with a length of 0.23% and orientation of 147° is drawn at the location of the SN which is shown with a square symbol. Hence, by assuming that the amount of polarization and the polarization angle due to the host galaxy are 0.23% and 147°, respectively, the Stokes parameters are estimated to be $Q_{ISP_{HG}} = 0.11\%$, $U_{ISP_{HG}} = -0.25\%$. To get the intrinsic Stokes parameters and hence the amount of polarization and polarization angles purely due to the SN 2012aw, these values were subtracted vectorially from the $\mathrm{ISP_{MW}}$ corrected Stokes parameters as described in Section 4.3.1. The intrinsic ($\mathrm{ISP_{MW}}$ + $\mathrm{ISP_{HG}}$ subtracted) polarization and polarization angles of the SN are listed in the columns 8 and 9 of Table 4.1 and plotted in Fig. 4.5 (a) and (b), respectively, with open circles connected with broken lines.

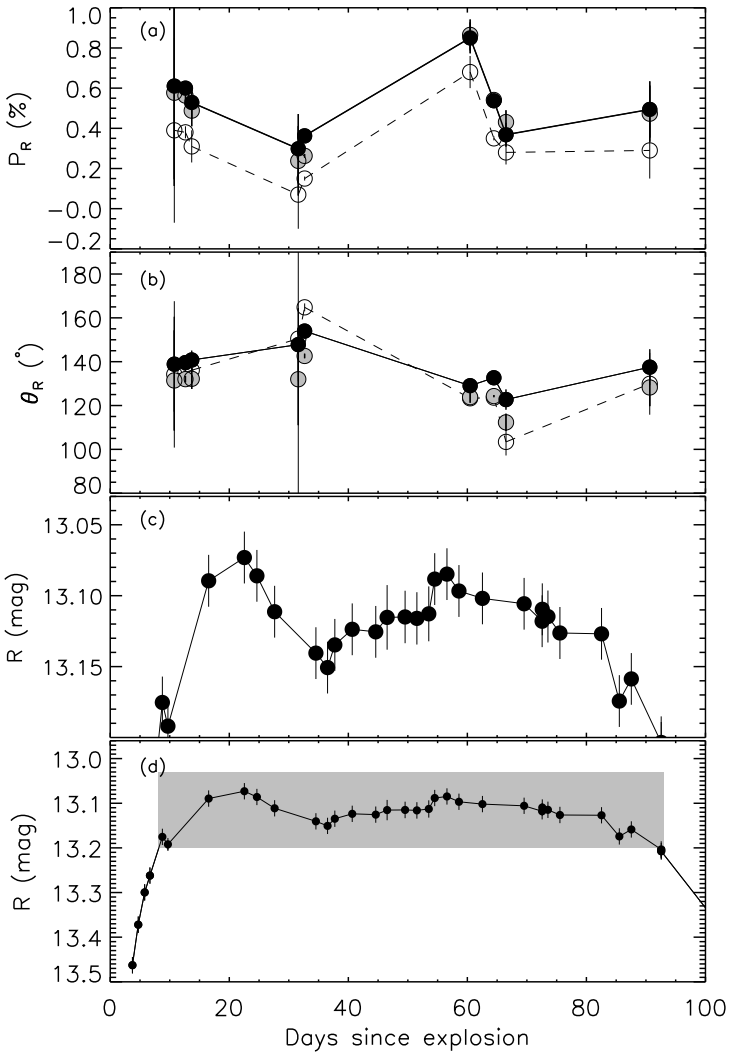

Figure 4.5: Panels (a) and (b): Temporal evolution of the polarization and polarization angles of SN 2012aw in R band, respectively. Filled circles connected with thick lines denote the temporal evolution of the polarization and polarization angles after subtracting the ISP_{MW} component only, whereas those corrected for both ISP_{MW} + ISP_{HG} components are represented with open circles connected with broken lines. The observed polarization parameters are shown with gray filled circles in panels (a) and (b). The bottom panel (d) shows the calibrated R band LC of SN 2012aw obtained with ST (see Bose et al., 2013). The photometric data shown within the shaded region in the bottom panel (d) is re-plotted in panel (c) for a better clarity.

Table 4.4: Observed and intrinsic (ISP_{MW} and ISP_{MW} + ISP_{HG} subtracted) $Q-U$ parameters for SN 2012aw.

UT Date (2012)	JD 2450000	Phase[a] (Days)	Observed		Intrinsic (ISP_{MW} subtracted)		Intrinsic (ISP_{MW} + ISP_{HG} subtracted)	
			$Q_R \pm \sigma_{Q_R}$ (%)	$U_R \pm \sigma_{U_R}$ (%)	$Q_R \pm \sigma_{Q_R}$ (%)	$U_R \pm \sigma_{U_R}$ (%)	$Q_R \pm \sigma_{Q_R}$ (%)	$U_R \pm \sigma_{U_R}$ (%)
Mar 26	6013.35	10.75	-0.072 ± 0.461	-0.573 ± 0.464	0.082 ± 0.461	-0.605 ± 0.464	-0.012 ± 0.461	-0.394 ± 0.464
Mar 28	6015.23	12.63	-0.058 ± 0.029	-0.560 ± 0.029	0.095 ± 0.029	-0.592 ± 0.029	0.002 ± 0.029	-0.382 ± 0.029
Mar 29	6016.28	13.68	-0.048 ± 0.079	-0.486 ± 0.078	0.106 ± 0.079	-0.518 ± 0.078	0.012 ± 0.079	-0.308 ± 0.078
Apr 16	6034.18	31.58	-0.025 ± 0.174	-0.237 ± 0.173	0.129 ± 0.174	-0.269 ± 0.173	0.035 ± 0.174	-0.059 ± 0.173
Apr 17	6035.25	32.65	0.069 ± 0.010	-0.254 ± 0.009	0.223 ± 0.010	-0.286 ± 0.009	0.129 ± 0.010	-0.076 ± 0.009
May 15	6063.05	60.45	-0.330 ± 0.077	-0.800 ± 0.077	-0.176 ± 0.077	-0.832 ± 0.077	-0.269 ± 0.077	-0.622 ± 0.077
May 19	6067.04	64.44	-0.198 ± 0.009	-0.504 ± 0.009	-0.044 ± 0.010	-0.536 ± 0.009	-0.137 ± 0.010	-0.326 ± 0.009
May 21	6069.08	66.48	-0.307 ± 0.059	-0.303 ± 0.059	-0.153 ± 0.059	-0.335 ± 0.059	-0.247 ± 0.059	-0.125 ± 0.059
Jun 14	6093.23	90.63	-0.111 ± 0.141	-0.460 ± 0.140	0.043 ± 0.141	-0.492 ± 0.140	-0.050 ± 0.141	-0.282 ± 0.140

[a] with reference to the explosion epoch JD 2456002.6 (days since explosion).

4.4 Discussion

4.4.1 Polarization light curve (PLC) analysis

In this section, we analyze the evolution of the PLC and its possible resemblance with the photometric light curve (LC) of SN 2012aw as shown in Fig 4.5. The calibrated R-band magnitudes have been taken from Bose et al. (2013) which shows different evolutionary phases of the LC as described in Falk & Arnett (1977); Grassberg et al. (1971); Utrobin (2007). Since in the present study, polarimetric data sets are limited up to the plateau phase, in Fig. 4.5 (panels c and d), only the adiabatic cooling phase and the phase of cooling and recombination wave are shown.

The temporal variation of the $\mathrm{ISP_{MW}}$ corrected degree of polarization (P_R) values (shown with filled circles, Fig. 4.5a) shows a maximum and minimum values of ∼0.9% and ∼0.3%, respectively with a possible trend of variations in accordance with the R-band LC as shown in panel 4.5(c). Although there is a significant reduction in $\mathrm{ISP_{MW}}$ + $\mathrm{ISP_{HG}}$ corrected P_R values (open circles, Fig. 4.5a), its resemblance with the photometric light curve (panel c) remains similar. However, both the $\mathrm{ISP_{MW}}$ and $\mathrm{ISP_{MW}}$ + $\mathrm{ISP_{HG}}$ corrected polarization angles (θ_R, shown with filled circles in Fig. 4.5(b)) do not show much variation during the similar epochs of observations and are distributed around a weighted mean value of ∼138°. Interestingly, the first (10-14 days) three measurements of $\mathrm{ISP_{MW}}$ corrected P_R and θ_R are almost constant. During this adiabatic cooling phase, the SN LC seems to be brightened by ∼0.12 magnitude as shown in Fig. 4.5c.

It is worthwhile to note that dips observed around 35 days in the LC of the SN and in the $\mathrm{ISP_{MW}}$ + $\mathrm{ISP_{HG}}$ corrected P_R are temporally correlated with a minimum amount of polarization (∼0.07%). This observed feature during the end of the adiabatic cooling or early recombination phase could be attributed to several reasons e.g., (i) changes in the geometry i.e., transition from more asphericity to sphericity of the SN, (ii) modification in the density of scatterers (electrons and/or ions), (iii) mechanism of scattering i.e., single and (or) multiple scattering, (iv) changes in the clumpiness of the SN envelope, (v) changes in the electron-scattering atmosphere of the SN, and (vi) interaction of the SN with a dense circumstellar medium. In the recombination phase (∼40 days onwards), the evolution in the values of $\mathrm{ISP_{MW}}$ + $\mathrm{ISP_{HG}}$ corrected P_R and θ_R are in such a way that the amount of polarization shows an increasing trend. This increasing trend could suggest that

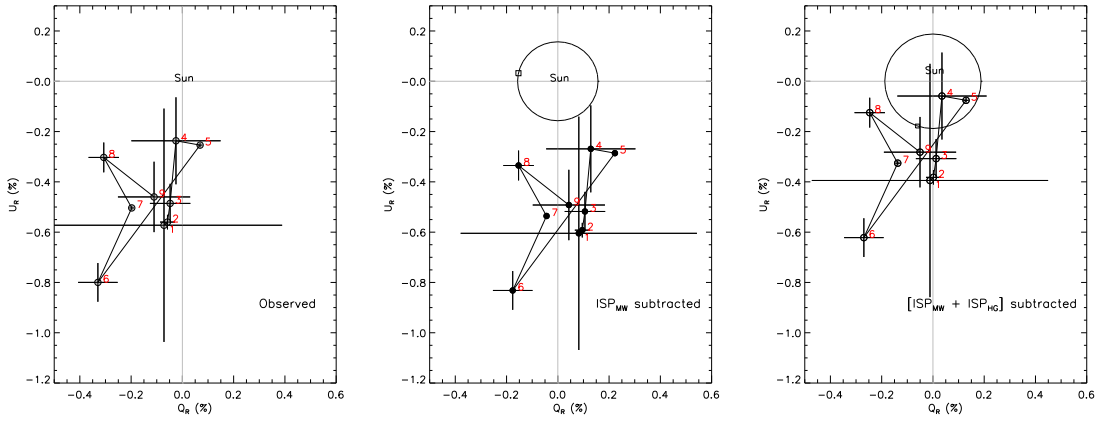

Figure 4.6: Stokes Q and U parameters of SN 2012aw. Left panel: Gray filled circles are the observed parameters. Middle panel: The data have been corrected for the $\mathrm{ISP_{MW}}$ component only (black filled circle; see text). Right panel: After correcting both the $\mathrm{ISP_{MW}}$ + $\mathrm{ISP_{HG}}$ components (open circle; see text). The square symbols connected with large circles drawn nearer to the solar neighborhood in the middle and right panels, respectively, indicate the $\mathrm{ISP_{MW}}$ and $\mathrm{ISP_{MW}}$ + $\mathrm{ISP_{HG}}$ components. Numbers labelled with 1 to 9 (red colour) and connected with continuous lines, indicate the temporal order.

during the recombination phase and onwards, the geometry of the SN envelope could have acquired more asphericity.

If we assume that the $\mathrm{ISP_{MW}}$ and $\mathrm{ISP_{HG}}$ components are constant, then the changes observed in the temporal variation of the intrinsic polarization measurements of the SN could purely be attributed to variations in the geometry of the SN along with the other possible reasons such as the interaction of the SN shock with the ambient medium. However, these properties could be well addressed using high resolution spectroscopic/spectropolarimetric investigations which are beyond the scope of this paper.

4.4.2 Q and U parameters

The $Q-U$ parameters, representing different projections of the polarization vectors, are used as a powerful tool to examine the simultaneous behavior of the polarization and the polarization angle with wavelength (see e.g. Wang et al., 2003a,b). The pattern of the variation in the $Q-U$ plane does not depend upon the $\mathrm{ISP_{MW}}/\mathrm{ISP_{HG}}$ corrections. However, the $\mathrm{ISP_{MW}}/\mathrm{ISP_{HG}}$ subtracted parameters are dependent on the corrections applied to the observed values. A small change in $\mathrm{ISP_{MW}}/\mathrm{ISP_{HG}}$

may considerably affect the polarization angle (PA) values.

The estimated $Q-U$ parameters (observed and intrinsic) for SN 2012aw are presented in Table 4.4 and are plotted in Fig. 4.6. The left and middle panels of this figure show the observed and $\mathrm{ISP_{MW}}$ subtracted parameters and, the right panel represents the intrinsic parameters after subtracting both the $\mathrm{ISP_{MW}}$ + $\mathrm{ISP_{HG}}$ contribution as discussed in Section 4.3. The square symbol connected with large circles drawn nearer to the solar neighborhood in the middle and right panels respectively indicate the $\mathrm{ISP_{MW}}$ ($Q_{ISP_{MW}} = -0.154$, $U_{ISP_{MW}} = 0.032$) and $\mathrm{ISP_{MW}}$ + $\mathrm{ISP_{HG}}$ ($Q_{ISP_{MW}+ISP_{HG}} = -0.060$, $U_{ISP_{MW}+ISP_{HG}} = -0.178$) components.

Since, in the present case, the data points are limited, a firm conclusion could not be robustly drawn on behalf of the Q and U parameters. However, it seems that in all three panels of Fig. 4.6, these data points show a scattered distribution, which seems to form a loop like structure in the $Q-U$ plane. This kind of structure has also been observed for SN 1987A (Cropper et al., 1988), SN 2004dj (Leonard et al., 2006) and SN 2005af (Pereyra et al., 2006). Although, it is to be noted that if we ignore one of the data points (observed on 21 May 2012), the variation of the $Q-U$ parameters will more likely follow a straight line and in this case the previous interpretation may not be true.

4.4.3 Comparison with other Type IIP events

We have collected the polarization parameters of a few well-observed Type IIP SNe from the literature: SN 2008bk (Leonard et al., 2012a), SN 2007aa and SN 2006ov (Chornock et al., 2010), 2005af (Pereyra et al., 2006) 2004dj (Leonard et al., 2006), 1999em (Leonard et al., 2001) and SN 1987A (Barrett, 1988) for which polarimetric observations have been performed during two or more epochs. Except for SN 1987A, SN 2005af and SN 2012aw, the data for the other events are spectropolarimetric only. The intrinsic polarization values of SN 2012aw along with those of other SNe are plotted in Fig. 4.7. It is worthwhile to note that the explosion epochs of SN 1987A (see Bionta et al., 1987; Hirata et al., 1987), SN 1999em (see Elmhamdi et al., 2003) and SN 2012aw are known precisely, but there is some uncertainty in the estimation of the explosion epoch for the other events (SN 2004dj, SN 2005af, SN 2006ov, SN 2007aa and SN 2008bk). In case of SN 2004dj, Leonard et al. (2006) considered the explosion epoch to occur on JD 2453200.5 but Zhang et al. (2006) estimated it on JD 2453167 $\pm$ 21. With an uncertainty of a few weeks, the explosion epoch for SN 2005af is estimated to be on JD 2453379.5 (see Kotak et al., 2006). For

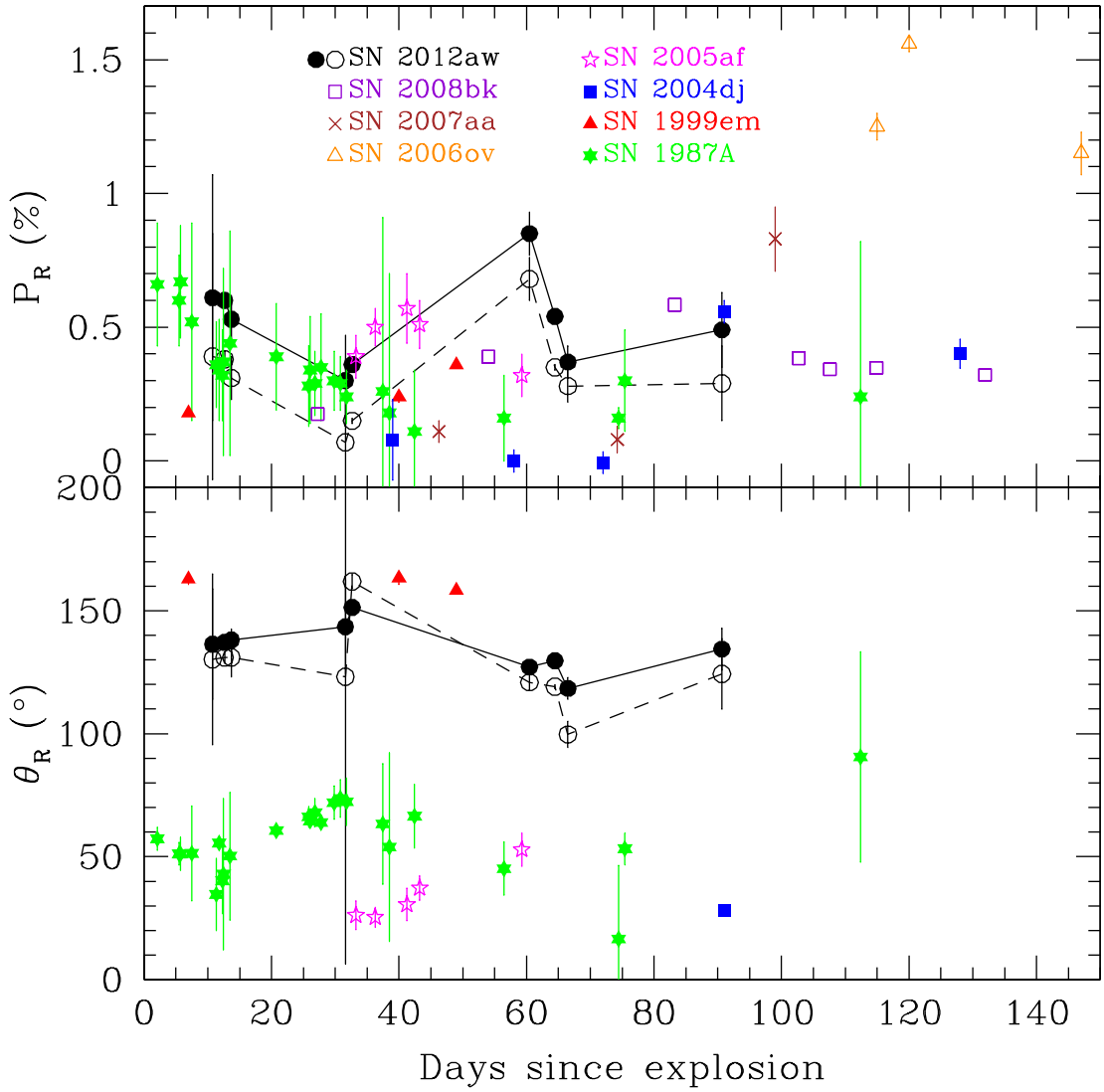

Figure 4.7: Comparison of the polarization and polarization angle values of SN 2012aw with those of other Type IIP SNe: SN 1987A, SN 1999em, SN 2004dj, SN 2005af, SN 2006ov, SN 2007aa and SN 2008bk. The upper and lower panels show the degree of polarization and polarization angle, respectively. All values are intrinsic to a particular SN and symbols used in both panels are same. Thick and broken lines denote ISP_{MW} and both ISP_{MW} + ISP_{HG} subtracted components, respectively for SN 2012aw.

SN 2006ov, Blondin et al. (2006) estimated the expected date of explosion ∼36 days before the discovery (Nakano et al., 2006) but Li et al. (2007) reasonably constrained its explosion to about 3 months before the discovery. We follow the later study in the present analysis. Similarly we considered the explosion epoch for SN 2007aa,

∼20 days before the discovery (see Doi et al., 2007; Folatelli et al., 2007) and for SN 2008bk, JD 2454550 (2008 March 24) has been considered as the explosion epoch (see Morrell & Stritzinger, 2008; Van Dyk et al., 2010).

Shifting the phase (days after the explosion) by 21 days, the evolution of the degree of polarization of SN 2004dj is very much similar to what has been seen for SN 2012aw as shown in Fig. 4.7. However, it is important to mention that for SN 2004dj the degree of polarization increased after the end of the plateau phase (when we see through the H-rich shell); whereas for SN 2012aw, the degree of polarization increased (around 60 days) during the plateau phase which could be a possible indication of a diverse nature of the two events. However, it is noticeable that like for SN 2008bk, SN 2012aw is also strongly polarized well before the end of the plateau (see Leonard et al., 2012a), indicating a possible similarity for both these events. In the early phase (∼10 − 30 days), the ISP_{MW} corrected PLC of SN 2012aw matched that of SN 1987A, whereas in the later phase (∼30 − 45 days) it closely matched that of SN 2005af. Nonetheless, it is worthwhile to mention that in order to derive the polarization parameters of SN 1987A and SN 2005af, the ISP_{HG} components were not subtracted in the respective studies. The polarimetric observations of SN 1999em are sparse; the polarization levels at different epochs seem to match the ISP_{MW} + ISP_{HG} corrected PLC of SN 2012aw. It is also obvious from Fig. 4.7 that the polarization values of SN 2006ov remained more than 1% during all three epochs of observation which is higher than that of any of the Type IIP events in the list. Fig. 4.7 gives an important information regarding the evolution of the ejecta for similar types of SNe. By comparing the PLCs of various IIP SNe shown with different symbols in Fig. 4.7 (filled star: SN 1987A, filled triangle: SN 1999em, filled square: SN 2004dj, open star: SN 2005af, open triangle: SN 2006ov, cross: SN 2007aa, open square: SN 2008bk and for SN 2012aw symbols are the same as in Fig. 4.5), it could be conjectured that the properties of the ejecta from Type IIP SNe are diverse in nature as noticed by Chornock et al. (2010).

We have also compared the ISP_{MW} and ISP_{HG} corrected PLCs of SN 2012aw with those of other Type Ib/c CCSNe. Type Ib/c SNe are naturally more asymmetric in comparison to Type IIP SNe because they lack a thick He blanket that smears out the internal geometry. Therefore, a higher degree of polarization is observed in case of Type Ib/c SNe. In the present analysis, the PLC of SN 2012aw is also clearly showing a lower degree of polarization in comparison to various well studied Type Ib/c CCSNe (e.g. SN 2007uy, SN 2008D; Gorosabel et al., 2010). However, it is

important to note that the P_R peak value for SN 2012aw seen at ∼60 days is slightly less than the intrinsic polarization value of ∼1% for Type Ic SN 2008D which was related to a violent X-ray transient (see Gorosabel et al., 2010). Here it is noticeable that present PLC interpretations of SN 2012aw depend a lot on a single data point (May 15) which is significantly higher in the percentage polarization than the data taken at other epochs.

4.5 Conclusions

We have presented results based on 9 epoch R band imaging polarimetric observations of Type IIP supernova SN 2012aw. To the best of our knowledge, the initial three epoch polarimetric observations presented here are the earliest optical polarimetric data reported for this event. It was not possible to monitor the SN during the beginning of the nebular or post-nebular phase due to observational constraintsi. However present observations cover almost up to the end of the plateau phase (∼90 days). The main results of our present study are the following:

- The observed broad-band polarization for the initial three epochs is ∼0.6%, then decreases down to ∼0.3% following a sudden increase up to ∼0.9% on 15 may 2013 and at later epochs it seems to show a declining trend. However, the observed polarization angle is almost constant, superimposed with slight variations.

- To study the intrinsic polarization properties of SN 2012aw, we subtracted the contribution due to $\mathrm{ISP_{MW}}$ and $\mathrm{ISP_{HG}}$ from the observed P and θ values of the SN. The $\mathrm{ISP_{MW}}$ component was determined using the polarimetric observations of 10 field stars distributed within a 10° radius around the SN and located beyond a 100 pc distance. The estimated Stokes parameters of $\mathrm{ISP_{MW}}$ are found to be $<Q_{ISP_{MW}}> = -0.154 \pm 0.002\%$ and $<U_{ISP_{MW}}> = 0.032 \pm 0.002\%$ (equivalent to $<P_{ISP_{MW}}> = 0.157 \pm 0.002$ and $<\theta_{ISP_{MW}}> = 84.10° \pm 0.56°$). We also estimated the degree of polarization (0.23%) and polarization angle (147°) at the location of the SN by using the extinction value from the Schlegel map assuming that the host galactic dust follows the mean polarization efficiency and that the magnetic field in the host galaxy follows the structure of the spiral arms.

- The intrinsic polarization parameters of SN 2012aw follow trends of the photometric LC which could be attributed to the small scale variations in the SN atmosphere or their interaction with the ambient medium.

- Polarimetric parameters of this SN are compared with other well studied Type IIP events. During the early phase ($\sim$10 $-$ 30 days), the ISP_{MW} subtracted PLC of SN 2012aw matches that of SN 1987A whereas at later epochs ($\sim$30 $-$ 45 days) it matches that of SN 2005af.

Part III

The 4m International Liquid Mirror Telescope and search for supernovae

Chapter 5

The 4m International Liquid Mirror Telescope project

5.1 Introduction

Presently, the Large Zenithal Telescope (LZT) is the largest working LMT (see Sect. 1.3.4 for other LMTs). But the conditions are not optimal in order to carry out astronomical observations. The site has average seeing of ∼2.2" and average 30% clear sky (Hickson et al., 2007). These numbers are not encouraging in terms of astronomical efficiency. Therefore, a full time LMT project entirely dedicated to astronomical observations was proposed and the idea of building an International Liquid Mirror Telescope (ILMT[1]) was born. During the last recent years, several experiments have been performed and the telescope is now ready for installation. First light is expected in the year 2015.

The ILMT project is a scientific collaboration between four countries: Belgium, India, Canada and Poland. The main participating institutions are: Liège Institute of Astrophysics and Geophysics (University of Liège, Belgium), the Royal Observatory of Belgium, the Aryabhatta Research Institute of Observational Sciences (ARIES, Nainital, India), the Observatory of Poznań (Poland) and several Canadian universities (British Columbia, Laval, Montréal, Toronto, Victoria and York). The AMOS (Advanced Mechanical and Optical Systems) company in Belgium has participated to the fabrication of the telescope.

It should be noted that the working principles of LZT and ILMT are the same but there are some technical differences as listed in Table 5.1.

[1]more details about the ILMT can be found at http://www.aeos.ulg.ac.be/LMT

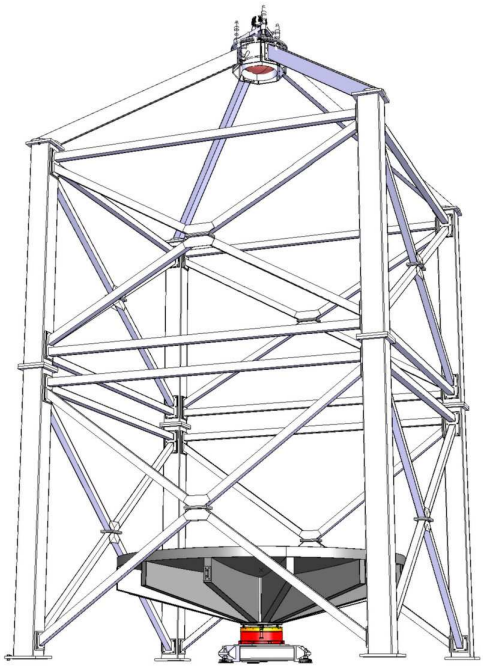

Figure 5.1: Main components of the ILMT: the container is gray, the air bearing is red, the three-point mount (white) sits below the air bearing and the vertical steel frames (white) hold the corrector and the CCD camera at the top. The tentative size and other parameters of this structure are listed in Table 5.1.

A sketch of the ILMT structure is shown in Fig. 5.1. It consists of three major parts, namely the air bearing, the container and the vertical structure which will hold the corrector and CCD camera. The primary mirror (4m diameter) of this telescope will be covered with mercury (Hg). Since the toxic mercury vapors are prevented by a thin layer of mercury oxide, which is created after mercury comes in contact with air, it will not be dangerous to health. Furthermore a mylar coverage of the primary mirror will prevent mercury vapors to contaminate the air in the dome. A CCD (4096×4096 pixels) will be positioned at the prime focus, located 8m above the mirror. Because the primary mirror is parabolic, a glass corrector will be used to obtain a good image quality over a field of view of $27'$ in diameter including TDI correction (see Hickson & Richardson, 1998; Vangeyte et al., 2002). The ILMT will be set up at the Devasthal observatory, India (79° $41'$ $04''$ E, $+29^\circ$ $21'$ $40''$, altitude 2450m). Fig. 5.2 represents the location of the ILMT on a map of India. In the next section, we present the advantages of this site in detail.

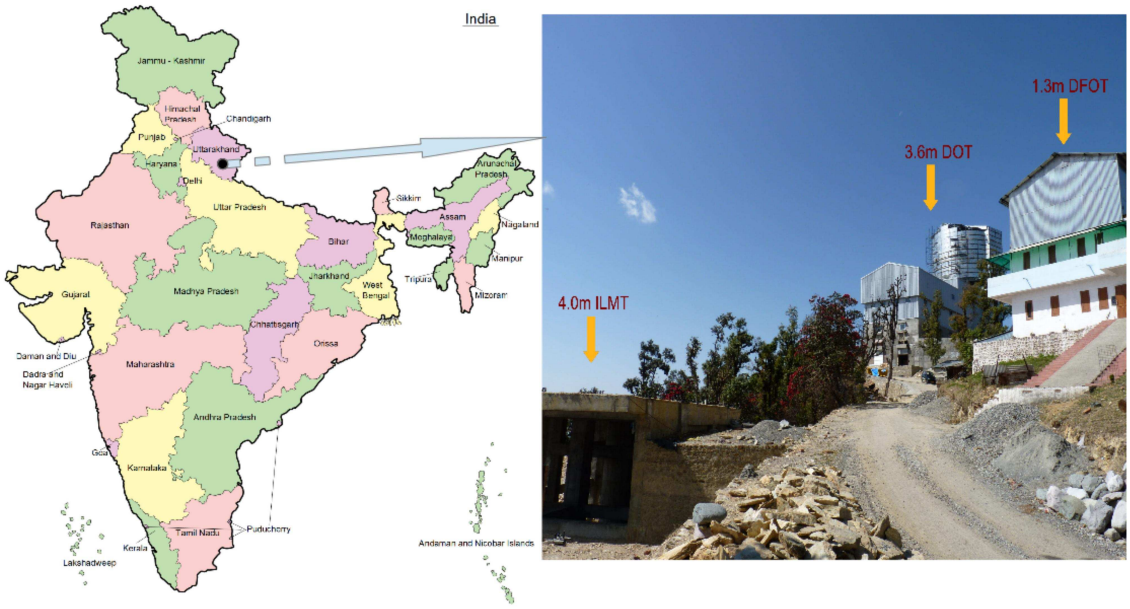

Figure 5.2: Left: Map of India showing all states including Uttarakhand where the ILMT will be set-up. Right: Present status of the ILMT (the dome floor can be seen on the present image), 1.3 m DFOT (already installed) and 3.6 m DOT (under construction in the background).

Importance of the Devasthal site

The ILMT will be installed at Devasthal (meaning "Abode of God") mountain peak, in the central Himalayan range. This place is situated near to the Nainital city of Uttarakhand state in India. The Devasthal site has been chosen for the ILMT project to take advantages of astronomical as well as basic infrastructure presently available there. In this context, it is important to highlight that this site also hosts two modern glass telescopes (see Fig. 5.2) along with the ILMT project. Therefore, in the framework of installing these two optical/infrared telescopes at this place, extensive site characterization has been performed during 1980 − 2001. The major site advantages are its dark skies, sub-arcsec seeing, low extinction, easily accessible and manageable (see Sagar et al., 2012, 2011, for details). The 1.3m *DFOT*[1] has already been installed in October 2010. The main scientific objective of *DFOT* is to monitor optical and near-infrared (350-2500 *nm*) flux variability of astronomical sources such as transient events (gamma-ray bursts, supernovae), episodic events (active galactic nuclei and X-ray binaries), stellar variables (pulsating, eclipsing and

[1]Devasthal Fast Optical Telescope (Sagar et al., 2012, 2011)

Table 5.1: Comparison between the characteristics of the LZT and ILMT.

Characteristics	LZT	ILMT
Location	Vancouver (Canada)	Devasthal (India)
Longitude	122.5731° W	79.6844° E
Latitude	49.2881° N	29.3611° N
Altitude	∼400 m	∼2500 m
Median seeing	2.2”	1.1”
Telescope		
Mirror diameter	6.0 m	4.0 m
Effective focal length (with optical corrector)	10.0 m	9.5 m
Primary mirror f-ratio	1.5	2
Primary mirror shape	parabolic	parabolic
Field of view	23’×23’	27’× 27’
Primary mirror rotation period	8.51 s	8.02 s
Detector and corrector		
CCD	2048×2048 pixels	4096×4096 pixels
Pixel size	24μm/pixel	15μm/pixel
Pixel angular size	0.48”/pixel	0.40”/pixel
TDI integration time	100 s	102 s
Corrector lenses	4	5

irregular), transiting extra-solar planets and to carry out photometric and imaging surveys of extended astronomical sources, e.g. HII regions, star clusters, and galaxies (see Sagar et al., 2012). DFOT has already produced several scientific contributions (e.g. Bose et al., 2013; Joshi & Chand, 2013; Kumar et al., 2013; Paliya et al., 2013, etc.). The other major facility of this place is the 3.6m DOT[1]. After completion of DOT, it will be India’s largest optical telescope. It will see its first light in the year 2015. Some of the technical details about the DOT and its back-end instruments are presented in Table 5.2 (adapted from Sagar et al., 2012).

There are several advantages to prefer this site in the context of the ILMT project. Due to the presence of foreground milky way stars, low galactic latitude fields are very crowded fields. Therefore, it is very difficult to detect fainter extra-galactic objects in low galactic regions. As the Earth rotates around the polar axis, the field of view (FOV) of the telescope makes a 360° turn which will give access to about 140 square degrees of the sky at the Devasthal observatory. Out of it,

[1]Devasthal Optical Telescope (Sagar et al., 2013, 2012)

Table 5.2: Technical specifications of the 3.6m DOT and its instruments.

Parameters	Value
Size of primary mirror	3.6m (Clear aperture)
Mounting type	Alt-azimuth
Configuration	Ritchey-Chretien (RC) with Cassegrain focus
Effective focal ratio	f/9
Mirror control	Active optics
CCD Optical imager:	
(first light instrument)	
Spectral coverage	300 - 900 nm
Field of view	6.5 × 6.5 arcmin^2
Spatial resolution	0.1 arcsec/pix
Faint Object Spectrograph and camera:	
(first light instrument)	
Spectral coverage	350 - 900 nm
Field-of-view	14 × 14 arcmin (imaging); 10 × 10 arcmin (spectroscopy)
Image quality	80% energy in 0.4 arcsec diameter
Resolving power	250 - 2000 @ 1 arcsec slit-width with single grisms 4000 @ 1 arcsec slit-width with VHP Gratings
High-resolution fiber-fed optical spectrograph:	
(first generation instrument)	
Spectral coverage	380-900 mm
Resolving power	30000 and 60000 (fixed)
Radial velocity resolution	20 km/s
Optical-NIR medium resolution	
spectrograph and imager:	
(first generation instrument)	
Spectral coverage	500 - 2500 nm
Resolving power	∼2000, in cross dispersed mode, ∼100 in prism mode
Field of view	10 × 10 arcmin^2

∼70 square degrees will be located at high galactic latitude ($|b| > 30°$, see Fig. 5.3). With the rotation of the Earth, the same strip of the sky will cross the FOV of the telescope each night. However, it should also be kept in mind that the Earth also revolves around the Sun. Consequently the same strip of sky will slightly differ from one night to another.

5.2 Major components of the ILMT

The ILMT consists of several important components as described below.

5.2.1 Air bearing and air supply system

The image quality of LMTs is very much dependent upon the vibrations. The role of the air bearing is thus very important to avoid such vibrations. Using air bearing systems, Borra et al. (1989, 1992) demonstrated that it is possible to achieve diffraction limited images with a 1.5 m diameter, a Strehl ratio of 0.8 and rms surface

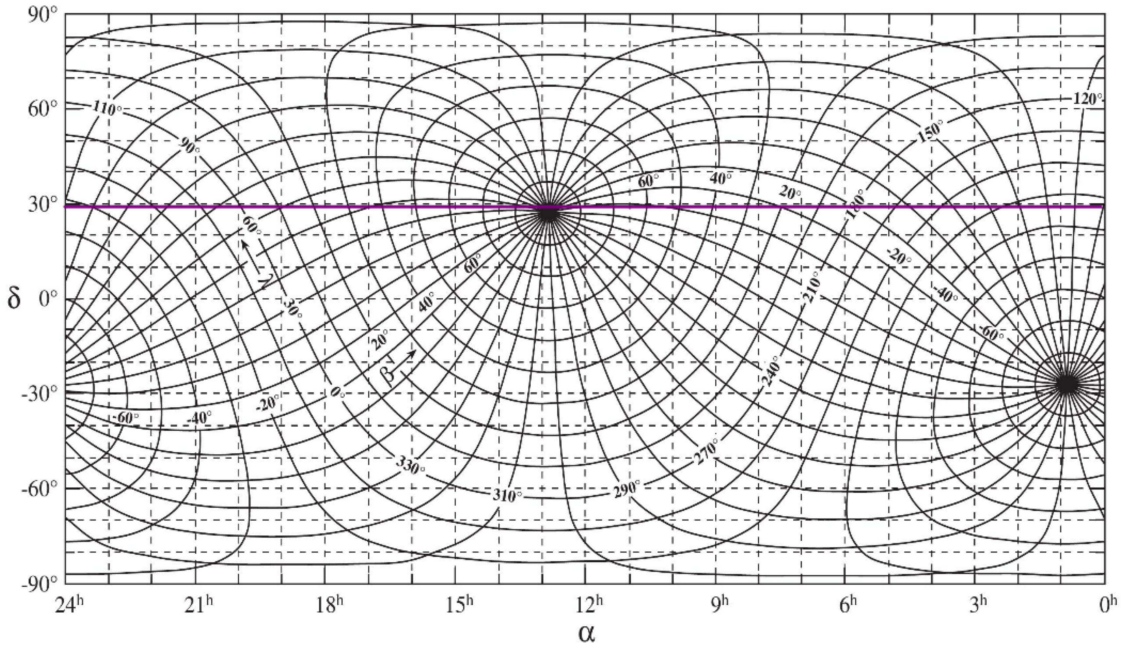

Figure 5.3: Graphical representation of the galactic coordinates in the right ascension (α) – declination (δ) plane. The thick magenta line represents the angular area which will be covered by the ILMT. Image reproduced from Leinert et al. (1998).

deviation of $\sim\lambda/20$. Borra (1993) further demonstrated with a 2.5 m mirror that using this technique can lead to liquid mirrors of astronomical optical quality.

A *Kugler* (model RT-600T) air bearing, mounted on a three-point mount has been used for the ILMT. This system is useful for the alignment of the axis of rotation. Borra (1982) has described the importance of the angular-velocity stability of LMs. It should be better than 10^{-5}, as instabilities in the rotational velocity will also lead to perturbations induced to the liquid mercury. In case of the ILMT, the rotational speed stability test has been performed during the mercury tests (see Sect. 6.3) and analyzed by Denis (2011).

A sketch of the ILMT air bearing is shown in Fig 5.4. A single axial thrust plate is attached to a spherical radial thrust surface. A separate air supply feeds the axial and radial thrust interfaces. The verticle load on the air bearing (i.e. the weight of the rotating dish and the mercury) is supported by an axial thrust with a working pressure of $\sim$6 bar and similarly the radial thrust (working pressure $\sim$3 bar) supports the rotator to stay in the center with respect to the stator. The air consumption in the axial and radial circuits is 2.0 and 0.6 m^3hr^{-1}, respectively. At a pressure of 6 bar, the maximum axial load of the bearing is 1272 kg (Hickson,

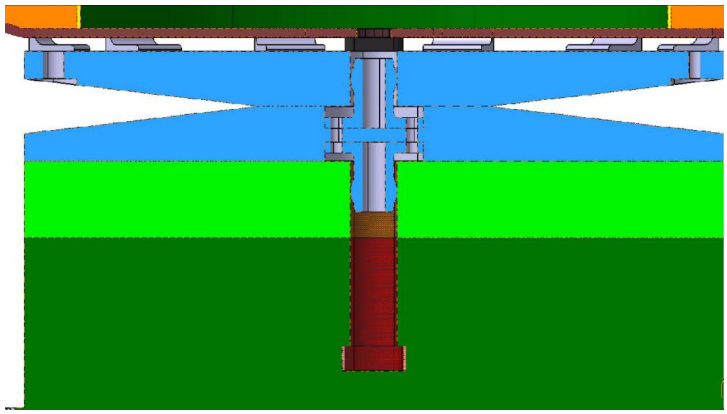

Figure 5.4: Sketch of the ILMT air bearing. Image credit: AMOS.

2008a). The maximum load to be submitted to the bearing is approximately 1010 kg (including the load of the empty mirror and about 410 kg of mercury).

The primary mirror dish is not fixed to the air bearing in order to avoid any damage to the rotating table in case of a break of the mercury layer while rotating. Two interface plates allow the dish to tilt with respect to the air bearing once an off axis load applies a torque that would be damageable to the air bearing (see Fig. 5.4). Since the rotation axis of the mirror should be aligned to better than 0.1 arcsecond (Hickson, 2008b); a three point mounting on which the air bearing is sitting, allows a manual adjustment of the rotation axis of the mirror.

At the AMOS premises where all major tests related to the ILMT have been performed, the air system delivers filtered and regulated air to the axial and radial thrust ports of the air bearing (Hickson, 2008a). The two lines of air have individual regulators, so that the axial and radial pressures may be adjusted individually. Individual flow meters are provided for these lines, as are sensors for air pressure. A single particulate filter is included in the main line (before division into axial and radial lines). Three small stainless steel tanks provide some backup air in case of pressure loss to the system, but it has not been demonstrated that the mirror will stop before the backup air pressure drops below that required to supply the air bearing. Presently the refrigerated dryer is used to remove moisture from the air but this procedure may not be effective for a long time as seen with the 2.7m UBC LMT. Therefore, at the Devasthal observatory, in place of a refrigerated dryer, membrane dryers will be used (see Sect. 5.4).

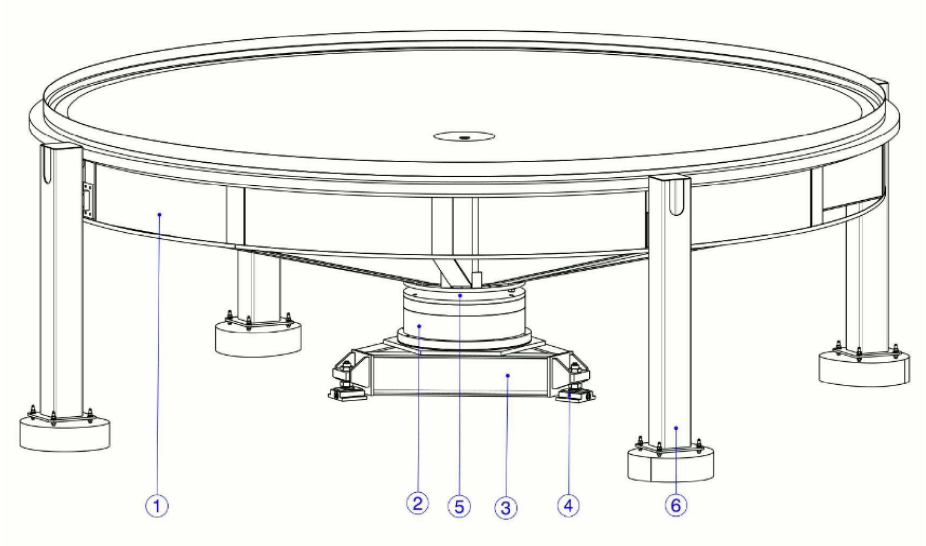

Figure 5.5: Sketch of the 4m primary mirror. (1) mirror (2) rotary table support (3) mounting base (4) leveling system (5) lower interface plate assembly (6) wheel support. Image credit: AMOS.

5.2.2 Primary mirror

The primary mirror of the ILMT is a 4.0 meter rotating dish with mercury. A sketch of the dish is shown in Fig. 5.5. It consists of a structure with twelve vertical ribs, covered by a circular plate. The core segments are made of styrofoam, surrounded by carbon fiber sheets to provide rigid structure so that it can bear the load of mercury covering the bowl.

The dish structure itself must also resist against the flexure induced by the load of the layer of mercury lying over the rotating dish. This flexure should not be larger than one tenth of the mercury layer thickness (Hickson et al., 1993, see also Finet (2013)). Furthermore, any vibration transmitted to the mercury results in the formation of wavelets (see Sect. 6.3.4 for different types of wavelets) on the mercury layer that affect the optical quality (Borra, 1994; Borra et al., 1992). Therefore, the resonance frequency of the mirror should be as high as possible to avoid the transmission of vibrations to the mercury (Hickson et al., 1993).

The top surface of the dish has a parabolic pre-shape with polyurethane so that the final mirror will require a smaller amount of mercury. The pre-shaping technique is known as spin casting (see Chapter 6 for more details).

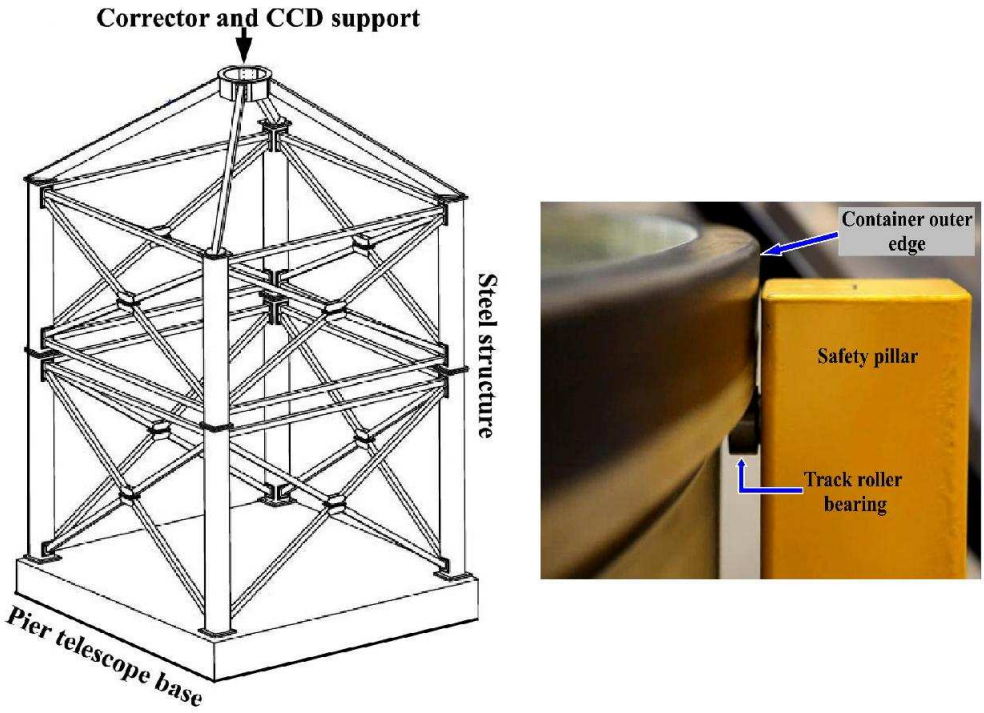

Figure 5.6: Left panel: ILMT support structure with different indicated elements. Image credit: AMOS. Right panel: Zoomed image of one of the safety pillars.

5.2.3 Support structure and safety pillars

There are segmented metallic frames to support the imaging equipments (see Fig. 5.6, left panel). On the top of it, the corrector and the CCD will be installed at the focal point of the ILMT. From the ground, the vertical height of the whole structure is around 8.8m. These pillars will also support the mercury pumping system (Finet, 2013). Furthermore, a laser source and detector will be fixed on two opposite pillars to enable test measurements of the surface quality of the ILMT (see also Finet, 2013).

There are four safety pillars. These pillars will be grouted just below the outer edge of the mercury container. Their distribution is in such a way that in case of any accidental tilt of the container they will hold it. The height of these pillars is about 1.35m from the ground level. A track roller bearing is attached to each of the pillars, maintaining a very small gap just below the container edge. A zoomed image of one pillar is shown in Fig. 5.6 where a roller bearing is also visible.

5.2.4 CCD camera and Time Delay Integration

CCD (charge coupled device) is commonly used in high resolution imaging. These devices are not only extensively used in scientific imaging (particularly in Astronomy), but also in digital photography of normal cameras. A CCD consists of a mosaic of light sensitive detectors (called "pixels") which are made of photo sensitive semi-conductor (silicon). In the normal mode of operation the CCD is exposed towards an object, photons hit the semi-conductor (pixels), the photo-electric effect plays its role, an electron is released and captured by the potential well associated with the pixels. The amount of electric charge produced depends on the amount of light falling upon it. Once the exposure is finished, the CCD shutter is closed so that no more light can fall on the CCD surface. The next step is to readout the CCD. The amount of electric charge from each pixel is measured and digitised. Finally this digitised image is stored on a computer for further action.

CCD detector charateristics

The main charateristics of a CCD chip are as follows:

- **Dark current and bias**

  Dark current is generated even though the chip is not exposed to light. It arises due to the thermal excitation of the electrons into the conduction band and collection in the CCD wells. The generation of dark electrons is a thermally activated process and is strongly temperature dependent. Although the dark current is not uniform for all pixels, it can be minimized by cooling the CCD-chip to very low temperatures (see Widenhorn et al., 2002). Dark frames are taken with the same exposure time as the science frames, but with no light reaching the CCD sensor.

  Pixel-to-pixel variation in the zero-point of the CCD camera is termed "bias". Ideally, a bias frame is an exposure of 0 sec duration. This must be subtracted from the science frames when reduction process takes place. Consequently, the bias level should ideally have a long-term stability.

- **Full well capacity**

  The maximum number of electrons which each CCD pixel can hold is called the 'Full Well Capacity'. This number depends mostly on the physical dimensions of the pixel (the bigger the pixel size, the more electrons it can hold). When

there are too many eletrons in a pixel, they spill into neighbor pixels and create an imaging artifacts known as 'blooming'.

- **Gain and ADU**

  The output voltage from a given pixel is converted into a digital number and is typically measured in ADUs (analog-to-digital units). The amount of voltage needed (i.e., the number of collected electrons or received photons) to produce 1 ADU is termed the gain of the device. Suppose the gain of a CCD is 10 electrons/ADU, it means that for every 10 electrons collected within a pixel, the output from that pixel will produce, on average, a count value of 1 (see Howell, 2000).

- **Quantum Efficiency**

  When light photons hit a CCD chip, they are converted into electrons which are stored and then read out at the end of the exposure. But it may be possible that every photon that hits the chip is not converted into an electron. The quantum efficiency (QE) of a CCD camera can be described as the measurement of electric sensitivity to light, high QE results in a more accurate detection in a particular wavelength range. Supercooled professional CCDs have QEs up to 98%.

ILMT CCD camera

A *Spectral Instruments* camera model SI-1100 having the chipset E2V CCD 231–84–1–E06, will be mounted at the ILMT focal plane for imaging. This camera is both capable of classical and TDI imaging. In Table 5.3, the general characteristics of the ILMT CCD chip are listed.

Time Delay Integration

The LMTs are limited to observe along the zenith direction as they cannot be tilted like traditional glass telescopes. Therefore, imaging with LMTs is done using a specific technique known as the *Time Delay Integration* (TDI) or drift-scanning (see Gibson & Hickson, 1992; Hickson & Richardson, 1998; Vangeyte et al., 2002, and references therein). As a stellar object passes across the field-of-view (FOV) of the telescope along the East-West direction, its image goes across the CCD sensor. The readout process is adjusted in such a manner that the shift rate of the lines

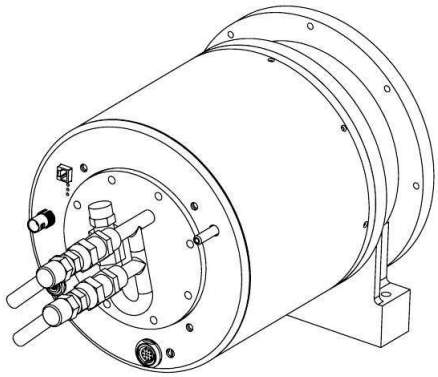

Figure 5.7: A sketch of the ILMT CCD camera. Image credit: *Spectral Instruments*.

Table 5.3: ILMT CCD chip (E2V-231) characteristics.

Characteristics	Values
Numbers of pixels	4096×4112
Filling factor	100%
Pixel size	15μm
Flatness	$< 20\mu$m
Illumination	Back illuminated
Pixel charge storage	≥ 250Ke$^-$
Digitization	16 bit
Max readout noise	5e$^-$
Dark Current (–100°C SI)	10^{-4} e$^-$/pix/s (quotes)

towards the readout register, matches the motion rate of the object image on the sensor. In this way the image formed on the detector follows the stellar objects moving with the sky. The integration lasts during the whole crossing time of the observed object. Fig. 5.8 illustrates the principle of the TDI technique.

There are several advantages in taking TDI images. As the Earth rotates, the passing stars over the zenith can be imaged continuously without losing observing time. At the end of the night a single long image of the strip of the sky is obtained. Although a single integration time is allowed however, as the same strip of sky is observed night after night, these observations can be co-added to increase the limiting magnitude.

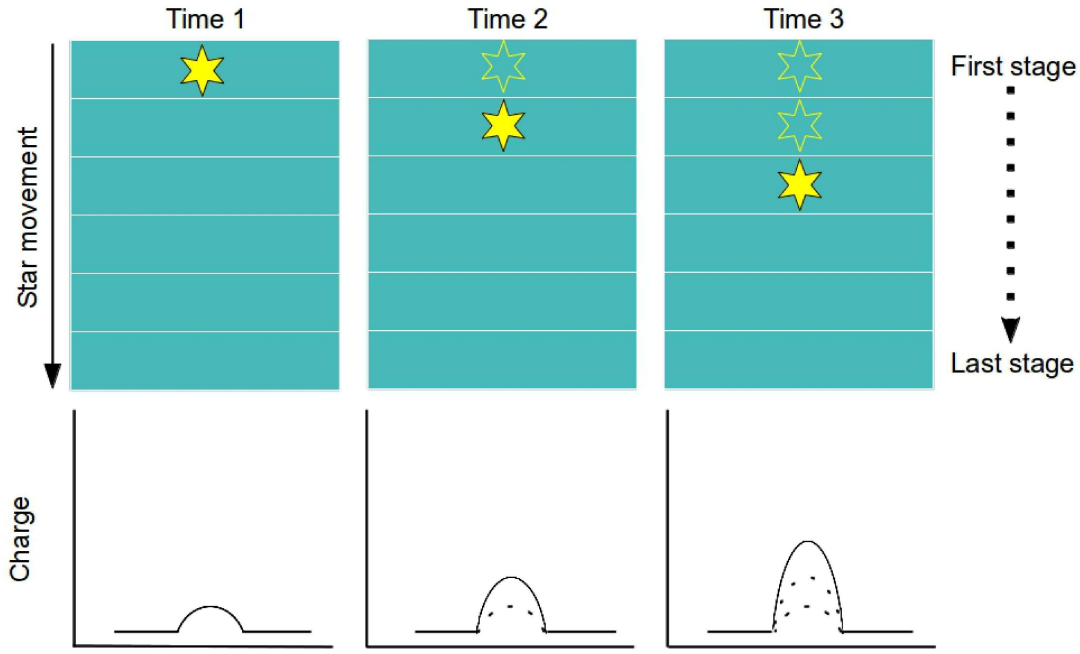

Figure 5.8: Illustration of TDI imaging.

5.2.5 Filters

The ILMT filter system comprises g', r' and i' which is based on the SDSS photometric system. These filters cover the optical and near infrared wavelength range. The adopted filters were prefered in order to directly compare the data produced by the ILMT with those from other large surveys e.g. SDSS, CFHT, etc. It should be mentioned that the SDSS has a slightly different photometric system (u, g, r, i, z bands instead of u', g', r', i', z') therefore, a straightforward colour transformation will be peformed (for example, see http://classic.sdss.org/dr4/algorithms/jeg_photometric_eq_dr1.html#usno2SDSS).

The telescope will mostly operate in the i' filter dedicated to the time variability survey. In addition, observations during a larger number of nights will be possible with the i' filter because this spectral range is less sensitive to the bright phases of the moon. Imaging in g' and r' will be performed in order to ensure a correct photometric calibration and rough characterization of all the detected objects. A few characteristics of the g', r', and i' filters are summarized in Table 5.4.

Table 5.4: Characteristics of the ILMT filters

Filter	Central wavelength (nm)	FWHM (nm)
g'	475	145
r'	625	150
i'	763	150

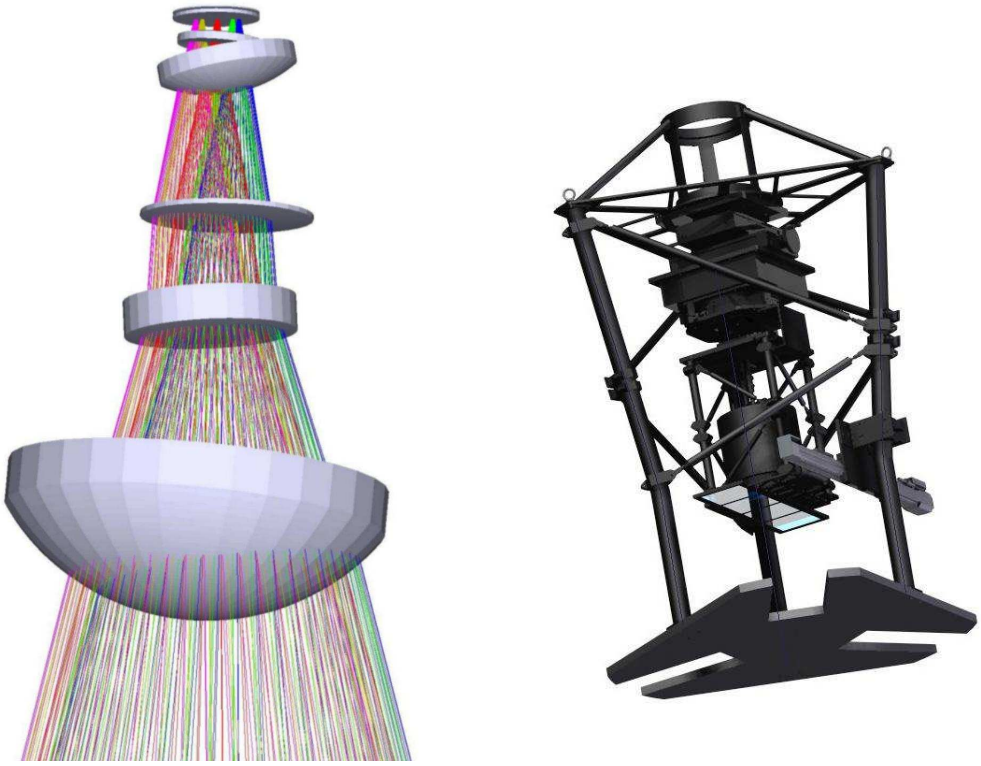

Figure 5.9: Left panel: The optical TDI corrector of the ILMT obtained from the Zemax model. The five lenses are spherical but they are tilted and displaced from the axis of the corrector. The diameter of the first lens is 550mm and the entrance window of the camera is 125mm wide. The distance between the first lens and the focal plane is around 885mm. Right panel: Interface structure between the corrector and the CCD camera. The drawer with the filters is well seen.

5.2.6 Optical corrector

In LMTs, the artificial tracking by electronically stepping the columns at the sidereal rate is not sufficient to get a good image because the tracks of objects are not rectilinear, i.e. they are slightly curved. When using the TDI CCD imaging technique, the trajectories of the stars projected on the CCD are also curved whereas the rows

of the CCD along which the photoelectrons are shifted are straight. Consequently, the telescope PSF gets spread along the N-S direction over several rows, producing a deformation of the PSF. Furthermore, since the primary mirror is parabolic, off-axis imaging is very quickly blurred due to a dominant coma aberration and astigmatism (Schroeder, 1987). Therefore, an optical corrector must be introduced in front of the sensor to rectify these problems (Hickson & Richardson, 1998). The star trail curvature should be compensated so that they are aligned with the CCD rows and the variation of the star crossing speed should also be accounted for.

To correct a field of 27 × 27 arcminutes, the ILMT is equipped with an optical corrector to obtain seeing limited images. The Zeemax model of the corrector is shown in Fig. 5.9 on the left hand panel and the right hand panel shows the whole corrector assembly with its mount. This corrector is the first attempt of correcting optically the TDI distortion, leading to a system of tilted lenses as seen on the Zeemax model. The assembly is equipped with a mechanical mount allowing a tip-tilt alignment of the corrector.

5.3 Science with the ILMT

The ILMT will be entirely dedicated to photometric and astrometric variability studies. The ILMT strip crosses the galactic plane twice which gives access to both very crowded low galactic fields and high galactic latitude fields. The detection of fainter and more distant objects (e.g. galaxies, quasars,...) will be possible in this survey. The ILMT survey will cover a total field of ∼140 sq. deg., with 70 sq. deg. at a galactic latitude $|b| > 30°$.

There are mainly two benefits of imaging each night the same strip of sky.

(1) We can co-add these images to increase the signal-to-noise ratio and thus obtain a longer integration time to detect fainter objects;

(2) or successive night images can be subtracted from a reference frame image to detect variable objects including transient objects such as supernovae.

The study of quasars and the statistical aspect of gravitational lensing in the population of QSOs consist of one of the main research topics to be carried out with the ILMT (see Finet, 2013). A detailed account of the science cases based upon the ILMT may be found in Borra (1982); Finet (2013); Magette (2010); Surdej et al. (2006). Some of the science drivers are as follows:

- statistical determination of the cosmological parameters H_0, Ω_M and Ω_Λ based upon surveys for multiply imaged quasars which consist of compact gravitational lens systems;
- statistical determination of these same cosmological parameters based upon surveys for supernovae;
- search for quasars and observational studies of large scale structures;
- trigonometric parallaxes of faint nearby objects (e.g. faint red, white, brown dwarfs, halo stars and other very low mass stars, etc.);
- detection of high stellar proper motions to probe a new range of small scale kinematics (stars, trans-neptunian objects, etc.);
- astrometry of multiple star systems;
- a wide range of photometric variability studies (cf. photometry of stars, RR Lyrae, micro-lensing effects, photometry of variable AGN over day to year time scales, etc.);
- detection of low surface brightness and star-forming galaxies, and other faint extended objects (galactic nebulae, supernova remnants, etc.);
- galaxy clustering and evolution;
- serendipitous phenomena;
- and, finally, production of a unique database for follow up studies with the 3.6m Devasthal Optical Telescope (DOT) and with other large telescopes (cf. VLT, Gemini, Keck, GranTecan, SALT, etc.).

Possibility of massive star studies with the ILMT

As previously stated, massive stars are the progenitors of core-collapse supernovae. Observationally, RSGs have been confirmed as SN progenitors for stars with up to 18 $M_\odot$ (Smartt, 2009). Out of $\sim$ 20 pre-explosion locations of SNe IIP which have been directly imaged with the *Hubble Space Telescope* or deep ground-based images, only a few detections of progenitor stars are found (Kleiser et al., 2011). These detected progenitor stars belong to SN 2003gd (Smartt et al., 2004; Van Dyk et al., 2003b), SN 2005cs (Li et al., 2006; Maund et al., 2005), SN 2004am (Smartt et al., 2009), SN 2004dj (Maund & Smartt, 2005; Van Dyk et al., 2003a), SN 2008bk (Mattila et al., 2008) and SN 2012aw (Van Dyk et al., 2012) (all are IIP SNe). The progenitor of SN 1987A was a compact blue supergiant (Arnett et al., 1989). There are several other SNe whose progenitors do not belong to RSG: Type IIb SN 1993J (Aldering et al., 1994; Maund et al., 2004), Type IIP SN 2008cn (Elias-Rosa et al.,

2009), Type IIL SN 2009kr (Elias-Rosa et al., 2010; Fraser et al., 2010), and Type IIb SN 2011dh (Maund et al., 2011), all have a yellow supergiant progenitor.

Although in the evolutionary phase of massive stars, WR stars belong to the progenitor stars of core-collapse supernovae. However, some of the theoretical overviews suggest that massive WR stars collapse to form black holes and that, at solar metallicity and below, they do not form bright SN explosions (see Heger et al., 2003b; Woosley et al., 2002). The observed WC/WN ratio is between 0.1 (SMC metallicity) and 1.2 (solar metallicity) (see Crowther, 2007; Massey & Olsen, 2003), but the Type Ib/Ic rate is 2 ± 0.8. This may suggest that in the estimate of the relative frequency of discovery of Type Ib/c SNe, at least a fraction of their progenitors come from interacting binaries. There are 10 SNe classified as Ib/c that have deep pre-explosion images available and none of them have a progenitor detected[1]. The only possible direct detection of a WR star as a SN progenitor (mass 25−30 $M_{\odot}$) has been found for SN 2008ax in NGC 4990. This object was a Type IIb SN. Crockett et al. (2008) analyzed the HST pre-explosion images in which they found a bright point-like source and they proposed that it is also a WNL star.

It will be an interesting objective to survey massive stars. There have been several survey programs devoted to the search of WR stars (e.g. Hadfield et al., 2007; Shara et al., 1999; van der Hucht, 2006). Such surveys require a large amount of telescope time. A continuous and unbiased imaging could be very fruitful in this contex and the ILMT can provide a great opportunity by imaging the strip of sky passing over it.

5.4 Essential ILMT equipment

We have already described various ILMT components in Sect. 5.2. Here, we briefly present some important equipment which will be used when operating the ILMT.

5.4.1 Air compressor and air receiver

The ILMT air bearing will be running at a pressure of ∼6 bar to support a load of ∼1000 kg (including mercury and empty container). For our specific purpose, two units of CompAir (model number L07) air compressor have been procured

[1]In a latest study of the supernova iPTF13bvn, there has been a debate about the possible progenitor of this object (see Bersten et al., 2014; Cao et al., 2013; Fremling et al., 2014; Groh et al., 2013a).

Figure 5.10: Air compressor (left panel) and air receiver (right panel) kept inside the storage room.

Figure 5.11: Air membrane dryer (left panel) and dew point sensor (right panel)

(see Fig. 5.10, left panel). Both compressors will be connected to a common air manifold by means of one-way valves. The automatic turn will switch to the second compressor in case of a drop of pressure, for any reason. In this way breaking of the mirror can be avoided and flawless operation of the telescope can be excuted. We also procured two vertical air receivers (see Fig. 5.10, right panel), each with a capacity of 500 L to ensure continuous air supply to the air bearing. Some of the technical specifications of the air compressor and air receiver can be found in Table 5.5.

Table 5.5: Technical specifications: air compressor and air receiver.

Air compressor	
Compressor model	L07, rotatory screw
Free air delivery at normal pressure m^3/min (CFM)	0.84 (30)
Minimum working pressure	5.0 bar g
Normal working pressure	13 bar g
Nominal motor rating (Kw)	7.5
Noise Level	70 dB
Dimensions in mm –(L×W×H)	667 × 630 × 1050
Weight (Kg)	205
Air receiver	
Type	Vertical air receiver
Capacity	500 Ltr
Normal working pressure	15 bar g

Table 5.6: Technical specifications: Beko membrane dryer.

Model No.	Drypoint M Plus DM20
Flow capacity	560 l/min. (at 7 bar)
Membrane material	Polyether sulphone
Temp. compressed-air/ambient	+2 up to +60 °C
Operating Pressure	4 to 12.5 bar g
Noise level	<< 45 dB
Weight	6.6 Kg

Table 5.7: Technical specifications: Vaisala dew point and temperature transmitter.

Model No.	DMT 347
Dew point measurement range:	−60°C to +80°C
(For continuous use)	(−60°C to +45°C)
Accuracy	±2°C (up to 20 bar)
Temperature range:	0°C to +80°C
Accuracy	± 0.2°C at room temperature
Humidity range:	0 to 70% RH
Accuracy	± 0.004 % RH at 20°C
Operating temperature (for probes)	−40°C to 80°C

5.4.2 Air membrane dryer and dew point sensor

The air entering inside the air bearing must be dry otherwise it will affect the life of the bearing as well as create maintenance problem. Therefore, to avoid it, two air membrane dryers (from BEKO technologies corp.) have been procured (Fig. 5.11, left panel). An electronic dew-point sensor (Vaisala) will be installed to control the humidity and temperature (Fig. 5.11, right panel). The technical specifications of the membrane dryer and dew point sensor are listed in Tables 5.6 and 5.7, respectively.

In addition to the above described equipment, several other items will be required such as solenoid valves, gate valves, one-way valves, tubs and fittings, etc.

Chapter 6

Preliminary tests with the 4m ILMT

In this section we discuss various procedures which were carried out during the developmental process of the ILMT. It includes reinforcement of the container, spin casting of the primary mirror, mercury tests and mylar film tests.

6.1 Container reinforcement

The ILMT primary mirror is a composite structure constructed of bi-directional carbon fiber cloth-epoxy skin over a closed-cell foam core. The principal elements are a concave upper shell, of uniform thickness, supported by 12 radial ribs. The air bearing interface presently employed by AMOS is a thin aluminum plate attached to the bottom of the ribs by six M6 machine screws anchored with blind nuts glued to the back of the lower skin. The plate is attached to the air bearing by three bolts whose lengths can be adjusted. The mass of the composite structure alone was measured by AMOS to be 210 kg (before spincasting). Although the composite structure was quite strong and stiff, it was found after the tests that the interface was not strong enough so that it could support an axial load of about 1000 kg (including the weight of epoxy and mercury).

Tilt-stiffness

The stability of the primary mirror depends upon the following condition of tilt-stiffness (Hickson, 2008a).

$$K > \frac{\pi}{4}\rho g R^4 \tag{6.1}$$

where K is the tilt stiffness (Nm/radian) of the entire support system, including the air bearing, ρ is the density of mercury, g is the gravitational acceleration and R is the radius of the wetted surface of the primary mirror. It is easier to work with tilt compliance which is the reciprocal of the stiffness and is given by

$$G = 1/K \tag{6.2}$$

The compliances of the various components of the support system add linearly to give the total compliance,

$$G = G_{\rm dish} + G_{\rm interface} + G_{\rm bearing} + G_{\rm base} + ... \tag{6.3}$$

For the ILMT mirror, the critical stiffness (Eq. 6.1) is 1.8506 Nm/μrad, which corresponds to a compliance of 0.5404 μrad/Nm.

To achieve these critical values, we reinforced the mirror while proceeding as follows. First we properly filled the gaps between the ribs and interfaces with some epoxy glue. After ∼24 hours of filling, the container was detached from the air bearing for further reinforcement (mainly all 12 ribs). We fabricated high grade carbon-fiber sheets over all the ribs along the different orientation angles to give a skin of roughly homogeneous mechanical properties. The structure was left for a few days for proper curing. After one week the container was again put back onto the air bearing to proceed with new measurements. To verify the compliance a 10 kg load was placed along one of the ribs (at 2.25m from the center) and deflections were measured at different radial positions. We found that without air and with air the compliance was between 76% to 78%. These results were found above the safe limit so it was decided to proceed with the spin casting of the container.

6.2 Primary mirror spin casting

The spin-casting technique is used in the production of large telescope mirrors. It allows the centrifugal forces to shape a natural parabolic surface for the molten glass/polyurethane resin. The curvature created in this way is close to the mirror's final parabolic figure. However, in case of liquid mirrors, spin casting has some additional advantages. The container is rotated with the optimal velocity to properly set the surface of the resin to match the required parabolic shape. In this way the whole structure may be lighter and also it will require a smaller amount of mercury in the final mirror.

Several precautionary steps were taken before spin casting the ILMT container, as described hereafter:

6.2.1 Initial preparations

- Cleaning
- Checking of the orientation of the rotation axis
- Checking of the rotational speed stability

The ILMT container is made of carbon fiber and cloth-epoxy, its surface has small bumps and depressions. The small dust particles lying on the container surface can lead to a bad bonding between the surface and the polyurethane. Therefore, the surface must be cleaned first. Checking of the orientation of the rotation axis and of the rotation speed stability of the mirror were the next steps before the spin casting.

Using sand paper, we smoothened the surface and properly cleaned it with the help of a vacuum cleaner. The orientation of the rotation axis was checked within μm precision. Two tests were performed to check the stability of the rotation speed. First, the mirror was rotated continuously up to around 90 hours, we did not find any significant variation (see Fig. 6.1). To verify this speed stability further, a similar test was carried out by pouring $\sim$60 L of water in the container. Approximately 6-7 L of water was poured one by one 9 times. Initially we found some instability which was due to the pouring of the water but once the whole water had been poured, we found the expected stabilization in speed (see Fig. 6.2).

After completing the initial preparations we continued with the next steps of spin casting. We decided to reach an 8 mm thickness of polyurethane in two steps of 4 mm layers. The following numbers have been considered for the spin casting.

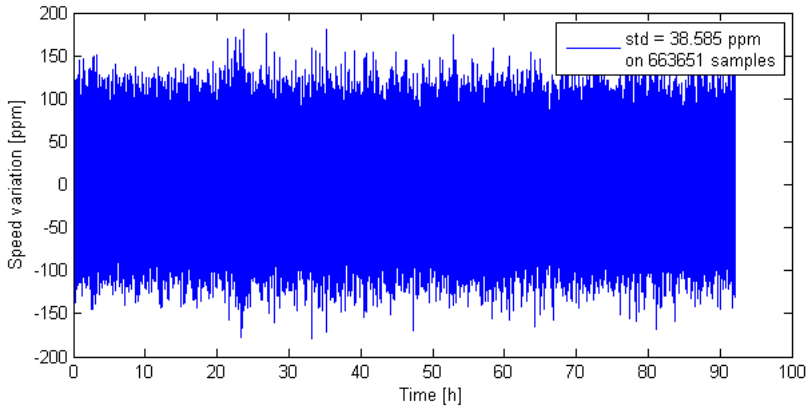

Figure 6.1: Speed variation during the continuous rotation of the mirror (up to 90h). Image credit: AMOS

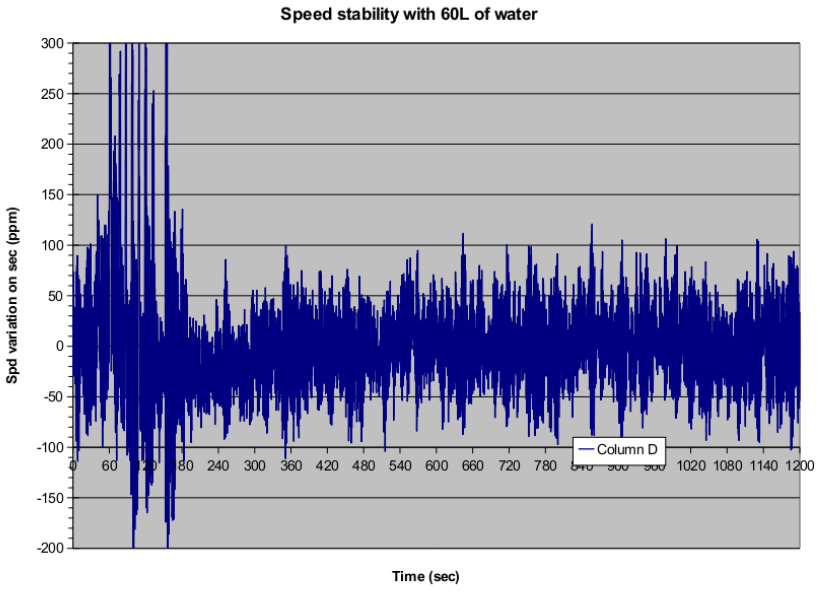

Figure 6.2: Speed variation test with 60 L of water. Peaks between ∼60s and ∼150s are seen because of water pouring disturbances. The system started to stabilize after 360s. Image credit: AMOS.

Rotation rate of the container = 8.024 sec

Surface area to be filled = 13.2 m^2

Required quantity of PU = 53 liters

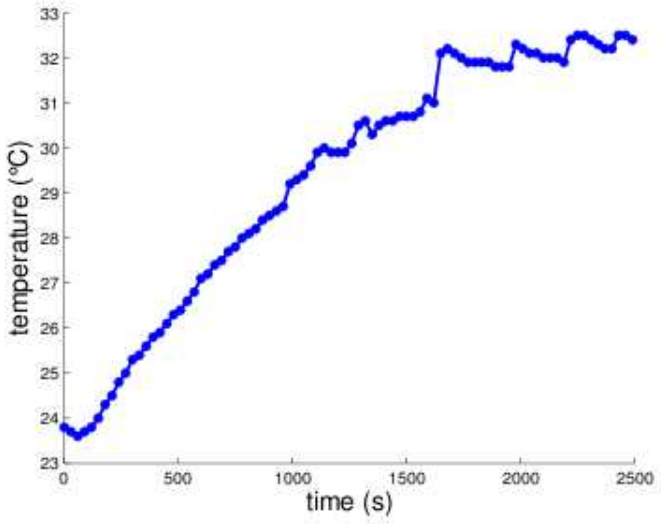

Figure 6.3: Evolution of the PU temperature with time.

6.2.2 Final preparations

After these initial preparations, the container was ready for the final spin casting.

Polymerization test of PU

For a greater tear strength and more durability we used LS-30 A/B (a polyurethane elastomer, product of BJB Enterprises, Inc.). It is resistant to moisture absorption and cures easily at room temperature. Some of the other physical and chemical properties are listed in Table 6.2. This product is available in two parts A and B. To check the starting time of polymerization we made separately a small test. We mixed up 8.8 liters of PU (45:100, A:B) and poured it in a tray. The temperature variation with time was recorded (see Fig. 6.3). It is obvious from this figure that for better bonding, we must complete the whole process of mixing and pouring within 15 minutes.

To mix and pour the PU within time, we decided to involve 6 persons. For a proper pouring of PU over a 13.2 m^2 surface area, the container was divided into 6 sections, each having an equal area of 2.199 m^2 (see Fig. 6.4). The radial position of each zone is given in Table 6.1. Each person was allowed to pour one section only. When the polyurethane was poured on the mirror, the viscosity prevented a fast spreading of the resin from one section to the next and finally we got a nearly uniform surface with the required thickness. Before starting the spin casting, the

Table 6.1: Zonal radial position

Zone (from center)	Radial distance (m)
1	0.837
2	1.184
3	1.450
4	1.674
5	1.871
6	2.050

angular speed was checked once again. We then started the main part of spin casting in following the next steps one by one.

Table 6.2: Polyurethane Properties [1]

Properties	**Part A**	**Part B**
Product Name	LS-30 PART A	LS-30 PART B
Product Class	Polyurethane pre-polymer (resin)	Polyurethane curing agent mixture
Chemical Type	Polyoxypropylene glycol polyol, 1,3-Diisocyanatomethylbenzene terminated	Glycol/aromatic diamine solution in plasticizer
Physical State	Viscous liquid	Liquid
mix ratio (by weight)	45 part	100 part
mix ratio (by volume)	42 part	100 part
Appearance and Odor	Pale yellow, odorless	Clear; Slight amine
Vapor Pressure	<1 mm Hg at 68°F (20°C)	<1
Vapor Density (Air=1)	N/A	N/A
Specific Gravity (H_2O=1)	1.08	1.03
pH	N/A	N/A
Water Solubility	Reacts slightly with water	Slightly soluble
Boiling Point	>480°F (249°C)	N/A
Freezing/Melting Point	N/A	N/A
Viscosity	13,500 cps	120 cps
% Volatile	None	<1

[1] http://www.bjbenterprises.com

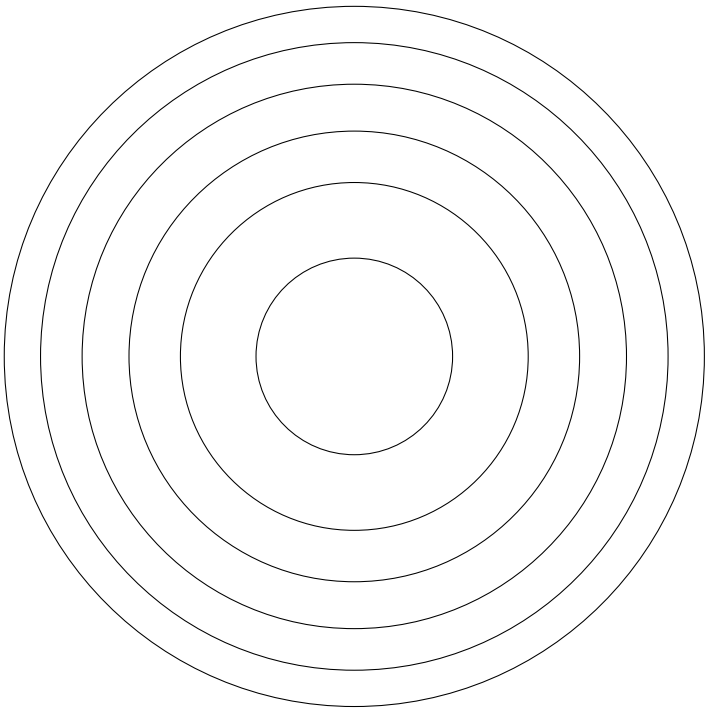

Figure 6.4: Equal surface sections drawn on the container before the spin casting.

Step -A: ***Measuring the proper amount of resin and hardener***

The first step can be done by two persons. The urethane comes in two parts. The proportions are known and the polymerization process begins only when the two parts are mixed. If they are exposed to air, some oxidation will occur but the major consequence is a slight change in the color of the final resin. If they are exposed for a short period of time, oxidation is negligible. Longer exposure to air (e.g. 24 hours) should be avoided. The first most important step is to properly identify each of the containers. We used two kinds of buckets of 15 liters (blue colour) & 20 liters (white colour) capacity to make a good mixing. The weight of the buckets were measured with and without PU. Part -A (resin) was measured in the white colour bucket and part -B (hardener) in the blue one. Since the hardener is less viscous than the resin, it is easier to mix part -B to part -A. We measured 2.596 kg and 5.768 kg of resin and hardener, respectively. In this way 12 buckets were properly filled-up with the appropriate quantity (Fig. 6.5(a)). We then proceeded with the next steps.

Step -B: ***Mixing the PU***

Considering the time limit we decided to mix both quantities within 6 minutes

(a)

(b)

Figure 6.5: Spin casting preparation. (a) Measured quantity of PU: Base resin, part -A (white bucket) and hardener part -B (blue bucket). (b) PU mixing process.

(Fig. 6.5(b)). A signal was given to mix part B in part A. This was done within 2 minutes and during the remaining 4 minutes, the whole liquid was homogeneously mixed by a hand held wooden mixer. It is very important to give at least ∼10% of time to scrape the side and the bottom of the bucket at the same time to avoid formation of bubbles in the process.

Step -C: ***Pouring the PU over the container surface***

Once the PU is mixed properly, the next step consisted in pouring it over the surface of the container. To pour each sector (as described previously), 4 persons used a ladder which was lying above the container and 2 persons near two opposite sides of the mirror (see Fig. 6.6). Due to its high viscosity all the resin will spread over each annular sector. Some small holes may remain on the container surface but they will eventually filled-up. The resin takes about ∼24 hours to polymerize

Figure 6.6: Pouring of the PU over the surface of the container. Each of the six sectors were poured at the same time with the continuously rotating container.

adequately however, complete polymerization will take much longer time. We left the rotating mirror for 24 hours for a perfect bonding.

6.3 Mercury tests: constructing the liquid mirror

In this section we present a short description about various liquids which have the ability to be used for LM and various safety equipments that were used in the process of mercury tests.

6.3.1 Mercury as a reflecting liquid

Mostly metals are good reflectors. To fabricate a rotating mirror a metal can be used which is liquid at the room temperature and at the same time it must be highly reflective. Francium (Fr), Cesium (Cs), Gallium (Ga) and Rubidium (Rb) melt a few degrees above room temperature but Bromine (Br), and Mercury (Hg) are liquid at room temperature. Laboratory experiments have shown that mercury, gallium, and

gallium-indium can be used to construct LMTs but these liquids have advantages and disadvantages relative to each other. Extensive tests of gallium, and gallium-indium LMs have been examined by Borra et al. (1997). They found that the image quality of Ga LM is comparable to that of Hg LM. But the use of Ga requires a particular process, like supercooling. Also Gallium oxidizes very rapidly and forms a transparent thin oxide skin that protects the liquid from additional oxidation. However, this skin is repeatedly broken upon start-up, ruining the optical quality of the mirror. This has been a major problem with Ga LM.

Mercury is a naturally occurring metal and exists in various forms: *elemental* (or metallic); *inorganic* (e.g. mercuric sulphide, mercuric oxide and mercuric chloride); and *organic* (e.g. methyl- and ethylmercury). Some of the properties of mercury are mentioned in Table 6.3.2. Mercury has a reflectivity between ∼75 to ∼78 percent in the wavelength range of 4000Å– 10000Å (see Boiani & Rice, 1969). This corresponds to 90 percent of the reflectivity of an aluminium-coated glass mirror. Therefore, in general mercury has been used primarily for constructing LMTs. It must be noted that human exposure to all forms of mercury is toxic however, the toxicity and implications depend upon its chemical form and the route of exposure. Both the liquid and vapors of elemental mercury are poorly absorbed through the skin but the vapors can be highly toxic if inhaled.

The toxic mercury vapors are greatly reduced after 7-8 hours, thanks to a mercury oxide layer which forms when the mercury reacts with the ambient air. Once it is created, the oxide layer "reinforces" the mirror as it prevents the surface to break because of small perturbations such as insects/dust falling on the mercury. Figure 6.7 represents the mercury vapor concentration as a function of time for the NASA liquid mirror at NODO. The initial peak (∼200 min) is because the mirror was halted after rotation otherwise mercury oxide layer could have begun to form to suppress these vapors. At ∼1350 min the mirror was cleaned and reformed. Then after around 8 hours a thin mercury oxide layer keeps the vapor below the Occupational Safety and Health Administration, U.S. (OSHA) limit ($25\mu g/m^3$, pink horizontal line).

6.3.2 Mercury exposure limit

Various organizations have set different threshold limit values[1] (TLV). The Scientific Committee on Occupational Exposure Limits for elemental mercury and inor-

[1]Daily exposure level above which it is believed a worker could suffer adverse health effects

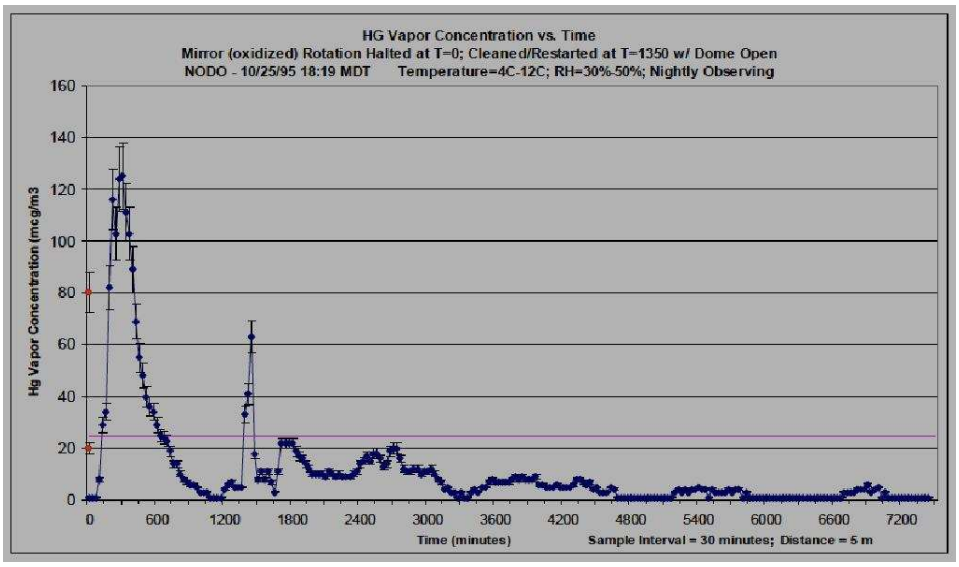

Figure 6.7: Mercury vapor concentration as a function of time for the NASA liquid mirror at NODO. Figure from Mulrooney PhD thesis.

ganic divalent mercury compounds, and the European Commission (May 2007) have adopted a critical value of 0.025 mg per m^3. The National Institute for Occupational Safety and Health (NIOSH) has a recommended exposure limit for mercury vapor of 0.05 mg per m^3 as a time-weighted average for up to a 10-hour work day and a 40-hour work week; the permissible exposure limit for mercury vapor is a ceiling value of 0.1 mg per m^3 in air according to the OSHA.

To prevent the mixing of mercury vapors with ambient air, we will cover the main mirror with a mylar film. A specially dedicated mercury vacuum cleaner will be used to absorb the spills of mercury. Mercury vapor detectors will also be installed for the continuous monitoring.

We briefly described below about some of the important protective equipments/procedures that were used/applied during our experiments of mercury tests.

Table 6.3: Some facts about mercury.

CAS#	7439-97-6
UN#	2024 (liquid mercury compounds); 2025 (solid mercury compounds); 2028 (mercury)
Molecular weight	200.59 g per mol

Melting point	− 38.87 °C
Boiling point	356.73 °C
Density of mercury	13.5 g per cm^3 at 25 °C
Vapor pressure of mercury	0.26 Pa at 20 °C or 2×10^{-3} mmHg at 25 °C
Relative vapor density of mercury	6.93 (air=1)
Occupational exposure limit (EU)	0.02 mg/m^3 in air
Threshold Limit Value (ACGIH)	0.025 mg/m^3 in air (8-hr day, 40-hr wk ave)
Solubility in water	62 g per liter at STP

6.3.3 Important safety equipments

Before the mercury tests, the ILMT surroundings were covered with plastic to prevent Hg spreading & contamination. An exhaust fan has also been installed. Major safety equipments used for the safe handling of mercury are described below:

- **Peristaltic Pump**: A peristaltic pump is a type of positive displacement pump used for pumping a variety of fluids. Peristaltic pumps are typically used to pump clean or sterile fluids. The peristaltic pump is based on the principle of compression and relaxation. The basic principle is illustrated in Fig 6.8. When the rotor passes along the length of the flexible tube totally compressing it and creating a seal between suction & discharge side of the pump. A strong vacuum is created inside the tube which drags the liquid. In this way the liquid inside the tube does not come into contact with any moving part and continuous flow of liquid is maintained. These pumps are in general used to pump aggressive chemicals, high solid slurries and other viscous materials.

  In the course of our experiments we used a peristaltic pump (Thoelen Pumpen GmbH: model TP 4000 E-S) to pump the mercury from the steel reservoir to the ILMT container and vice versa. For this purpose a specially designed pumping system has been developed for the ILMT (see Finet, 2013, for more details). This pump has a water flow rate up to 3.5 L/min (see http://www.peristalticpumps.org) which can be controlled through a speed controller switch. We found that at full speed, the mercury flow rate was about 40L/h. A variable control system is very important. When mercury

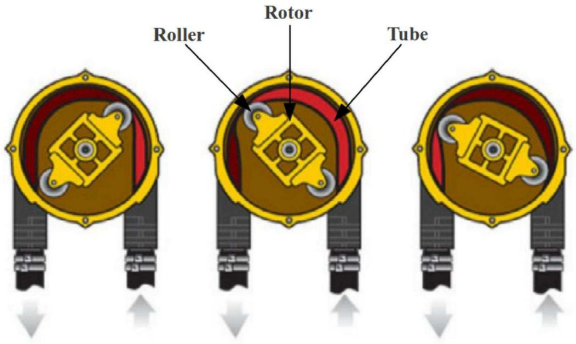

(a) Illustration of the working principle of the peristaltic pump. Figure reproduced from http://www.vectorpump.com.

(b) Mercury reservoir and the peristaltic pump used in our experiment at AMOS.

Figure 6.8: Peristaltic pump

is pumped into the ILMT container, the whole mercury (∼40L) should be transferred quickly to avoid the formation of oxidizing layer of mercury. But once the mirror is formed, the mercury should be suck very slowly so that the oxidizing layer should not break.

- **Mercury vapor detector**: We used two mercury vapor detectors to cross check our readings.
  - **1. Mercury vapor monitor VM-3000:**[1]

    It is based on UV-absorption principles and works at wavelength 253.7 nm. It has three measuring ranges (1−100, 1−1000 and 1−2000 $\mu g/m^3$) and a sensitivity of 0.1 $\mu g/m^3$ (0.01 ppb). There is a programmable alarm which rings in case of a higher value reached than the normal limit.
  - **2. Mercury vapor indicator V1.6:**[2]

    This is a hand held detector comprising a dual beam UV absorption module for the detection of Mercury vapors. We may choose two ranges 0−200 $\mu g/m^3$ with a resolution of 0.1 $\mu g/m^3$ and 0−2000 $\mu g/m^3$ with a resolution of 1 $\mu g/m^3$. With a response time of 3 sec it has a sensitivity of ±5 $\mu g/m^3$.
- **Mercury vacuum cleaner: Tiger-Vac MRV-1000 SS**:

[1] http://www.mercury-instruments.de/en-Mercury_Instruments_Products_VM_3000.html

[2] http://www.ionscience.com/products/portable-mercury-detector

(a) Mercury vapor monitor VM-3000: detecting on the ground surface just below the mirror.

(b) Mercury vapor detector: detection above 3 feet from the ground (range 1-2000 $\mu g/m^3$).

Figure 6.9: Setup to measure mercury vapors generated during the mercury tests.

Consisting of "High-Efficiency Particulate Air"(HEPA) and "Ultra Low Penetration Air" (ULPA) filters, this device is very efficient for cleaning the mercury up to 99.999% for the particle size of 0.12 μm or above.

- **Mercury spill kits**: These kits are important in case of a small spilling of mercury.
- **Gloves**: In general rubber or nitrile gloves are used for the protection of hands and also to rotate the mirror by hand.
- **Mercury masks: 3M Half mask Respirators 6200 and filters**: Before entering inside the covered area of the site this mask must be properly worn.

There are some other protective equipments like apron, disposable shoe covers and safety goggles , etc.

Construction of the liquid mirror

The following operational steps were performed when forming the liquid mirror.

- **Leveling of the bowl**: The leveling of the bowl was done within 10 arcsec.

(a) (b)

Figure 6.10: Panel (a) Testing and cleaning the container with water. Panel (b) Pouring mercury into the container. The shining mercury can be seen in the central part of the dish.

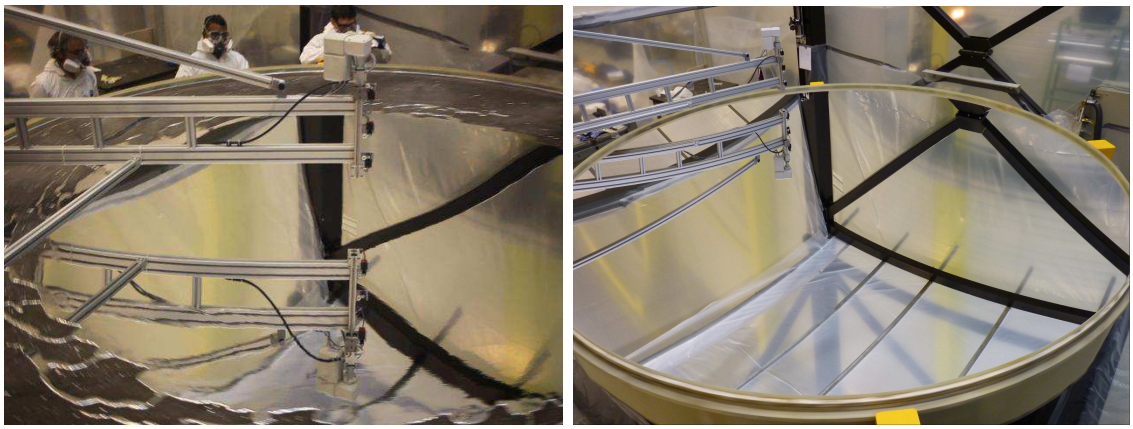

(a) (b)

Figure 6.11: Panel (a): Rotating mercury filled container by hand. Panel (b) Final shape of the rotating mercury mirror.

- **Checking of the tilt**: We checked the tilt of the container by placing a dial indicator tool at different positions over the container.

- **Test with water**: The water test was carried out to check any leakage and at the same time this process also cleans the surface of the bowl (Fig. 6.10(a)).

- **Cleaning the mirror surface with ISOPROPANOL**: Isopropanol is a good solvent because of its high dielectric constant and low acidity, therefore this chemical was used to clean the surface of the bowl just before pumping

the mercury.

- **Pouring the mercury**: Around 525 kg (38.6 liters) of mercury was poured directly in the bowl to avoid any spill (Fig. 6.10(b)).

Once the whole quantity of mercury is poured into the dish, the next step is to form the mirror. For this purpose, first we slowly rotate the dish and further increase the speed of rotation. High surface tensions prevent the mercury to spread and the surface brakes many times. Again by rotating the mirror and filling the gap finally we get a 3 mm thick liquid mirror (see Fig. 6.11).

6.3.4 ILMT surface quality test

The surface quality of liquid mirrors may be affected by the possible presence of wavelets propagating over the mercury layer. These wavelets are of different types: transitory waves, spiral shaped waves and concentric ones (see Mulrooney, 2000).

- **Concentric waves**: The vibrations from the bearing transmitted to the bowl are the primary cause of concentric waves. They are formed with a pattern of concentric wavelets propagating radially. By improving the rotation stability such wavelets may be avoided. The problem of the concentric wave generation can be rectified using an air bearing system and a sufficiently stiffened bowl.

- **Spiral shaped waves**: These waves may be present all the time. The cause behind the generation of these waves is due to the relative wind between the air and the mercury layer. Spiral waves can be reduced by covering the mirror container with a mylar film (see Sect. 6.4).

- **Secondary transitory waves**: are caused due to any perturbation transmitted to the mirror (e.g. a gust of wind, a fly or a debris impacting the mercury layer). Using a thinner mercury layer, such waves can be minimized (Borra, 1994).

To examine the wavelets, we have performed an experiment inside the workshop of AMOS which is presented in detail by Finet (2013). Here, we briefly describe it. The experimental set-up is similar to that shown in Fig. 6.12. A laser source and a detector are fixed inside two diagonally opposite pillars of the ILMT structure. The laser beam is reflected by the liquid mirror surface which is then received at

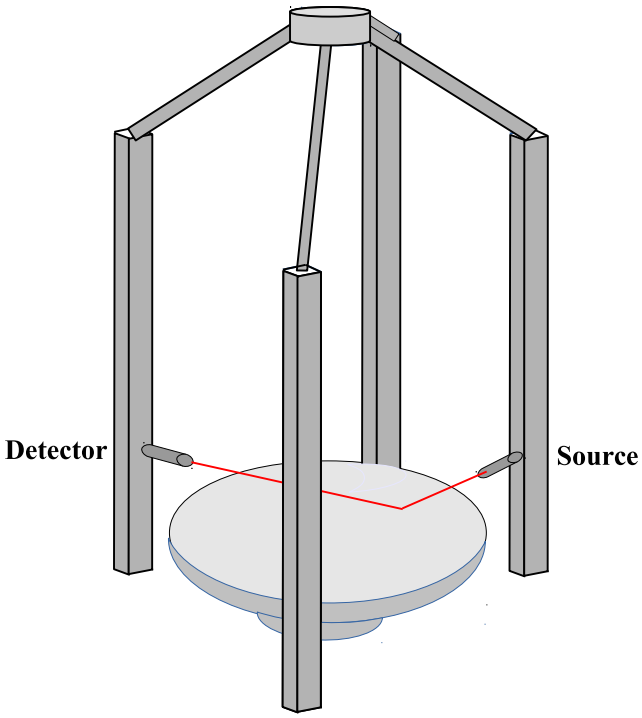

Figure 6.12: Experimental set-up for the surface quality test.

the detector. The presence of wavelets on the mirror changes the slope at the laser impact point and thus modifies the position of the reflected beam on the detector. By measuring the modification of the reflected beam position on the detector, one can retrieve the local slope modifications at the impact point on the mirror and characterize the wavelets. We carried out measurements for 3mm and 2mm thicknesses of mercury layers.

The analysis indicates that there is absence of concentric wavelets on the mirror however, spiral wavelets are present (for detail, see Finet, 2013). It should be noted that these experiments were limited due to sensitivity of the instrument, work place but to verify the optical quality, it will be mandatory to repeat these experiments once again when the ILMT will be installed at site.

6.4 Mylar film experiment

The spiral shaped waves generated due to the relative wind between the air and the mercury layer can be reduced by covering the mirror container with a mylar film.

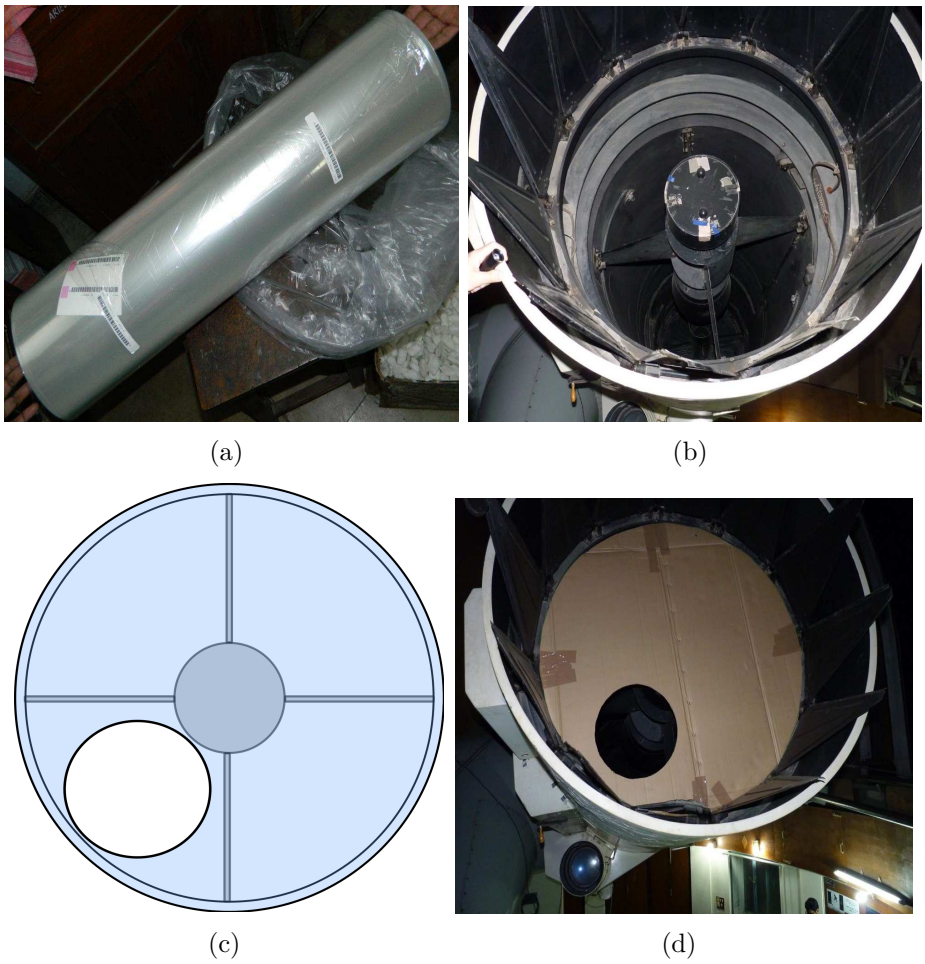

(a) (b) (c) (d)

Figure 6.13: The experimental set-up for the mylar film test. (a) A roll of mylar film to be used to cover the ILMT primary mirror. (b) Top view of the 1.04-m ST after opening the tube flaps, mirror flaps are still closed. All four spiders holding the secondary mirror are also visible. (c) Sketch of the top view: a hole between two spiders is indicated. (d) A brown colour card board covering the entire mirror but with a hole (∼36.0 cm diameter) over which the mylar film was fixed.

A co-moving transparent mylar film covered over the spinning bowl should suppress the friction between the air and the mercury. In this way spiral waves will almost disappear. Furthermore, the mylar film also protects from the expansion of harmful mercury vapors. This technique of mylar covering has already been verified at the large zenithal telescope (Hickson et al., 2007). In the following section we present the experimental set-up to test the optical quality of the mylar film which will be used to cover-up the ILMT container.

6.4.1 Experimental set-up and analysis

The experimental set-up to check the optical quality of the mylar film is shown in Fig. 6.13. We used a 2k × 2k liquid nitrogen cooled CCD camera mounted at the f/13 Cassegrain focus of the 1-m *Sampurnanand Telescope* (ST) at Manora Peak, Nainital. This telescope is operated by the Aryabhatta Research Institute of Observational Sciences (ARIES), India. The CCD chip has square pixels of $24 \times 24\,\mu$m, a plate scale of 0.38 arcsec/pixel and the entire chip covers a field of 13 × 13 arcmin^2 on the sky. The gain and readout noise of the CCD camera are 10 e^-/ADU and 5.3 electrons, respectively.

From the top of the tube flap, the whole mirror was covered with a hard card board of diameter ∼104cm but a hole (∼36cm diameter) was kept open (cf. Fig. 6.13b,c). Then a small sheet of mylar was tightly fixed over this hole (Fig. 6.13c). Three sets of images in *R*-band were collected with the mylar and then three additional images of the same field were obtained without the mylar film. Each frame was exposed for 300sec. To improve the signal-to-noise ratio (S/N), these photometric observations were carried out with a 2×2 binning. The observations were performed by pointing the telescope near the zenith position. Along with the science frames, we also collected flat frames in *R*-band and several bias frames as well. Image alignment and determination of the mean FWHM over all the science frames were performed after the usual bias subtraction, flat fielding and cosmic-ray removal. The standard tasks available in *IRAF* and *DAOPHOT* (Stetson, 1987, 1992) were used for pre-processing and photometry.

To perform the photometry, first we identified 15 isolated and medium brightness stars in the images with and without mylar film. These stars are marked with numbers 1-15 in Fig. 6.14(a,b). Their coordinates were obtained using the *IMEXAM* task in *IRAF*. Then we separately performed *Point Spread Function* (PSF) and aperture photometry both at the same coordinates in all images to verify the consistency in the magnitudes derived with both techniques.

We used the following relation to check the magnitude variation:

$$\mathrm{M_m} - \mathrm{M_{wm}} = -2.5 \log \left(\frac{\mathrm{F_m}}{\mathrm{F_{wm}}} \right) \tag{6.4}$$

$$\text{i.e.} \left(\frac{\mathrm{F_m}}{\mathrm{F_{wm}}} \right) = 10^{-\left(\frac{\mathrm{M_m} - \mathrm{M_{wm}}}{2.5}\right)} \tag{6.5}$$

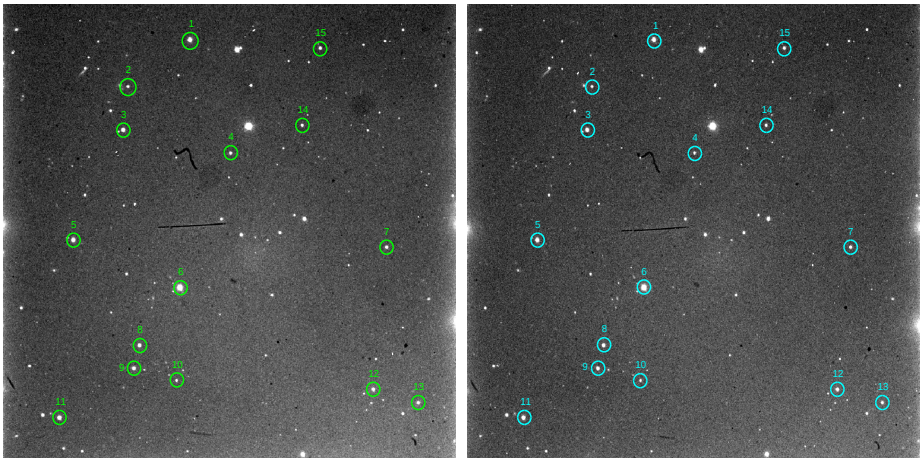

(a) (b)

Figure 6.14: The *R*-band image of the field observed with the 1-m ST, India. Fig. (a) and (b) Images recorded without and with mylar film, respectively. The reference stars (without mylar - green colour; with mylar - cyan colour) used to check the magnitude variation are marked with numbers 1-15.

where M_m and M_{wm} are the magnitudes with and without mylar, respectively. F_m and F_{wm} denote the flux with and without mylar, respectively.

To estimate the ratio of fluxes obtained with and without mylar, first the flux ratio of each of the 15 stars was calculated. Then these were averaged, leading to a mean value of $F_m/F_{wm} = 0.785 \pm 0.012$. This ratio implies that the mylar film is diffusing around 21% ± 1.2% of the incident light. This flux diffusion corresponds to a loss of 0.3 magnitude.

6.5 TDI mode observations and preliminary data reduction

In order to contribute to the data reduction pipeline of the ILMT, we have actively participated to observational campaigns using the 1.3m telescope in Devasthal (2-7 June 2013) and a C-14" telescope in Nainital (29 May – 6 June 2014), both equipped with a SBIG STL-4020M CCD camera operated in the TDI mode. The experimental set-up is shown in Fig. 6.15.

First of all, during each observing run, we have obtained multiple CCD dark frames in the TDI mode, using the same TDI rate and integration time as the real observations, in order to later subtract them from all CCD science frames. In fact,

Figure 6.15: TDI set-up at the 1.3m DFOT and C-14" telescopes. From left to right: SBIG camera installed at the focal plane of both telescopes and zoomed image of the SBIG CCD at the DFOT.

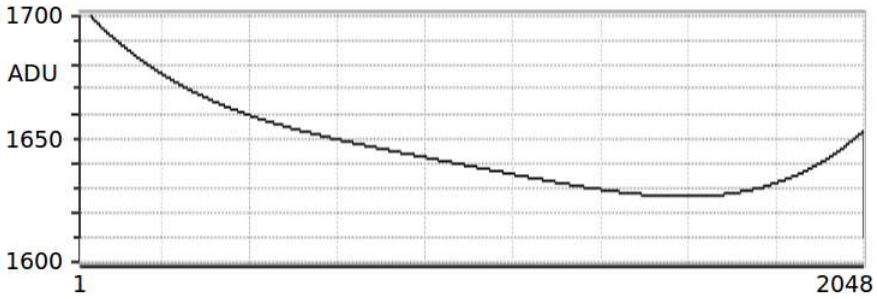

Figure 6.16: Master dark frame: 1-D 4^{th} order polynomial fit of a selected dark frame.

we found out that the dark frames were not uniform. They essentially show a small gradient along the column direction (corresponding to the declination axis). We thus constructed an average image of all the rows of the dark frames, resulting in a 1-D column image which signal could be easily modelled by means of a polynomial. We chose to fit it with a 4^{th} order polynomial (see Fig. 6.16). We subsequently subtracted this 1-D 4^{th} order polynomial (including the bias value), named the master dark frame, from each CCD science frame. While doing so, no additional noise is introduced.

In fact we noticed that it was best to use four different master dark frames pertaining to 4 different groups of observations (G1-G4). It is as if the dark frames could slightly vary depending on the cooling rate of the CCD camera. The G1, G2, G3 and G4 groups correspond to: G1: 29 & 30 May, i' spectral band; G2: 31 May, 1 & 2 June, i' spectral band; G3: 3 June, r' spectral band & 4 June, g' spectral

band; G4: 6 June, i' spectral band, 2014.

From each CCD science frame, we then constructed a flat field frame as follows. First of all, we subtracted from each column of the CCD science frames the corresponding 1-D master dark frame.

Since the observations were taken in the TDI mode, all stellar images were naturally trailed through all the columns of the CCD camera (30000 columns in our case). This means that unlike for the case of classical CCD observations, but alike for the master dark frame, the flat field frame needs to be just one-dimensional. Typically, it was either obtained by taking the median value of each row of the science CCD frames (excluding in this way all stellar objects and other defects like cosmic rays, etc.). We similarly found out that it was even better to take the average value of all individual rows of the science frames after applying a sigma clipping. Considering the CCD frames obtained with the C-14" telescope in May-June 2014, we found out that the best was to adopt a one-sigma clipping and 6 iterations. This led to very nice results (see below).

The 1-D flat field frame is thus obtained using the background sky light of each science frame which exposure time was typically 15 min. It could have been longer but was limited (to 30000 columns) due to the RAM memory of the PC being used to run the *MaxImDL* program when collecting the data in the TDI mode. This ensures that when we shall deal with the photometry of very faint objects observed in the TDI mode with the ILMT, the resulting flat field will be the most appropriate one since the dominating light affecting the faint objects is mainly due to the sky background. Constructing a 1-D flat field from so many columns (typically 30000 in our case during an average exposure time of approximately 15 minutes) ensures a very good S/N ratio for the resulting flat fields.

We then normalized each individual 1-D flat field by their average value.

The G1, G2, G3 and G4 1-D master normalized flat fields were obtained by taking the average of all 1-D normalized flat fields pertaining to each individual science frame integrations belonging to those individual groups (see Fig. 6.17). All resulting 1-D master normalized flat fields look very similar (even when considering the different broadband filters i', g' and r' that were used).

In summary, we recommend at this moment to flat field each science frame using the normalized 1-D flat field obtained from their own sky background. After checking that all those normalized 1-D flat fields are the same, one may of course

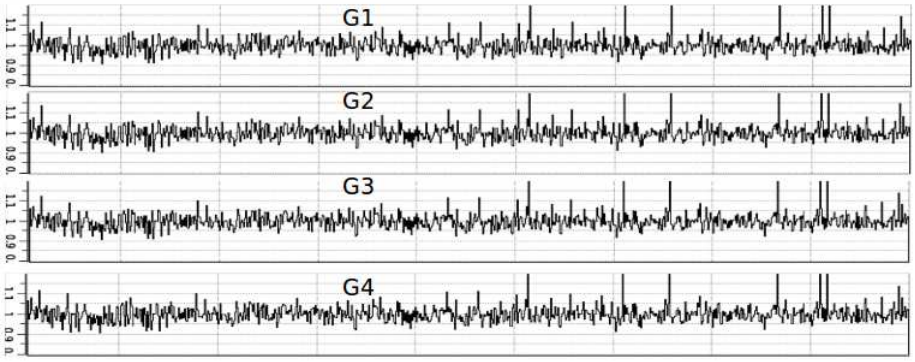

Figure 6.17: Normalized 1-D flat fields for the 4 groups of observations. G1: 29 & 30 May (i'); G2: 31 May, 1 & 2 June (i'); G3: 3 (r') & 4 (g') June: G4: 6 June (i') 2014.

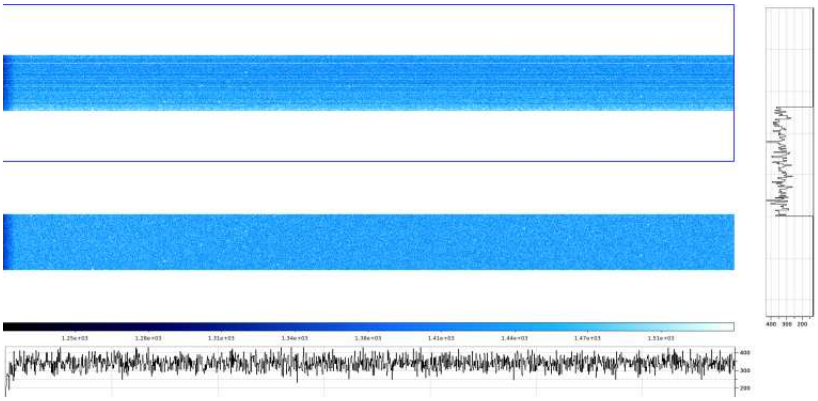

Figure 6.18: Original (up) and flat fielded (down) CCD frame TDI-03-F3790-01-06-2014 recorded in the TDI mode (i' spectral band) with the C-14" telescope on 1^{st} of June 2014. The horizontal and vertical graphs illustrate the flat response along one arbitrarily chosen row and one column of the flat fielded frame.

construct a master flat field out of them and perform a final reduction of all science observations.

An example of raw and flat fielded science frame obtained in the TDI mode with the C-14" telescope equipped with a i' filter is shown in Figs. 6.18 - 6.20. As it can be seen, our proposed way of correcting CCD frames recorded in the TDI mode by means of a 1-D normalized flat field looks very promising.

Photometric and astrometric measurements of objects detected on those reduced frames were later performed using standard *IRAF* applications.

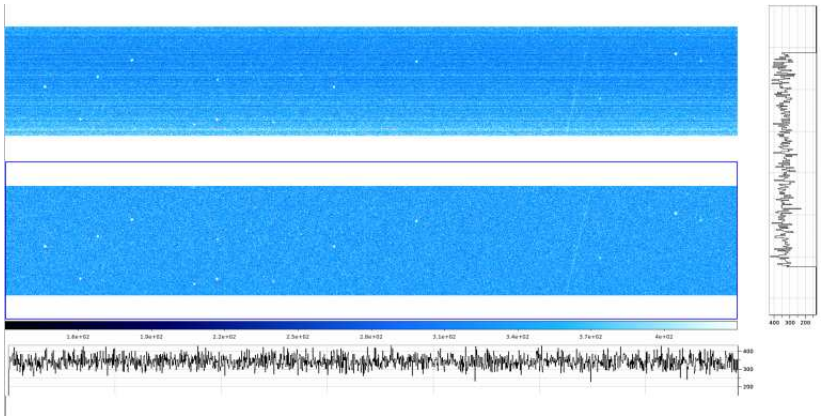

Figure 6.19: Same as Fig. 6.18 after zooming on the central region of the CCD image.

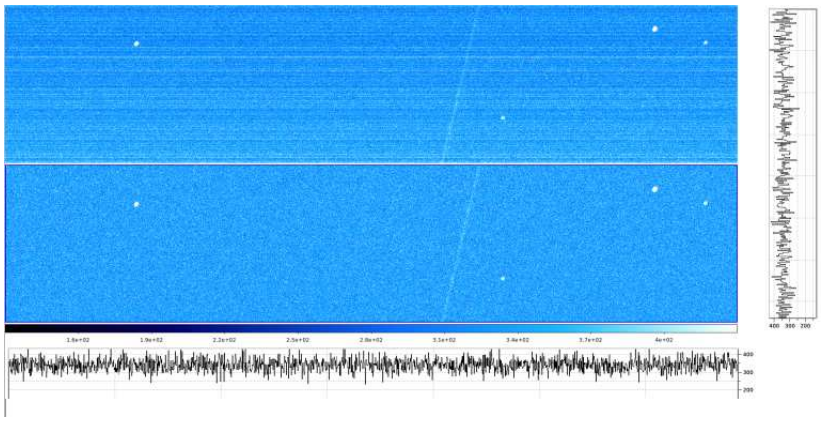

Figure 6.20: Same as Fig. 6.19 after zooming even more on the central region of the CCD image. Some stars are visible as well as a trail due to a space debris.

Chapter 7

Supernovae detection in the 4m ILMT strip

7.1 Introduction

A possible link between the star formation history and the cosmic supernova (SN) rate has been an open question. Madau et al. (1998) estimated that if integrated over all redshifts, the all-sky SN event rate may turn out to be huge, $\simeq$5 – 15 events/sec. It is generally believed that Type Ia SNe originate from intermediate to old population stars whereas core-collapse supernovae (CCSNe, i.e. Type II & Ib/c) result from young and massive stars (Branch et al., 1991). The CCSNe rate is expected to reflect the star-formation rate, increasing with redshift as $(1 + z)^{\beta}$ (for $z \approx 0.5$) where β is in the range 2.5 to 3.9 (see Cucciati et al., 2012; Hopkins, 2004; Hopkins & Beacom, 2006; Le Floc'h et al., 2005; Rujopakarn et al., 2010; Schiminovich et al., 2005). However, the SN Ia rate rise is rather slow with redshift, $\sim(1 + z)^{\beta}$ (see Perrett et al., 2012; Pritchet et al., 2008, and references therein), where β is 2.11 ± 0.28 up to $z \sim 1$. Therefore, the SN rate can be used to study the basic properties of galaxy evolution like mass, star formation history, metallicity and environment, etc.

The astronomical community is deeply interested in understanding the nature of different kinds of SNe and their evolution with redshift (Blanc et al., 2004; Dahlen et al., 2008; Graur et al., 2011, 2014; Okumura et al., 2014, and references therein). The new generation large area survey programs are already contributing with their invaluable data to discover new SNe everyday; like the Sloan Digital

Sky Survey[1] (SDSS), Supernova Cosmology Project[2] (SCP) and intermediate Palomar Transient Factory[3] (iPTF), Supernova Legacy Survey[4] (SNLS), Catalina Real-Time Transient Survey[5] (CRTS), Southern inTermediate Redshift ESO Supernova Search (STRESS), Panoramic Survey Telescope & Rapid Response System[6] (Pan-STARRS) etc. Some upcoming facilities will continue to grow these efforts such as the Large Synoptic Survey Telescope[7] (LSST) and the Zwicky Transient Facility[8] (ZTF), SkyMapper[9] All-Sky Automated Survey for Supernovae[10] (ASAS-SN).

It is notable that despite their great contribution to SN search programs, these kinds of projects are observationally expensive, requiring many hours of valuable telescope time to complete. The Liquid Mirror Telescopes (LMTs) may provide a unique way to overcome some of these issues in a certain fashion. For the SNe study, LMT observations are useful over the generic facilities in several aspects as described below.

- **Unbiased imaging:** Most nearby SNe are discovered by repeated imaging of cataloged galaxies (Filippenko et al., 2001) which introduces a possible bias. But the ILMT will image a same strip of sky without any selection bias.

- **Inexpensive technology:** The cost of building such a mirror (4m diameter) is roughly 1/50 that of building a conventional instrument of the same class (Borra, 2001b, 2003; Poels et al., 2012).

- **Continuous data flow:** There will be no loss of precious observing time as the ILMT will observe continuously during the nights except for bad weather or technical problems. It is expected that during one night it will produce around 10 GB of scientific data (see Surdej et al., 2006).

- **Deeper imaging:** Since each night the same strip of sky will pass over the telescope, we can co-add the consecutive night data to produce deeper images.

[1] http://www.sdss.org/
[2] http://supernova.lbl.gov/
[3] http://www.ptf.caltech.edu/iptf
[4] http://cfht.hawaii.edu/SNLS/
[5] http://crts.caltech.edu/
[6] http://pan-starrs.ifa.hawaii.edu/public/
[7] http://www.lsst.org/lsst/
[8] http://www.ptf.caltech.edu/ztf
[9] http://rsaa.anu.edu.au/research/projects/skymapper-southern-sky-survey
[10] http://www.astronomy.ohio-state.edu/~assassin/index.shtml

In a given cosmic volume, the frequency or rate of these SNe can be measured by counting the number of SNe discovered within a specific region of the sky and dividing it by the time span over which the observations have been made. Fig. 7.1 represents the expected number of SNe events as discussed by Lien & Fields (2009). However, due to observational limits, the local SNe rate is found to be comparatively very less as there are many constraints. For example,

- It requires several years or decades to collect sufficient statistics.
- In order to obtain accurate estimates of the SN rate, it is necessary to know the sample of galaxies which have been searched for SNe, the frequency and the limiting magnitude of the observations and the instruments/techniques which are used for the detection in order to assess the observational biases (see also, Cappellaro et al., 1999).

The International Liquid Mirror Telescope, having a 4m diameter primary mirror and equipped with a modern optical CCD detector, will scan the same strip of sky every night. By co-adding the consecutive night images, the liming magnitude will be increased which will further allow to detect much fainter stellar objects (Surdej et al., 2006). Once a SN like transient will be discovered by the ILMT, the spectroscopic confirmation and further follow-up can be performed using other available facilities (see Sect. 7.4.1). The ILMT observations will be mainly performed with the i' filter (although there are additional filters g' and r'). This will allow us for a maximum number of nights because the spectral range covered by the i' filter is less sensitive to the bright phases of the moon. Initially the ILMT project will be for 5 years which will allow us to collect a large sample of SNe data.

In the past decade, Type Ia SNe have played a crucial role for cosmology. Due to their high luminosity at explosion and their narrow range of observational properties, they are reliably standard candles (see Branch & Miller, 1993; Branch & Tammann, 1992; Saha et al., 1999). These powerful explosions are detectable out to very high redshift and are very useful for the distance determination. In this way, they are generally supposed to constrain the geometry of the universe. However, it is notable that a variation of about 0.2 to 0.4 magnitudes have been found near the light curve (LC) peak in different studies (e.g. Tammann & Leibundgut, 1990; Tammann & Sandage, 1995) of Type Ia SNe which translate into uncertainties of about 10% to 20% in distances.

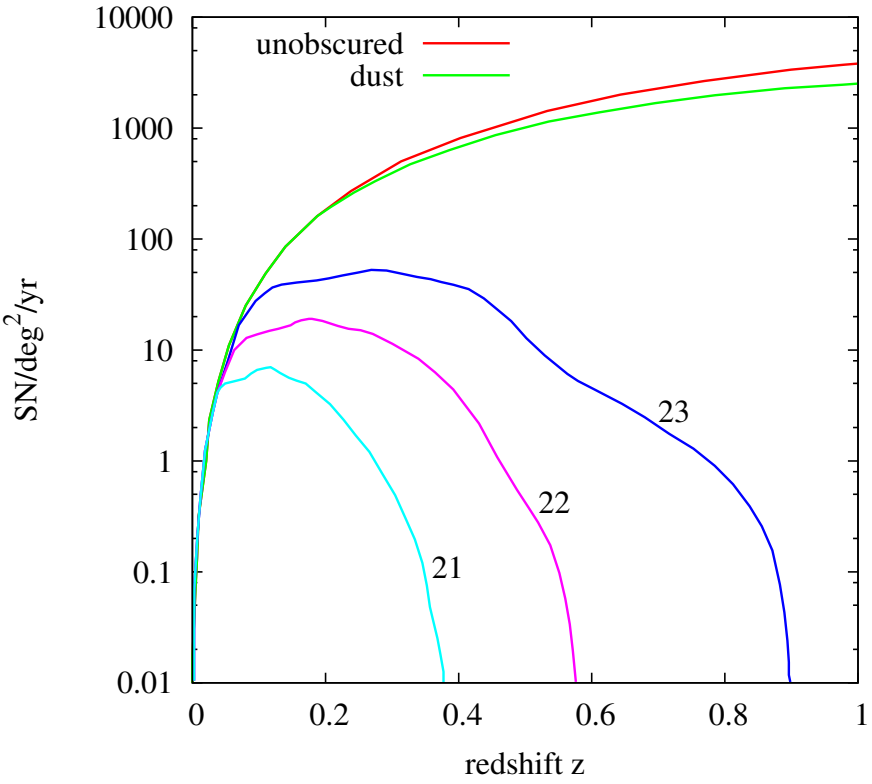

Figure 7.1: The cosmic SN detection rate shown as a function of redshift. The curve "unobscured" ignores all effects (dust extinction, flux limit) and "dust" curve includes dust extinction. The remaining curves are for the SN limiting magnitudes (r-band) 23, 22 and 21 and include dust extinction. Figure reproduced from Lien & Fields (2009).

It is noteworthy to mention that while Type Ia SNe studies have received an enormous attention because of their cosmological importance, there has been relatively less focus on the detection/study of core-collapse supernovae (CCSNe). The properties of CCSNe are found to be diverse in nature. Nonetheless, in a manner similar to that of Ia SNe, Type IIP SNe, a subset of CCSNe have shown to be good "standardizable candles" and potential cosmological probes (Baron et al., 2004; Dessart & Hillier, 2005a; Kirshner & Kwan, 1974). Additionally, CCSNe events are of great importance for cosmology, astrophysics, and particle physics. These events play a crucial role in cosmic energy feedback processes and thus in the formation and evolution of galaxies and of cosmological structure (see Lien & Fields, 2009). The rate of CCSNe is more difficult to measure because the observed CCSNe have shown a magnitude distribution that peaks roughly 1.5 mag fainter than SN Ia and covers a range of more than 5 mag (Richardson et al., 2002) and they have generally

been discovered in diverse types of galaxies.

7.2 Throughput and limiting magnitude of a telescope

The scientific performance of an instrument depends on the maximization of its throughput. The system throughput of an optical telescope (without a detector like CCD) is generally expected to be about ∼60% for imaging mode. The expected counts (N_e) from a star of certain brightness can be estimated considering the transmission coefficients from the mirrors, filters, CCD glass, sky, extinction, quantum efficiency of the CCD chip etc. using the formula given in McLean 1989, see also Mayya (1991):

$$N_e = 3.95 \times 10^{11}\ D^2\ \lambda_n\ \Delta\lambda_n\ F_0^n\ 10^{-0.4m} A_F\ \eta \tag{7.1}$$

where D is the diameter of the telescope, λ_n and $\Delta\lambda_n$ are the effective wavelength and bandwidth of the filters, F_0^n is the flux density from a star of magnitude 0 at the wavelength λ_n above the Earth atmosphere, A_F is the fractional reflecting area of the mirror surface and η is the efficiency of the system.

Assuming that each optical photon will be able to produce a corresponding photoelectron, the full well capacity of the required CCD pixel could be estimated by assuming a certain integration time for a star of a known brightness. Also, if the sky brightness is known, for a given CCD and the parameters like pixel size, dark current, read out noise, we can also calculate the sky counts and the underlying noise.

$$N = \sqrt{(N_e\ e_t + S_e\ e_t\ n_p + D_c\ e_t\ n_p + R_n^2\ n_p)} \tag{7.2}$$

here N_e indicates the number of electrons (per sec), e_t the exposure time (sec), S_e the sky electrons, n_p the number of pixels, D_c the dark current (e^-/pix/sec), R_n the read out noise.

The signal-to-noise ratio can also be calculated for the stars of different brightness (McLean, 1989).

$$Signal/Noise = \left(\frac{N_e \times e_t}{N}\right). \tag{7.3}$$

The CCD readout noise is Gaussian while the star counts, dark counts are Poisson in nature. The aperture to calculate the star light is considered as circular. For the calculations, the FWHM is considered as 1.5 arcsec, nearly equal to the median seeing at Devasthal. The optimal aperture is considered to be 1 × FWHM (see Howell, 1989, 2000).

We can also estimate the corresponding error in the magnitude estimation by knowing the value of the signal-to-noise ratio (Deep et al., 2011).

$$\sigma_{mag} = 2.5 \times log10(1 + 1/(Signal/Noise)). \tag{7.4}$$

Estimation of the ILMT limiting magnitudes

We have estimated the limiting magnitudes of the ILMT for different filters (g', r' and i') using the previous equations. The various parameters used for these estimations are listed in Table 7.1. The limiting magnitudes for different filters are overplotted in Fig. 7.2 with different symbols. It is obvious from this figure that with an exposure time of 102 sec, the limiting magnitudes are ∼21.4, ∼22.2 and ∼22.8 for the i', r' and g' filters, respectively. Furthermore, since during each night the same strip of sky will pass over the telescope, successive night images can be co-added. This will yield longer integration times. Therefore, we have also estimated the limiting magnitudes for 306 sec (3 night images) exposure time, using the same parameters. The estimated magnitude limit improves to ∼22.0, ∼22.8 and ∼23.4 mag for g', r' and i' filters, respectively. The co-addition technique is not limited only for 3 nights but it can also be applied for several night imaging data. Consequently, we may reach still fainter magnitude levels. It is also described in Borra (2001a,b, 2003).

7.3 Area and accessible volume of the ILMT strip

Pointing towards zenith, the ILMT field-of-view (FOV) is centered at the Devasthal observatory latitude which is 29.3611° N. The ILMT FOV is 27' by 27'. As the

Table 7.1: Different parameters used to calculate the ILMT limiting magnitude. See also Finet (2013).

Diameter	4.0m
Fraction of reflecting area	0.95
Reflectivity	0.77
Mylar transmission	0.80
FWHM	1.5"
CCD pixel size	0.4"/pixel
CCD dark noise	0.00083 e^-/pixel/sec
CCD readout noise	5.0 e^-
Wavelength (g', r', i')	4750, 6250, 7630 Å
Wavelength FWHM (g', r', i')	1450, 1500, 1500 Å
Extinction $(\sim g', \sim r', \sim i')$	0.21, 0.13, 0.08 mag
Sky mag $(\sim g', \sim r', \sim i')$	21.3, 20.5, 18.9 mag/arcsec^2
CCD quantum efficiency (g', r', i')	0.70, 0.91, 0.91
Filter transmission (g', r', i')	0.92, 0.95, 0.95

Earth rotates, the ILMT will access a strip of sky. We can estimate the total solid angle $\Omega_{\rm ILMT}$ accessible by the ILMT using the following relation (see Finet, 2013):

$$\Omega_{\rm ILMT} = \int_0^{2\pi} \int_{-\delta}^{+\delta} cos(\delta)\, {\rm d}\delta\, {\rm d}\alpha \tag{7.5}$$

The sky coverage comes out to be 141.2 square degrees. Here α and δ denote the right ascension and declination, respectively in radians. $\delta_\pm = \delta_{\rm ILMT} \pm \Delta_{\rm ILMT}/2$ represent the declinations of the accessible strip borders. $\Delta_{\rm ILMT} = 27$ arcmin.

The area accessible with the ILMT is indicated in Fig. 5.3. It should be noted that considering the site advantage, out of 141.2 square degrees of sky, ∼72 square degrees will belong to high galactic latitude ($|{\rm b}| > 30°$). In this high galactic region detection of fainter and more distant objects (e.g. SNe, galaxies, quasars,...) will be possible (see Finet, 2013; Magette, 2010; Surdej et al., 2006).

For different redshifts, we calculated the volume of sky expected to be covered by the ILMT using the formula given in Taylor et al. (2014, see eq. 7).

$$V = \frac{1}{3}\Delta\theta\Delta\phi(D_{z2}^3 - D_{z1}^3) \tag{7.6}$$

where D_{z1} and D_{z2} are the co-moving distances at redshift z_1 and z_2, respectively. $\Delta\theta$ is the declination range (0.45°) and $\Delta\phi$ is the right ascension (R.A.) range –50°

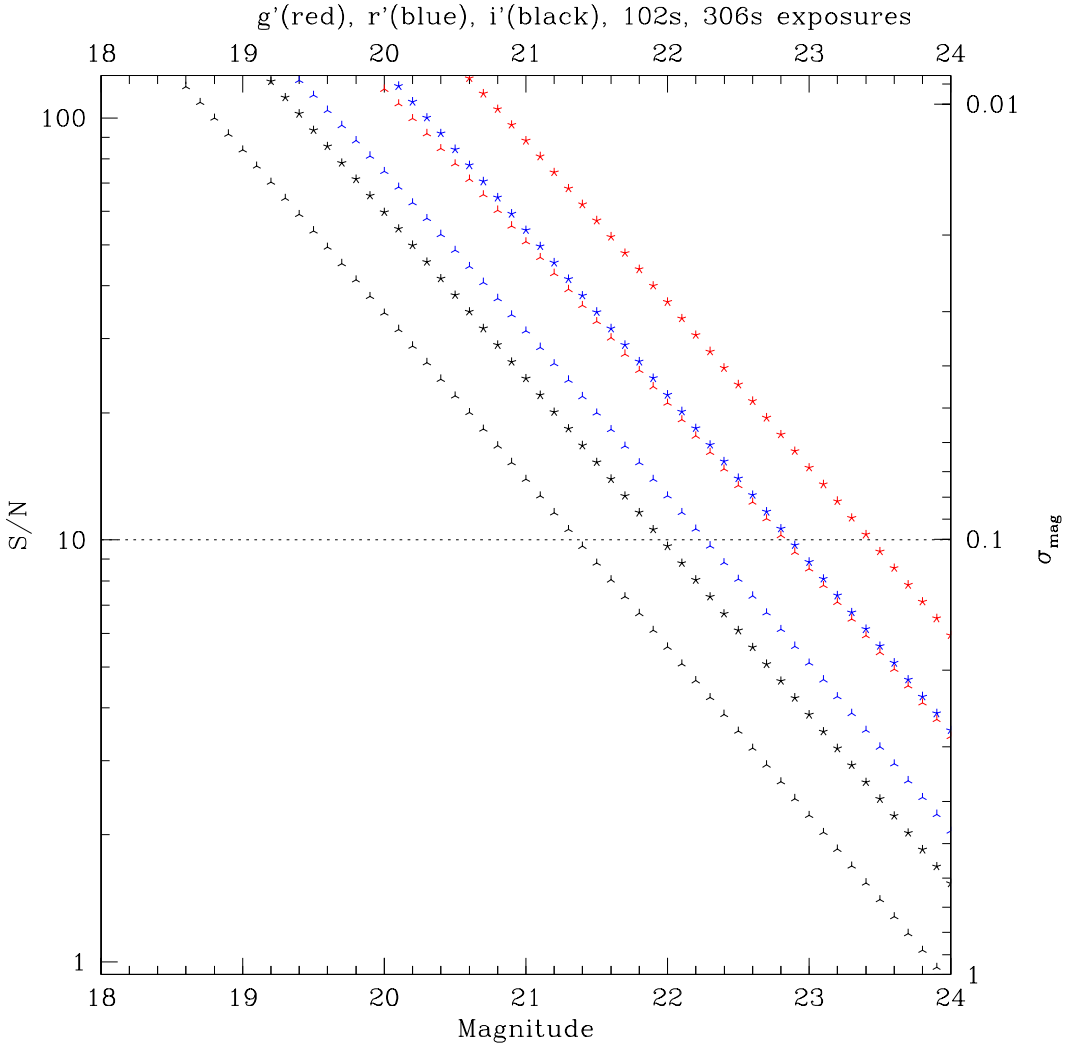

Figure 7.2: A plot showing the ILMT limiting magnitudes for the g', r' and i' filters. The parameters to estimate these values are discussed in Sect. 7.2. The X-axis represents the magnitude and the Y-axis represents the signal-to-noise ratio and the corresponding error in magnitude. In this plot, the results for the three filters i.e. g' (in red), r' (in blue) and i' (in black) have been reproduced for the exposure of a single scan (i.e. 102 sec) and three scans (i.e. 306 sec). Around 0.5 mag is gained once we stage images taken on three nights in any single filter.

to 50°. It should be highlighted that here we considered the average R.A. as nights will be of longer duration in winters (i.e. observing time is longer) but shorter duration in summers (i.e. observing time is shorter). The estimated volumes for different redshifts are listed in Table 7.2.

Table 7.2: Volume of the sky for different redshifts.

z range	volume (Mpc^3)
0.03 – 0.09	2.35×10^5
0.03 – 0.40	1.69×10^7

7.4 Estimation of the supernova rate

There are several studies of supernova rate available in the literature. It belongs to both kinds of SNe i.e. thermonuclear (type Ia) and core-collapse (type II, Ib/c). Some of the recent Type Ia SN rate studies can be found in Bazin et al. 2009; Blanc et al. 2004; Botticella et al. 2008; Dahlen et al. 2008, 2004; Dilday et al. 2008; Graur et al. 2011, 2014; Hardin et al. 2000; Horesh et al. 2008; Kuznetsova et al. 2008; Neill et al. 2006; Okumura et al. 2014; Pain et al. 2002; Perrett et al. 2012; Poznanski et al. 2007b, and references therein.

At low reshift (z ∼0.3), rates of SNe Ia have been measured by STRESS (Botticella et al., 2008), SDSS II (Dilday et al., 2010) and LOSS[1] (Li et al., 2011). The Ia rates from SNLS (Neill et al., 2006) at $z \sim 0.5$ are based on a large number of SNe consisting of a sample of 73 spectroscopically verified SNe. In the same survey program, Perrett et al. (2012) measured the SN Ia rate over the redshift range of 0.1 $\leq z \leq$ 1.1 using 286 spectroscopically confirmed and 400 photometrically identified SNe Ia. Similarly from the IfA Deep Survey, Rodney & Tonry (2010) reported their rate up to $z = 1.05$.

Some recent surveys have shown even higher redshift studies. Graur et al. (2011) derived the SN Ia rate up to z ∼ 2.0 using 150 SNe from a SN survey in the Subaru Deep Field. Furthermore, Graur et al. (2014) measured SN Ia rates in the redshift range $1.8 < z < 2.4$. These results show consistent results with the rates measured by the HST/GOODS[2] and Subaru Deep Field SN surveys. Recently, Okumura et al. (2014) have measured the SN Ia rate over the redshift range $0.2 \lesssim z \lesssim 1.4$ using 39 SNe from the data set of the Subaru/XMM-Newton Deep Survey. Up to a redshift of ∼2.5, Rodney et al. (2014) presented these rates using 24 Ia SNe in the Cosmic Assembly Near-infrared Deep Extragalactic Legacy Survey (CANDELS) program with the Hubble Space Telescope.

[1]Lick Observatory Supernova Search (Filippenko et al., 2001).
[2]Great Observatories Origins Deep Survey (Giavalisco et al., 2004).

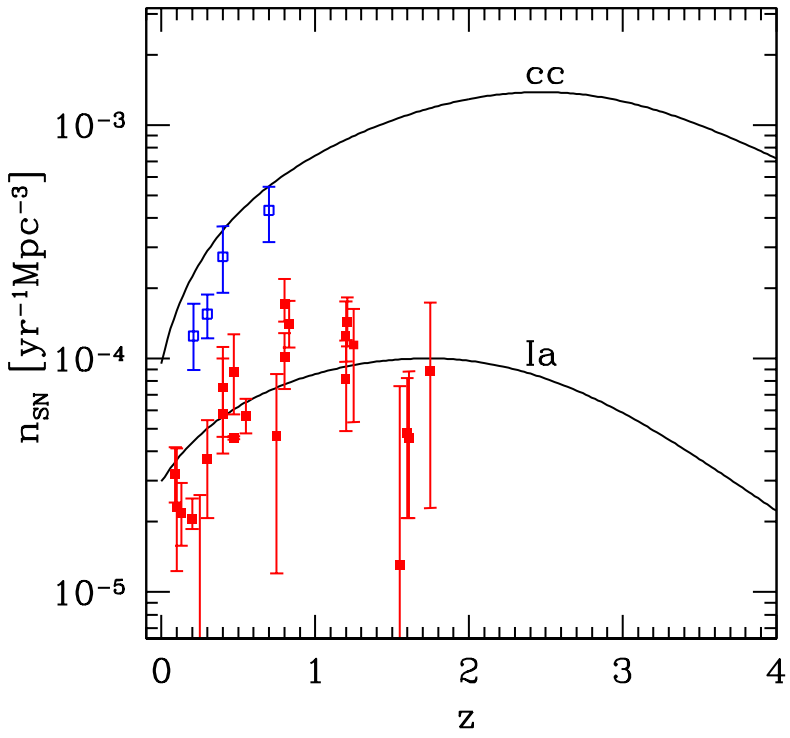

Figure 7.3: Evolution of the SN rate with the redshift (z) for CCSNe and Type Ia. The continuous curves indicate the modelled SNe rate from Oguri & Marshall (2010). Open squares are from recent CCSNe studies of Bazin et al. (2009); Botticella et al. (2008); Dahlen et al. (2004) and the filled squares represent Type Ia studies from Blanc et al. (2004); Botticella et al. (2008); Dahlen et al. (2008, 2004); Dilday et al. (2008); Hardin et al. (2000); Horesh et al. (2008); Kuznetsova et al. (2008); Neill et al. (2006); Pain et al. (2002); Poznanski et al. (2007b). Figure taken from Oguri & Marshall (2010).

Core collapse SNe are harder to find, being intrinsically fainter than Ia and more subject to the host galaxy extinction. Also, these SNe were found less interesting in terms of cosmological implications than SNe Ia. Therefore, fewer rate measurements have been reported for Core collapse SNe events. At low redshift the rates determined by the LOSS survey (Li et al., 2011) provide a rate estimate, which was found to be similar to the CCSNe rate measurement of Cappellaro et al. (1999). At a moderately higher redshift (∼0.3), CCSNe rates have been studied in the survey of STRESS (Botticella et al., 2008) and SNLS (Bazin et al., 2009). The GOODS survey CCSNe rate has been presented in Dahlen et al. (2004) which is up to redshift 0.7. Recently Taylor et al. (2014) presented a study based upon a sample of 89 CCSNe events from the SDSS II survey and found results similar to the previous studies. Fig. 7.3 represents the SNe rate measured in various studies.

Table 7.3: Predicted SNe Ia discovery rates for different redshifts. These numbers are estimated for a 4m diameter LMT similar to the ILMT.

z	events/year
0.2	500
0.4	1000
0.6	1500
0.8	1900
1.0	2000

Borra (2001a,b, 2003) has described the cosmological implications of SNe study in the framework of liquid mirror telescopes. He has estimated the number of SNe for a strip of sky using the expected rate of SNe given in Pain et al. (1996). Table 7.3 lists the expected SNe Ia rate with redshift for a magnitude limit of ∼22 in R band. Lien & Fields (2009) estimated the potential core collapse SNe events for different synoptic surveys (see their Table 2). If we consider similar magnitude limits and the detection efficiency in case of ILMT, we may expect around 160 CCSNe events each year. We carefully mention that these numbers are very crude and a large variation in SNe numbers may be found during real observations.

7.4.1 Supernovae observations with the ILMT and follow-up scheme

Since the ILMT will work in a continuous data acquisition mode by looking only towards zenith, once a patch of sky has passed over its FOV, it cannot be observed again during the same night. Therefore, a collaborative observation will be helpful for the study of transients like SNe. Thanks to the ARIES observational facilities which presently host the 1.04m and 1.30m optical telescopes and the upcoming 3.6m telescope. A guaranteed-time allocation strategy to follow-up newly discovered objects will fulfil our needs, specially in case of any transient such as SN discovery.

One of the major goals of the ILMT is the detection of transients[1] and variable sources. To consistently find these objects above a certain signal-to-noise level, the detection of sources in images is normally not done manually but using specialized computer codes. For the source detection in the ILMT images an automated realtime data reduction pipeline will be applied.

[1]Those astronomical events, which can be observed during a short duration (seconds to some days e.g. gamma ray bursts, supernovae etc.) and then they disappear.

Typically there are two ways for transient detection i.e. comparison with a catalog and image subtraction (see also Schmidt, 2012). The catalog method is good where very high precision is required, but it results in poor detection efficiency near the detection threshold, or in crowded regions. Using the image subtraction method, images are matched to a template and the template subtracted. The later method is more computationally demanding and has poorer absolute precision, but leads to a much better transient detection efficiency across a survey.

In the process of extracting SNe, knowing their redshifts, identifying their types, there are numerous challenges (Blondin & Tonry, 2007; Dahlen & Goobar, 2002; Kim & Miquel, 2007; Kunz et al., 2007; Wang, 2007). Additionally, there may be a significant level of contamination by other stellar objects (see also Sect. 7.4.1.3), for example, Active Galactic Nuclei (AGN[1]). AGNs can be extremely luminous and appear as point sources in imaging surveys. Additionally, they are situated in the center of their host galaxies and may show optical variability (e.g. Stalin et al., 2004). In a study of the local SN rate, Cappellaro et al. (2005) found a large number of AGNs situated in the center of their host galaxies. It is possible that they may be mis-identified as SNe in surveys without spectra and with short observation periods.

SN identification and classification require monitoring of the light curve. Therefore, it is important to observe them near peak brightness and also follow up it later. It is very important to detect a SN at its early phase of explosion as some of the CCSNe are expected to emit a short burst of high energy (soft γ-rays, X-ray, see Nakar & Sari, 2010) radiation at the moment of shock breakout, which should last not more than $\sim$15 minutes. Thereafter, the cooling will bring the emission into the UV-optical range, which is very important to detect. This phase should last at most a few hours, typically less than a day. A cadence of a few hours per field would thus allow to systematically detect the shock breakout cooling tail of such SNe. These early observations will be crucial to derive the progenitor radius with a good precision (see e.g. Bersten et al., 2011, 2012, 2013; Taddia et al., 2014).

However, since the filter system of the ILMT is limited, it will not be sufficient enough to measure the colour, light curve information. Furthermore, to examine the spectral features of transients, a spectrum will be required. Therefore, larger aperture size traditional mirror telescopes will be needed as complementary to the ILMT observations. In Fig. 7.4, a proposed processing data flow is illustrated and described below.

[1]These are super-massive black holes in the center of galaxies (Salpeter, 1964; Shields, 1978)

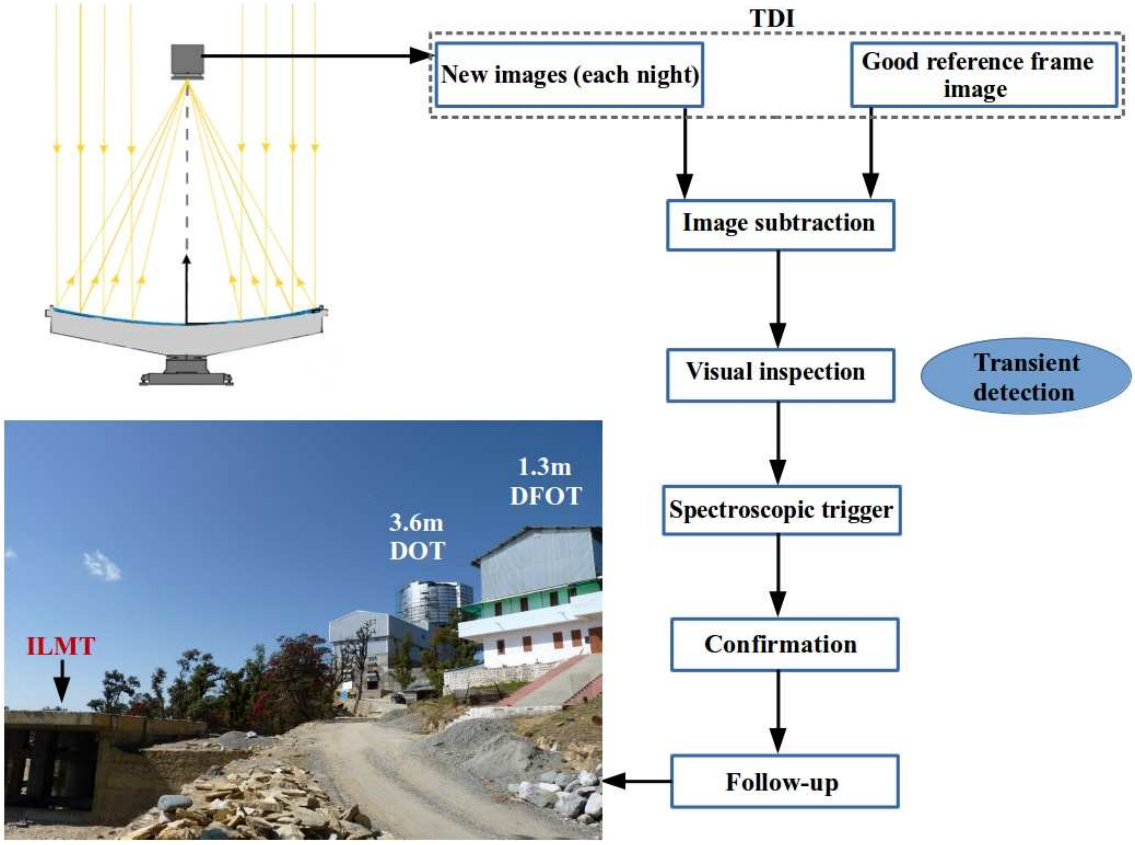

Figure 7.4: Illustration of the proposed processing data flow for SNe detection and follow-up scheme. Upper left is a sketch of the ILMT and lower left: images of the 3.6m and 1.3m optical telescopes and ILMT are indicated.

7.4.1.1 TDI mode imaging

As we explained previously, the ILMT will work in the TDI (Time Delay Integration) mode. There are several advantages to work in this mode. As the Earth rotates, the passing stars over the zenith can be imaged continuously. At the end of the night a single long image of the strip of the sky is produced. Although a single integration time is imposed however, as the same strip of sky is observed night after night, these observations can be co-added to increase the limiting magnitude. Additionally, TDI imaging also provides an easy and robust way of data reduction. While in conventional imaging, the sensitivity irregularities of the CCD sensors are corrected by using a two dimensional flat, in TDI mode observations, as the objects go all across the detector along the sensor row, the sensitivity irregularities are averaged over the detector rows. Consequently, the image reduction is done by dividing each column by a one-dimensional flat field. Furthermore, this flat field

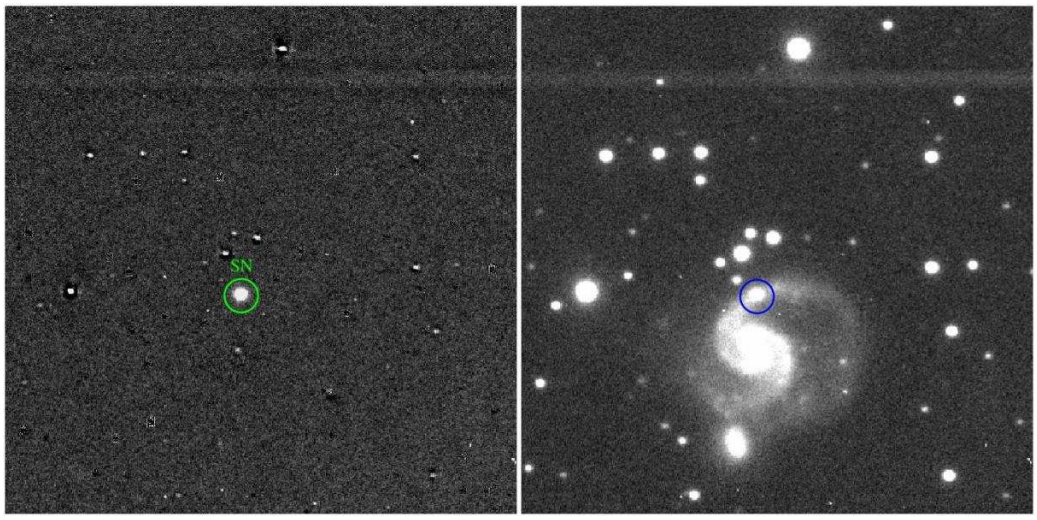

Figure 7.5: Image subtraction. Right panel: Galaxy UGC 01626 image with SN 2011fu. The SN can be seen in one of the spiral arms indicated by a circle. Left panel: Subtracted image where the SN is clearly visible without galaxy contamination.

can be directly estimated from the scientific data, contrary to what is done during conventional imaging where flat field images must be taken before and/or after scientific imaging. In this way precious telescope time is saved.

7.4.1.2 Image subtraction

Discovering a SN is not an easy task as in most cases the SN light will be a small part of light measured from the galaxy. Furthermore, for high redshift galaxies, the galaxies themselves will not be fully resolved by ground based observations so a SN will be even less distinct and can be easily missed when looking in the individual search epoch images.

However, in case of the ILMT since the same strip of sky will pass over the telescope each night, observations will be performed under the best seeing conditions by looking at the zenith during each clear night. Then previous night images or a good reference image will be subtracted from the search night images using the *Optimal Image Subtraction* (OIS) technique presented in Alard & Lupton (1998) and further refined in Alard (ISIS, 2000). This method of image subtraction has already been used to detect SNe in many projects (e.g. Botticella et al., 2008; Cappellaro et al., 2005; Poznanski et al., 2007b; Wood-Vasey et al., 2007). In Fig. 7.5, we demonstrate one example of the image subtraction technique.

7.4.1.3 Transient detection and possible contamination

The subtracted images may consist of astrophysical and non-astrophysical sources. However, it has been found that in other transient surveys which use image subtraction techniques, that non-astrophysical sources always engulf the real sources (e.g. Bloom et al., 2012; Brink et al., 2013). Non-astrophysical sources include cosmic rays that are not removed by cosmic ray removal software, extended features around very bright saturated stars, and bad subtractions due to a mis-alignment of the images. To remove these false detections, we must exclude the sources around the bright, saturated stars and at the edges of the images.

Variable stars, quasars, active galaxies and moving objects also contaminate the data. We can cross-match the detected object catalog with quasar and AGN catalogs (Pâris et al., 2014; Véron-Cetty & Véron, 2010). Variable stars can be verified from SIMBAD[1]. The proper motion of asteroids is larger so they will show significant variation in their position and can be removed easily. Furthermore, the solar system objects can be checked from the Minor Planet Checker[2].

7.4.1.4 Further observations

The light curves, the absolute luminosity and the colour evolution of SNe have provided major insights into the supernova phenomenon. Furthermore, the temporal evolution of the energy release by the SNe is one of the major sources of information about the nature of these events. Therefore, obtaining multi-band light curve observations is very important. Through light curves it has been possible to distinguish between progenitor models, infer some aspects of the progenitor evolution, measure the power sources, detail the explosion models, and probe the local environment of the supernova explosions (Leibundgut & Suntzeff, 2003). The spectrum of a supernova contains a wealth of information about the composition and distribution of elements in the exploding star. It also contains information on its redshift and age (defined as the number of days from maximum light in a given filter). It is very important to launch follow-up (photometric and spectroscopic) observations right after the discovery of any transient.

[1] http://simbad.u-strasbg.fr/simbad/
[2] http://scully.cfa.harvard.edu/cgi-bin/checkmp.cgi

Detection of the supernovae candidates

It should be highlighted that in general the classification of supernovae is done by inspecting the spectra and checking the presence of emission lines. But supernovae, especially at high redshift, may be too faint for the spectroscopy, even with the largest class telescopes currently available and in many cases the supernova spectrum is contaminated by the host galaxy light. Furthermore, with the increasing number of survey programs, the followup spectroscopy will not be possible/practical for all transients detected in these surveys. At the same time unless we confirm that whether a particular event is a core collapse SN or Type Ia, the scientific usefulness will be affected.

Therefore, in response to this need, many techniques targeted at SNe photometric classification have been developed which are mostly based on some form of template fitting. These include the methods of Falck et al. (2010); Gong et al. (2010); Johnson & Crotts (2006); Kunz et al. (2007); Kuznetsova & Connolly (2007); Poznanski et al. (2002, 2007a); Rodney & Tonry (2009); Sullivan et al. (2006). In each of these approaches, typically the light curves in different filters for the SN under consideration are compared with those from SNe whose types are well established. Usually, composite templates are constructed for each class, using the observed light curves of a number of well-studied, high signal-to-noise ratio SNe (see Nugent et al., 2002). Some of these light curve fitting models are SALT[1] (Guy et al., 2007, 2005), MLCS/MLCS2k2[2] (Jha et al., 2007; Riess et al., 1995, 1996) and SiFTO (Conley et al., 2008).

For the classification of SNe, Poznanski et al. (2002) presented a method using multicolour broadband photometry. Their study is based upon the general assumption that SNe Ic are redder compared to SNe Ia at a similar redshift (Riess et al., 2001). They found that although rising (pre-maximum) SNe Ic have colours similar to those of older ($\sim$2 weeks past maximum) SNe Ia but near the peak brightness, SNe Ia are typically 0.5 mag bluer in the $r-i$ colour than SNe Ic. Dahlen & Goobar (2002) and Johnson & Crotts (2006) also demonstrated similar type determination methods based on colour cuts and colour evolution.

The beauty of ILMT imaging is its ability to observe at the zenith i.e. under the best seeing conditions. Since the same strip of sky will pass over the telescope each night, once a supernova will be discovered in one night image, eventually the

[1]spectral adaptive light curve template
[2]multicolour light-curve shape

same field will be observed again during the next nights. In this way a very good sampling of data will be achieved to finally produce good sampled light curves in different filters. If the ILMT observations could be performed in at least two filters each night, the colour information or template fitting technique could be very much useful to identify the supernova candidates for further followup.

Although a major drawback of the light curve fitting method is that its typing determination is less accurate than the spectral method, it is much easier to obtain photometry and construct light curves of faint SNe at high redshift in comparison to obtaining spectra (see Melinder, 2011).

Spectroscopic trigger

Followup spectroscopy of a subset of events will be essential to calibrate the accuracy of the photometric typing (and host redshifts). In particular, spectroscopy will be invaluable in identifying and quantifying catastrophic failures in the typing algorithms; on the basis of these it may be possible to refine the routines. As SNe are random events i.e. there is no advance knowledge of where they will occur. Therefore, it is not easy to obtain observing time in advance as in general the time allocation is allotted on the basis of research proposals written about more than six months in advance. Over that successful proposals are granted only a few nights in a semester on bigger telescopes. Thanks to the upcoming 3.6m DOT telescope situated near the ILMT site, it can be triggered in the target of opportunity observation mode in case of any transient like a SN is detected. Additionally, we can collaborate with other existing facilities in India and world wide.

Confirmation

The individual emission/absorption lines in the spectra provide information about the progenitor system and the new elements created in the explosion. Since the classification of SNe is based on their optical spectra around maximum light (for a review see Filippenko, 1997), therefore, for a rapid confirmation we can use available SN classification codes e.g. GELATO[1] and/or SNID[2]. The SNID tool is developed to determine the type, redshift, and age of a SN, using a single spectrum. The algorithm is based on the correlation techniques of Tonry & Davis (1979) and relies on the comparison of an input spectrum with a database of high-S/N template

[1]GEneric cLAssification TOol https://gelato.tng.iac.es/
[2]Supernova Identification http://people.lam.fr/blondin.stephane/software/snid/

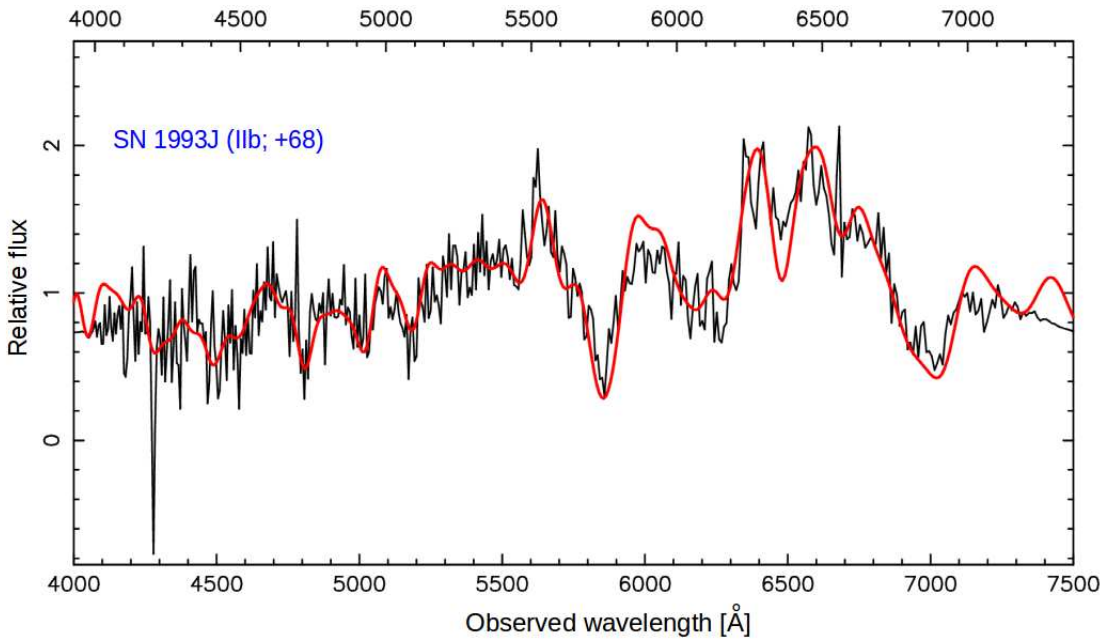

Figure 7.6: Demonstration of the spectra identification with the SNID code. The flux is in arbitrary units. Observed and template spectra are shown with black and red, respectively. The best fitted template is SN 1993J (shown in the top left, blue characters with the estimated phase (+68) relative to the light maximum).

spectra (for more detail see Blondin & Tonry, 2007). Furthermore, GELATO is a online software for objective classification of SN spectra. Similar to SNID, it performs an automatic comparison of a given (input) spectrum with a set of well-studied SN spectra (templates), in order to find the template spectrum that is most similar to the given one. The GELATO algorithm is presented in Harutyunyan et al. (2008).

Follow-up

Presently there are three optical telescopes existing at ARIES (Fig. 7.7). The 1.04m Sampurnanad telescope (ST) and 0.5m Schmidt telescope are situated at Manora peak. Both telescopes are equipped with modern CCD detectors. There is another optical telescope of 1.3m diameter, the Devasthal Fast Optical Telescope (DFOT) which has been recently installed at the Devasthal observatory (Sagar et al., 2013, 2012). The upcoming 3.6m diameter Devasthal Optical Telescope (DOT, Fig. 7.7: lower right panel) facility is expected to be installed in 2015. Since there are multiple observation facilities available at ARIES, our plan is to quickly trigger these facilities once a transient candidate existence is confirmed on the ILMT images. Up to the

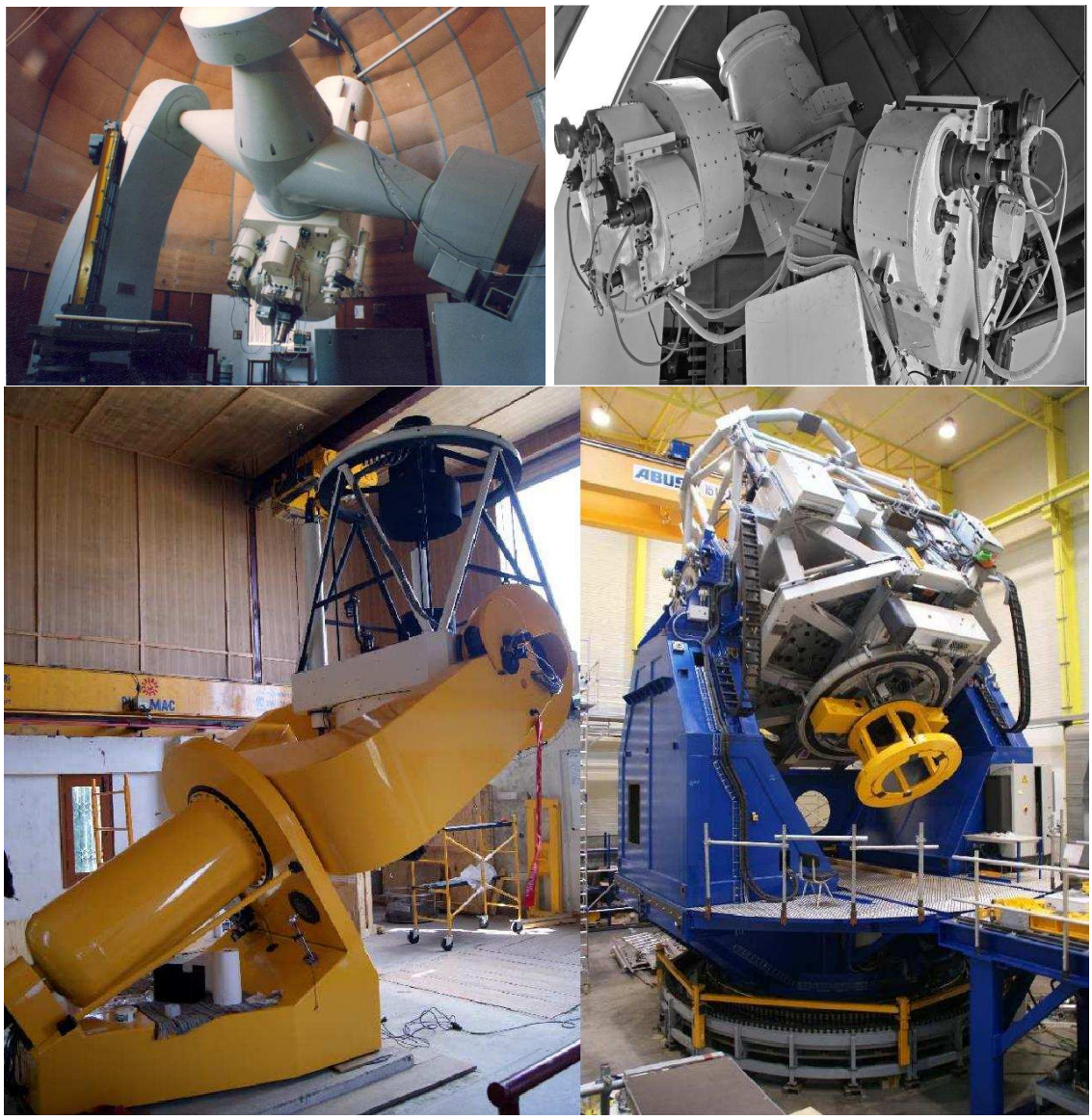

Figure 7.7: Present and upcoming facilities at ARIES, Manora peak and Devasthal observatories. Top left and right panels: 1.04m ST and 0.5m Schmidt telescope, respectively. Bottom left and right panels are the images of the 1.3m DFOT and upcoming 3.6m DOT telescopes, respectively. These facilities will be used for the followup observations of the ILMT detected SNe and other transient events for photometry and/or spectroscopy.

bright phase (∼19 magnitude) of SN , photometric observations will be performed with different filters using small aperture telescopes and when it will become fainter larger aperture telescopes (1.3m and 3.6m) will be utilized. However, spectroscopic observations will be performed with the 3.6m DOT and other larger telescopes in India and/or abroad.

7.5 Summary

We have presented the plans of SNe observations with the ILMT along with an operational strategy and follow-up scheme. The ILMT survey will play an important role is SNe detection with precise and unbiased imaging of a strip of sky at Devasthal. During each night, the typical ILMT limiting magnitudes are 22.8, 22.2 and 21.4 mag in g', r' and i' filters which can be obtained even deeper if we co-add the successive night images. The multi-band and well sampled observations will enable photometric type determination (by template fitting, colour information) of SNe more accurately. Because of the tight link between SNe and star formation, the ILMT with complementary observations and along with other sky surveys may provide better measurements of the moderate red-shift history of the cosmic star-formation rate.

Furthermore, the ILMT will provide an untargeted search with plentiful anonymous galaxies in each night images, which may allow us to construct a SN sample without host-galaxy biases. By knowing the cosmic SN rate more precisely, the cosmological uncertainties in the study of the wealth of observable properties of the cosmic SN populations and their evolution with environment and redshift can be removed. We are expecting to detect hundreds of Type Ia as well as core-collapse SNe thanks to the ILMT survey over one year. New SNe discoveries and their light curves could improve our knowledge on a variety of problems including cosmology and SN physics.

Part IV

Conclusions and future prospects

Chapter 8

Conclusions and future prospects

This thesis is mainly based upon photometric and spectroscopic observations of core-collapse supernovae (CCSNe), massive stars and activities related to the construction and installation work of the 4m International Liquid Mirror Telescope (ILMT) project. In addition to the photometric and spectroscopic observations, we also performed polarimetric observations of a supernova to understand the effects of the explosion from these highly energetic events on the ejected material.

The organization of this thesis is distributed into four parts having eight Chapters. **Part I** gives a brief introduction about the massive stars and their evolution. We briefly described various types of SNe along with their photometric, spectroscopic and polarimetric properties. Finally, we present the technological advancement of liquid mirror telescopes and discussed their role in the context of the present era of large astronomical telescopes.

In **Part II** "Study of supernovae and massive stars", there are three Chapters. We investigate the stellar content in the western part of the Carina nebula in Chapter 2. The light curve and spectral properties of Type IIb SN 2011fu and broad band polarimetric analysis of Type IIP SN 2012aw are presented in Chapters 3 and 4, respectively.

The low obscuration and proximity of the Carina nebula make it an ideal place to study the ongoing star formation process and impact of massive stars on low-mass stars in their surroundings. To investigate this process, we generated a new catalog of the pre-main-sequence (PMS) stars in the Carina west (CrW) region and studied their nature and spatial distribution. We also determined various parameters (reddening, reddening law, age, mass), which are used further to estimate the initial mass function (IMF) and K-band luminosity function (KLF) for the region under study.

8. CONCLUSIONS AND FUTURE PROSPECTS

We obtained deep *UBVRI* $H\alpha$ photometric data of the field situated to the west of the main Carina nebula and centered on WR 22. Medium-resolution optical spectroscopy of a subsample of X-ray selected objects along with archival data sets from *Chandra*, *XMM-Newton* and 2MASS surveys were used for the present study. Different sets of colour-colour and colour-magnitude diagrams are used to determine reddening for the region and to identify young stellar objects (YSOs) and estimate their age and mass.

Our spectroscopic results indicate that the majority of the X-ray sources are late spectral type stars. The region shows a large amount of differential reddening with minimum and maximum values of $E(B-V)$ as 0.25 and 1.1 mag, respectively. Our analysis reveals that the total-to-selective absorption ratio R_V is $\sim$3.7 $\pm$ 0.1, suggesting an abnormal grain size in the observed region. We identified 467 YSO candidates and studied their characteristics. The ages and masses of the 241 optically identified YSOs range from $\sim$0.1 to 10 Myr and $\sim$0.3 to 4.8 $M_\odot$, respectively. However, the majority of them are younger than 1 Myr and have masses below 2 $M_\odot$.

The high mass star WR 22 does not seem to have contributed to the formation of YSOs in the CrW region. The initial mass function slope, Γ, in this region is found to be -1.13 ± 0.20 in the mass range of $0.5 < M/M_\odot < 4.8$. The K-band luminosity function slope (α) is estimated as 0.31 ± 0.01. We also performed minimum spanning tree analysis of the YSOs in this region, which reveals that there are at least ten YSO cores associated with the molecular cloud, and that leads to an average core radius of 0.43 pc and a median branch length of 0.28 pc.

In Chapter 3, we have presented low-resolution spectroscopic and *UBVRI* broadband photometric investigations of the Type IIb supernova (SN) 2011fu, discovered in the galaxy UGC 01626. The photometric follow-up of this event was initiated within a few days after the explosion and covers a period of about 175 days. The early-phase light curve shows a rise followed by a steep decay in all bands, and shares properties very similar to those seen for SN 1993J, with a possible detection of the adiabatic cooling phase. Modelling of the quasi-bolometric light curve suggests that the progenitor had an extended ($\sim 1 \times 10^{13}$ cm), low-mass ($\sim 0.1\ M_\odot$) H-rich envelope on top of a dense, compact ($\sim 2 \times 10^{11}$ cm), more massive ($\sim 1.1\ M_\odot$) He-rich core. The nickel mass synthesized during the explosion was found to be $\sim$ 0.21 $M_\odot$, slightly larger than that seen for the other Type IIb SNe. The spectral modelling performed with `SYNOW` suggests that the early-phase line velocities of the H

and Fe II features were $\sim$ 16000 km s^{-1} and $\sim$ 14000 km s^{-1}, respectively. Then, the velocities declined up to day +40 (after the explosion) and became nearly constant at later epochs.

We have studied the polarimetric properties of the nearby ($\sim$10 Mpc) Type II-plateau SN 2012aw. Our analysis and results are presented in Chapter 4 which is based upon the R-band polarimetric follow-up observations of this object. Starting from $\sim$10 days after the SN explosion, these polarimetric observations cover $\sim$90 days (during the plateau phase) and are distributed over nine epochs. To characterize the Milky Way interstellar polarization (ISP_{MW}), we have observed 14 field stars lying within a radius of 10° around the SN. We have also tried to subtract the host galaxy dust polarization component assuming that the dust properties in the host galaxy are similar to those observed for Galactic dust and the general magnetic field follows the large scale structure of the spiral arms of the galaxy.

After correcting for the ISP_{MW}, our analysis infers that SN 2012aw has a maximum polarization of 0.85% $\pm$ 0.08% and that the polarization angle does not show much variation with a weighted mean value of $\sim$138°. However, if both the ISP_{MW} and host galaxy polarization components are subtracted from the observed polarization values of the SN, the maximum polarization of the SN becomes 0.68% $\pm$ 0.08%. The distribution of the Q and U parameters appears to follow a loop like structure. The evolution of the polarimetric light curve properties of this event is also compared with other well studied core-collapse supernovae of similar type.

In **Part III**, we present our large efforts to make the liquid mirror technology useful for the astronomical observations in the Northern hemisphere and in India for the first time. We performed various experiments in the framework of building the International Liquid Mirror Telescope. With a very simple structure, combined with a CCD camera and an optical corrector, the ILMT will work in the time delay integration imaging mode taking advantage of the best seeing conditions i.e. at the zenith. This facility will be entirely dedicated and optimized for specific scientific projects such as photometric and astrometric variability studies.

During the past few years, a number of experiments were executed to solve many issues and technical problems related to the ILMT project. It includes spin casting of the primary mirror, optical quality tests of the mercury surface and mylar film experiments. The spin casting was performed to provide a pre-parabola shape of the container so that later during the telescope operations it will require a smaller amount of mercury which will finally lead to a better image quality.

To examine the optical quality of the mercury surface we performed experiments using a laser source and a detector and verified the wavelets propagating on the mercury surface. Measurements were carried out for different thicknesses of the mercury layers. Our analysis indicates that there is absence of concentric wavelets on the mirror however, signature of spiral wavelets was present. It is notable that these experiments were limited due to sensitivity of the instrument, work place but, it will be mandatory to repeat these experiments again when the ILMT will be installed at site.

We have studied the influence of a mylar film by placing it on top of the tube of the 1.04m Sampurnanad Telescope at ARIES, Nainital, in order to later suppress the spiral waves induced by the rotation of the ILMT container. Our results infer that use of this mylar film, diffuses ∼21% of the incident flux which is equivalent to a loss of about 0.3 mag when imaging point-like celestial objects.

Along with the supernovae observations with the ILMT, we discussed its possible scientific contributions. To detect the SNe candidates in the ILMT images, we can co-add several night images and consequently deeper images will be obtained. By applying the image subtraction technique we will be able to identify SN like transients. The SNe type determination will be performed by spectral analysis and also by the well established light curve template fitting methods. Further follow-up observations will be done using ARIES as well as other observational facilities. We are expecting to detect hundreds of supernovae every year thanks to the ILMT observations.

Now the ILMT telescope is ready for its installation at Devasthal (Nainital, India) observatory. For this purpose we have already procured several equipments essential for the installation and smooth running of the ILMT facility. Some of these items include air compressor, air receiver, dew point sensor, compressed air membrane dryer, mercury vapor detectors, mercury vacuum cleaner, mercury safety mask, etc. Many items are still to be procured in the near future such as computers, storage devices, electrical UPS, automatic weather station, etc.

Future prospects

Major parts of the ILMT have already been shipped to India and safely reached at the Devasthal observatory. Figures 8.1 and 8.2, respectively illustrate the proposed layout of the ILMT location at Devasthal and the enclosure sketch. Along with

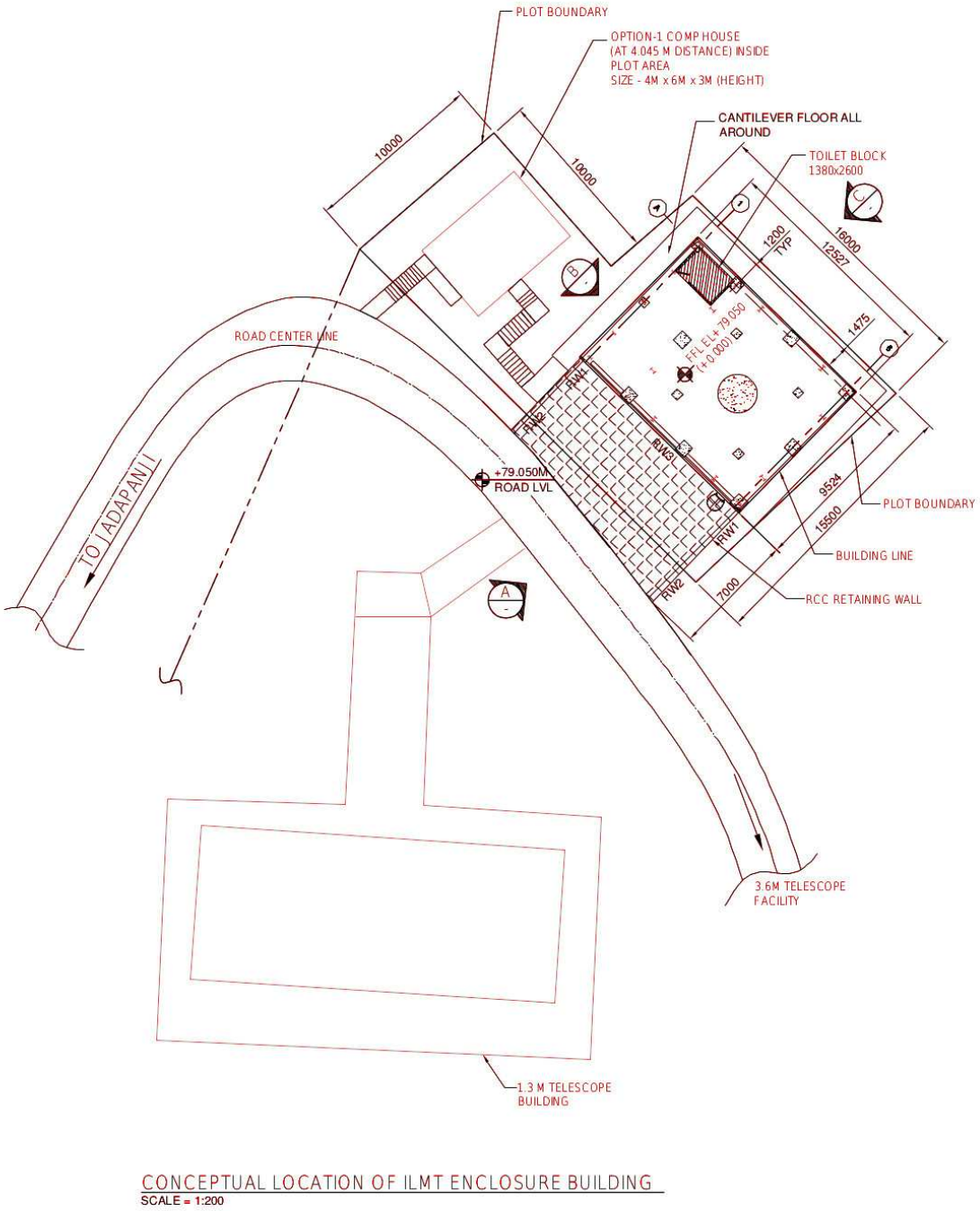

Figure 8.1: Lay-out of the ILMT location at Devasthal, India. The main enclosure is on the right side of the image where the central pier is indicated with a circle. The air compressor room is located left to the main enclosure (central top in the image). Image credit: PPS.

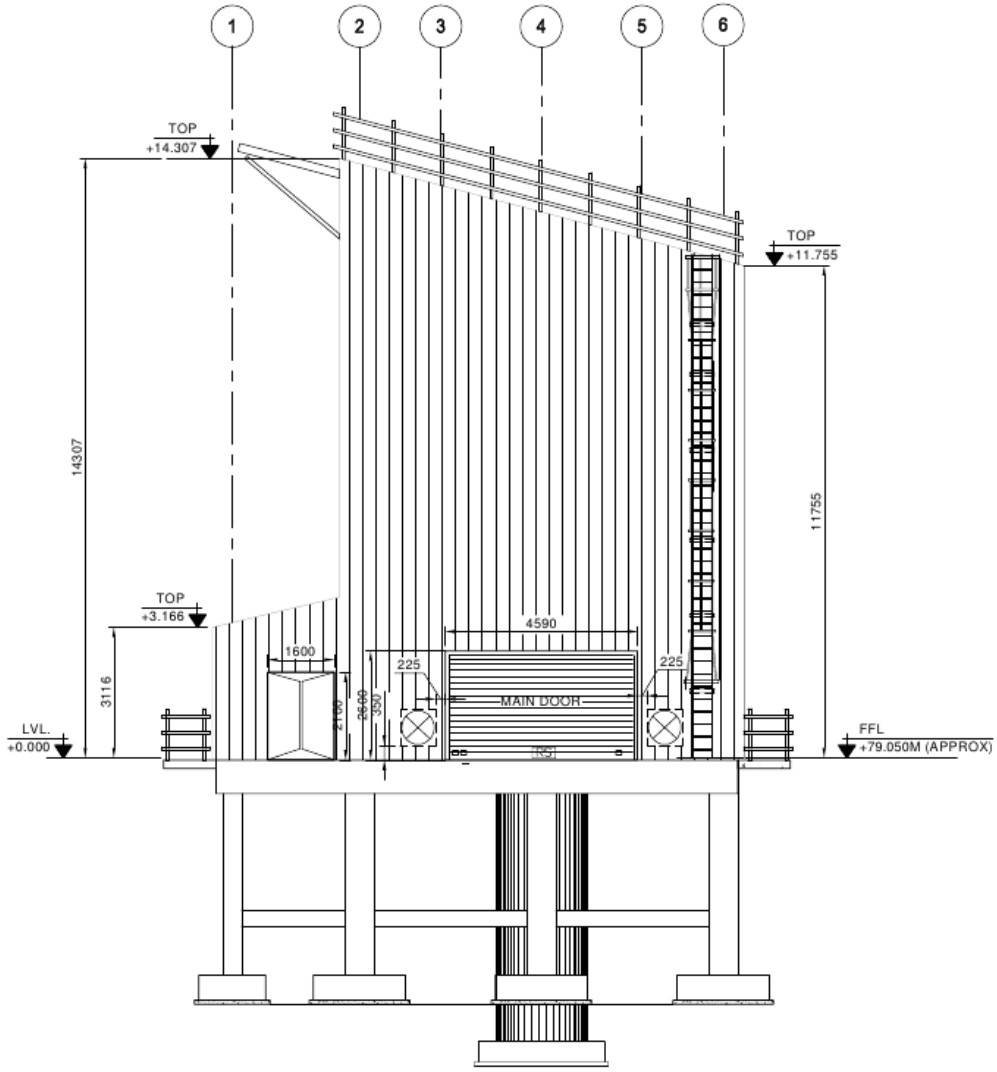

Figure 8.2: Sketch of the front face of the proposed ILMT enclosure. The full structure will be established over the concrete pillars. The top of the roof is inclined in order to avoid as much as possible the effects of the prevailing wind. Image credit: PPS.

an air compressor room ($\sim$24 m^2), the main enclosure part where the telescope will be located has an area of $\sim$119 m^2. The civil construction part is almost over (see Fig. 8.3) and the remaining metallic enclosure manufacturing is under progress. The installation of the telescope will start soon just after completion of the dome enclosure.

The telescope installation and alignment constitute the most important tasks before first light or scientific observations. A wrong alignment results in a bad image quality which can spoil great efforts of many years. A conventional telescope

Figure 8.3: Present status of the ILMT enclosure along with the compressor room (front). The enclosure of the upcoming 3.6m DOT telescope is also visible in the background.

is usually aligned by pointing it toward a bright star and various sophisticated elements are tuned in a very precise manner. Several images are taken while moving the different optical elements in order to find their optimal position that minimizes the aberrations. Depending upon the complex nature of the instruments, the whole alignment process may take several weeks to months.

The situation is entirely different for the case of liquid mirror telescopes. It is true that the structure and complexity wise liquid mirror telescopes are much simpler than the conventional glass mirror telescopes. However, the presence of a TDI optical corrector and the TDI acquisition mode, which involves two more degrees of freedom (East-West alignment and TDI drift speed), make it an unusual, complex instrument to align. In addition to the above, the situation becomes more complex since a LMT cannot track celestial objects in a similar manner like conventional telescopes by looking towards all possible directions in the sky. They can image only those stellar objects which are passing over the zenith. In case of the ILMT, the

imaging instruments will be positioned at a height of around 8m above the rotating mercury container and consequently the characterization and alignment will be a difficult process. The astronomers involved in the large zenithal telescope project which is presently the largest working liquid mirror facility are also associated with the ILMT project. With their great expertise and dedicated team members, we are extremely hopeful to install the ILMT facility in the near future and dedicate it to the whole interested astronomical community.

An efficient software pipeline is necessary for the detection of transients and real time observations. For a quick and responsive follow-up, image subtraction technique must be included in the software so that each night, the previous night images (or a good reference frame image) can be subtracted and spectroscopic trigger can be requested immediately. Softwares have already been developed in due course of time and preliminary processing tests have also been performed on it using previously acquired TDI images with the 1.3m DFOT and a C-14" telescope. This segment requires further involvement.

During night operation, the temperature inside the dome must be similar to the temperature outside, within typically one °C. Similar to a conventional telescope enclosure building, it is necessary to design the ILMT enclosure so that the "dome" seeing is minimized. Artificial sources of heat inside the mirror room, during the day and, especially, at night must be minimized. The difference of temperature inside and outside the dome shall in no time exceed 5°C. Therefore, a rudimentary air conditioning system is planned inside the ILMT dome in order to maintain a temperature close to the external one at the beginning of the night.

Safety Related

Since mercury will be used to create the liquid mirror, safe handling of the mercury constitutes one most important aspect during operations of the ILMT. In our experiments for the surface quality verification over the mercury layer, we have learnt many procedures for safe handling of the mercury. During our experiments we have learnt how to properly operate mercury vapor detectors, mercury vacuum cleaner, etc. We will follow all possible safety measures for the mercury vapor protection.

Four safety pillars just below the periphery of the bowl will be installed so that if the mercury filled bowl accidently tilts in any direction, these pillars will prevent it to tumble. To avoid the spread of mercury spilling, the floor of the enclosure base

Figure 8.4: Computer clusters installed at the Poznań Observatory, Poland. These machines will be later used for the ILMT data base as well as for the image processing.

will be painted with an epoxy paint after filling all the gaps and holes. Up to one foot epoxy paint will also be applied around the inside walls of the main enclosure. The spinning bowl will be covered with a co-moving transparent mylar film which will eventually improve the image quality and will also protect from the expansion of the harmful mercury vapors. Along with the software documentations, we will keep each user manuals related to the safety and maintenance inside the ILMT office as well as on intranet. Some of them are already prepared and remaining are under preparation.

A huge amount of data (around 10 GB) will be obtained from the ILMT each night therefore, dedicated powerful computer clusters will be a must. In these regards, a network of 27 workstations is already installed at the Poznań observatory (Poland), thanks to a grant provided by the Adam Mickiewicz University (Poland). One of these stations works as the database server and will store all the data from the reduction pipeline. Our plan is to establish at least 3 data base centers at three

different places. One base will be located at the Devasthal observatory, India. We have to purchase large storage capacity devices along with high processing computers. We will also install a good quality video camera and an automatic weather station for the continuous monitoring of the telescope and weather conditions, respectively. A complete observatory control system is also planned in a later phase.

As obvious from Figs. 8.2 and 8.3, for cost saving purposes, the ILMT base has been constructed on concrete pillars. There is ample space below the top portion. We plan to manage this space for making offices, rest rooms and storage area for the ILMT purposes.

The Devasthal observatory is soon going to host the 3.6m telescope (DOT) which will be equipped with sophisticated instruments for low spectral resolution observations and imaging capabilities in the visible and near-infrared bands. First light of DOT is expected at the beginning of 2015. Once the 3.6m telescope will be installed, it will be the largest telescope in Asia. Along with other science goals, this telescope will be extremely useful for complementary observations of the stellar objects detected with the ILMT (specially for the transients). We will continue our follow-up programs (photometry, spectroscopy and polarimetry) to study core collapse supernovae and other transients. The investigation of these events may further tell us about some of the underlying question related to massive star evolution.

Appendix

A. APPENDIX

Table A.1: List of the optically identified YSOs along with their derived ages and masses. Error bars in magnitude and colour represent formal internal (comparative) errors and do not include the colour transformation and zero-point uncertainties. The numbers in the technique column indicate the YSOs identified with different schemes (1: Spitzer identified sources, 2: $H\alpha$ sources, 3: CTTS, [4] *Chandra* sources, 5: *XMM-Newton* sources and 6: Probable NIR excess)

ID	α(J2000) (°)	δ(J2000) (°)	$V \pm \sigma$ (mag)	$(V-I) \pm \sigma$ (mag)	Age $\pm\sigma$ (Myrs)	Mass $\pm\sigma$ ($M_\odot$)	Technique [1,2,3,4,5,6]
(1)	(2)	(3)	(4)	(5)	(6)	(7)	(8)
1	160.544858	-59.643538	12.316± 0.009	0.373± 0.018	0.9± 0.2	3.7± 0.2	1
2	160.586232	-59.898926	12.726± 0.011	0.211± 0.018	2.6± 2.1	4.8± 0.3	1
3	160.556561	-59.735036	13.079± 0.011	0.422± 0.014	1.4± 0.2	2.8± 0.3	1
4	159.827622	-59.759030	13.508± 0.006	0.677± 0.010	2.5± 0.4	2.0± 0.3	1
5	160.509158	-59.674841	13.527± 0.009	1.000± 0.014	1.4± 0.2	3.4± 0.3	1
6	160.773246	-59.888387	13.783± 0.014	0.890± 0.013	2.5± 0.4	2.7± 0.2	1
7	160.070496	-59.624432	14.001± 0.009	1.743± 0.010	0.1± 0.1	2.9± 0.1	1 2
8	160.314363	-59.631949	14.056± 0.037	0.899± 0.041	3.1± 0.5	2.5± 0.2	1
9	160.623657	-59.813984	14.220± 0.022	0.762± 0.016	5.0± 0.8	2.1± 0.3	1
10	160.580895	-59.847589	14.317± 0.020	1.014± 0.010	2.4± 0.4	2.8± 0.1	1
11	159.838120	-59.632839	14.342± 0.014	1.137± 0.010	1.2± 0.2	3.4± 0.1	2
12	160.705831	-59.767138	14.584± 0.024	0.923± 0.015	4.3± 0.6	2.1± 0.2	1
13	160.069977	-59.534346	14.720± 0.012	1.386± 0.007	0.3± 0.1	3.2± 0.1	5
14	160.671981	-59.794835	14.746± 0.018	0.965± 0.013	4.3± 0.7	2.2± 0.2	1
15	160.841873	-59.445595	14.917± 0.026	1.254± 0.041	0.8± 0.2	3.2± 0.1	1
16	160.101377	-59.846255	14.918± 0.015	1.184± 0.012	1.3± 0.3	3.0± 0.1	1 2
17	159.820572	-59.738407	15.208± 0.008	1.105± 0.012	3.0± 0.5	2.5± 0.1	2
18	160.214424	-59.622191	15.365± 0.008	1.332± 0.008	0.7± 0.1	2.8± 0.1	4 5
19	160.307350	-59.844427	15.454± 0.015	0.918± 0.014	8.6± 0.6	1.8± 0.1	1
20	160.642834	-59.703229	15.534± 0.012	2.053± 0.015	0.1± 0.1	1.2± 0.1	1 6
21	160.522348	-59.407467	15.739± 0.009	0.962± 0.007	9.3± 0.7	1.7± 0.1	3
22	160.700775	-59.424721	15.741± 0.010	1.622± 0.019	0.3± 0.1	1.6± 0.1	1 2 6
23	160.684442	-59.902335	15.749± 0.011	1.344± 0.012	0.9± 0.1	2.5± 0.1	1
24	160.206885	-59.738959	15.806± 0.009	1.207± 0.011	2.4± 0.5	2.4± 0.1	4
25	160.552671	-59.769595	15.833± 0.009	1.208± 0.007	2.3± 0.5	2.4± 0.1	1
26	160.187629	-59.842736	15.910± 0.017	1.974± 0.035	0.1± 0.1	1.0± 0.1	4
27	160.601418	-59.453720	15.936± 0.009	1.693± 0.012	0.3± 0.1	1.3± 0.1	4
28	160.190377	-59.720193	15.953± 0.009	1.517± 0.012	0.5± 0.1	1.8± 0.1	4

Continued on next page

Table A.1 – *Continued from previous page*

ID	α(J2000)	δ(J2000)	$V \pm \sigma$	$(V-I) \pm \sigma$	Age $\pm\sigma$	Mass $\pm\sigma$	Technique
29	160.674731	-59.414808	16.064± 0.008	1.226± 0.013	2.5± 0.5	2.3± 0.1	1
30	160.636112	-59.611374	16.242± 0.012	1.834± 0.015	0.2± 0.1	1.0± 0.1	4 5
31	160.042786	-59.571266	16.300± 0.008	1.334± 0.013	1.5± 0.3	2.2± 0.1	2
32	160.842665	-59.415265	16.335± 0.020	1.098± 0.037	7.9± 1.7	1.7± 0.1	3
33	160.441833	-59.445591	16.359± 0.012	2.867± 0.007	0.1± 0.1	0.8± 0.1	2
34	160.671367	-59.887454	16.390± 0.011	1.521± 0.011	0.6± 0.1	1.6± 0.1	4
35	160.795544	-59.856471	16.739± 0.011	1.676± 0.017	0.5± 0.1	1.1± 0.1	1 4
36	160.778691	-59.724057	16.778± 0.011	2.072± 0.019	0.1± 0.1	0.7± 0.1	1
37	160.781664	-59.598402	16.923± 0.010	2.029± 0.024	0.1± 0.1	0.7± 0.1	4
38	160.369311	-59.683696	16.996± 0.009	1.789± 0.010	0.4± 0.1	0.9± 0.1	4
39	160.102520	-59.854395	17.003± 0.007	2.040± 0.013	0.1± 0.1	0.7± 0.1	1
40	160.788150	-59.459459	17.056± 0.009	1.803± 0.022	0.4± 0.1	0.9± 0.1	4
41	160.569565	-59.783939	17.135± 0.012	1.606± 0.009	0.9± 0.1	1.3± 0.1	4
42	160.775419	-59.425857	17.158± 0.011	1.627± 0.023	0.8± 0.1	1.2± 0.1	4
43	159.939581	-59.868466	17.220± 0.009	1.653± 0.014	0.8± 0.1	1.1± 0.1	4
44	160.647160	-59.848076	17.226± 0.015	1.815± 0.015	0.5± 0.1	0.9± 0.1	4
45	160.252862	-59.821800	17.251± 0.011	1.496± 0.012	1.7± 0.2	1.5± 0.1	4
46	160.251850	-59.851481	17.373± 0.010	1.371± 0.017	3.6± 0.6	1.7± 0.1	4
47	160.093637	-59.894499	17.384± 0.008	1.332± 0.021	4.7± 0.8	1.7± 0.1	4
48	160.229239	-59.639602	17.422± 0.010	1.552± 0.014	1.6± 0.2	1.4± 0.1	4 5
49	160.040654	-59.771253	17.437± 0.021	1.665± 0.008	0.9± 0.1	1.1± 0.1	4
50	159.889716	-59.858138	17.478± 0.009	2.220± 0.013	0.1± 0.1	0.6± 0.1	1
51	160.525457	-59.424653	17.506± 0.010	1.295± 0.008	6.4± 1.1	1.6± 0.1	4
52	160.642884	-59.885239	17.516± 0.012	1.389± 0.014	3.9± 0.6	1.6± 0.1	1
53	160.184003	-59.826372	17.565± 0.007	3.222± 0.015	0.1± 0.1	0.5± 0.1	4
54	160.287114	-59.830240	17.572± 0.028	1.363± 0.010	4.8± 0.8	1.6± 0.1	4
55	160.268963	-59.528737	17.585± 0.012	2.006± 0.013	0.5± 0.1	0.7± 0.1	4
56	159.994660	-59.821534	17.622± 0.008	1.656± 0.011	1.2± 0.2	1.1± 0.1	4
57	160.042973	-59.619011	17.720± 0.011	2.299± 0.012	0.1± 0.1	0.5± 0.1	5
58	160.792917	-59.784237	17.742± 0.012	2.065± 0.019	0.5± 0.1	0.6± 0.1	1 3 4
59	160.653482	-59.794156	17.750± 0.012	1.661± 0.012	1.4± 0.2	1.1± 0.1	4
60	160.531930	-59.529227	17.755± 0.016	1.251± 0.014	9.6± 0.7	1.4± 0.1	4
61	160.078278	-59.689249	17.800± 0.011	2.436± 0.015	0.1± 0.1	0.5± 0.1	1
62	160.444594	-59.687601	17.809± 0.011	2.014± 0.010	0.6± 0.1	0.7± 0.1	4
63	160.194121	-59.782661	17.835± 0.012	1.692± 0.011	1.3± 0.2	1.1± 0.1	4
64	160.840546	-59.498472	17.838± 0.013	2.234± 0.026	0.1± 0.1	0.5± 0.1	1 3
65	160.449423	-59.869630	17.858± 0.010	1.826± 0.010	0.8± 0.1	0.8± 0.1	4

Continued on next page

A. APPENDIX

Table A.1 – *Continued from previous page*

ID	α(J2000)	δ(J2000)	$V \pm \sigma$	$(V-I) \pm \sigma$	Age $\pm\sigma$	Mass $\pm\sigma$	Technique
66	160.808515	-59.826145	17.859± 0.013	1.667± 0.018	1.5± 0.2	1.1± 0.1	4
67	160.287467	-59.875219	17.869± 0.009	1.284± 0.008	9.3± 0.8	1.4± 0.1	4
68	160.181222	-59.914918	17.893± 0.009	1.955± 0.017	0.7± 0.1	0.7± 0.1	4
69	160.225893	-59.487413	17.906± 0.012	2.274± 0.015	0.1± 0.1	0.5± 0.1	4
70	160.666085	-59.465952	17.910± 0.010	2.446± 0.013	0.1± 0.1	0.5± 0.1	4
71	160.844931	-59.923162	17.926± 0.018	1.970± 0.016	0.7± 0.1	0.7± 0.1	1
72	160.141630	-59.751331	17.949± 0.008	1.601± 0.015	2.3± 0.4	1.2± 0.1	4
73	160.262140	-59.537419	17.970± 0.012	3.017± 0.011	0.1± 0.1	0.5± 0.1	4
74	160.347645	-59.859192	17.987± 0.010	1.707± 0.011	1.4± 0.2	1.0± 0.1	4
75	160.725325	-59.439794	18.003± 0.011	1.572± 0.016	2.9± 0.5	1.3± 0.1	4
76	160.360772	-59.499924	18.043± 0.011	2.634± 0.010	0.1± 0.1	0.5± 0.1	4
77	160.330190	-59.817178	18.086± 0.011	1.885± 0.009	0.9± 0.4	0.8± 1.4	4
78	160.735424	-59.704699	18.089± 0.014	1.998± 0.016	0.7± 0.1	0.7± 0.1	1 4
79	160.835598	-59.771479	18.095± 0.011	2.102± 0.021	0.6± 0.1	0.6± 0.1	4
80	160.620634	-59.742206	18.104± 0.015	1.391± 0.012	7.8± 1.1	1.4± 0.1	4
81	160.255001	-59.512966	18.109± 0.013	2.419± 0.013	0.1± 0.1	0.5± 0.1	4
82	160.594788	-59.655849	18.122± 0.016	1.324± 0.025	9.6± 0.6	1.3± 0.1	2
83	160.029372	-59.837043	18.128± 0.017	1.894± 0.018	0.9± 0.1	0.8± 0.1	1
84	160.231943	-59.830059	18.131± 0.013	2.192± 0.013	0.4± 0.1	0.5± 0.1	4
85	159.825531	-59.774998	18.143± 0.023	1.892± 0.014	0.9± 0.1	0.8± 0.1	2
86	160.517051	-59.802745	18.165± 0.014	2.389± 0.009	0.1± 0.1	0.5± 0.1	1
87	160.556738	-59.599388	18.204± 0.010	2.910± 0.013	0.1± 0.1	0.4± 0.1	1 3 4 5
88	160.655576	-59.847457	18.224± 0.014	2.149± 0.014	0.5± 0.1	0.5± 0.1	1 4
89	160.388550	-59.606377	18.232± 0.011	1.267± 0.011	10.0± 0.1	1.3± 0.1	2
90	160.218962	-59.583514	18.249± 0.013	1.990± 0.012	0.8± 0.1	0.7± 0.1	4
91	160.815765	-59.767838	18.366± 0.016	2.667± 0.020	0.1± 0.1	0.4± 0.1	1
92	160.667867	-59.861518	18.376± 0.018	2.603± 0.012	0.1± 0.1	0.4± 0.1	4
93	160.596668	-59.773186	18.391± 0.018	2.567± 0.018	0.1± 0.1	0.4± 0.1	1
94	159.965824	-59.779383	18.464± 0.011	2.424± 0.009	0.1± 0.1	0.4± 0.1	1
95	160.179539	-59.850030	18.488± 0.019	2.512± 0.012	0.1± 0.1	0.4± 0.1	4
96	160.213470	-59.779138	18.496± 0.011	1.473± 0.010	8.7± 1.0	1.2± 0.1	4
97	160.710477	-59.720586	18.506± 0.020	2.703± 0.017	0.1± 0.1	0.4± 0.1	1
98	160.750182	-59.452148	18.512± 0.014	1.908± 0.021	1.2± 0.1	0.8± 0.1	4
99	159.910376	-59.736938	18.524± 0.013	2.572± 0.010	0.1± 0.1	0.4± 0.1	1
100	160.811693	-59.705286	18.537± 0.019	1.777± 0.025	2.1± 0.3	0.9± 0.1	1
101	160.398495	-59.855793	18.544± 0.023	2.506± 0.012	0.1± 0.1	0.4± 0.1	4
102	159.942832	-59.605503	18.544± 0.017	5.495± 0.007	0.1± 0.1	0.3± 0.1	3

Continued on next page

Table A.1 – *Continued from previous page*

ID	α(J2000)	δ(J2000)	$V \pm \sigma$	$(V-I) \pm \sigma$	Age $\pm\sigma$	Mass $\pm\sigma$	Technique
103	160.664289	-59.830835	18.579± 0.015	1.978± 0.016	1.1± 0.1	0.7± 0.1	4
104	160.803200	-59.458130	18.580± 0.017	3.858± 0.029	0.1± 0.1	0.4± 0.1	3
105	160.811839	-59.693843	18.656± 0.018	2.215± 0.021	0.6± 0.1	0.5± 0.1	1
106	160.682370	-59.665064	18.668± 0.024	1.816± 0.024	2.0± 0.3	0.9± 0.1	4
107	159.897828	-59.785528	18.685± 0.011	2.709± 0.014	0.1± 0.1	0.4± 0.1	1
108	160.811217	-59.852238	18.725± 0.028	2.591± 0.017	0.1± 0.1	0.4± 0.1	1
109	160.267273	-59.745434	18.728± 0.015	1.747± 0.014	3.1± 0.5	1.0± 0.1	2
110	160.423381	-59.476106	18.763± 0.013	2.270± 0.012	0.6± 0.1	0.5± 0.1	4
111	160.734603	-59.804400	18.786± 0.022	2.284± 0.017	0.6± 0.1	0.5± 0.1	4
112	160.055612	-59.846394	18.814± 0.017	1.711± 0.019	4.3± 0.8	1.1± 0.1	1
113	160.827144	-59.763835	18.815± 0.016	1.911± 0.021	1.7± 0.2	0.8± 0.1	4
114	160.472680	-59.810504	18.824± 0.028	2.203± 0.014	0.7± 0.1	0.5± 0.1	4
115	160.814573	-59.785304	18.831± 0.022	2.212± 0.023	0.7± 0.1	0.5± 0.1	1
116	160.841959	-59.750535	18.861± 0.018	2.261± 0.021	0.7± 0.1	0.5± 0.1	4
117	160.603096	-59.893202	18.896± 0.022	1.836± 0.011	2.5± 0.4	0.9± 0.1	1
118	160.479202	-59.662464	18.923± 0.021	1.695± 0.018	5.5± 0.9	1.1± 0.1	2
119	160.299744	-59.661736	18.944± 0.024	1.754± 0.020	4.2± 0.8	1.0± 0.1	2
120	160.048587	-59.883686	18.954± 0.022	1.854± 0.017	2.5± 0.4	0.8± 0.1	4
121	160.473225	-59.490778	18.959± 0.018	3.038± 0.013	0.1± 0.1	0.3± 0.1	3
122	160.758392	-59.840868	18.974± 0.047	2.330± 0.049	0.7± 0.1	0.4± 0.1	4
123	160.315017	-59.515005	18.999± 0.019	2.740± 0.021	0.1± 0.1	0.3± 0.1	4
124	160.179037	-59.867334	19.019± 0.015	2.561± 0.015	0.1± 0.1	0.4± 0.1	1
125	160.458471	-59.743140	19.024± 0.014	2.301± 0.011	0.7± 0.1	0.4± 0.1	1
126	160.460874	-59.741973	19.038± 0.017	2.429± 0.010	0.5± 0.2	0.4± 0.1	1
127	160.686126	-59.776816	19.047± 0.021	2.004± 0.017	1.5± 0.2	0.7± 0.1	4
128	160.748557	-59.918314	19.048± 0.021	2.339± 0.016	0.7± 0.1	0.4± 0.1	4
129	160.485868	-59.709275	19.084± 0.018	2.705± 0.011	0.1± 0.1	0.3± 0.1	3
130	160.685242	-59.876530	19.113± 0.021	2.038± 0.014	1.4± 0.2	0.6± 0.1	4
131	160.541305	-59.799465	19.141± 0.020	2.608± 0.009	0.1± 0.1	0.3± 0.1	4
132	160.158020	-59.430286	19.152± 0.017	2.128± 0.015	1.1± 0.1	0.6± 0.1	2
133	160.730694	-59.673915	19.232± 0.020	2.761± 0.020	0.1± 0.1	0.3± 0.1	4
134	160.109048	-59.792470	19.286± 0.019	2.738± 0.012	0.1± 0.1	0.3± 0.1	1
135	160.211645	-59.500247	19.291± 0.016	2.170± 0.014	1.1± 0.1	0.5± 0.1	4
136	160.213782	-59.860526	19.340± 0.017	1.871± 0.018	4.0± 0.7	0.8± 0.1	4
137	160.738044	-59.827113	19.377± 0.023	3.059± 0.016	0.1± 0.1	0.3± 0.1	4
138	160.650328	-59.896608	19.388± 0.022	2.131± 0.014	1.4± 0.2	0.6± 0.1	1 2
139	160.473904	-59.790978	19.419± 0.025	2.938± 0.010	0.1± 0.1	0.3± 0.1	4

Continued on next page

A. APPENDIX

Table A.1 – *Continued from previous page*

ID	α(J2000)	δ(J2000)	$V \pm \sigma$	$(V-I) \pm \sigma$	Age $\pm\sigma$	Mass $\pm\sigma$	Technique
140	160.616269	-59.820951	19.424± 0.028	2.671± 0.013	0.1± 0.1	0.3± 0.1	1 4
141	160.434405	-59.751046	19.459± 0.021	2.200± 0.012	1.2± 0.1	0.5± 0.1	4
142	160.672447	-59.613541	19.472± 0.024	2.962± 0.016	0.1± 0.1	0.3± 0.1	3
143	160.575360	-59.842498	19.480± 0.025	2.665± 0.009	0.1± 0.1	0.3± 0.1	1
144	160.545693	-59.793922	19.497± 0.024	1.999± 0.012	2.8± 0.4	0.7± 0.1	4
145	160.832667	-59.712682	19.503± 0.026	2.434± 0.021	0.9± 0.1	0.4± 0.1	1 4
146	160.720734	-59.446641	19.504± 0.023	2.217± 0.015	1.2± 0.1	0.5± 0.1	4
147	160.514297	-59.885788	19.545± 0.025	1.488± 0.015	10.0± 0.1	1.0± 0.1	2
148	160.663088	-59.839060	19.556± 0.026	2.027± 0.018	2.6± 0.4	0.7± 0.1	4
149	160.563171	-59.830609	19.562± 0.024	2.448± 0.011	0.9± 0.1	0.4± 0.1	4
150	160.220291	-59.442047	19.576± 0.019	1.950± 0.017	3.9± 0.6	0.8± 0.1	2
151	160.196478	-59.823254	19.579± 0.027	2.040± 0.018	2.5± 0.4	0.6± 0.1	4
152	160.745052	-59.417833	19.582± 0.024	2.623± 0.018	0.4± 0.2	0.3± 0.1	1
153	160.596159	-59.798524	19.616± 0.025	2.621± 0.016	0.5± 0.2	0.3± 0.1	4
154	160.718048	-59.775805	19.638± 0.031	2.975± 0.016	0.1± 0.1	0.3± 0.1	1
155	160.697581	-59.448190	19.674± 0.023	2.420± 0.018	1.0± 0.1	0.4± 0.1	4
156	160.761116	-59.796485	19.686± 0.031	2.283± 0.019	1.2± 0.1	0.5± 0.1	4
157	160.250616	-59.867685	19.755± 0.030	2.434± 0.017	1.0± 0.1	0.4± 0.1	4
158	160.771447	-59.488738	19.763± 0.031	2.835± 0.022	0.1± 0.1	0.3± 0.1	4
159	159.839658	-59.665863	19.775± 0.024	2.352± 0.012	1.1± 0.1	0.4± 0.1	6
160	160.775899	-59.423859	19.780± 0.026	1.503± 0.026	10.0± 0.1	0.9± 0.1	4
161	160.184555	-59.474705	19.789± 0.026	1.699± 0.023	10.0± 0.1	0.9± 0.1	2
162	160.381356	-59.467540	19.833± 0.027	3.818± 0.013	0.1± 0.1	0.3± 0.1	3
163	160.406433	-59.745941	19.841± 0.046	2.780± 0.016	0.2± 0.1	0.3± 0.1	2
164	160.562288	-59.846880	19.853± 0.030	2.944± 0.010	0.1± 0.1	0.3± 0.1	1
165	160.359589	-59.826420	19.886± 0.029	1.720± 0.017	10.0± 0.1	0.9± 0.1	2
166	160.774516	-59.902272	19.909± 0.048	2.355± 0.018	1.3± 0.1	0.4± 0.1	1
167	160.701834	-59.809824	19.915± 0.029	2.331± 0.022	1.3± 0.1	0.4± 0.1	1
168	160.760216	-59.453766	19.966± 0.032	2.488± 0.019	1.1± 0.1	0.4± 0.1	4
169	159.897143	-59.917791	19.968± 0.026	1.692± 0.029	10.0± 0.1	0.9± 0.1	6
170	160.488870	-59.702407	19.985± 0.029	2.939± 0.011	0.1± 0.1	0.3± 0.1	1
171	160.331375	-59.530715	19.991± 0.032	2.968± 0.010	0.1± 0.1	0.3± 0.1	4
172	160.681093	-59.747899	20.024± 0.050	3.616± 0.014	0.1± 0.1	0.3± 0.1	1
173	160.173294	-59.827023	20.063± 0.033	2.715± 0.013	0.8± 0.1	0.3± 0.1	2
174	160.436726	-59.825358	20.075± 0.029	2.223± 0.014	2.1± 0.2	0.5± 0.1	4
175	160.020751	-59.880788	20.082± 0.043	2.535± 0.024	1.1± 0.1	0.4± 0.1	4
176	160.602032	-59.658140	20.082± 0.044	3.143± 0.015	0.1± 0.1	0.3± 0.1	1

Continued on next page

Table A.1 – *Continued from previous page*

ID	α(J2000)	δ(J2000)	$V \pm \sigma$	$(V-I) \pm \sigma$	Age $\pm\sigma$	Mass $\pm\sigma$	Technique
177	160.837272	-59.507790	20.163± 0.048	2.063± 0.027	5.0± 1.0	0.6± 0.1	4
178	160.801848	-59.767580	20.214± 0.035	2.589± 0.021	1.2± 0.1	0.3± 0.1	1
179	160.820948	-59.555584	20.216± 0.036	3.420± 0.025	0.1± 0.1	0.3± 0.1	4
180	159.850860	-59.636697	20.270± 0.027	3.128± 0.012	0.1± 0.1	0.3± 0.1	3
181	160.626818	-59.741319	20.289± 0.035	2.285± 0.027	2.2± 0.2	0.5± 0.1	4
182	160.773279	-59.827574	20.363± 0.040	2.649± 0.024	1.2± 0.1	0.3± 0.1	1
183	159.894496	-59.737510	20.386± 0.031	2.860± 0.014	0.7± 0.3	0.3± 0.1	5
184	160.073586	-59.839734	20.388± 0.034	3.324± 0.014	0.1± 0.1	0.2± 0.1	1
185	160.820832	-59.439064	20.479± 0.055	2.703± 0.031	1.2± 0.1	0.3± 0.1	4
186	159.841354	-59.664940	20.486± 0.042	2.550± 0.014	1.4± 0.1	0.3± 0.1	2
187	160.467667	-59.654774	20.488± 0.044	2.551± 0.014	1.4± 0.1	0.3± 0.1	2
188	160.649510	-59.842151	20.508± 0.034	2.638± 0.020	1.3± 0.1	0.3± 0.1	4
189	160.243190	-59.573888	20.523± 0.036	2.465± 0.017	1.7± 0.1	0.4± 0.1	4
190	160.773423	-59.433648	20.556± 0.046	2.931± 0.021	0.6± 0.3	0.3± 0.1	4
191	160.785809	-59.423738	20.621± 0.045	3.068± 0.025	0.2± 0.1	0.3± 0.1	4
192	160.545773	-59.484644	20.630± 0.037	2.773± 0.013	1.3± 0.1	0.3± 0.1	4
193	160.660687	-59.847911	20.635± 0.048	2.512± 0.019	1.7± 0.1	0.4± 0.1	4
194	160.468475	-59.662941	20.647± 0.045	2.234± 0.021	4.0± 0.6	0.5± 0.1	2
195	160.077556	-59.843072	20.680± 0.043	2.773± 0.017	1.3± 0.1	0.3± 0.1	4
196	160.308868	-59.871311	20.728± 0.084	1.669± 0.048	10.0± 0.1	0.7± 0.1	2
197	160.806156	-59.429061	20.730± 0.062	3.167± 0.028	0.1± 0.1	0.2± 0.1	4
198	160.213868	-59.779419	20.737± 0.052	2.987± 0.014	0.7± 0.3	0.3± 0.1	4
199	160.801895	-59.664165	20.816± 0.051	2.433± 0.034	2.5± 0.3	0.4± 0.1	2
200	159.966965	-59.661163	20.818± 0.053	3.093± 0.026	0.3± 0.2	0.3± 0.1	2
201	160.832401	-59.750670	20.830± 0.055	2.719± 0.023	1.5± 0.1	0.3± 0.1	4
202	160.038696	-59.479828	20.834± 0.053	2.279± 0.030	4.2± 0.6	0.5± 0.1	2
203	160.814697	-59.463681	20.840± 0.088	3.041± 0.027	0.6± 0.4	0.3± 0.1	4
204	160.644553	-59.813771	20.851± 0.052	2.053± 0.028	10.0± 0.1	0.6± 0.1	1
205	160.519581	-59.742278	20.870± 0.059	3.013± 0.035	0.8± 0.3	0.3± 0.1	4
206	160.214417	-59.874210	20.893± 0.048	1.899± 0.034	10.0± 0.1	0.6± 0.1	2
207	160.019358	-59.737023	20.897± 0.063	2.536± 0.019	2.0± 0.2	0.3± 0.1	1
208	160.296672	-59.757082	20.904± 0.057	2.690± 0.014	1.6± 0.1	0.3± 0.1	4
209	160.674684	-59.510640	20.920± 0.047	2.765± 0.018	1.5± 0.1	0.3± 0.1	4
210	160.230347	-59.915180	20.921± 0.054	1.832± 0.029	10.0± 0.1	0.6± 0.1	2
211	160.739090	-59.446106	20.957± 0.059	3.107± 0.017	0.6± 0.4	0.3± 0.1	4
212	160.033722	-59.549648	21.008± 0.057	2.176± 0.037	8.5± 1.4	0.5± 0.1	2
213	160.844292	-59.498935	21.021± 0.096	3.003± 0.025	1.0± 0.4	0.3± 0.1	1

Continued on next page

A. APPENDIX

Table A.1 – *Continued from previous page*

ID	α(J2000)	δ(J2000)	$V \pm \sigma$	$(V-I) \pm \sigma$	Age $\pm\sigma$	Mass $\pm\sigma$	Technique
214	159.968704	-59.730141	21.027± 0.063	2.255± 0.023	6.0± 0.9	0.5± 0.1	2
215	160.826294	-59.759949	21.090± 0.064	2.969± 0.027	1.4± 0.2	0.3± 0.1	2
216	160.803892	-59.661895	21.105± 0.064	3.602± 0.026	0.1± 0.1	0.2± 0.1	4
217	160.800372	-59.416345	21.112± 0.061	3.250± 0.035	0.2± 0.1	0.2± 0.1	1 4
218	160.351673	-59.679949	21.184± 0.071	3.210± 0.021	0.5± 0.4	0.2± 0.1	1
219	160.723160	-59.790199	21.227± 0.070	2.550± 0.025	2.8± 0.3	0.3± 0.1	2
220	159.993534	-59.912747	21.276± 0.072	3.024± 0.044	1.5± 0.2	0.3± 0.1	4
221	160.439468	-59.559692	21.334± 0.071	2.893± 0.021	1.8± 0.1	0.3± 0.1	4
222	160.343887	-59.823700	21.344± 0.083	2.762± 0.024	2.1± 0.1	0.3± 0.1	2
223	160.811241	-59.406493	21.353± 0.078	2.952± 0.031	1.7± 0.1	0.3± 0.1	1
224	160.019917	-59.736905	21.394± 0.083	2.762± 0.021	2.2± 0.1	0.3± 0.1	1
225	160.048386	-59.537445	21.396± 0.084	1.958± 0.038	10.0± 0.1	0.5± 0.1	2
226	160.780893	-59.421121	21.418± 0.085	3.160± 0.027	1.0± 0.5	0.2± 0.1	4
227	160.314316	-59.752392	21.433± 0.077	2.051± 0.033	10.0± 0.1	0.5± 0.1	2
228	160.825318	-59.819315	21.448± 0.097	2.798± 0.027	2.1± 0.1	0.3± 0.1	1
229	159.922999	-59.723528	21.471± 0.065	1.496± 0.051	10.0± 0.1	0.5± 0.1	1 2
230	160.713921	-59.426703	21.522± 0.090	3.217± 0.021	1.0± 0.5	0.2± 0.1	1 4
231	160.797460	-59.418385	21.539± 0.088	3.612± 0.029	0.1± 0.1	0.2± 0.1	1
232	160.050271	-59.760285	21.540± 0.096	3.738± 0.012	0.1± 0.1	0.2± 0.1	4
233	160.033386	-59.480370	21.588± 0.095	2.558± 0.026	4.1± 0.4	0.3± 0.1	2
234	160.040878	-59.479084	21.601± 0.097	2.340± 0.034	8.5± 1.2	0.4± 0.1	2
235	159.837477	-59.663673	21.631± 0.086	3.356± 0.022	0.6± 0.4	0.2± 0.1	6
236	159.903859	-59.910158	21.636± 0.084	3.043± 0.026	2.0± 0.1	0.3± 0.1	1
237	160.457133	-59.729012	21.655± 0.095	3.236± 0.021	1.5± 0.4	0.2± 0.1	1 2
238	160.601535	-59.615857	21.655± 0.087	2.646± 0.065	3.5± 0.5	0.3± 0.1	1 3
239	159.906247	-59.911665	21.661± 0.087	2.880± 0.039	2.3± 0.1	0.3± 0.1	1
240	160.418249	-59.474977	21.791± 0.097	3.738± 0.020	0.1± 0.1	0.2± 0.1	3 6
241	160.512606	-59.524536	21.794± 0.095	3.600± 0.018	0.1± 0.1	0.2± 0.1	4

References

Abbott D. C., 1982, ApJ, 263, 723 3

Abbott D. C., Conti P. S., 1987, ARA&A, 25, 113 39

Adelman-McCarthy J. K., Agüeros M. A., Allam S. S., et al., 2006, ApJS, 162, 38 xxxii, 109

Akerlof C., Amrose S., Balsano R., et al., 2000, AJ, 119, 1901 23

Alard C., 2000, A&AS, 144, 363 194

Alard C., Lupton R. H., 1998, ApJ, 503, 325 194

Aldering G., Humphreys R. M., Richmond M., 1994, AJ, 107, 662 84, 152

Allen L. E., Myers P. C., Di Francesco J., Mathieu R., Chen H., Young E., 2002, ApJ, 566, 993 76

Anderson J. P., Covarrubias R. A., James P. A., Hamuy M., Habergham S. M., 2010, MNRAS, 407, 2660 108

Anderson J. P., James P. A., 2009, MNRAS, 399, 559 83

Arcavi I., Gal-Yam A., Kasliwal e. a. M. M., et al., 2010, ApJ, 721, 777 9, 23, 108, 109

Arcavi I., Gal-Yam A., Yaron O., et al., 2011, ApJ, 742, L18 17, 84, 92

Arnett D., 1995, ARA&A, 33, 115 3, 39

Arnett D., 1996, Supernovae and nucleosynthesis: an investigation of the history of matter, from the Big Bang to the present, Princeton University Press. 3, 39

Arnett W. D., 1980, ApJ, 237, 541 98

Arnett W. D., 1982, ApJ, 253, 785 98

Arnett W. D., Bahcall J. N., Kirshner R. P., Woosley S. E., 1989, ARA&A, 27, 629 152

Arnett W. D., Fu A., 1989, ApJ, 340, 396 98, 100, 102, 110

Ascenso J., Alves J., Vicente S., Lago M. T. V. T., 2007, A&A, 476, 199 74

Atwood W. B., Abdo A. A., Ackermann M., et al., 2009, ApJ, 697, 1071 23

REFERENCES

Ballesteros-Paredes J., Klessen R. S., Mac Low M.-M., Vazquez-Semadeni E., 2007, Protostars and Planets V, 63–80 76

Barbon R., Benetti S., Cappellaro E., Patat F., Turatto M., Iijima T., 1995, A&AS, 110, 513 xxxi, 17, 92, 93, 106

Barentsen G., Vink J. S., Drew J. E., et al., 2011, MNRAS, 415, 103 67, 68

Barkat Z., Rakavy G., Sack N., 1967, Physical Review Letters, 18, 379 17

Baron E., Nugent P. E., Branch D., Hauschildt P. H., 2004, ApJ, 616, L91 184

Baron E., Nugent P. E., Branch D., Hauschildt P. H., 2005, in 1604-2004: Supernovae as Cosmological Lighthouses, edited by M. Turatto, S. Benetti, L. Zampieri, W. Shea, vol. 342 of Astronomical Society of the Pacific Conference Series, 351 102

Barrett P., 1988, MNRAS, 234, 937 114, 130

Barthelmy S. D., Barbier L. M., Cummings J. R., et al., 2005, Space Sci. Rev., 120, 143 23

Bayless A. J., Pritchard T. A., Roming P. W. A., et al., 2013, ApJ, 764, L13 116

Bazin G., Palanque-Delabrouille N., Rich J., et al., 2009, A&A, 499, 653 xxxvii, 189, 190

Beauchemin M., 1985, M.Sc. Thesis, Laval University 26

Becker W., Fenkart R., 1971, A&AS, 4, 241 48

Benetti S., 2000, Mem. Soc. Astron. Italiana, 71, 323 16

Benetti S., Cappellaro E., Turatto M., Pastorello A., 2000, IAU Circ., 7375, 2 83

Benson P. J., Herbst W., Salzer J. J., et al., 1994, AJ, 107, 1453 17

Bergemann M., Kudritzki R.-P., Plez B., Davies B., Lind K., Gazak Z., 2012, ApJ, 751, 156 5

Bergemann M., Kudritzki R.-P., Würl M., Plez B., Davies B., Gazak Z., 2013, ApJ, 764, 115 5

Bersten M. C., Benvenuto O., Hamuy M., 2011, ApJ, 729, 61 192

Bersten M. C., Benvenuto O. G., Folatelli G., et al., 2014, AJ, 148, 68 153

Bersten M. C., Benvenuto O. G., Nomoto K., et al., 2012, ApJ, 757, 31 84, 91, 99, 101, 102, 192

Bersten M. C., Hamuy M., 2009, ApJ, 701, 200 xl, 104, 105, 111

Bersten M. C., Tanaka M., Tominaga N., Benvenuto O. G., Nomoto K., 2013, ApJ, 767, 143 192

Bertout C., 1989, ARA&A, 27, 351 53

Bertout C., Basri G., Bouvier J., 1988, ApJ, 330, 350 64

Bessell M. S., Brett J. M., 1988, PASP, 100, 1134 xxviii, 58

Bester M., Danchi W. C., Hale D., et al., 1996, ApJ, 463, 336 12

Bethe H. A., Wilson J. R., 1985, ApJ, 295, 14 19

Beuther H., Linz H., Henning T., eds., 2008, Massive Star Formation: Observations Confront Theory, vol. 387 of Astronomical Society of the Pacific Conference Series 10

Bietenholz M. F., Brunthaler A., Soderberg A. M., et al., 2012, ApJ, 751, 125 84

Bionta R. M., Blewitt G., Bratton C. B., Casper D., Ciocio A., 1987, Physical Review Letters, 58, 1494 130

Bisnovatyi-Kogan G. S., Kazhdan Y. M., 1967, SvA, 10, 604 17

Blaauw A., 1964, ARA&A, 2, 213 10, 11

Blaauw A., 1991, in NATO ASIC Proc. 342: The Physics of Star Formation and Early Stellar Evolution, edited by C. J. Lada, N. D. Kylafis, 125 11

Blanc G., Afonso C., Alard C., et al., 2004, A&A, 423, 881 xxxvii, 181, 189, 190

Blinnikov S. I., Eastman R., Bartunov O. S., Popolitov V. A., Woosley S. E., 1998, ApJ, 496, 454 91

Blondin S., Modjaz M., Kirshner R., Challis P., Berlind P., 2006, Central Bureau Electronic Telegrams, 757, 1 131

Blondin S., Tonry J. L., 2007, ApJ, 666, 1024 85, 92, 192, 198

Bloom J. S., Richards J. W., Nugent P. E., et al., 2012, PASP, 124, 1175 195

Boiani J., Rice S. A., 1969, Physical Review, 185, 931 166

Borra E. F., 1982, JRASC, 76, 245 26, 27, 30, 142, 151

Borra E. F., 1993, A&A, 278, 665 142

Borra E. F., 1994, ArXiv Astrophysics e-prints 144, 172

Borra E. F., 2001a, ArXiv Astrophysics e-prints 186, 190

Borra E. F., 2001b, ArXiv Astrophysics e-prints 182, 186, 191

Borra E. F., 2003, A&A, 404, 47 182, 186, 191

Borra E. F., Beauchemin M., Arsenault R., Lalande R., 1985, PASP, 97, 454 26

Borra E. F., Content R., Boily E., 1988, PASP, 100, 1399 27

Borra E. F., Content R., Drinkwater M. J., Szapiel S., 1989, ApJ, 346, L41 141

Borra E. F., Content R., Girard L., Szapiel S., Tremblay L. M., Boily E., 1992, ApJ, 393, 829 141, 144

Borra E. F., Tremblay G., Huot Y., Gauvin J., 1997, PASP, 109, 319 166

REFERENCES

Bose S., Kumar B., Sutaria F., et al., 2013, MNRAS, 433, 1871 xxxiii, 115, 117, 123, 126, 128, 140

Botticella M. T., Riello M., Cappellaro E., et al., 2008, A&A, 479, 49 xxxvii, 189, 190, 194

Bouwman J., Lawson W. A., Dominik C., et al., 2006, ApJ, 653, L57 68

Branch D., Baron E., Jeffery D. J., 2001, ArXiv Astrophysics e-prints, arXiv:astro-ph/0111573 102

Branch D., Benetti S., Kasen D., et al., 2002, ApJ, 566, 1005 83, 102, 107

Branch D., Miller D. L., 1993, ApJ, 405, L5 183

Branch D., Nomoto K., Filippenko A. V., 1991, Comments on Astrophysics, 15, 221 181

Branch D., Tammann G. A., 1992, ARA&A, 30, 359 183

Briceño C., Preibisch T., Sherry W. H., et al., 2007, Protostars and Planets V, 345–360 10, 59

Brink H., Richards J. W., Poznanski D., et al., 2013, MNRAS, 435, 1047 195

Brooks K. J., Cox P., Schneider N., et al., 2003, A&A, 412, 751 74

Brooks K. J., Storey J. W. V., Whiteoak J. B., 2001, MNRAS, 327, 46 41

Broos P. S., Townsley L. K., Feigelson E. D., Getman K. V., Bauer F. E., Garmire G. P., 2010, ApJ, 714, 1582 63

Bruenn S. W., Mezzacappa A., Hix W. R., et al., 2009, Journal of Physics Conference Series, 180, 1, 012018 9

Bruenn S. W., Mezzacappa A., Hix W. R., et al., 2013, ApJ, 767, L6 9

Burrows A., 2000, Nature, 403, 727 xxv, 19

Burrows A., 2013, Reviews of Modern Physics, 85, 245 9, 21

Burrows A., Hayes J., Fryxell B. A., 1995, ApJ, 450, 830 19

Cabanac R. A., 1997, ArXiv Astrophysics e-prints 32

Cabanac R. A., Borra E. F., Beauchemin M., 1998, ApJ, 509, 309 xxvi, 32

Cao Y., Kasliwal M. M., Arcavi I., et al., 2013, ApJ, 775, L7 153

Cappellaro E., Evans R., Turatto M., 1999, A&A, 351, 459 183, 190

Cappellaro E., Riello M., Altavilla G., et al., 2005, A&A, 430, 83 192, 194

Cappellaro E., Turatto M., Tsvetkov D. Y., et al., 1997, A&A, 322, 431 23

Carraro G., Patat F., 2001, A&A, 379, 136 41, 48

Carraro G., Patat F., Baumgardt H., 2001, A&A, 371, 107 41

Carraro G., Romaniello M., Ventura P., Patat F., 2004, A&A, 418, 525 41, 48, 50

Cartwright A., Whitworth A. P., 2004, MNRAS, 348, 589 76

Castor J. I., Abbott D. C., Klein R. I., 1975, ApJ, 195, 157 10

Chabrier G., 2003, PASP, 115, 763 69

Chatzopoulos E., Wheeler J. C., Vinko J., 2009, ApJ, 704, 1251 98

Chatzopoulos E., Wheeler J. C., Vinko J., 2012, ApJ, 746, 121 102

Chauhan N., Pandey A. K., Ogura K., et al., 2009, MNRAS, 396, 964 67

Chauhan N., Pandey A. K., Ogura K., et al., 2011, MNRAS, 415, 1202 67

Chevalier R. A., 1992, ApJ, 394, 599 92

Chevalier R. A., Fransson C., 2008, ApJ, 683, L135 92

Chevalier R. A., Soderberg A. M., 2010, ApJ, 711, L40 17, 84

Chini R., Kruegel E., 1983, A&A, 117, 289 49

Chini R., Wargau W. F., 1990, A&A, 227, 213 48, 49

Chiosi C., Maeder A., 1986, ARA&A, 24, 329 5, 6, 8

Chornock R., Filippenko A. V., Li W., et al., 2011, ApJ, 739, 41 84

Chornock R., Filippenko A. V., Li W., Silverman J. M., 2010, ApJ, 713, 1363 114, 130, 132

Chugai N. N., 1991, MNRAS, 250, 513 16

Chugai N. N., 1992, Soviet Astronomy Letters, 18, 168 113

Chugai N. N., 2006, Astronomy Letters, 32, 739 22, 114

Ciabattari F., Mazzoni E., Jin Z., et al., 2011, Central Bureau Electronic Telegrams, 2827, 1 85, 92

Claeskens J.-F., Gosset E., Nazé Y., Rauw G., Vreux J.-M., 2011, A&A, 525, A142 xxxix, 41, 45, 51, 52, 60, 61, 62, 80

Clariá J. J., 1977, A&AS, 27, 145 48

Clayton G. C., Wolff M. J., Gordon K. D., Smith P. S., Nordsieck K. H., Babler B. L., 2004, AJ, 127, 3382 125

Clocchiatti A., Wheeler J. C., Phillips M. M., et al., 1997, ApJ, 483, 675 84

Cohen J. G., Persson S. E., Elias J. H., Frogel J. A., 1981, ApJ, 249, 481 xxviii, 58, 59, 64

Conley A., Sullivan M., Hsiao E. Y., et al., 2008, ApJ, 681, 482 196

Conti P. S., 1984, in Observational Tests of the Stellar Evolution Theory, edited by A. Maeder, A. Renzini, vol. 105 of IAU Symposium, 233 6

REFERENCES

Conti P. S., Massey P., 1989, ApJ, 337, 251 7

Conti P. S., Niemela V. S., Walborn N. R., 1979, ApJ, 228, 206 42

Contini T., Treyer M. A., Sullivan M., Ellis R. S., 2002, MNRAS, 330, 75 108

Corbelli E., Palla F., Zinnecker H., eds., 2005, The Initial Mass Function 50 years later, vol. 327 of Astrophysics and Space Science Library 69

Covino S., Stefanon M., Sciuto G., et al., 2004, in Ground-based Instrumentation for Astronomy, edited by A. F. M. Moorwood, M. Iye, vol. 5492 of Society of Photo-Optical Instrumentation Engineers (SPIE) Conference Series, 1613–1622 23

Cox P., 1995, in The Eta Carinae Region: A Laboratory of Stellar Evolution, eds. V. Niemela, N. Morrell, & A. Feinstein, Rev. Mexicana Astron. Astrofis. Ser. Conf., 2, 105 41

Crockett R. M., Eldridge J. J., Smartt S. J., et al., 2008, MNRAS, 391, L5 84, 153

Cropper M., Bailey J., McCowage J., Cannon R. D., Couch W. J., 1988, MNRAS, 231, 695 114, 130

Crowther P. A., 2007, ARA&A, 45, 177 6, 7, 40, 153

Crowther P. A., Hillier D. J., Smith L. J., 1995, A&A, 293, 403 42

Cucciati O., Tresse L., Ilbert O., et al., 2012, A&A, 539, A31 181

Cutispoto G., Zerbi F. M., Chincarini G., REM/Ross Team, 2004, Baltic Astronomy, 13, 307 23

Cutri R. M., Skrutskie M. F., van Dyk S., et al., 2003, VizieR Online Data Catalog, 2246, 0 45

Dahlen T., Goobar A., 2002, PASP, 114, 284 192, 196

Dahlen T., Strolger L.-G., Riess A. G., 2008, ApJ, 681, 462 xxxvii, 181, 189, 190

Dahlen T., Strolger L.-G., Riess A. G., et al., 2004, ApJ, 613, 189 xxxvii, 189, 190

Davies B., Kudritzki R.-P., Figer D. F., 2010, MNRAS, 407, 1203 5

de Graauw T., Lidholm S., Fitton B., et al., 1981, A&A, 102, 257 41

Deep A., Fiorentino G., Tolstoy E., et al., 2011, A&A, 531, A151 186

DeGioia-Eastwood K., Throop H., Walker G., Cudworth K. M., 2001, ApJ, 549, 578 43, 48

Denis S., 2011, Test report - angular velocity stability of ILMT primary mirror with mercury (3mm). Tech. Rep., AMOS 142

Dessart L., Hillier D. J., 2005a, A&A, 439, 671 184

Dessart L., Hillier D. J., 2005b, A&A, 437, 667 xl, 104, 105, 111

Dessart L., Hillier D. J., 2011, MNRAS, 410, 1739 113

Dessart L., Hillier D. J., Waldman R., Livne E., Blondin S., 2012, MNRAS, 426, L76 18

Dickel H. R., 1974, A&A, 31, 11 41

Dilday B., Kessler R., Frieman J. A., et al., 2008, ApJ, 682, 262 xxxvii, 189, 190

Dilday B., Smith M., Bassett B., et al., 2010, ApJ, 713, 1026 189

Doi T., Nakano S., Itagaki K., Naito H., Iizuka R., 2007, Central Bureau Electronic Telegrams, 848, 1 132

Drake A. J., Djorgovski S. G., Mahabal A., et al., 2009, ApJ, 696, 870 23

Drissen L., Moffat A. F. J., Walborn N. R., Shara M. M., 1995, AJ, 110, 2235 10

Drout M. R., Massey P., Meynet G., 2012, ApJ, 750, 97 6

Drout M. R., Soderberg A. M., Gal-Yam A., et al., 2011, ApJ, 741, 97 92, 94, 96

Dufour R. J., van Orsow D., Walter D. K., Hester J. J., Currie D. G., 1998, in Astrophysical plasmas - near and far, eds. R. J. Dufour, & S. Torres-Peimbert, Rev. Mexicana Astron. Astrofis. Ser. Conf., 7, 217 41

Ekström S., Georgy C., Eggenberger P., et al., 2012, A&A, 537, A146 5

Eldridge J. J., Fraser M., Smartt S. J., Maund J. R., Crockett R. M., 2013, MNRAS, 436, 774 xxvi, 9, 24, 25

Elias-Rosa N., Van Dyk S. D., Li W., et al., 2009, ApJ, 706, 1174 152

Elias-Rosa N., Van Dyk S. D., Li W., et al., 2010, ApJ, 714, L254 153

Elmegreen B. G., 1998, in Origins, edited by C. E. Woodward, J. M. Shull, H. A. Thronson, Jr., vol. 148 of Astronomical Society of the Pacific Conference Series, 150 10, 39

Elmhamdi A., Danziger I. J., Branch D., Leibundgut B., Baron E., Kirshner R. P., 2006, A&A, 450, 305 83, 102

Elmhamdi A., Danziger I. J., Chugai N., et al., 2003, MNRAS, 338, 939 130

Ergon M., Sollerman J., Fraser M., et al., 2014, A&A, 562, A17 98

Espinoza P., Selman F. J., Melnick J., 2009, A&A, 501, 563 69

Eswaraiah C., Maheswar G., Pandey A. K., Jose J., Ramaprakash A. N., Bhatt H. C., 2013, A&A, 556, A65 120

Eswaraiah C., Pandey A. K., Maheswar G., et al., 2011, MNRAS, 411, 1418 120

Eswaraiah C., Pandey A. K., Maheswar G., Chen W. P., Ojha D. K., Chandola H. C., 2012, MNRAS, 419, 2587 120

REFERENCES

Fagotti P., Dimai A., Quadri U., et al., 2012, Central Bureau Electronic Telegrams, 3054, 1 115

Falck B. L., Riess A. G., Hlozek R., 2010, ApJ, 723, 398 196

Falk S. W., Arnett W. D., 1977, ApJS, 33, 515 84, 128

Feigelson E. D., Broos P., Gaffney III J. A., et al., 2002, ApJ, 574, 258 63

Feigelson E. D., Montmerle T., 1999, ARA&A, 37, 363 11, 52

Feinstein A., 1981, PASP, 93, 202 48

Feinstein A., 1983, Ap&SS, 96, 293 48

Feinstein A., 1995, in The Eta Carinae Region: A Laboratory of Stellar Evolution, eds. V. Niemela, N. Morrell, & A. Feinstein, Rev. Mexicana Astron. Astrofis. Ser. Conf., 2, 57 39

Feinstein A., Marraco H. G., Muzzio J. C., 1973, A&AS, 12, 331 47, 48

Fesen R. A., 2001, ApJS, 133, 161 21

Filippenko A. V., 1988, AJ, 96, 1941 83, 84

Filippenko A. V., 1991, in Supernovae and Stellar Evolution, edited by A. Ray, T. Velusamy, 58 13, 15

Filippenko A. V., 1997, ARA&A, 35, 309 13, 83, 197

Filippenko A. V., Chornock R., 2003, IAU Circ., 8084, 4 83

Filippenko A. V., Leonard D. C., 2004, in Cosmic explosions in three dimensions, edited by P. Höflich, P. Kumar, J. C. Wheeler, 30 21, 114

Filippenko A. V., Li W. D., Treffers R. R., Modjaz M., 2001, in IAU Colloq. 183: Small Telescope Astronomy on Global Scales, edited by B. Paczynski, W.-P. Chen, C. Lemme, vol. 246 of Astronomical Society of the Pacific Conference Series, 121 182, 189

Finet F., 2013, in PhD Thesis, University of Liège, Belgium, 13–170 xxvi, xl, 27, 28, 144, 145, 151, 168, 172, 173, 187

Fisher A., Branch D., Nugent P., Baron E., 1997, ApJ, 481, L89 102

Fitzgerald M. P., Mehta S., 1987, MNRAS, 228, 545 48

Folatelli G., Gonzalez S., Morrell N., 2007, Central Bureau Electronic Telegrams, 850, 1 132

Forte J. C., 1978, AJ, 83, 1199 47

Fowler W. A., Hoyle F., 1964, ApJS, 9, 201 3, 17

Fraley G. S., 1967, Supernovae Explosions Induced by Pair Production Instability., Ph.D. thesis, CALIFORNIA INSTITUTE OF TECHNOLOGY. 17

Fraser M., Maund J. R., Smartt S. J., et al., 2012, ApJ, 759, L13 115, 116

Fraser M., Takáts K., Pastorello A., et al., 2010, ApJ, 714, L280 153

Freedman W. L., Madore B. F., Gibson B. K., et al., 2001, ApJ, 553, 47 115

Fremling C., Sollerman J., Taddia F., et al., 2014, A&A, 565, A114 153

Freyer T., Hensler G., Yorke H. W., 2003, ApJ, 594, 888 10

Fryer C. L., 1999, ApJ, 522, 413 21, 83

Gaczkowski B., Preibisch T., Ratzka T., Roccatagliata V., Ohlendorf H., Zinnecker H., 2013, A&A, 549, A67 42, 54, 58, 64, 72, 74

Gal-Yam A., 2012, Science, 337, 927 17

Gal-Yam A., Kasliwal M. M., Arcavi I., et al., 2011, ApJ, 736, 159 84

Gal-Yam A., Leonard D. C., 2009, Nature, 458, 865 9, 16

Gal-Yam A., Leonard D. C., Fox D. B., et al., 2007, ApJ, 656, 372 16

Gal-Yam A., Mazzali P., Ofek E. O., et al., 2009, Nature, 462, 624 17, 18

Garay G., Lizano S., 1999, PASP, 111, 1049 39

Garmire G. P., Bautz M. W., Ford P. G., Nousek J. A., Ricker Jr. G. R., 2003, in Society of Photo-Optical Instrumentation Engineers (SPIE) Conf. Ser., eds. J. E. Truemper & H. D. Tananbaum, vol. 4851, 28–44 62

Garnett D. R., 2002, ApJ, 581, 1019 109

Getman K. V., Flaccomio E., Broos P. S., et al., 2005, ApJS, 160, 319 63

Ghosh S. K., Iyengar K. V. K., Rengarajan T. N., Tandon S. N., Verma R. P., Daniel R. R., 1988, ApJ, 330, 928 41

Giavalisco M., Ferguson H. C., Koekemoer A. M., et al., 2004, ApJ, 600, L93 189

Gibson B. K., 1991, JRASC, 85, 158 25, 26

Gibson B. K., Hickson P., 1991, in The Space Distribution of Quasars, edited by D. Crampton, vol. 21 of Astronomical Society of the Pacific Conference Series, 80–83 31

Gibson B. K., Hickson P., 1992, MNRAS, 258, 543 147

Glassgold A. E., Huggins P. J., 1986, ApJ, 306, 605 12

Gomez M., Hartmann L., Kenyon S. J., Hewett R., 1993, AJ, 105, 1927 76

Gong Y., Cooray A., Chen X., 2010, ApJ, 709, 1420 196

Gorosabel J., de Ugarte Postigo A., Castro-Tirado A. J., et al., 2010, A&A, 522, A14 132, 133

REFERENCES

Gorosabel J., Larionov V., Castro-Tirado A. J., et al., 2006, A&A, 459, L33 23, 113

Gosset E., Nazé Y., Sana H., Rauw G., Vreux J.-M., 2009, A&A, 508, 805 42, 48, 60

Gosset E., Remy M., Manfroid J., et al., 1991, Information Bulletin on Variable Stars, 3571, 1 42

Grabelsky D. A., Cohen R. S., Bronfman L., Thaddeus P., 1988, ApJ, 331, 181 39

Grassberg E. K., Imshennik V. S., Nadyozhin D. K., 1971, Ap&SS, 10, 28 128

Graur O., Poznanski D., Maoz D., et al., 2011, MNRAS, 417, 916 181, 189

Graur O., Rodney S. A., Maoz D., et al., 2014, ApJ, 783, 28 181, 189

Green D. A., Stephenson F. R., 2003, in Supernovae and Gamma-Ray Bursters, edited by K. Weiler, vol. 598 of Lecture Notes in Physics, Berlin Springer Verlag, 7–19 12

Gritschneder M., Burkert A., Naab T., Walch S., 2010, ApJ, 723, 971 10, 72

Groh J. H., Georgy C., Ekström S., 2013a, A&A, 558, L1 153

Groh J. H., Meynet G., Georgy C., Ekström S., 2013b, A&A, 558, A131 8, 25

Guetter H. H., Vrba F. J., 1989, AJ, 98, 611 47

Günther H. M., Wolk S. J., Spitzbart B., et al., 2012, AJ, 144, 101 78

Gutermuth R. A., Megeath S. T., Myers P. C., Allen L. E., Pipher J. L., Fazio G. G., 2009, ApJS, 184, 18 55, 76, 78

Gutermuth R. A., Megeath S. T., Pipher J. L., et al., 2005, ApJ, 632, 397 55, 76

Gutermuth R. A., Myers P. C., Megeath S. T., et al., 2008, ApJ, 674, 336 76

Guy J., Astier P., Baumont S., et al., 2007, A&A, 466, 11 196

Guy J., Astier P., Nobili S., Regnault N., Pain R., 2005, A&A, 443, 781 196

Hadfield L. J., Crowther P. A., Schild H., Schmutz W., 2005, A&A, 439, 265 8

Hadfield L. J., van Dyk S. D., Morris P. W., Smith J. D., Marston A. P., Peterson D. E., 2007, MNRAS, 376, 248 153

Hadjiyska E., Rabinowitz D., Baltay C., et al., 2011, The Astronomer's Telegram, 3812, 1 23

Hamaguchi K., Petre R., Matsumoto H., et al., 2007, PASJ, 59, 151 41

Hamann W.-R., Duennebeil G., Koesterke L., Wessolowski U., Schmutz W., 1991, A&A, 249, 443 42

Hamuy M., Deng J., Mazzali P. A., et al., 2009, ApJ, 703, 1612 xxxi, 84, 96, 106

Hamuy M., Walker A. R., Suntzeff N. B., Gigoux P., Heathcote S. R., Phillips M. M., 1992, PASP, 104, 533 45

Han J., 2009, in IAU Symposium, edited by K. G. Strassmeier, A. G. Kosovichev, J. E. Beckman, vol. 259 of IAU Symposium, 455–466 125

Hardin D., Afonso C., Alard C., et al., 2000, A&A, 362, 419 xxxvii, 189, 190

Harper G. M., Brown A., 2006, ApJ, 646, 1179 12

Harper G. M., Brown A., Guinan E. F., 2008, AJ, 135, 1430 12

Harper G. M., Brown A., Lim J., 2001, ApJ, 551, 1073 12

Harutyunyan A. H., Pfahler P., Pastorello A., et al., 2008, A&A, 488, 383 198

Harvey P. M., Hoffmann W. F., Campbell M. F., 1979, ApJ, 227, 114 41

Hatano K., Branch D., Fisher A., Millard J., Baron E., 1999, ApJS, 121, 233 107

Heger A., Fryer C. L., Woosley S. E., Langer N., Hartmann D. H., 2003a, ApJ, 591, 288 xxv, 20, 83

Heger A., Fryer C. L., Woosley S. E., Langer N., Hartmann D. H., 2003b, ApJ, 591, 288 21, 153

Heger A., Woosley S. E., 2002, ApJ, 567, 532 17

Heger A., Woosley S. E., 2010, ApJ, 724, 341 18

Heiles C., 1996, in Polarimetry of the Interstellar Medium, edited by W. G. Roberge, D. C. B. Whittet, vol. 97 of Astronomical Society of the Pacific Conference Series, 457 125

Heiles C., 2000, AJ, 119, 923 xxxii, 117, 121

Herbig G. H., Bell K. R., 1988, Third Catalog of Emission-Line Stars of the Orion Population : 3 : 1988 53

Herbst W., 1976, ApJ, 208, 923 47

Hickson P., 2008a, Analysis and recommendations concerning the ILMT primary mirror, air bearing, interface and air system, Tech. Rep. R01, The University of British Columbia 142, 143, 158

Hickson P., 2008b, Requirements for the ILMT primary mirror system, Tech. Rep. R02, The University of British Columbia 143

Hickson P., Borra E. F., Cabanac R., et al., 1998, in Advanced Technology Optical/IR Telescopes VI, edited by L. M. Stepp, vol. 3352 of Society of Photo-Optical Instrumentation Engineers (SPIE) Conference Series, 226–232 34

Hickson P., Borra E. F., Cabanac R., Content R., Gibson B. K., Walker G. A. H., 1994, ApJ, 436, L201 xxvi, 31, 32

Hickson P., Gibson B. K., Hogg D. W., 1993, PASP, 105, 501 144

REFERENCES

Hickson P., Mulrooney M. K., 1998, ApJS, 115, 35 32

Hickson P., Pfrommer T., Cabanac R., et al., 2007, PASP, 119, 444 27, 34, 137, 174

Hickson P., Racine R., 2007, PASP, 119, 456 34

Hickson P., Richardson E. H., 1998, PASP, 110, 1081 138, 147, 151

Hillenbrand L. A., 1997, AJ, 113, 1733 10

Hillenbrand L. A., 2005, arXiv:astro-ph/0511083 67

Hillenbrand L. A., Bauermeister A., White R. J., 2008, in 14th Cambridge Workshop on Cool Stars, Stellar Systems, and the Sun, edited by G. van Belle, ASP Conf. Ser., 384, 200 67

Hillenbrand L. A., Hartmann L. W., 1998, ApJ, 492, 540 10

Hillenbrand L. A., Strom S. E., Vrba F. J., Keene J., 1992, ApJ, 397, 613 59

Hillier D. J., Davidson K., Ishibashi K., Gull T., 2001, ApJ, 553, 837 41

Hirata K., Kajita T., Koshiba M., Nakahata M., Oyama Y., 1987, Physical Review Letters, 58, 1490 130

Hodapp K. W., Kaiser N., Aussel H., et al., 2004, Astronomische Nachrichten, 325, 636 23

Hoeflich P., 1995, ApJ, 440, 821 22, 114

Hoflich P., 1991, A&A, 246, 481 113, 114

Höflich P., Khokhlov A., Wang L., 2001, in 20th Texas Symposium on relativistic astrophysics, edited by J. C. Wheeler, H. Martel, vol. 586 of American Institute of Physics Conference Series, 459–471 113

Hopkins A. M., 2004, ApJ, 615, 209 181

Hopkins A. M., Beacom J. F., 2006, ApJ, 651, 142 181

Horesh A., Poznanski D., Ofek E. O., Maoz D., 2008, MNRAS, 389, 1871 xxxvii, 189, 190

Horesh A., Stockdale C., Fox D. B., et al., 2013, MNRAS, 436, 1258 84

Horne K., 1986, PASP, 98, 609 88

Hough J. H., Bailey J. A., Rouse M. F., Whittet D. C. B., 1987, MNRAS, 227, 1P 124

Houk N., Cowley A. P., 1975, University of Michigan Catalogue of two-dimensional spectral types for the HD stars. Volume I 51

Howell S. B., 1989, PASP, 101, 616 186

Howell S. B., 2000, Handbook of CCD Astronomy 147, 186

Hoyle F., Fowler W. A., 1960, ApJ, 132, 565 3, 19

Humphreys R. M., 1978, ApJS, 38, 309 10, 48

Humphreys R. M., Davidson K., 1994, PASP, 106, 1025 6

Hur H., Sung H., Bessell M. S., 2012, AJ, 143, 41 47, 48, 50

Immler S., Brown P. J., 2012, The Astronomer's Telegram, 3995, 1 116

Itoh R., Ui T., Yamanaka M., 2012, Central Bureau Electronic Telegrams, 3054, 2 115

Ivezic Z., Axelrod T., Brandt W. N., et al., 2008, Serbian Astronomical Journal, 176, 1 23

Iwamoto K., Mazzali P. A., Nomoto K., et al., 1998, Nature, 395, 672 15

Jahoda K., Swank J. H., Giles A. B., et al., 1996, in EUV, X-Ray, and Gamma-Ray Instrumentation for Astronomy VII, edited by O. H. Siegmund, M. A. Gummin, vol. 2808 of Society of Photo-Optical Instrumentation Engineers (SPIE) Conference Series, 59–70 23

Janka H.-T., 2012, Annual Review of Nuclear and Particle Science, 62, 407 9, 21

Janka H.-T., Müller E., 1993, in Frontiers of Neutrino Astrophysics, edited by Y. Suzuki, K. Nakamura, 203–217 19

Jayawardhana R., Mohanty S., Basri G., 2003, ApJ, 592, 282 53

Jeffery D. J., 1991, ApJS, 77, 405 114

Jeffries R. D., Thurston M. R., Pye J. P., 1997, MNRAS, 287, 350 60

Jerkstrand A., Smartt S. J., Fraser M., et al., 2014, MNRAS, 439, 3694 117

Jha S., Riess A. G., Kirshner R. P., 2007, ApJ, 659, 122 196

Johnson B. D., Crotts A. P. S., 2006, AJ, 132, 756 196

Jose J., Pandey A. K., Ojha D. K., et al., 2008, MNRAS, 384, 1675 63, 70

Joshi R., Chand H., 2013, MNRAS, 429, 1717 140

Kasen D., Bildsten L., 2010, ApJ, 717, 245 18

Kasen D., Thomas R. C., Nugent P., 2006, ApJ, 651, 366 113

Kasen D., Woosley S. E., Heger A., 2011, ApJ, 734, 102 17

Kawabata K. S., Deng J., Wang L., et al., 2003, ApJ, 593, L19 23, 113

Kawabata K. S., Jeffery D. J., Iye M., et al., 2002, ApJ, 580, L39 23, 113

Kelly P. L., Kirshner R. P., 2012, ApJ, 759, 107 108

Kelly P. L., Kirshner R. P., Pahre M., 2008, ApJ, 687, 1201 13

REFERENCES

Khokhlov A., Höflich P., 2001, in Explosive Phenomena in Astrophysical Compact Objects, edited by H.-Y. Chang, C.-H. Lee, M. Rho, I. Yi, vol. 556 of American Institute of Physics Conference Series, 301–312 113

Kim A. G., Miquel R., 2007, Astroparticle Physics, 28, 448 192

Kingsburgh R. L., Barlow M. J., Storey P. J., 1995, A&A, 295, 75 7

Kippenhahn R., Weigert A., 1990, Stellar Structure and Evolution 17

Kirshner R. P., 1990, in Supernovae, edited by A. G. Petschek, 59–75 13

Kirshner R. P., Kwan J., 1974, ApJ, 193, 27 184

Kleiser I. K. W., Poznanski D., Kasen D., et al., 2011, MNRAS, 415, 372 152

Kobulnicky H. A., Zaritsky D., 1999, ApJ, 511, 118 108

Kochanek C. S., Khan R., Dai X., 2012, ApJ, 759, 20 116

Kolmogorov A., 1941, Akademiia Nauk SSSR Doklady, 30, 301 3

Kotak R., Meikle P., Pozzo M., et al., 2006, ApJ, 651, L117 130

Kotake K., Sumiyoshi K., Yamada S., et al., 2012, Progress of Theoretical and Experimental Physics, 2012, 1, 010000 9

Kozyreva A., Yoon S.-C., Langer N., 2014, A&A, 566, A146 17

Krause O., Birkmann S. M., Usuda T., et al., 2008, Science, 320, 1195 12

Krauss M. I., Soderberg A. M., Chomiuk L., et al., 2012, ApJ, 750, L40 84

Kroupa P., 2002, Science, 295, 82 69

Kudritzki R.-P., Puls J., 2000, ARA&A, 38, 613 10

Kumar B., Pandey S. B., Eswaraiah C., Gorosabel J., 2014a, MNRAS, 442, 2 vii, x

Kumar B., Pandey S. B., Sahu D. K., et al., 2013, MNRAS, 431, 308 vii, ix, xxxix, 17, 100, 140

Kumar B., Sagar R., Rautela B. S., Srivastava J. B., Srivastava R. K., 2000, Bulletin of the Astronomical Society of India, 28, 675 87

Kumar B., Sharma S., Manfroid J., et al., 2014b, A&A, 567, A109 vii, ix, xxvii, 40

Kunz M., Bassett B. A., Hlozek R. A., 2007, Phys. Rev. D, 75, 10, 103508 192, 196

Kuroda T., Kotake K., Takiwaki T., 2012, ApJ, 755, 11 9

Kuznetsova N., Barbary K., Connolly B., et al., 2008, ApJ, 673, 981 xxxvii, 189, 190

Kuznetsova N. V., Connolly B. M., 2007, ApJ, 659, 530 196

Lada C. J., Alves J., Lada E. A., 1996, AJ, 111, 1964 76

Lada C. J., Lada E. A., 2003, ARA&A, 41, 57 10, 70

Lançon A., Gallagher J. S., Mouhcine M., Smith L. J., Ladjal D., de Grijs R., 2009, Ap&SS, 324, 241 5

Landolt A. U., 2009, AJ, 137, 4186 87

Le Floc'h E., Papovich C., Dole H., et al., 2005, ApJ, 632, 169 181

Leaman J. F., Li W., Filippenko A., LOSS, 2009, in American Astronomical Society Meeting Abstracts 214, vol. 214 of American Astronomical Society Meeting Abstracts, 316.02 23

Leibundgut B., Suntzeff N. B., 2003, in Supernovae and Gamma-Ray Bursters, edited by K. Weiler, vol. 598 of Lecture Notes in Physics, Berlin Springer Verlag, 77–90 195

Leinert C., Bowyer S., Haikala L. K., et al., 1998, A&AS, 127, 1 xxxiv, 142

Leitherer C., Robert C., Drissen L., 1992, ApJ, 401, 596 3

Leloudas G., Gallazzi A., Sollerman J., et al., 2011, A&A, 530, A95 108

Lennarz D., Altmann D., Wiebusch C., 2012, A&A, 538, A120 xxvi, 15, 24

Leonard D. C., 2007, ArXiv e-prints xxvi, 22

Leonard D. C., Dessart L., Hillier D. J., Pignata G., 2012a, in American Institute of Physics Conference Series, edited by J. L. Hoffman, J. Bjorkman, B. Whitney, vol. 1429 of American Institute of Physics Conference Series, 204–207 114, 130, 132

Leonard D. C., Filippenko A. V., 2001, PASP, 113, 920 23, 113, 114

Leonard D. C., Filippenko A. V., 2005, in 1604-2004: Supernovae as Cosmological Lighthouses, edited by M. Turatto, S. Benetti, L. Zampieri, W. Shea, vol. 342 of Astronomical Society of the Pacific Conference Series, 330 113, 114

Leonard D. C., Filippenko A. V., Ardila D. R., Brotherton M. S., 2001, ApJ, 553, 861 113, 114, 125, 130

Leonard D. C., Filippenko A. V., Chornock R., Li W., 2002, AJ, 124, 2506 125

Leonard D. C., Filippenko A. V., Ganeshalingam M., et al., 2006, Nature, 440, 505 114, 130

Leonard D. C., Pignata G., Dessart L., et al., 2012b, The Astronomer's Telegram, 4033, 1 117

Levato H., Malaroda S., 1981, PASP, 93, 714 48

Levato H., Malaroda S., 1982, PASP, 94, 807 48

Lewis J. R., Walton N. A., Meikle W. P. S., et al., 1994, MNRAS, 266, L27 xxxi, 84, 90, 92, 93, 94, 96, 98, 99, 106

REFERENCES

Li W., Leaman J., Chornock R., et al., 2011, MNRAS, 412, 1441 23, 96, 189, 190

Li W., Van Dyk S. D., Filippenko A. V., et al., 2006, ApJ, 641, 1060 152

Li W., Wang X., Van Dyk S. D., Cuillandre J.-C., Foley R. J., Filippenko A. V., 2007, ApJ, 661, 1013 131

Lien A., Fields B. D., 2009, J. Cosmology Astropart. Phys., 1, 47 xxxvi, 183, 184, 191

Lim B., Sung H. S., Karimov R., Ibrahimov M., 2011, Journal of Korean Astronomical Society, 44, 39 47

Liu Q., de Grijs R., Deng L. C., Hu Y., Baraffe I., Beaulieu S. F., 2009, MNRAS, 396, 1665 70

Mackey J., Bromm V., Hernquist L., 2003, ApJ, 586, 1 9

Madau P., della Valle M., Panagia N., 1998, MNRAS, 297, L17 181

Maeda K., 2013, ApJ, 762, 14 17

Maeder A., Meynet G., 2001, A&A, 373, 555 8

Maeder A., Meynet G., 2012, Reviews of Modern Physics, 84, 25 7, 8

Magette A., 2010, in PhD Thesis, University of Liege, Belgium, 7–253 27, 33, 151, 187

Mailly E., 1872, De l'astronomie dans l'Académie royale de Belgique. Rapport séculaire (1772-1872) 26

Mallick K. K., Ojha D. K., Samal M. R., et al., 2012, ApJ, 759, 48 57

Manchester R. N., 1987, A&A, 171, 205 21

Marek A., Janka H.-T., 2009, ApJ, 694, 664 9

Marigo P., Girardi L., Bressan A., Groenewegen M. A. T., Silva L., Granato G. L., 2008, A&A, 482, 883 xxviii, xxix, 64, 65, 66

Marraco H. G., Vega E. I., Vrba F. J., 1993, AJ, 105, 258 49

Martí-Vidal I., Tudose V., Paragi Z., et al., 2011, A&A, 535, L10 84

Martin D. C., Fanson J., Schiminovich D., et al., 2005, ApJ, 619, L1 23

Massey P., Hunter D. A., 1998, ApJ, 493, 180 10

Massey P., Johnson J., 1993, AJ, 105, 980 43, 48

Massey P., Olsen K. A. G., 2003, AJ, 126, 2867 8, 153

Matsuoka M., Kawasaki K., Ueno S., et al., 2009, PASJ, 61, 999 23

Mattila S., Smartt S. J., Eldridge J. J., Maund J. R., Crockett R. M., Danziger I. J., 2008, ApJ, 688, L91 152

Maund J. R., Fraser M., Ergon M., et al., 2011, ApJ, 739, L37 84, 153

Maund J. R., Smartt S. J., 2005, MNRAS, 360, 288 152

Maund J. R., Smartt S. J., Danziger I. J., 2005, MNRAS, 364, L33 152

Maund J. R., Smartt S. J., Kudritzki R. P., Podsiadlowski P., Gilmore G. F., 2004, Nature, 427, 129 84, 152

Maund J. R., Spyromilio J., Höflich P. A., et al., 2013, MNRAS, 433, L20 23, 113

Maund J. R., Wheeler J. C., Patat F., Wang L., Baade D., Höflich P. A., 2007, ApJ, 671, 1944 23, 113, 125

Maurer I., Mazzali P. A., Taubenberger S., Hachinger S., 2010, MNRAS, 409, 1441 83

Mauron N., Josselin E., 2011, A&A, 526, A156 5

Mayya Y. D., 1991, Journal of Astrophysics and Astronomy, 12, 319 185

Mazzali P. A., Deng J., Hamuy M., Nomoto K., 2009, ApJ, 703, 1624 84

Mazzali P. A., Deng J., Maeda K., et al., 2002, ApJ, 572, L61 15

Mazzali P. A., Deng J., Tominaga N., et al., 2003, ApJ, 599, L95 15

Mazzali P. A., Iwamoto K., Nomoto K., 2000, ApJ, 545, 407 15

McCall M. L., 1984, MNRAS, 210, 829 114

McLean I. S., 1989, Electronic and computer-aided astronomy: From eyes to electronic sensors 185

Medhi B. J., Maheswar G., Pandey J. C., Tamura M., Sagar R., 2010, MNRAS, 403, 1577 119

Melbourne J., Salzer J. J., 2002, AJ, 123, 2302 108

Melinder J., 2011, in PhD Thesis, Stockholm University, Sweden, 1–71 197

Mendez M., Clocchiatti A., Benvenuto O. G., Feinstein C., Marraco H. G., 1988, ApJ, 334, 295 114

Meyer M. R., Calvet N., Hillenbrand L. A., 1997, AJ, 114, 288 xxviii, 58

Meynet G., Maeder A., Schaller G., Schaerer D., Charbonnel C., 1994, A&AS, 103, 97 9

Milisavljevic D., Margutti R., Soderberg A. M., et al., 2013, ApJ, 767, 71 84, 92, 96

Miller G. E., Scalo J. M., 1978, PASP, 90, 506 70

Miller G. E., Scalo J. M., 1979, ApJS, 41, 513 69

Minkowski R., 1941, PASP, 53, 224 13

REFERENCES

Modjaz M., Kewley L., Bloom J. S., Filippenko A. V., Perley D., Silverman J. M., 2011, ApJ, 731, L4 108

Moffat A. F. J., Drissen L., Shara M. M., 1994, ApJ, 436, 183 10

Monard L. A. G., 2007, Central Bureau Electronic Telegrams, 845, 1 83

Morrell N., Garcia B., Levato H., 1988, PASP, 100, 1431 48

Morrell N., Stritzinger M., 2008, Central Bureau Electronic Telegrams, 1335, 1 132

Moskvitin A. S., Sonbas E., Sokolov V. V., Fatkhullin T. A., Castro-Tirado A. J., 2010, Astrophysical Bulletin, 65, 132 107

Motte F., Andre P., Neri R., 1998, A&A, 336, 150 76

Muench A. A., Lada E. A., Lada C. J., 2000, ApJ, 533, 358 70

Müller E., 1994, in Supernovae, edited by S. A. Bludman, R. Mochkovitch, J. Zinn-Justin, 393 19

Mulrooney M., 2000, A 3.0 meter liquid mirror telescope, Ph.D. thesis, RICE UNIVERSITY 172

Munari U., Henden A., Belligoli R., et al., 2013, New A, 20, 30 116

Munari U., Vagnozzi A., Castellani F., 2012, Central Bureau Electronic Telegrams, 3054, 3 115

Munari U., Zwitter T., 1997, A&A, 318, 269 94

Nakano S., Itagaki K., Kadota K., 2006, Central Bureau Electronic Telegrams, 756, 1 131

Nakar E., Sari R., 2010, ApJ, 725, 904 92, 192

Neill J. D., Sullivan M., Balam D., et al., 2006, AJ, 132, 1126 xxxvii, 189, 190

Niemela V. S., 1979, in Mass Loss and Evolution of O-Type Stars, edited by P. S. Conti, C. W. H. De Loore, vol. 83 of IAU Symposium, 291–293 42

Ninane N. M., Jamar C. A., 1996, Appl. Opt., 35, 6131 33

Nomoto K., Maeda K., Umeda H., Ohkubo T., Deng J., Mazzali P., 2003, in A Massive Star Odyssey: From Main Sequence to Supernova, eds. K. van der Hucht, A. Herrero, & C. Esteban, vol. 212 of IAU Symposium, 395 39

Nugent P., Kim A., Perlmutter S., 2002, PASP, 114, 803 196

Oates S. R., Bayless A. J., Stritzinger M. D., et al., 2012, MNRAS, 424, 1297 84, 96

Oguri M., Marshall P. J., 2010, MNRAS, 405, 2579 xxxvii, 190

Ojha D. K., Tamura M., Nakajima Y., et al., 2004, ApJ, 608, 797 59

Okada Y., Onaka T., Shibai H., Doi Y., 2003, A&A, 412, 199 49

Okumura J. E., Ihara Y., Doi M., et al., 2014, PASJ, 66, 49 181, 189

Olsson-Steel D., 1986, JRASC, 80, 128 25

Pain R., Fabbro S., Sullivan M., et al., 2002, ApJ, 577, 120 xxxvii, 189, 190

Pain R., Hook I. M., Deustua S., et al., 1996, ApJ, 473, 356 191

Paliya V. S., Stalin C. S., Kumar B., et al., 2013, MNRAS, 428, 2450 140

Pandey A. K., Ogura K., Sekiguchi K., 2000, PASJ, 52, 847 48

Pandey A. K., Sharma S., Ogura K., et al., 2008, MNRAS, 383, 1241 63, 70

Pandey A. K., Upadhyay K., Nakada Y., Ogura K., 2003, A&A, 397, 191 48, 49

Pandey J. C., Medhi B. J., Sagar R., Pandey A. K., 2009, MNRAS, 396, 1004 120

Papaliolios C., Krasovska M., Koechlin L., Nisenson P., Standley C., 1989, Nature, 338, 565 21

Pâris I., Petitjean P., Aubourg É., et al., 2014, A&A, 563, A54 195

Parker J. W., Garmany C. D., 1993, AJ, 106, 1471 10

Pastorello A., Kasliwal M. M., Crockett R. M., et al., 2008, MNRAS, 389, 955 xxxi, 84, 92, 95, 96, 98, 99, 106

Patat F., Barbon R., Cappellaro E., Turatto M., 1993, A&AS, 98, 443 16

Patat F., Barbon R., Cappellaro E., Turatto M., 1994, A&A, 282, 731 16

Patat F., Carraro G., 2001, MNRAS, 325, 1591 48

Patat F., Höflich P., Baade D., Maund J. R., Wang L., Wheeler J. C., 2012, A&A, 545, A7 23, 113

Paturel G., Petit C., Prugniel P., et al., 2003, A&A, 412, 45 115

Pauldrach A., Puls J., Kudritzki R. P., 1986, A&A, 164, 86 10

Pauldrach A., Puls J., Kudritzki R. P., Mendez R. H., Heap S. R., 1988, A&A, 207, 123 9

Pereyra A., Magalhães A. M., Rodrigues C. V., et al., 2006, A&A, 454, 827 130

Perrett K., Sullivan M., Conley A., et al., 2012, AJ, 144, 59 181, 189

Pfrommer T., Hickson P., She C.-Y., Vance J. D., 2008, in Society of Photo-Optical Instrumentation Engineers (SPIE) Conference Series, vol. 7015 of Society of Photo-Optical Instrumentation Engineers (SPIE) Conference Series 34

Pires A. M., Motch C., Turolla R., Treves A., Popov S. B., 2009, A&A, 498, 233 41

Podsiadlowski P., Joss P. C., Hsu J. J. L., 1992, ApJ, 391, 246 84

Poels J., Borra E., Hickson P., et al., 2012, in IAU Symposium, edited by E. Griffin, R. Hanisch, R. Seaman, vol. 285 of IAU Symposium, 394–396 182

REFERENCES

Potter A. E., Mulrooney M., 1997, Advances in Space Research, 19, 213 32

Povich M. S., Smith N., Majewski S. R., et al., 2011, ApJS, 194, 14 39, 42, 50, 54, 57, 58, 72, 75

Poznanski D., Gal-Yam A., Maoz D., Filippenko A. V., Leonard D. C., Matheson T., 2002, PASP, 114, 833 196

Poznanski D., Maoz D., Gal-Yam A., 2007a, AJ, 134, 1285 196

Poznanski D., Maoz D., Yasuda N., et al., 2007b, MNRAS, 382, 1169 xxxvii, 189, 190, 194

Poznanski D., Prochaska J. X., Bloom J. S., 2012, MNRAS, 426, 1465 123

Preibisch T., 2011, in Reviews in Modern Astronomy: Zooming in: The Cosmos at High Resolution, Volume 23 (ed R. von Berlepsch), Wiley-VCH Verlag GmbH & Co. KGaA, Weinheim, Germany. doi: 10.1002/9783527644384.ch13 11

Preibisch T., Hodgkin S., Irwin M., et al., 2011a, ApJS, 194, 10 11, 49

Preibisch T., Ratzka T., Gehring T., et al., 2011b, A&A, 530, A40 55

Preibisch T., Ratzka T., Kuderna B., et al., 2011c, A&A, 530, A34 10, 11, 42, 59, 60, 70

Preibisch T., Schuller F., Ohlendorf H., Pekruhl S., Menten K. M., Zinnecker H., 2011d, A&A, 525, A92 11, 42

Preibisch T., Zinnecker H., 2007, in IAU Symposium, edited by B. G. Elmegreen, J. Palous, vol. 237 of IAU Symposium, 270–277 10

Prieto J., 2009, Central Bureau Electronic Telegrams, 2087, 1 84

Prieto J. L., Stanek K. Z., Beacom J. F., 2008, ApJ, 673, 999 xxxii, 108, 109

Prisinzano L., Micela G., Flaccomio E., et al., 2008, ApJ, 677, 401 52

Pritchet C. J., Howell D. A., Sullivan M., 2008, ApJ, 683, L25 181

Puls J., Vink J. S., Najarro F., 2008, A&A Rev., 16, 209 84

Qiu Y., Li W., Qiao Q., Hu J., 1999, AJ, 117, 736 84, 93, 94, 96

Quimby R. M., Kulkarni S. R., Kasliwal M. M., et al., 2011, Nature, 474, 487 17

Quimby R. M., Wheeler J. C., Höflich P., Akerlof C. W., Brown P. J., Rykoff E. S., 2007, ApJ, 666, 1093 106, 108

Quimby R. M., Yuan F., Akerlof C., Wheeler J. C., 2013, MNRAS, 431, 912 17

Rakavy G., Shaviv G., 1967, ApJ, 148, 803 17

Ramaprakash A. N., Gupta R., Sen A. K., Tandon S. N., 1998, A&AS, 128, 369 119

Rana N. C., 1991, ARA&A, 29, 129 69

Rathborne J. M., Burton M. G., Brooks K. J., Cohen M., Ashley M. C. B., Storey J. W. V., 2002, MNRAS, 331, 85 41, 74

Rau A., Kulkarni S. R., Law N. M., et al., 2009, PASP, 121, 1334 23

Rautela B. S., Joshi G. C., Pandey J. C., 2004, Bulletin of the Astronomical Society of India, 32, 159 xxxii, 118, 119, 120

Rauw G., Manfroid J., De Becker M., 2010, A&A, 511, A25 53

Rauw G., Vreux J.-M., Gosset E., Hutsemékers D., Magain P., Rochowicz K., 1996, A&A, 306, 771 42

Remillard R. A., McClintock J. E., 2006, ARA&A, 44, 49 3

Richardson D., Branch D., Baron E., 2006, AJ, 131, 2233 92

Richardson D., Branch D., Casebeer D., Millard J., Thomas R. C., Baron E., 2002, AJ, 123, 745 96, 184

Richer M. G., McCall M. L., 1995, ApJ, 445, 642 108

Richmond M. W., Treffers R. R., Filippenko A. V., et al., 1994, AJ, 107, 1022 17, 84

Riess A. G., Nugent P. E., Gilliland R. L., et al., 2001, ApJ, 560, 49 196

Riess A. G., Press W. H., Kirshner R. P., 1995, ApJ, 438, L17 196

Riess A. G., Press W. H., Kirshner R. P., 1996, ApJ, 473, 88 196

Robin A. C., Reylé C., Derrière S., Picaud S., 2003, A&A, 409, 523 70

Robitaille T. P., Meade M. R., Babler B. L., et al., 2008, AJ, 136, 2413 57

Robitaille T. P., Whitney B. A., Indebetouw R., Wood K., Denzmore P., 2006, ApJS, 167, 256 59

Roccatagliata V., Preibisch T., Ratzka T., Gaczkowski B., 2013, A&A, 554, A6 11, 42, 49, 72, 73

Rodney S. A., Riess A. G., Strolger L.-G., et al., 2014, AJ, 148, 13 189

Rodney S. A., Tonry J. L., 2009, ApJ, 707, 1064 196

Rodney S. A., Tonry J. L., 2010, ApJ, 723, 47 189

Roming P., Prieto J., Milne P. A., 2009a, Central Bureau Electronic Telegrams, 2093, 1 84

Roming P., Pritchard T., Brown P., et al., 2010, in American Astronomical Society Meeting Abstracts #215, vol. 42 of Bulletin of the American Astronomical Society, 342.03 93

Roming P. W. A., Pritchard T. A., Brown P. J., et al., 2009b, ApJ, 704, L118 84, 92

Rujopakarn W., Eisenstein D. J., Rieke G. H., et al., 2010, ApJ, 718, 1171 181

Russell D. G., 2002, ApJ, 565, 681 115

REFERENCES

Ryder S. D., Murrowood C. E., Stathakis R. A., 2006, MNRAS, 369, L32 84

Sagar R., Kumar B., Omar A., 2013, ArXiv e-prints 140, 198

Sagar R., Kumar B., Omar A., Joshi Y. C., 2012, in Astronomical Society of India Conference Series, vol. 4 of Astronomical Society of India Conference Series, 173 87, 139, 140, 198

Sagar R., Omar A., Kumar B., et al., 2011, Current Science, 101, 8 87, 139

Saha A., Sandage A., Tammann G. A., Labhardt L., Macchetto F. D., Panagia N., 1999, ApJ, 522, 802 183

Salpeter E. E., 1955, ApJ, 121, 161 3, 69, 70, 81

Salpeter E. E., 1964, ApJ, 140, 796 192

Sanders N. E., Soderberg A. M., Foley R. J., et al., 2013, ApJ, 769, 39 13

Sanders N. E., Soderberg A. M., Levesque E. M., et al., 2012, ApJ, 758, 132 108, 109

Scalo J., 1998, in The Stellar Initial Mass Function (38th Herstmonceux Conference), eds. G. Gilmore, & D. Howell, ASP Conf. Ser., 142, 201 69

Scalo J. M., 1986, Fund. Cosmic Phys., 11, 1 69

Scarrott S. M., Rolph C. D., Semple D. P., 1990, in Galactic and Intergalactic Magnetic Fields, edited by R. Beck, R. Wielebinski, P. P. Kronberg, vol. 140 of IAU Symposium, 245–251 125

Scarrott S. M., Rolph C. D., Wolstencroft R. W., Tadhunter C. N., 1991, MNRAS, 249, 16P 125

Schiminovich D., Ilbert O., Arnouts S., et al., 2005, ApJ, 619, L47 181

Schlegel D. J., Finkbeiner D. P., Davis M., 1998, ApJ, 500, 525 94, 123

Schmidt B., 2012, in IAU Symposium, edited by E. Griffin, R. Hanisch, R. Seaman, vol. 285 of IAU Symposium, 9–10 192

Schmidt B. P., Kirshner R. P., Eastman R. G., et al., 1993, Nature, 364, 600 84

Schmidt G. D., Elston R., Lupie O. L., 1992, AJ, 104, 1563 120

Schmidt-Kaler T., 1982, in Landolt-Börnstein: Numerical Data and Functional Relationship in Science and Technology, Vol. 2b. eds. K. Schaifers, H. H. Voigt, H. Landolt (Springer-Verlag), Berlin, p. 19 xxvii, 45, 46

Schnurr O., Moffat A. F. J., St-Louis N., Morrell N. I., Guerrero M. A., 2008, MNRAS, 389, 806 8

Schroeder D. J., 1987, Astronomical optics 151

Serkowski K., 1970, ApJ, 160, 1083 21

Serkowski K., Mathewson D. S., Ford V. L., 1975, ApJ, 196, 261 123, 125

Shapiro P. R., Sutherland P. G., 1982, ApJ, 263, 902 21, 114

Shara M. M., Moffat A. F. J., Smith L. F., Niemela V. S., Potter M., Lamontagne R., 1999, AJ, 118, 390 153

Sharma S., Pandey A. K., Ojha D. K., et al., 2007, MNRAS, 380, 1141 70

Sharma S., Pandey A. K., Pandey J. C., et al., 2012, PASJ, 64, 107 63

Shields G. A., 1978, Nature, 272, 706 192

Shigeyama T., Suzuki T., Kumagai S., Nomoto K., Saio H., Yamaoka H., 1994, ApJ, 420, 341 91

Siess L., Dufour E., Forestini M., 2000, A&A, 358, 593 xxviii, xxix, 64, 65, 66, 67, 70

Siviero A., Tomasella L., Pastorello A., et al., 2012, Central Bureau Electronic Telegrams, 3054, 4 115

Skillman E. D., Kennicutt R. C., Hodge P. W., 1989, ApJ, 347, 875 108

Smartt S. J., 2009, ARA&A, 47, 63 83, 152

Smartt S. J., Eldridge J. J., Crockett R. M., Maund J. R., 2009, MNRAS, 395, 1409 9, 23, 152

Smartt S. J., Maund J. R., Hendry M. A., et al., 2004, Science, 303, 499 152

Smith N., 2002, MNRAS, 331, 7 47

Smith N., 2006a, MNRAS, 367, 763 11, 39, 40, 74

Smith N., 2006b, ApJ, 644, 1151 50

Smith N., 2010, in Hot and Cool: Bridging Gaps in Massive Star Evolution, edited by C. Leitherer, P. D. Bennett, P. W. Morris, J. T. Van Loon, vol. 425 of Astronomical Society of the Pacific Conference Series, 63 xxv, 7, 16

Smith N., Bally J., Morse J. A., 2003, ApJ, 587, L105 41

Smith N., Brooks K. J., 2007, MNRAS, 379, 1279 11

Smith N., Brooks K. J., 2008, The Carina Nebula: A Laboratory for Feedback and Triggered Star Formation, 138 11, 39, 40, 41, 42, 46, 50, 74

Smith N., Chornock R., Li W., et al., 2008a, ApJ, 686, 467 9

Smith N., Egan M. P., Carey S., Price S. D., Morse J. A., Price P. A., 2000, ApJ, 532, L145 xxvii, 40, 41

Smith N., Foley R. J., Bloom J. S., et al., 2008b, ApJ, 686, 485 9

Smith N., Hinkle K. H., Ryde N., 2009, AJ, 137, 3558 12, 16

Smith N., Li W., Filippenko A. V., Chornock R., 2011, MNRAS, 412, 1522 xxvi, 9, 24, 25

REFERENCES

Smith N., McCray R., 2007, ApJ, 671, L17 9

Smith N., Povich M. S., Whitney B. A., et al., 2010, MNRAS, 406, 952 11, 42, 64, 74, 78, 80

Smith R. G., 1987, MNRAS, 227, 943 47

Soderberg A. M., Chevalier R. A., Kulkarni S. R., Frail D. A., 2006, ApJ, 651, 1005 83

Soderberg A. M., Margutti R., Zauderer B. A., et al., 2012, ApJ, 752, 78 84

Sonbas E., Moskvitin A. S., Fatkhullin T. A., et al., 2008, Astrophysical Bulletin, 63, 228 84, 104

Stalin C. S., Gopal Krishna, Sagar R., Wiita P. J., 2004, Journal of Astrophysics and Astronomy, 25, 1 192

Stassun K. G., Ardila D. R., Barsony M., Basri G., Mathieu R. D., 2004, AJ, 127, 3537 52

Stetson P. B., 1987, PASP, 99, 191 43, 87, 175

Stetson P. B., 1992, in Astronomical Data Analysis Software and Systems I, eds. D. M. Worrall, C. Biemesderfer, & J. Barnes, ASP Conf. Ser., 25, 297 43, 87, 175

Stockdale C. J., Ryder S. D., Van Dyk S. D., et al., 2012, The Astronomer's Telegram, 4012, 1 116

Stoll R., Prieto J. L., Stanek K. Z., Pogge R. W., 2013, ApJ, 773, 12 108

Stritzinger M., 2010, Central Bureau Electronic Telegrams, 2158, 1 84

Stritzinger M., Mazzali P., Phillips M. M., et al., 2009, ApJ, 696, 713 83

Sullivan M., Howell D. A., Perrett K., et al., 2006, AJ, 131, 960 196

Sung H., Bessell M. S., Lee S.-W., 1997, AJ, 114, 2644 xxvii, 53, 54

Surdej J., Absil O., Bartczak P., et al., 2006, in Society of Photo-Optical Instrumentation Engineers (SPIE) Conference Series, vol. 6267 of Society of Photo-Optical Instrumentation Engineers (SPIE) Conference Series 151, 182, 183, 187

Taddia F., Sollerman J., Leloudas G., et al., 2014, ArXiv e-prints 192

Taddia F., Stritzinger M. D., Sollerman J., et al., 2013, A&A, 555, A10 16

Tammann G. A., Leibundgut B., 1990, A&A, 236, 9 183

Tammann G. A., Sandage A., 1995, ApJ, 452, 16 183

Tanaka M., Kawabata K. S., Hattori T., et al., 2012, ApJ, 754, 63 23, 113

Tapia M., Roth M., Marraco H., Ruiz M. T., 1988, MNRAS, 232, 661 47, 48

Tapia M., Roth M., Vázquez R. A., Feinstein A., 2003, MNRAS, 339, 44 43, 48, 50

Taubenberger S., Navasardyan H., Maurer J. I., et al., 2011, MNRAS, 413, 2140 84

Taylor M., Cinabro Y., Dilday B., et al., 2014, The Astrophysical Journal, 792, 2, 135 187, 190

Teixeira P. S., Lada C. J., Young E. T., et al., 2006, ApJ, 636, L45 76

Telleschi A., Güdel M., Briggs K. R., Audard M., Palla F., 2007, A&A, 468, 425 52

Thé P. S., Bakker R., Tjin A Djie H. R. E., 1980, A&A, 89, 209 47, 48

Thé P. S., Vleeming G., 1971, A&A, 14, 120 48

Tomasella L., Valenti S., Ochner P., Benetti S., Cappellaro E., Pastorello A., 2011, Central Bureau Electronic Telegrams, 2827, 2 86

Tonry J., Davis M., 1979, AJ, 84, 1511 197

Townsley L. K., Broos P. S., Corcoran M. F., et al., 2011, ApJS, 194, 1 42, 54, 62, 63

Tremonti C. A., Heckman T. M., Kauffmann G., et al., 2004, ApJ, 613, 898 108

Turatto M., 2003, in Supernovae and Gamma-Ray Bursters, edited by K. Weiler, vol. 598 of Lecture Notes in Physics, Berlin Springer Verlag, 21–36 xxv, 13, 15

Turner D. G., Grieve G. R., Herbst W., Harris W. E., 1980, AJ, 85, 1193 48

Ugliano M., Janka H.-T., Marek A., Arcones A., 2012, ApJ, 757, 69 21

Umeda H., Nomoto K., 2002, ApJ, 565, 385 17

Umeda H., Nomoto K., 2008, ApJ, 673, 1014 18

Utrobin V. P., 2007, A&A, 461, 233 128

van der Hucht K. A., 2001, New A Rev., 45, 135 8

van der Hucht K. A., 2006, A&A, 458, 453 153

van der Hucht K. A., Conti P. S., Lundstrom I., Stenholm B., 1981, Space Sci. Rev., 28, 227 42

Van Dyk S. D., Cenko S. B., Poznanski D., et al., 2012, ApJ, 756, 131 116, 152

Van Dyk S. D., Davidge T. J., Elias-Rosa N., et al., 2010, ArXiv e-prints 132

Van Dyk S. D., Li W., Cenko S. B., et al., 2011, ApJ, 741, L28 84

Van Dyk S. D., Li W., Filippenko A. V., 2003a, PASP, 115, 1 152

Van Dyk S. D., Li W., Filippenko A. V., 2003b, PASP, 115, 1289 152

van Genderen A. M., 2001, A&A, 366, 508 6

van Leeuwen F., 2007, A&A, 474, 653 xxxii, xl, 12, 117, 121

Vanbeveren D., De Loore C., Van Rensbergen W., 1998, A&A Rev., 9, 63 8

Vangeyte B., Manfroid J., Surdej J., 2002, A&A, 388, 712 138, 147

Vazquez R. A., Baume G., Feinstein A., Prado P., 1996, A&AS, 116, 75 43, 47, 48, 50

REFERENCES

Véron-Cetty M.-P., Véron P., 2010, A&A, 518, A10 195

Vink J. S., 2008, in IAU Symposium, edited by L. Deng, K. L. Chan, vol. 252 of IAU Symposium, 271–281 10

Vink J. S., 2012, in Astrophysics and Space Science Library, edited by K. Davidson, R. M. Humphreys, vol. 384 of Astrophysics and Space Science Library, 221 6

Vinkó J., Takáts K., Szalai T., et al., 2012, A&A, 540, A93 84, 95, 96

Walborn N. R., 1973, ApJ, 179, 517 48

Walborn N. R., 1982, AJ, 87, 1300 48

Wang J., Townsley L. K., Feigelson E. D., et al., 2007, ApJS, 168, 100 63

Wang L., Baade D., Höflich P., et al., 2003a, ApJ, 591, 1110 23, 113, 124, 129

Wang L., Baade D., Höflich P., Wheeler J. C., 2003b, ApJ, 592, 457 129

Wang L., Howell D. A., Höflich P., Wheeler J. C., 2001, ApJ, 550, 1030 113

Wang L., Wheeler J. C., 1996, ApJ, 462, L27 114

Wang L., Wheeler J. C., 2008, ARA&A, 46, 433 22

Wang Y., 2007, ApJ, 654, L123 192

Ward-Thompson D., André P., Crutcher R., Johnstone D., Onishi T., Wilson C., 2007, Protostars and Planets V, eds. B. Reipurth, D. Jewitt, & K. Keil, 33–46 76

Waxman E., Mészáros P., Campana S., 2007, ApJ, 667, 351 92

Wheeler J. C., 2000, in American Institute of Physics Conference Series, edited by S. S. Holt, W. W. Zhang, vol. 522 of American Institute of Physics Conference Series, 445–466 113

Wheeler J. C., Barker E., Benjamin R., et al., 1993, ApJ, 417, L71 92, 93

Wheeler J. C., Filippenko A. V., 1996, in IAU Colloq. 145: Supernovae and Supernova Remnants, edited by T. S. Kuhn, 241 114

Wheeler J. C., Harkness R. P., 1990, Reports on Progress in Physics, 53, 1467 xxv, 14

White R. J., Basri G., 2003, ApJ, 582, 1109 53

Whittet D. C. B., ed., 2003, Dust in the galactic environment 47

Widenhorn R., Blouke M. M., Weber A., Rest A., Bodegom E., 2002, in Sensors and Camera Systems for Scientific, Industrial, and Digital Photography Applications III, edited by M. M. Blouke, J. Canosa, N. Sampat, vol. 4669 of Society of Photo-Optical Instrumentation Engineers (SPIE) Conference Series, 193–201 146

Williams J. P., Blitz L., McKee C. F., 2000, Protostars and Planets IV, 97 10

Wilson J. R., 1983, Energy Technology Review, 12–19 19

Winston E., Megeath S. T., Wolk S. J., et al., 2007, ApJ, 669, 493 76

Wolf B., Appenzeller I., Stahl O., 1981, A&A, 103, 94 6

Wood-Vasey W. M., Miknaitis G., Stubbs C. W., et al., 2007, ApJ, 666, 694 194

Woosley S., Janka T., 2005, Nature Physics, 1, 147 83

Woosley S. E., 2010, ApJ, 719, L204 18

Woosley S. E., Blinnikov S., Heger A., 2007, Nature, 450, 390 18

Woosley S. E., Eastman R. G., Weaver T. A., Pinto P. A., 1994, ApJ, 429, 300 91, 110

Woosley S. E., Heger A., Weaver T. A., 2002, Reviews of Modern Physics, 74, 1015 18, 153

Woosley S. E., Pinto P. A., Martin P. G., Weaver T. A., 1987, ApJ, 318, 664 83

Woosley S. E., Weaver T. A., 1982, in NATO ASIC Proc. 90: Supernovae: A Survey of Current Research, edited by M. J. Rees, R. J. Stoneham, 79 15

Woosley S. E., Weaver T. A., 1995, ApJS, 101, 181 3, 18, 39

Yadav N., Ray A., Chakraborti S., et al., 2014, ApJ, 782, 30 117

Yonekura Y., Asayama S., Kimura K., et al., 2005, ApJ, 634, 476 75

Young T. R., Baron E., Branch D., 1995, ApJ, 449, L51 102

Zerbi F. M., Chincarini G., Ghisellini G., et al., 2004, in Ground-based Instrumentation for Astronomy, edited by A. F. M. Moorwood, M. Iye, vol. 5492 of Society of Photo-Optical Instrumentation Engineers (SPIE) Conference Series, 1590–1601 23

Zhang T., Wang X., Li W., et al., 2006, AJ, 131, 2245 130

Zinnecker H., McCaughrean M. J., Wilking B. A., 1993, in Protostars and Planets III, edited by E. H. Levy, J. I. Lunine, 429–495 70

Zinnecker H., Yorke H. W., 2007, ARA&A, 45, 481 39